Fakultät für Naturwissenschaften
Institut für Elektrochemie

From Normal Electrolysis to anodic Contact Glow Discharge Electrolysis: Stability of Materials and Influence on the Electrolyte

Dissertation zur Erlangung des Doktorgrades Dr. rer. nat.
der Fakultät für Naturwissenschaften der
Universität Ulm

vorgelegt von
Evelyn Artmann
aus Ulm
2023

Amtierender Dekan: Herr Prof. Dr. Thorsten Bernhardt
Erstgutachter: Herr Prof. Dr. Timo Jacob
Zweitgutachter: Herr PD Dr. Joachim Bansmann
Dissertation eingereicht am: 21.03.2023
Mündliche Prüfung am: 27.06.2023

Contents

Acronyms

AE Auxiliary Electrode.

CA Chronoamperometry.

CAFF Controlled-Atmosphere Flame Fusion.

CE Counter Electrode.

CGDE Contact Glow Discharge Electrolysis.

CV Cyclic Voltammogram.

DC Direct Current.

ECE Electrochemical Counter Electrode.

ECSA Electrochemical Surface Area.

ELOXAL Electrolytic Oxidation of Aluminium.

ETD Everhart-Thornley Detector.

EWE Electrochemical Working Electrode.

FTIR Fourier-Transform Infrared Spectroscopy.

GDE Glow Discharge Electrolysis.

HER Hydrogen Evolution Reaction.

HOR Hydrogen Oxidation Reaction.

HV High Voltage.

LSV Linear Sweep Voltammetry.

ML Monolayer.

NE Normal Electrolysis.

NP Nanoparticle.

NPG Nanoporous Au.

OER Oxygen Evolution Reaction.

ORR Oxygen Reduction Reaction.

PCE Plasma Counter Electrode.

PEO Plasma Electrolytic Oxidation.

PEP Plasma Electrolytic Polishing.

POSC Poly-Oriented Single Crystal.

PWE Plasma Working Electrode.

RF Roughness Factor.

RHE Reversible Hydrogen Electrode.

rSCV Reversed Staircase Voltammetry.

SCV Staircase Voltammetry.

SEM Scanning Electron Microscope.

SPST Single Point Single Temperature.

UVAS UV Absorption Spectroscopy.

WE Working Electrode.

XPS X-Ray Photoelectron Spectroscopy.

1 Introduction

Electrolysis is the process during which an electrolyte or components in the electrolyte decompose. In this process, an (electro)chemical transformation takes place at the electrode | electrolyte interface.[1, 2]
Standard electrode potentials can be used to predict which products are formed during electrolysis. The standard electrode potentials are defined under standard conditions against a reference electrode, usually the standard hydrogen electrode.[3] The electrode potentials can, under certain experimental conditions, be determined using the Nernst equation.[4] Additionally, both the direction of the reaction and the voltage required for the reaction can be predicted.[5] One of the most intensively studied electrolysis reaction is the electrolysis of water, whereby water (H_2O) is split into its components oxygen (O_2) and hydrogen (H_2). This reaction is used in so-called electrolyzers.[6–8] The reverse reaction, namely the formation of water from O_2 and H_2, is used in fuel cells.[9–11] Both the formation of water from O_2 and H_2[9–11], and its splitting[6–8] play a decisive role in the development of energy and conversion technologies in the renewable energy sector. The decomposition of water takes place beyond the stability window of water, i.e., in a range which is denoted as normal electrolysis (NE) in this thesis. Depending on the polarity of the electrode (positive or negative), O_2 or H_2 is formed at the anode or cathode, respectively.
If one considers the *I–U* curve over a larger voltage range for gas-evolving electrodes, the curve can be divided into different regions. Figure 1.1 schematically illustrates the *I–U* curve for both positive and negative electrode polarization. The units are chosen arbitrarily and can vary depending on the experimental parameters.Here, the stability window of water is marked in green. The entire region under consideration (above the stability range of water) is referred to as HV electrolysis region in this thesis.

If the voltage is increased in the NE region the current increases linearly with the

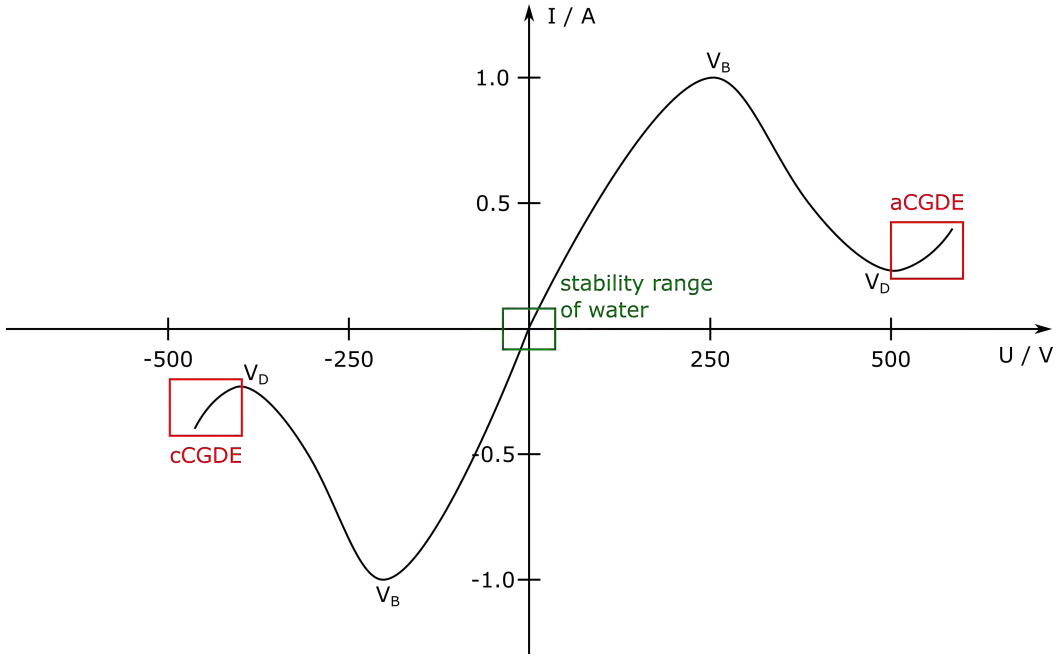

Figure 1.1: Schematic representation of an *I–U* curve over the range from cCGDE to aCGDE. The stability window of water is marked in green, the regions of cCGDE (negative current density) and aCGDE (positive current density) are marked in red.

voltage and bubbles form around the electrodes. At the breakdown voltage (V_B), the contact area between the electrode and the electrolyte decreases due to significant bubble formation, and the current drops. Above the breakdown of NE, contact glow discharge electrolysis (CGDE) takes place, i.e. a gas sheath is formed around the electrode in which a plasma ignites. CGDE usually starts at the minimum of the *I–U* curve (midpoint voltage, V_D) after the breakdown of NE. This region, of anodic CGDE (aCGDE, positive current density) and cathodic CGDE (cCGDE, negative current density), is shown in red in Fig. 1.1. The gas layer in which the plasma is ignited is in contact with both the electrode and the electrolyte. Hence, both a solid | gas interface and a gas | liquid interface are formed. Above V_D the current increases again.

Already several decades ago, but increasingly in recent years, electrolysis has not only been carried out in the range of a few volts, but also in the range of a few hundred volts, where additional effects occur, such as the formation of a plasma in-liquid in the forming gas layer around the electrode.

A plasma is a quasi-neutral ionized gas in which free charge carriers are present.[12,

13] Plasmas can be perceived in nature, e.g., in the form of lightnings during thunderstorms or in certain regions of the world in the form of auroras.[13] Because of their unique properties, plasmas are also referred to as the fourth state of matter, in addition to the states of solid, liquid, and gas.[14]

Early reports, at around 1950, that can be attributed to the occurrence of a plasma in-liquid, frequently mention the so-called "anode effect". In this context, often a plasma is meant which appears during the electrolysis of, e.g., molten salts.[15–17] Pioneers in the field of in-liquid plasma include Kellogg, as well as Hickling and Ingram.[17, 18]

In their work, the focus is entirely on plasma in-liquid, in particular on contact glow discharge electrolysis (CGDE) of gas-evolving electrodes. Hereby, two electrodes, the plasma working electrode (PWE) and the plasma counter electrode (PCE) are immersed into an aqueous electrolyte and a sufficiently high voltage is applied to cause the formation of a gas sheath around the electrode, in which a plasma ignites. The plasma is apparent by a characteristic glow where the color is determined by species in or near the plasma, e.g., H_2, O_2, or ions from the electrolyte.[17, 18]

Both for NE and CGDE applications, a fundamental understanding of the processes at the working electrode, the stability of the working electrode, and the influence of the current flow, induced by the applied voltage, on the electrolyte is essential. In both voltage ranges, either a stable or a restructured electrode is desired, depending on the application, and the stability of the electrode thus defines its possible uses.

Electrodes can for example be restructured by HV electrolysis (including the plasma region). For the formation of nanoparticles in solution,[14, 19, 20] for surface modification and nanostructuring of electrodes,[21, 22] as well as in the field of anodization[23, 24] or plasma electrolytic oxidation (PEO),[25–27] electrode restructuring is desired. In other cases stable electrodes are required which would otherwise comprise their application. For example in the field of catalysis[28–30] or plasma catalysis,[31–33] or the use of plasmas in the field of wastewater treatment[14, 34–37]. Interestingly, despite the very different voltages, the NE and CGDE area have similar application possibilities. If, for example, an oxide film is formed on the electrodes by electrolysis, this process is called anodization in the NE area, and plasma electrolytic oxidation (PEO) in the plasma range. Another example is electropolishing or plasma electrolytic polishing (PEP). In both cases, a surface can be flattened. In addition to these very similar procedures for electrode modification at very dif-

ferent voltages, there are also similarities in the interaction or modification of the electrolyte in both voltage regimes. In both cases, electrolysis induces a voltage drop in the electrolyte and changes the product composition.
Despite the suitability of both areas for electrode modifications and electrolyte modifications, the voltage range in between NE and CGDE has remained largely unexplored and the question arises what actually happens in the voltage range and if it is possible to achieve the desired electrode or electrolyte changes also in the region of HV electrolysis? In order to close this gap, an investigation with stepwise approach towards high voltages, i.e., a detailed investigation of the HV electrolysis range can provide new insights.
Starting from low voltages or from an electrochemical point of view, catalytically active materials such as Pt, Au and Cu are of special interest.
Pt is often used as a model (catalyst) and benchmark system, as it is used in a wide range of applications, including fuel cells and electrolyzers, making it a very well studied system.[28, 38–41] Au electrodes are also often used as a model system due to their noble character.[29, 42, 43] Au nanoparticles, as well as nanoporous Au electrodes, are part of intensive research due to their modified properties compared to the bulk material.[44–48] For example, they are suitable as catalysts for CO oxidation or can be used as sensors in the field of biosensors[45, 49–51] or biomedicine[51] due to their optically modified properties. Cu, as a non-noble metal, shows great potential in terms of electrochemical reduction of CO_2 to higher value carbon compounds, making it also electrocatalytically highly interesting.[14, 30, 52, 53]
Systematic studies with these materials at high voltages (under HV electrolysis conditions) and under in-liquid plasma conditions can elicit the suitability of each material for various applications.
Thereby, (material dependent) structural changes of the electrodes, as well as insights into the changes in the electrolyte induced by HV electrolysis or CGDE can be gained and evaluated.
In a further step, single crystals can be investigated and the knowledge gained through them can be transferred to poly-crystalline samples. Single crystals are often used as model systems in electrocatalysis due to their atomically well-defined surfaces. The study of single crystals under HV electrolysis and CGDE conditions thus allows, on the one hand, to investigate the influence of the crystallographic orientation on the structural changes of the electrode under these conditions. On

the other hand, single crystals also allow comparing the behavior of the materials at high voltages and in the plasma region with moderate conditions (typical electrochemical conditions).
In this work, for the structural characterization of the electrodes, an optical microscope, scanning electron microscopy (SEM), and X-ray photoelectron spectroscopy (XPS) measurements are used. Electrochemical methods include cyclic voltammetry (CV) and chronoamperometry (CA).
In order to gain a fundamental understanding of the behavior of various materials under HV electrolysis and CGDE conditions and to be able to more reliably attribute effects occurring at high voltages to the high voltage or plasma formed at high voltages, this work systematically investigates the catalytically relevant metals, Pt, Au and Cu with respect to their stability at high voltages and in the plasma region in alkaline electrolytes and illustrates resulting structural changes. Using Au as an example, structural changes that occur at high voltages and the influence of species formed during the plasma on the structure formation of the electrode are then further explored. In a further step, the structure formation on poly-oriented single crystals (POSCs) is considered. As a final step, *in situ* time- and distance-dependent influence of species formed during plasma at an electrode stable under plasma conditions on another electrode in solution is investigated. This investigation is a first step towards in- / post-plasma catalysis and combines for the first time a plasma with a classical electrochemical three-electrode setup.

1.1 Outline

This thesis is structured as follows. In Chapter 2, the objective of this work is first explained in more detail and brought into the context with state of the art research. Chapter 3 covers the fundamentals relevant to this work. Here, different approaches for the generation of in-liquid plasma will initially be examined. Subsequently, the focus is placed on CGDE.
Thereby, important processes and properties of the electrodes during HV electrolysis, such as the characteristic behavior of gas-evolving electrodes at different voltages (*I*–*U* curves), the transition from HV electrolysis to aCGDE and the impact of bubble formation on the current density at the electrode is elaborated. Various parameters affecting the behavior of plasma electrodes in solution at high voltages

or under CGDE conditions, already known in the literature, are addressed and explained, and important parameters are evaluated.
The influence of voltage, both in the NE and CGDE region, on the electrode, as well as the electrolyte, is elaborated.
Thereby, the restructuring of electrodes and the formation of nanoparticles in solution are considered. Known methods for the production of nanoporous Au (NPG) films and the processes occuring are described.
The influence on the electrolyte is considered in terms of voltage drop in the electrolyte and product formation during electrolysis.
Chapter 4 provides an overview on the experimental procedures, the equipment used, and the general evaluation processes.
In Chapter 5, all results obtained during the time of this work are shown. Chapters 5.1-5.3 are all publications that list me as first author. In these, the structural evolution of Pt, Au, and Cu anodes at high voltages in alkaline electrolyte is discussed, how an in-liquid plasma impacts a nearby electrode in solution, and how the structure of nanoporous Au films on a Au substrate can be controlled. Chapter 5.4 contains results published on a preprint server on Au poly-oriented single crystals. Here, the structure formation in a facet-dependent manner on Au is discussed. Finally, the Chapters 6 and 7 summarize the main results and elicit their relevance to the current state of science.

2 Objective

While the properties and stability of (electro)catalytically relevant electrodes under mild electrolysis conditions (at voltages of a few volts) are generally well studied and several studies also focus on the CGDE range (at voltages of several hundred volts), the range in between has received hardly any attention so far. Within this HV electrolysis region it is unclear if and under which conditions electrodes restructure in these rather harsh environments. Moreover, in the CGDE region, in most cases, little is also known about the stability and possible restructuring of the electrodes and changes occurring in the electrolyte. Thus the following questions can be raised, which will subsequently be addressed:

1. How does the structure of the electrodes behave over the entire voltage range from 50 V to 580 V and which parameters are relevant for the structure formation of the electrodes?
2. What is the origin of the restructuring and is there a dependence of the surface structure formation on the crystallographic orientation?
3. What is the product distribution of the electrolysis products in the solution at such high voltages?

Stability of Catalytically Relevant Materials: The focus of this work is to examine the stability of various electrocatalytically relevant materials, i.e., Pt, Au, and Cu, when a continuous DC voltage is applied between a PWE and a PCE in alkaline electrolyte (KOH) in the range of NE to aCGDE (50 V to 580 V). The aim is to clarify whether their behavior in the HV electrolysis region differs from that in the aCGDE region and to what extent the stability of the materials is affected under these conditions.
While Pt electrodes are more commonly used in the aCGDE regime as it is suggested to be stable under these conditions,[17, 18, 54–57] Au and Cu electrodes are more frequently used in the cCGDE range for the production of Au and Cu

nanoparticles (NPs).[14, 19] However, all three materials have (electro)catalytic significance. Pt and Au electrodes are often used as model or benchmark systems,[29, 42, 58–63] while Cu is the only metal capable of catalyzing reactions of CO_2 to higher valuable hydrocarbon compounds.[14, 30]

Designing Nanostructures: A central question here is to what extend the resulting surface structures of the PWE obtained after HV electrolysis can be specifically modified by changing individual parameters. Experimental parameters that will be investigated in this work are, apart from the electrode material,[18, 56] in particular the value of the voltage, the duration of the electrolysis and the temperature of the electrolyte.[17, 18] These parameters are investigated in this work especially on the example of Au electrodes in order to produce and tune specific structures on the electrode surface.
Further experimental parameters which can be varied and whose influence has already been investigated in the literature for certain systems are for example the anode length, radius, and inclination, as well as the surface tension, the wettability of the electrode, [18, 57], the chemical composition of the electrolyte, the electrolyte concentration or rather the conductivity of the electrolyte [18, 55, 56, 64], the influence of stirring the electrolyte, the electrolyte volume or radius of the cell, and the pressure at which the experiments were performed [18]. Some of these parameters are also considered in this work to validate the results.
Nonetheless, comparing results at high voltages or during CGDE with the literature is often difficult, since characteristic points in the published *I–U* curves can sometimes differ by several hundred volts, depending on the experimental setup.[17, 65, 66]

Effect of Crystallographic Orientation: In a further step, Au poly-oriented single crystals (POSCs) are investigated in order to gain a better understanding of the structure formation on Au under HV electrolysis conditions and to determine possible facet-dependent differences in structure formation.

Influence and Detection of H_2O_2: Another interesting aspect, which can have a decisive influence on the surface structures of the electrodes are non-faradayic processes, which can occur in the plasma region.[54, 55, 67] This means that at high voltages H_2 and H_2O_2 can be detected in solution in addition to the expected product O_2.[18, 54, 67] The influence of these species on the surface structures of the electrodes will be evaluated in a material-dependent manner.

The effect of H_2O_2 on the formed surface structures is then further investigated using Au electrodes as an example. For this purpose, the electrodes were on the one hand kept in the electrolysis solution with the non-faradaic products after HV electrolysis and on the other hand exposed to electrolyte solutions containing H_2O_2 with varying H_2O_2 concentrations and electrolyte temperatures after HV electrolysis. The resulting structural differences were subsequently determined.
A common approach in literature to determine the amount of H_2O_2 formed during the plasma is the use of titration after the plasma.[54, 67] This approach has the disadvantage that H_2O_2 can be detected neither local, nor time-resolved. In this work, we will for the first time attempt to detect H_2O_2 formed during aCGDE in a five-electrode setup *in-situ* in a time- and distance-dependent manner. Here, the detection is performed electrochemically at an auxiliary electrode (AE) in solution. In this way, both the time-and distance-dependence of the occurrence of H_2O_2 formed during the plasma will be analyzed. For this purpose, a stable plasma electrode will be used and the influence of H_2O_2 formed on another electrode in solution (auxiliary electrode, AE) will be investigated.

3 General Concepts and Application Possibilities

In this Chapter, some fundamentals and general concepts that are relevant to this thesis will be addressed in more detail.
First, the different experimental approaches for the study of in-liquid plasmas are described in Section 3.1. Then, the focus is set on the *I*–*U* curve obtained during HV electrolysis at gas evolving electrodes, which is described in Section 3.2. The individual voltage regions in the *I*–*U* characteristic, their current density, and the transition of HV electrolysis to CGDE and differences between aCGDE and cCGDE will be highlighted.
The influence of experimental parameters, such as the choice and assembly of electrodes, conductivity of the electrolyte, and bubbles on the *I*–*U* characteristic will be elaborated in Section 3.2.1.
Possible applications of electrolysis, both in the field of NE and CGDE, are subsequently considered. Applications aiming at modifying the electrode are discussed in Section 3.3, while those aiming at modifying the electrolyte are discussed in Section 3.4.
Possibilities to modify electrodes include surface oxide formation, electrode restructuring, and nanoparticle formation by dissolving the working electrode material.
In the electrolyte, electrolysis can change the product compositions and increase the electrolytes temperature. Furthermore, during electrolysis, there is a voltage drop/electric field due to the applied voltage inside the electrolyte.
For each field of application, examples from both NE and CGDE are provided. The examples given here refer mainly to the metals Pt, Au, and Cu which are relevant to this work.

3.1 Experimental Approaches for the Study of in-liquid Plasmas

Plasmas in general can be categorized based on different aspects. Possible classifications are, for example, based on the pressure (low-pressure, atmospheric-pressure, and high-pressure plasmas), the content of charged particles in the plasma, the aggregate state of the medium in which they are generated (gas phase plasma, in-liquid plasma, or solid state plasma), the modulation of the applied voltage to the electrodes (AC or DC and/or AC/DC pulsed).[14, 68]
This work focused on plasmas ignited in-liquid. The experimental approaches to study such plasmas can be grouped into several categories, [14, 19, 69, 70] and a selection is provided in Fig. 3.1.[19, 70] Note, that the schematic drawing of each approach represents only one of many possible setup realizations.[19] Since the plasma in each category differs, a brief overview of different plasma in-liquid approaches is given below before the in-liquid approach used in this work (Fig. 3.1) is addressed.

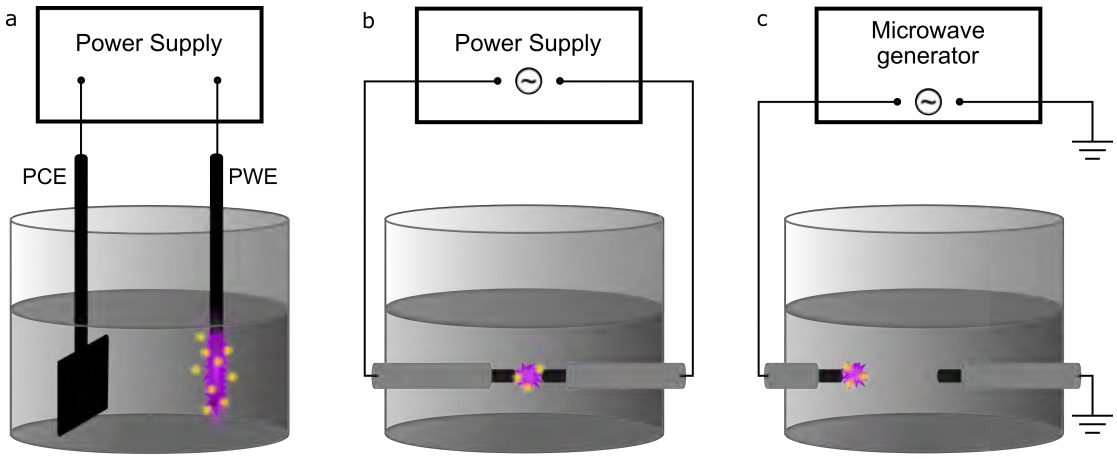

Figure 3.1: Experimental approaches for studying plasmas in contact with a liquid. In a) two electrodes of very different sizes are immersed in the solution and the plasma is ignited at the smaller electrode. In approach b) both electrodes have the same size, and the plasma is ignited in between the electrodes, and in approach c) the plasma is generated using a RF or microwave generator. Figure according to [19].

Approach 1 is shown in Fig. 3.1a, where two electrodes of significantly different sizes are immersed in the solution.[19] This approach is used, for example, for plasma electrolytic oxidation (PEO), contact glow discharge electrolysis (CGDE), or plasma electrolysis experiments. By applying a (pulsed) DC or AC voltage, bubbles form on the electrodes and Joule heating takes place. By evaporation of the electrolyte, a gas layer forms around the smaller of the two electrodes.[71] The Leidenfrost effect, i.e., the movement of a liquid on a gas film caused by a very hot substrate, which is the working electrode in this case, can be observed.[72] A plasma is then ignited in the gas layer formed around the electrode. The temperature is locally very high within the gas layer that is formed. Sen Gupta determined the electron temperature during aCGDE and cCGDE and found electron temperatures in the order of 10^4 K ($8.6 \cdot 10^{-4}$ eV).[35] Moreover, this approach is highly variable in terms of experimental possibilities. For example, the distance between electrodes can be readily adjusted.

Approach 2 is shown in Fig. 3.1b, where two identical electrodes are immersed in the solution.[19, 73] The distance between the electrodes is very small. By applying a DC, pulsed DC, or AC voltage, plasma is generated between them.[14, 19] One caveat of the approach is that if the electrodes dissolve during the plasma measurement, the distance between the electrodes increases over time. Once a critical distance between the electrodes is reached, a stable plasma can no longer be maintained. To maintain a stable plasma over longer periods of time, it is suggested to slightly adjust the position of one electrode during the measurement in order to keep the distance between the electrodes constant.[19]

Approach 3 is shown in Fig. 3.1c[14, 19], where a plasma is generated in-liquid by AC voltage with radio frequency or a frequency in the microwave range. The advantages of this approach are that the energy required to form a plasma is rather small and that the plasma can be maintained for a large electrolyte conductivity range.[19]

In this work, exclusively Approach 1 illustrated in Fig. 3.1a is used, where the plasma is ignited at the anode applying a continuous DC voltage (see Section 4.4.1).

3.2 *I–U* Characteristic

The potential dependent processes occurring at the solid (| gas) | liquid interface during HV electrolysis can be inferred from *I–U* curves. A schematic illustration of such an *I–U* curve for gas-evolving electrodes is shown above in Fig. 1.1. It is apparent that for positive and negative voltage, the run of the curves is similar, but the features are located at different potentials. In general, the shape of the *I–U* curve can be explained as follows.

OER/HER: First, at small voltages, above the thermodynamically required voltage for water splitting electrolysis of water takes place. Here, hydrogen evolution takes place below 0.0 V and oxygen evolution above 1.23 V, according to the following equations (in an alkaline electrolyte). The voltages refer to the reversible hydrogen scale.[74, 75]

$$2H_2O + 2e^- \rightarrow H_2 + 2OH^- \tag{3.1}$$

$$4OH^- \rightarrow O_2 + 2H_2O + 4e^- \tag{3.2}$$

In reality, however, the decomposition voltage of water is higher and thus deviates from the thermodynamically required voltage due to overpotentials.[74, 76] The overpotential is composed of different contributions, which can be divided into overpotentials resulting from resistances of the reaction at the electrodes and transport limitations.[2]
At low currents, the activation overpotential of the reaction dominates. Additionally, at high currents, the voltage drop in the solution is much more relevant. The transfer of more electrons in the case of OER and the resulting more complex mechanism and slow kinetics (low exchange current density) lead to a much higher overpotential compared to the HER and a low current flow in the case of the OER.[75, 77] Many efforts to lower the overpotentials in water splitting, therefore, focus on the OER, to achieve a higher efficiency during electrolysis. Thus, the choice of a suitable and also stable catalyst is crucial.[78]
The kinetics of electron transfer at the electrode | electrolyte interface for the respective half-cell reaction can in general be described for small overpotentials by

the Butler-Volmer equation.[3, 79, 80] At the equilibrium potential the overall current flow is zero. At higher potentials, oxidation occurs (positive currents), and at lower potentials, reduction occurs (negative currents).[5] In each case, oxidation or reduction, the current increases/decreases exponentially as the potential increases/decreases[3, 5] and finally reaches a linear progression defined by the voltage drop in the solution according to Ohms law.[81]

Normal Electrolysis: In electrochemistry, NE is often referred to as the potential region around the water splitting potential. In the field of plasma and also in this work the region above the water splitting potential up to V_B is referred to as NE.
If the voltage is increased within the NE region, the current increases linearly with the voltage. This region is also known as "Ohmic region". The kinetics of the processes at the electrode can be described by Faraday's law.[54, 67, 82] Furthermore, as the voltage increases, the amount of bubbles formed on the electrode increases continuously.

Breakdown Voltage V_B: At the breakdown voltage V_B, the number of bubbles formed at the electrode is finally so high that a gas film forms around the electrode, which leads to a drop in current.[83] The initially rather unstable gas film becomes more stable when the voltage is further increased. Before the minimum in the *I–U* characteristic is reached, partial CGDE develops, which means that individual plasma spots are formed in the gas layer around the electrode.

Midpoint Voltage V_D: At the minimum of the *I–U* characteristic, a plasma ignites in the entire gas layer that has formed around the electrode. This point is called midpoint voltage (V_D). If the voltage is increased even further, the current increases again since the gas layer formed around the electrode is quite stable and thus an almost constant resistance around the electrode can be assumed.[18, 56, 82, 84–86]
The transition from NE to CGDE depends hereby on the contact area of the electrode | electrolyte interface. The transition has been rationalized in the literature by effects such as Joule heating,[35, 57, 71, 87] the occurrence of hydrodynamic instabilities,[17, 35, 57, 71] the influence of the number of emitted secondary electrons[35] or a mechanism change in the OER[87].
Yerokhin *et al.* who attributed the transition from NE to CGDE to a mechanism change in the OER concluded, that the mechanistic aspects during CGDE are sim-

ilar to those of a fully oxidized electrode, where all active sites are occupied by reaction intermediates of the OER.[87] CGDE, according to Yerokhin *et al.*, thus represents an extreme case of NE and the appearance of CGDE cannot solely be explained in terms of Joule heating and hydrodynamic instabilities.[87]
Slovetskii and Terent'ev, instead, assume that the transition from bubbles to a stable gas layer around the electrode is related to the dissipation of heat from the electrode to the electrolyte. They observed that a stable gas layer forms around the electrode when the heat dissipation and thus the electrode temperature reaches a steady state condition.[88]

aCGDE vs. cCGDE: As mentioned above and shown in Fig. 1.1, in the case of cCGDE the characteristic points in the *I–U* curve, especially above V_B are shifted to smaller voltages compared to aCGDE. As a reason for this, the literature suggests the nature of the cathode and the Townsend secondary electron emission coefficient. The Townsend secondary electron emission coefficient expresses the number of generated secondary electrons and differs significantly in the case of aCGDE and cCGDE.[71, 85, 89, 90] During aCGDE, cations are accelerated away from the anode, whereas, in the case of cCGDE, cations are accelerated towards the cathode, leading to the generation of secondary electrons.[12] This results in a significantly higher Townsend secondary electron emission coefficient for cCGDE compared to aCGDE. The fraction of secondary electrons emitted from the cathode with high kinetic energy in turn facilitates the transition from NE to CGDE. V_D is thus located at significantly lower voltages for cCGDE and the formation of a plasma occurs much earlier.[35, 71, 85]

3.2.1 Parameters Influencing the *I–U* Characteristic

The shape of the *I–U* curve for gas-evolving electrodes depends on a number of factors. Several reasons are discussed in the literature, which are presented in the following.

Electrode Material: The influence of different electrode materials was already investigated by Hickling and Ingram in 1964. They found that platinized Pt, Pd, and Au have a similar *I–U* characteristic in 0.05 M Na_2HPO_4, while Cu and nichrome corroded strongly. Tungsten, which is a commonly used material in plasma research,

formed a poorly conducting oxide film.[18]
These differences can be explained by the observation that some electrodes continuously evolve a gas, while others form oxides. The aforementioned description of the *I–U* characteristic apply to gas-evolving electrodes. Oxide-forming electrodes show a deviating and much more complex behavior. A schematic *I–U* curve for gas-evolving and oxide-forming electrodes is shown in Fig. 3.2.[82] In the case of oxide-forming electrodes, the current initially follows Ohm's law. However, as the name suggests, oxide-forming electrodes form a passive film around the electrode. At sufficiently high voltages, this passive oxide film begins to dissolve again. In the *I–U* characteristic, this behavior is apparent by a current peak. At even higher voltages, a porous oxide film forms. Tunnel ionization through the pores of the porous oxide film leads to the formation of sparks on the surface of the porous oxide film. At even higher voltages, additionally, thermal ionization occurs. The emerging charge on the electrolyte surface blocks the oxide film, resulting in micro-arc discharges. The micro-arc discharges can migrate to the electrode and thermally crack the formed oxide film.[82] Since more processes are taking place on oxide-forming electrodes and the individual processes (formation, dissolution of the oxide layer, etc.) can be less clearly separated from one another in the *I–U* characteristic, oxide-forming electrodes are much more complex systems than gas-evolving electrodes.
As mentioned before, in this work only gas-evolving electrodes are considered.

Experimental Procedure: A decisive factor in the experimental procedure is, for example, whether the voltage is increased stepwise (staircase voltammetry - SCV),[85] linear (linear sweep voltammetry - LSV),[91, 92] i.e., in both cases all voltages are investigated successively in one experiment, or whether the investigation of each voltage is a separate experiment with the same initial conditions (single point single temperature - SPST)[22] (see Chapter 5.1 Fig. 5.14). In the first case (one experiment for all voltages), the changes that occur at the electrode in the course of the measurement play a much larger role than in the second case (one experiment for each voltage). Deviations in the *I–U* characteristic for different materials are thus much more likely with a stepwise increase of the voltage since the conditions at different voltages vary as the measurement progresses.
Another parameter that should be taken into account is whether the electrolyte is stirred or not since stirring the electrolyte affects the temperature distribution in the electrolyte.[18] If the electrolyte is not stirred, the temperature distribution in the

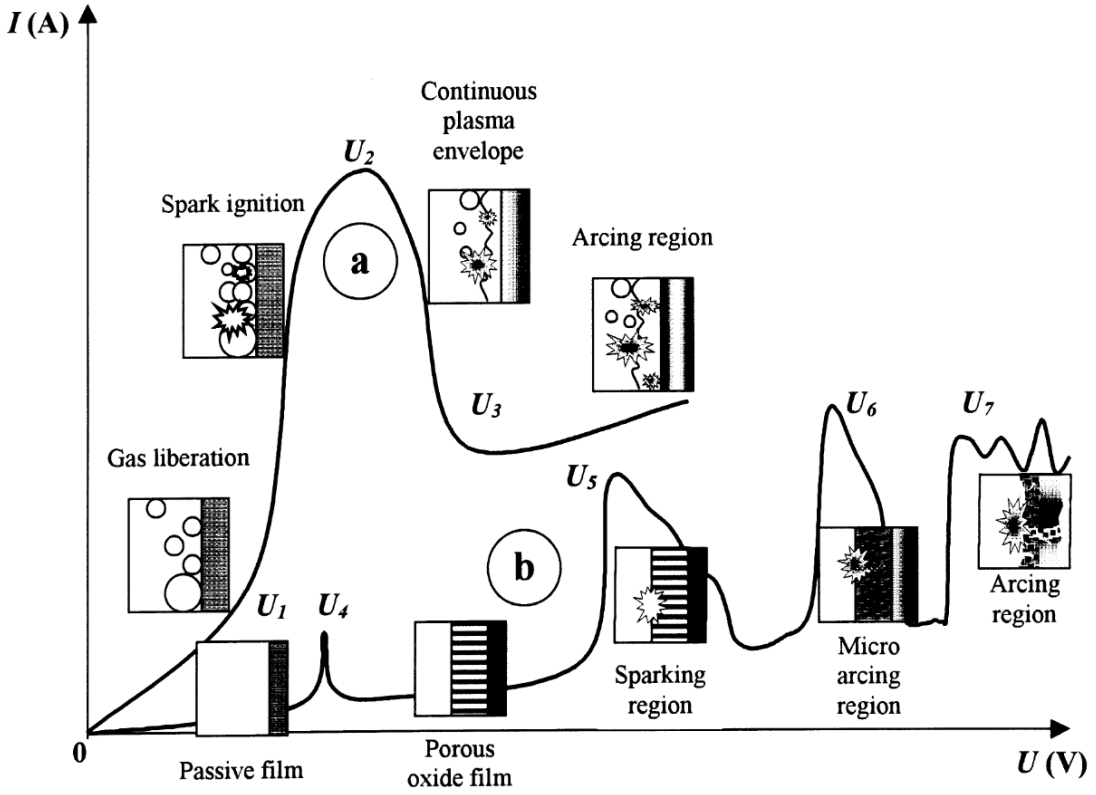

Figure 3.2: *I–U* curve of a) a gas-evolving and b) an oxide-forming electrode.[82] Reprinted from Surf. Coat. Technol., 122, A.L.Yerokhin *et al.*, "Plasma electrolysis for surface engineering", 73-93, Copyright 1999, with permission from Elsevier.

electrolyte during and also shortly after HV electrolysis is significantly less homogeneous than if the electrolyte is stirred. In this regard, the lower the initial electrolyte temperature, the larger the influence of stirring on the *I–U* characteristic, since with stirring the boiling point of the electrolyte near the electrode is reached much later.[18] The effect of conductivity on the *I–U* characteristic is described further below.

Electrode Geometry: The *I–U* characteristic also depends on the electrodes' geometry.

Often a wire is used as the smaller electrode at which the plasma is ignited. Hickling and Ingram found that the angle at which the wire is immersed in solution is not important as long as it is less than 45 °, to ensure that bubbles can be removed efficiently.[18, 93] In addition, the length of the wire immersed in the electrolyte also plays a minor role as long as the ratio of length to radius is $\geq$ 20:1. A longer length of wire immersed in the electrolyte only increases the current.[18, 57]

The situation is different if the radius of the wire is changed. Sen Gupta and Singh found that the energy required to reach V_B decreases with an increasing wire radius for a constant wire length.[85] This behavior was also observed in this work and is described in Chapter 4 Section 4.4.1.2. The higher current density with decreasing wire diameter can be explained by the thickness of the gas layer around the electrode since the thickness of the gas layer formed around the electrode is not proportional to the wire diameter.

Electrolyte Conductivity: Another parameter that has a decisive impact on the *I–U* characteristic is the conductivity of the electrolyte. The conductivity of the electrolyte can be changed by the (initial) electrolyte temperature and the electrolyte concentration.[17, 64, 70, 92, 94]

The conductivity of the electrolyte is inverse proportional to the electrolyte resistance. That means higher conductivity of the electrolyte leads to a lower electrolyte resistance and thus to higher currents. This can be observed in particular below V_B, i.e. in the ohmic range.[18] According to Jin *et al.* V_D decreases as the electrolyte conductivity increases and remains unchanged above a certain conductivity value, which depends on the electrolyte.[56]

Chemical Composition of the Electrolyte: For electrolytes with different chemical compositions but similar conductivity, similar *I–U* characteristics are obtained.[18,

55] This has been demonstrated by Hickling and Ingram by comparing measurements performed in Na_2HPO_4, H_2SO_4, NaOH, azide, chloride, and acetate containing electrolytes. Despite the partially different products formed during HV electrolysis depending on the electrolyte, V_B and V_D remained almost unchanged.[18]

Electrolyte Temperature: If the initial electrolyte temperature is higher, less energy is required to evaporate the electrolyte, i.e., to form a gas layer around the electrode. Therefore, V_B shifts to lower voltages. Since the energy required to evaporate the electrolyte is lower, the currents at V_B are also lower.[18, 70, 71, 85, 92] At voltages above V_B, the lower the electrolyte resistance, i.e., the higher the initial electrolyte temperature, the smaller the currents, since less energy is needed to form a plasma.

If the voltage is increased at a constant rate starting from NE up to the CGDE region and then gradually decreased again, significant differences in the *I–U* characteristic can be seen as long as the temperature of the electrolyte is not constant.[84] Thus, for repeated potential cycling between high and low voltages without cooling the electrolyte, the *I–U* characteristic differs from cycle to cycle until the electrolyte temperature reaches the boiling point and thereby a constant electrolyte temperature. In this context, it is also relevant whether the electrolyte was stirred[70] or not[84] during the experiment, since stirring influences the temperature distribution in the electrolyte.
Measurements and discussion along the problematic of heating the electrolyte depending on the experimental procedure are described in Chapter 4 Section 4.4.1.4.

Bubbles: The resistance in the cell is also related to bubbles that form on and around the electrode during electrolysis. Even when the resistance of the bulk electrolyte remains constant, the resistance near the plasma working electrode changes due to the (partial) coverage of the electrode surface with bubbles. As a result, the electrochemical active surface area is (locally) reduced and thus the overall resistance is increased, leading to two phenomena.[93] On the one hand, the actual current density at the electrode is larger than the measured current density suggests,[95] and, on the other hand, the voltage drop across the electrode | electrolyte interface is larger when bubbles are present on the electrode surface.[96]
The current drop due to bubbles in the electrolyte has already been demonstrated experimentally by Kellogg.[17] He found that in the NE region, which means below V_B, the bubbles ascend, while at voltages above V_B the bubbles are pushed away from the electrode into the electrolyte. This effect increases the electrolyte resis-

tance and is leading to a drop in the current.[17]
According to Kellogg, the higher the initial electrolyte temperature, and thus the smaller the temperature difference between the electrode and the electrolyte, the more stable is the gas film that forms around the electrode. Consequently, the gas film formed around the electrode is thinner at low electrolyte temperatures because heat dissipation is easier, and the electrode is thus hotter because there is less resistance in the cell and hence higher currents are possible.[17]
Except for the study by Yerokhin *et al.*[87] (see Section 3.2), the literature suggests that the transition from NE to CGDE at a critical point is caused by Joule heating and the transition from bubbles to a stable gas layer is induced through hydrodynamic instabilities.[17, 57, 71, 87] Accordingly, the formation and the amount of bubbles could play a decisive role regarding the transition from bubbles to a stable gas layer and thus also to a plasma in-liquid.[95] Furthermore, the maximum possible heat flux is reduced through the bubbles, which in turn favors the transition to a plasma in-liquid.[57, 87] Electrodes with lower surface tension show more wetting compared to hydrophobic surfaces and consequently form more stable gas films. The formation of bubbles on the electrode surface often represents an undesirable effect in the field of electrochemistry.[93, 97, 98] Therefore, if possible, in electrochemistry, potentials are studied where no or at least very few bubbles are formed at the electrode surface.[99]
To obtain correct values for the current density, the bubble coverage would have to be determined at any time during the experiment. Then, using the known bubble coverage, the current density of the electrode could be corrected. A quantitative evaluation of the amount of bubbles at the electrode, or the thickness of the gas layer that has formed around the electrode can be carried out, for example, using time-resolved shadowgraphy imaging measurements.[17, 100, 101] Such measurements were not performed within the scope of this work. An alternative approach to describe the bubble formation at the electrode is by using mathematical models. Such models have already been developed for gas-evolving electrodes.[96, 102] The application of such models to correct the current density for to bubble coverage is not part of this work. The influence of bubbles on the current density will be critically discussed.

Final remarks - Parameters reexamined for this work: In Chapter 4.4.1.4 we will show that the measurement procedure has a significant influence on the *I–U* curve.

Additionally, due to the strong influence of individual parameters on the *I–U* curve, some parameters, such as the influence of anode material, wire length and wire radius, as well as the influence of a protective cap at the end of the wire on the *I–U* curve, were reexamined for this work. The parameters initial electrolyte temperature and electrolyte concentration, influencing the conductivity of the electrolyte, were also investigated in this work. Details of these measurements can be found in Chapter 4 Section 4.4.1.

3.3 Electrode Modification

Possible fields of application for electrodes modified by electrolysis are very diverse and range from improved corrosion protection through the formation of a passivating oxide layer on the electrode surface, to the restructuring of the surface for potentially increased (electro)catalytic activity, to the dissolution of the electrode for the formation of nanoparticles, which can in turn also be used in (electro)catalysis. The possible applications listed in this Section are grouped by the desired outcome (oxide formation, restructuring, nanoparticle formation). For each intended electrode modification, at least two examples are presented of how the modification could be achieved (i) in the NE regime (at low voltages) and (ii) by CGDE or through plasma in-liquid approaches (at high voltages).

3.3.1 Electrochemical Oxide Formation

The metals investigated in this work, Pt, Au, and Cu, exhibit different behavior regarding oxide formation. While Pt and Au belong to the noble metals and are corrosion resistant, Cu is less noble and forms a natural oxide layer making it passivated and protected against further reaction with oxygen. In Section 3.3.1.1, the mechanisms of anodic oxide formation for Pt, Au, and Cu in alkaline electrolyte in the field of NE are discussed and special features in the behavior of the individual metals are elaborated.
Passivation is typical for base metals and can be exploited in terms of corrosion protection. Corrosion can be understood as the degradation of an existing workpiece, which can make it unsuitable for further use. The origin of corrosion is the

(electro-)chemical reaction of a workpiece with its environment, which often involves oxygen or water.[103–105]
Electrochemically, an oxide film can be formed on a metal by applying a positive potential to the workpiece/metal to be passivated, which will ideally protect it against subsequent corrosion. Therefore, the workpiece/metal itself has to be in an aqueous (O_2-containing) solution and conductively connected to a more noble metal. Depending on the voltage applied, this procedure is called anodization (low voltage) or plasma electrolytic oxidation (PEO) (high voltage along with the appearance of a plasma). Both anodization and PEO are important electrolysis methods for improving the corrosion resistance of metals by forming oxide films. For this reason, both processes are mainly applied to base metals. The processes taking place in each case, as well as their most industrially relevant applications, will be discussed in Section 3.3.1.2 and Section 3.3.1.3. In Section 3.3.1.2, corrosion protection by anodization is first discussed on the example of Al. PEO is described in Section 3.3.1.3.

3.3.1.1 Oxide Formation on Pt, Au, and Cu

Anodization is generally understood as the formation of oxide films on a metal. For this purpose, a positive potential is applied to the electrode, immersed in an electrolyte, on which an oxide film should be formed.[106, 107] The formation of an oxide film on the electrode is energetically beneficial for all metals except Au with regard to the free energy change.[25] Often the oxide layer formed by applying a voltage to the anode, should preferably, subsequently protect the metal from corrosion. The oxide film formed can hereby be influenced by several parameters, such as the temperature, composition, and pH of the electrolyte or the current during anodization.[24, 108]
In the case of Pt and Au, the formation of an oxide film on the surface for protection against corrosion is not necessary, since Au represents the noblest of all metals[42] and Pt is also corrosion–resistant. Nevertheless, oxide films can be produced on both metals by applying positive voltages.[43, 61, 99, 109, 110] The formation of oxide films on the surface begins for all three metals investigated in this work, Pt, Au, and Cu, by the adsorption of OH^- ions.[43, 61, 110–112] All potentials mentioned below refer to the RHE scale.

Pt: On Pt, adsorption of OH^- ions and the formation of OH_{ad} on the surface in 0.1 M KOH takes place at potentials between 0.6 V and 0.9 V. Above 0.9 V, the formation of oxide begins.[62, 113] A Pt CV measured at room temperature in 0.01 M KOH can be seen in Chapter 5.1 Fig. 5.4. When considering the three low-indices facets, the Pt(111) facet shows the highest onset potential to form oxides, while Pt(110) shows the lowest. Accordingly, the Pt(100) facet shows an intermediate onset potential to oxidize the surface.[113, 114] Favaro *et al.* investigated the different Pt oxide structures forming on the surface of a polycrystalline Pt surface and the mechanism of the OER in 1.0 M KOH. The authors reported that the oxide layer formed on the Pt electrode can be separated into three regions. A $Pt(OH)_{ad}$ layer directly on the Pt surface of the electrode, a Pt(II) layer consisting of $Pt(OH)_2$ and PtO and a PtO_2 layer on the electrolyte side.[62, 111] The sub-surface $Pt(OH)_{ad}$ layer localized directly on the Pt electrode is the oxide layer, which is crucial for O_2 formation. For its formation, OH^- must diffuse from the electrolyte through the existing oxide layer to the Pt electrode.[62] Using anodization in alkaline electrolytes, Pt oxide films (up to approximately 5 nm) can be produced.[110, 111]

Au: In the case of Au, the formation of oxide or hydroxide films starts in 0.1 M KOH at 293 K above a potential of 1.1 V.[113] Adsorption of OH^- ions on the Au surface takes place at the same conditions in the range of 0.7 V to 1.1 V.[113, 115] A Au CV measured in 0.01 M KOH at room temperature is shown in Chapter 5.1 in Fig. 5.8. As for Pt, the electron transfer processes of oxide formation in the positive going scan and oxide dissolution in the negative going scan increase with increasing electrolyte temperature for Au. Additionally, unlike Pt, the adsorption of OH^- ions on the Au surface starts already at smaller potentials, if the temperature is increased.[113]
Au oxide (Au_2O_3) is a thermally unstable semiconductor that decomposes into Au above 121 °C.[43, 116–119] In this process, Au_2O is a metastable intermediate.[29, 118, 119]

Cu: The oxide formation behavior of Cu is slightly different from Pt and Au. Since the solubility of Cu hydroxide decreases in alkaline electrolytes, Cu oxide can be formed in alkaline, while Cu^{2+} ions are formed in acidic electrolytes, which means that usually no oxide can be formed under acidic conditions.[120–122] Focusing on the oxide formation of Cu in alkaline electrolytes, mechanistically, similarly to Pt

and Au, also on Cu, OH^- is first adsorbed on the surface.[112] In 0.1 M NaOH the adsorption of OH^- occurs for Cu at potentials above E > 0.21 V.[123]
Oxide formation starts above a potential of E > 0.56 V with the formation of single non-crystalline grains. In the CV, two peaks can be identified here, which can be attributed to the formation of different oxides. In the range from 0.53 V to 0.83 V, first Cu_2O is formed. In the potential range from 1.18 V to 1.68 V, both CuO and $Cu(OH)_2$ are formed. In this range, the electrode is passivated. Above a potential of E > 1.68 V, oxygen evolution begins.[123] Additionally, the formation of Cu_2O_3 takes place at OER potentials.[124] The Cu electrode is in the transpassive region, i.e., the passivated Cu dissolves.[123]
In the negative going scan, Cu_2O_3 decomposes as soon as the potential is below the OER region and the CuO formed during the anodic scan, as well as $Cu(OH)_2$, is first reduced to Cu_2O and then further reduced to Cu.[123, 124] A CV of a Cu wire electrode in 0.1 M KOH is shown in Chapter 5.1 Fig. 5.12.

3.3.1.2 Anodization

The best known anodization process is probably the Eloxal process, which refers to "Electrolytic Oxidation of Aluminium".[23, 125, 126] In this anodizing process, a thick insulating oxide layer is produced on an Al substrate by electrolytic oxidation (anodizing). Compared to the native oxide film on Al (max. $0.3 \cdot 10^{-4}$ mm), the oxide films formed through anodization are harder and much less susceptible to mechanical stress upon the substrate, as they are significantly thicker (one hundred times thicker than the native oxide layer), making them significantly more resistant to corrosion.[125, 126]
To produce such an oxide film, a voltage is applied to the substrate. The voltage hereby initially causes the formation of an insulating Al_2O_3 layer on the Al surface, and the resistance at the electrode increases. If the voltage is sufficiently high, the oxide layer is dissolved locally, since high electric fields are present which promote the dissolution of the previously formed oxide film (field-enhanced dissolution).[127] At these points, the electrolyte can again penetrate to the Al substrate and oxidize it. At the same time, these points also enable charge compensation. The oxide layer on the substrate grows and pores are formed, which further enable charge balance

and transport of ions.[24, 108, 127, 128] The pore size in the formed microporous oxide film is determined by the electrolyte, while the thickness of the pore walls is defined by the applied voltage.[129] The formation of microstructures is typical for anodization.[23, 25, 129]
To narrow the pores in the oxide film formed, the substrate is further treated with hot water or steam (sealing). In this process, $Al(OH)_3$ or boehmite (AlO(OH)) is formed by reaction with Al_2O_3. The latter has a larger volume than Al_2O_3. The pores of the oxide film are thus narrowed, and the workpiece becomes more resistant to corrosion.[23, 24]

3.3.1.3 Plasma Electrolytic Oxidation (PEO)

The formation of oxide films to protect the underlying substrates from corrosion can also be carried out under in-liquid plasma conditions (at high voltages). This process is called plasma electrolytic oxidation (PEO). PEO is usually performed with metals such as Al, Mg, or Ti alloy substrates.[21, 25, 26, 130] Since, in addition to the voltage, other parameters such as the local temperature of the substrate as well as the mechanism of oxide film formation differ, the oxide films resulting from PEO have a different nature than the oxide films obtained from anodization. The differences in the nature of the films compared to anodization can be explained as follows.
As for anodizing, PEO involves immersing two electrodes in a solution and applying a voltage, but the voltage used for PEO is significantly higher than for anodization, in order to form a plasma. Moreover, AC voltage is used for these measurements. During PEO, local dielectric breakdowns occur, which are accompanied by local (micro-)discharges. These occur at points where the oxide film is still relatively thin or where a pore is present in the coating. Locally, high temperatures are generated, which vaporize the metal and form an oxide with the oxygen formed by the electrolysis. The high temperatures can also favor the crystallization of the oxide film. The oxide films are thus not formed by the transport of ions and their reaction thereafter, but by evaporation of the substrate and reaction of the evaporated metal during the cooling process.[21, 25, 131] The resulting oxide films formed on the electrodes show strong adhesion properties.[21, 25] Furthermore, the oxide-forming reaction during the cooling process offers the possibility of integrating foreign atoms into the

resulting coating and thus doping or selectively modifying the oxide film.[25, 26]
A current challenge in the field of PEO is the processing of PEO films on substrates that are not suitable for PEO. In these cases, a PEO-suitable material is deposited on a metal and then PEO is carried out. The oxide films produced in this way currently still have weaknesses, such as problems in the durability of the oxide layers formed, and are part of current research.[25]
However, in addition, PEO can also be used to initiate the formation of nanoparticles in solution. The formation of nanoparticles, by the dissolution of the electrode, is discussed among other processes, in Section 3.3.3.3.
Compared to anodization, in which the oxide film has micropores (see Section 3.3.1.2), PEO can produce thicker oxide films as well as harder ones. Moreover, the oxide films formed by PEO have a ceramic character.[21, 25, 27, 130, 132] The limiting factor for the thickness of the resulting oxide films is the formation of (micro-)discharges.[25, 130, 131] However, the control and targeted modification of the resulting films is much more challenging for PEO than for anodization, since the substrate changes after each (micro-)discharge.

3.3.2 General Remarks to the Oxide Formation on Electrodes

The processes and mechanisms that can underlie the formation of oxides in the NE region (adsorption, place exchange, etc.) and under plasma conditions (evaporation of the substrate at high local temperatures due to the occurrence of local discharges) provide an important basis for this work, since both the processes occurring at low voltages and those occurring at high voltages could also occur at intermediate voltages.
Chapter 5.1 discusses the oxide formation on Au and Cu over the entire HV electrolysis range, and also possible reasons why oxide formation is not observed on Pt. A more detailed analysis of the parameters influencing the oxide formation behavior of Au is subsequently given in Chapter 5.3 and Chapter 5.4.

3.3.3 Restructuring

Modification of the electrode structure does not always mean the formation of oxide layers on the surface of the electrode, as obtained through anodization or PEO on

the electrode described in the previous section. Instead, completely new surface structures can also be formed through restructuring, by rearranging, in the simplest case, the atoms near the surface to generate new or different sites. The restructured surfaces can in turn exhibit different and thus interesting properties for certain applications, for example in the field of (electro)catalysis. A highly pronounced modification of the surface takes place, for example, during cathodic corrosion or during the formation of nanoporous Au (NPG). In addition, the surface can also be smoothed through restructuring. Smoothing basically also only means in the end that other sites are generated.
Moreover, electrode modification can result in the formation of nanoparticles by i) dissolving the electrode or ii) reducing ions in solution (see Section 3.4.2).
In addition, both effects, electrode restructuring, and nanoparticle formation can also occur simultaneously. An example in this respect in the field of NE is cathodic corrosion. Cathodic corrosion is described in Section 3.3.3.1. Subsequently, various aspects of nanoporous Au (NPG), such as fabrication processes reported in the literature, are discussed in Section 3.3.3.2. These are within the area of NE. Examples of electrode restructuring and NP formation in the CGDE region are considered in Section 3.3.3.3.
The fact that restructuring does not always involve roughening of the surface is shown in Section 3.3.3.4 and Section 3.3.3.5. Electropolishing at low voltages (Section 3.3.3.4) and plasma electrolytic polishing (PEP) at high voltages or rather in the CGDE range (Section 3.3.3.5) can also be used to remove and thus smooth surfaces.

3.3.3.1 Cathodic Corrosion

During cathodic corrosion, a metal electrode is negatively polarized, usually in a highly concentrated alkaline electrolyte, which leads to a strong restructuring of the electrode surface.[103, 133] Additionally, nanoparticles (NPs) can be formed. The number of NPs formed can thereby be increased by using alternating current or by strong polarization.[103, 134]
Cathodic corrosion occurs in the voltage range beyond the stability window of water, which means near the onset of the Ohmic region (see Chapter 1 Fig. 1.1).
Upon cathodic corrosion, the restructuring of the electrode surface and the forma-

tion of nanoparticles, takes place in such a way that facets with preferential orientation are formed. The processes taking place thus exhibit a certain anisotropy.[135] Hersbach *et al.* suggest that this anisotropy is caused by the adsorption of cations on the strongly negatively polarized electrode surface (surface charge-induced adsorption).[136]
For cathodic corrosion of Pt in a very alkaline solution (10 M NaOH), it was found that Pt(100) facets are preferentially formed both, on the electrode and during the formation of NPs[103, 135, 137, 138], and Pt(110) facets are degraded.[136] Furthermore, the Pt(111) facet corrodes fastest during cathodic corrosion, while the Pt(110) facet corrodes the slowest of the three low-indices facets.[139] In addition, geometric changes in the individual facets are observed. These local geometric structures differ depending on the facet since the formation of Pt(100) structures seems to be favored.[103, 136, 139] Arulmozhi *et al.* have shown that this anisotropy leads to triangular holes in the Pt(111), square holes in the Pt(100), and rectangular holes in the Pt(110) facet.[139] In the case of Pt, even larger fractal structures form from these local geometric structures.[103]
In the case of Au, the formation of Au(111) facets is preferred on the electrode surface and during the formation of NPs.[140, 141] This leads to the formation of octahedral NPs on the Au surface of the electrode.[133, 141]
In contrast to Pt, no fractal structures are formed.[103]
Cathodic corrosion was discovered at the beginning of the 20th century,[136] however, the exact processes at the electrode and thus also the mechanism of cathodic corrosion have not been clarified yet. Currently, the literature suggests that the occurrence of cathodic corrosion requires the presence of metals, protons, and a non-protic cation. In the absence of protons, as well as in the absence of a non-protic cation, cathodic corrosion could not be observed.[136, 142]
The processes occuring during cathodic corrosion suggested in the literature are schematically shown in Fig. 3.3 and are described as follows.[103]

Applying a negative voltage or potential to the electrode first leads to the adsorption of hydrogen on its surface, as well as hydrogen evolution. In addition to hydrogen, the non-protic cation of the solution will also adsorb on the electrode to a certain extent. Additionally, it is observed that metal atoms are dissolved from the surface by the applied voltage or potential. The origin of this process is still debated. In the literature, these are believed to be metastable anionic species stabilized by the

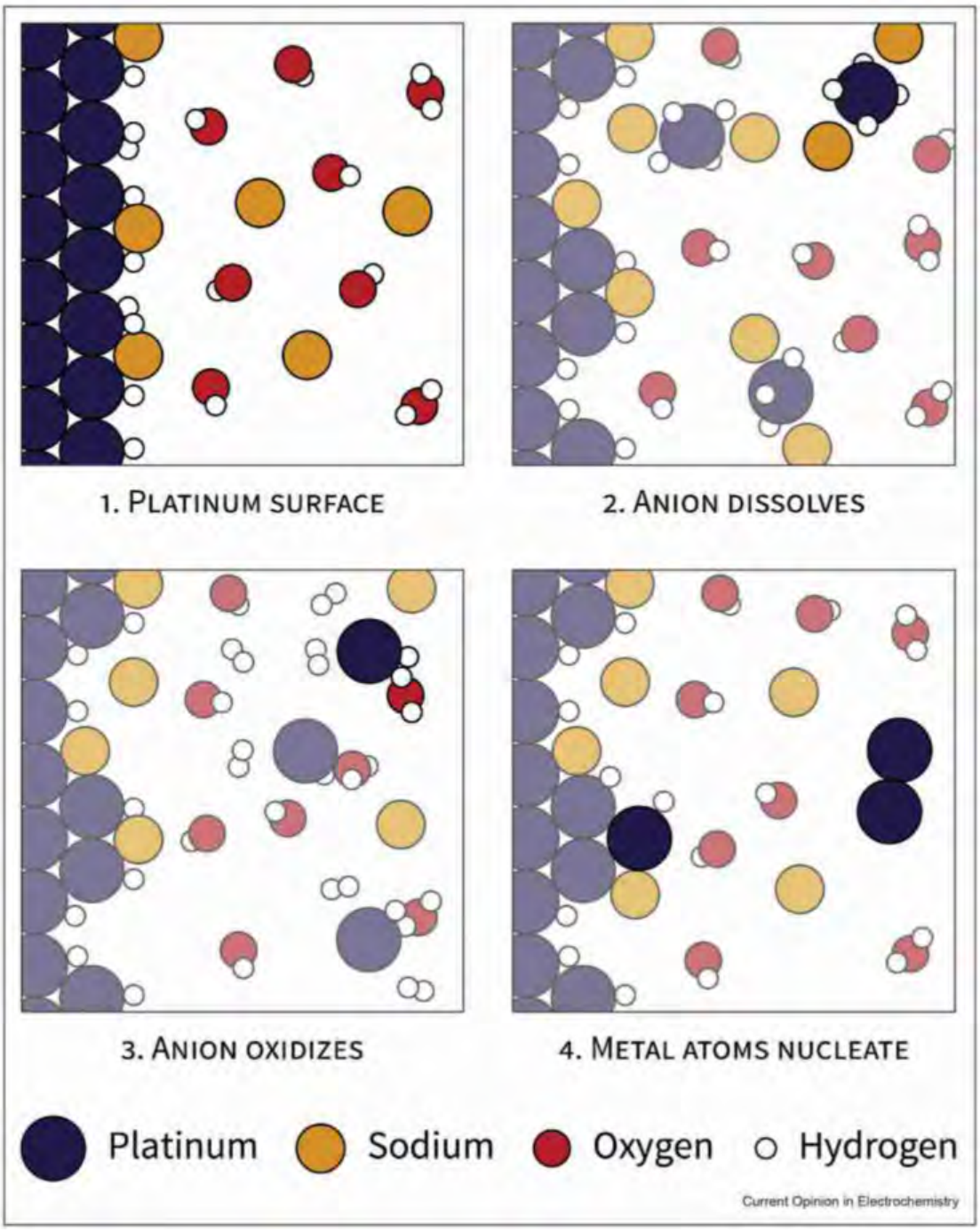

Figure 3.3: Schematic illustration of the processes occurring during cathodic corrosion of Pt.[103] Reprinted from Curr. Opin. Electrochem., 26, T.J.P. Hersbach and M.T.M. Koper, "Cathodic corrosion: 21st century insights into a 19th century phenomenon", 100653, "CC BY 4.0, https://creativecommons.org/licenses/by/4.0/".

non-protic cations of the electrolyte, as well as hydrogen. Such species could be ternary metal hydrides, but the nature and composition of these metastable anionic species are still topics of ongoing research.[103, 136, 139, 143]
Once formed, the metastable anionic species diffuse away from the electrode until they encounter a water molecule. Reaction with water oxidizes the anionic species to form the metal. Water is reduced to OH^- and H_2.[103]
The metal atoms formed by oxidation can now either redeposit on the metal electrode, changing the structure of the electrode or form NPs in solution.[103] The ternary metal hydrides, thereby not only promote the restructuring of the electrode, but also the formation of NPs. In the case of NP formation, they act as nucleation seeds.[103]
As already mentioned, the anisotropy during cathodic corrosion strongly depends on the electrode material since the preference to form a particular facet can vary. Apart from that, cathodic corrosion also depends on the metal cation, the electrolyte concentration, and the orientation of the surface. Depending on the parameters, the onset potential of cathodic corrosion and also the resulting electrode structure will change.[103, 133, 141–143] The formation rate and orientation of the NPs, however, can be influenced by the cation in the electrolyte, the electrolyte concentration, the current density during cathodic corrosion, and the initial electrode structure of the electrode, which serves as a source of material for NP formation.[103, 135, 137] Yanson *et al.* found that for Pt, the fraction of Pt(100) on the surface of the NPs increases as the size of the NPs increases.[137]
The possibility to selectively adjust the properties of NPs through the experimental parameters during cathodic corrosion thus opens up many possible fields of application.

3.3.3.2 Nanoporous Au (NPG)

(Nano-)porous materials are for example characterized in terms of a low density and a high surface area,[144] i.e. the porosity of the material is above 40 %.[51] Depending on the pore size of the materials, the pores are also referred to as macro- (> 50 nm), micro- (2 nm to 50 nm) meso- (< 2 nm) or nanopores (0.1 nm and 100 nm).[51, 145–147] A classic example of a nanoporous material is nanoporous Au (NPG). NPG is a sponge-like structure, usually on a support material, with pores

of a few to a few hundred nanometers in size interconnected by ligaments ranging in size from a few nanometers to a few micrometers.[47, 49] A SEM image, as well as a cross-sectional SEM image of a NPG surface is shown in Chapter 5.3 in Figs. 5.32f and h, respectively. Compared to bulk Au, the porous structure of NPG exhibits, among other aspects, a different behavior for the adsorption of molecules which makes it interesting for applications, e.g., in the field of biosensors.[45, 49–51] Applications for NPG are also conceivable in other areas, such as electrocatalysis [45, 46, 51, 148], in battery systems,[45, 46] biofuel cells[51] or other biomedical applications, such as in the field of drug delivery.[51]
Nanoporous Au can be prepared through several methods, such as dealloying,[44, 46, 49, 50, 149–156], the reduction of ions in solution,[156], which is often combined with template-based methods,[46, 156, 157], by anodization and subsequent electrochemical reduction,[99, 109] glancing angle deposition, i.e., by sputtering a Au target in a vacuum and deposition of the Au on a rotating substrate,[158] or by combinations of different methods, such as electrodeposition and anodization.[159]
In the most common dealloying process, the less noble metal (e.g. Ag) of a binary alloy is dissolved from the alloy, resulting in the formation of a NPG film.[50, 149, 151–155]
Erlebacher investigated the processes leading to the formation of NPG films during dealloying of an Au-Ag alloy illustrated in Fig. 3.4.[160–162]

Dissolution of the less noble metal initially forms pits on the surface. Clusters of the more noble metal (Au) form within these pits. The distance between the clusters depends on various parameters and has a characteristic length. During the progress of dealloying, more layers dissolve. The clusters grow and form hills, which are composed of the noble metal at the top and the base metal at the bottom. As dissolution proceeds, the mounds are undermined and the distance between the mounds grows. When the distance between the mounds reaches approximately twice the characteristic length, a new cluster is formed in the center. The porosity of the surface increases.[160–163]
Regardless of the preparation procedure, the purity and porosity of the NPG films are crucial parameters for characterizing and comparing the NPG films.[161, 164] The resulting porosity of the NPG films depends not only on the method used to prepare the NPG films but also on parameters such as the temperature and the electrolyte concentration. According to the employed approach, there are further

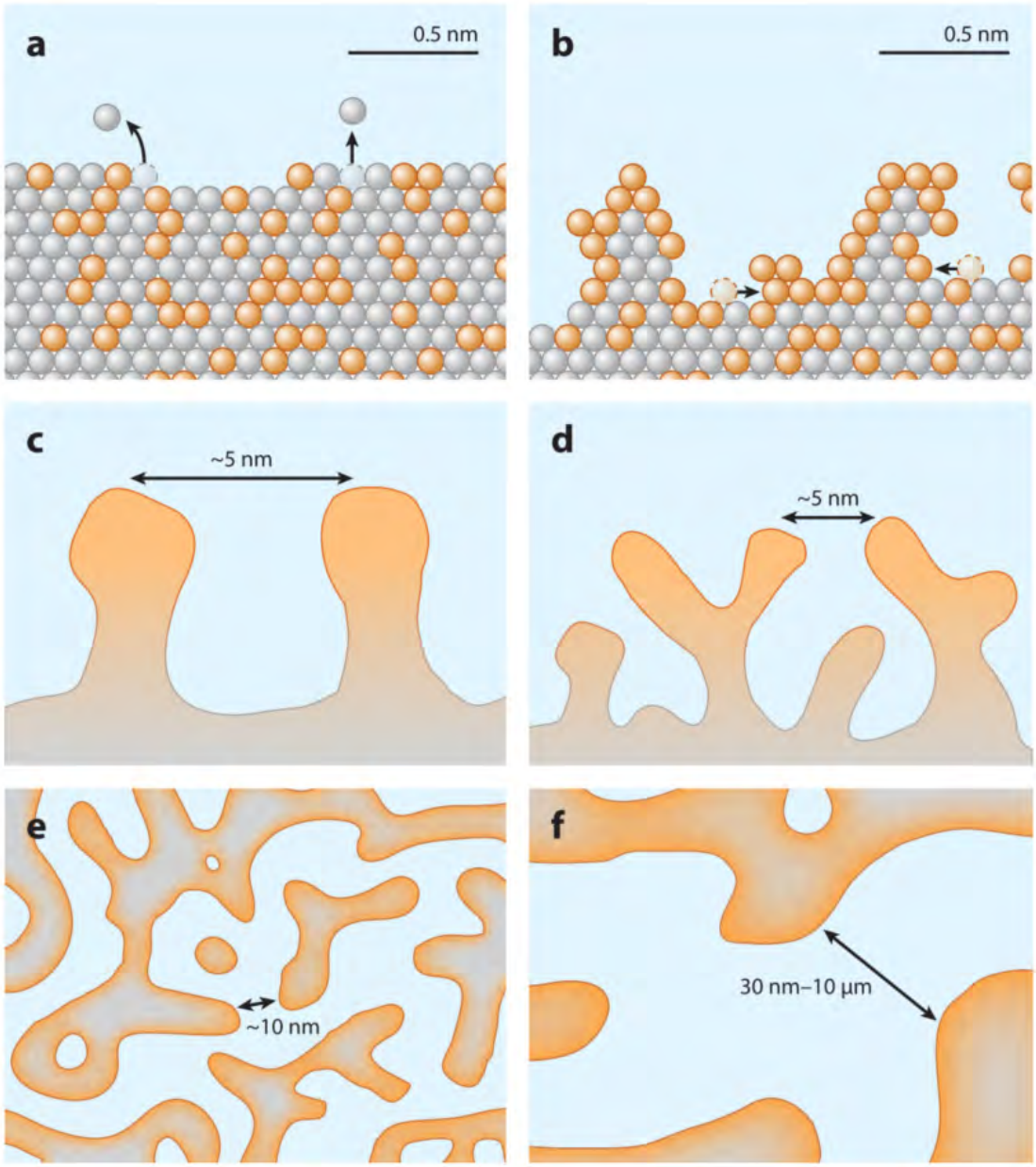

Figure 3.4: Schematic illustration of the dealloying processes and the resulting formation of NPG films starting from a Ag-Au alloy. Ag atoms are shown in gray, Au atoms in orange.[162] See text for details. Used with permission of Annual Reviews, Inc., from "Dealloying and Dealloyed Materials", I. McCue *et al.*, 46, 263-286, copyright 2016; permission conveyed through Copyright Clearance Center, Inc.

parameters by which the NPG film can be tuned, e.g., in the case of dealloying by the composition of the alloy, the thickness of the alloy layer on an underlying substrate, or the dealloying time.[49, 154] Changing these parameters leads to different pore sizes, as well as ligaments, and thus to changes in the NPG films. To determine the porosity of the prepared NPG films, various methods were reported. Most frequently the porosity is determined with a gray balance.[154] Hereby, a SEM image is evaluated by setting a gray tone as a threshold value, based on which all individual pixels in the SEM image are converted into either black or white pixels. The proportion of black to white areas subsequently provides information about the porosity of the NPG film.[154]
Another possibility to determine the porosity of a surface is provided by BET adsorption measurements. Here, a gas, usually N_2 is physisorbed on the surface of the sample. The larger the surface of the sample, i.e., the more porous the surface is, the more gas can be adsorbed. Using the geometric area of the sample or its mass, and the amount of gas physisorbed on the surface, the porosity of the sample can then be calculated.[145, 164, 165] A problem that often occurs with NPG films grown on a Au substrate is that the formed NPG films detach from the Au substrate. This issue was studied in more detail by Henkelmann *et al.*[166] They found that gradients in the mean curvature of the pore surface occur both at the outer interface of the nanoporous layer and at the interface between the nanoporous layer and the substrate. These gradients lead to surface atom diffusion and thus to densification or detachment of the surface. Surface densification usually occurs at the outer interface, while a detachment of the nanoporous surface tends to be near the substrate. To avoid both effects, the outer surface would have to be convex, i.e., curved outward, while the inner would have to be concave, i.e., curved inward. According to Henkelmann *et al.* a planar substrate surface also preferentially leads to the detachment of nanoporous films.[166]

The wide range of applications for NPG requires a controlled and preferably a simple manufacturing process.
Although dealloying is a very simple procedure, this method often leaves residues of the alloying partner in the NPG film.[50, 163] These impurities often influence the properties of the NPG film in later applications, which can pose problems for example in the field of electrocatalysis.[50, 167, 168]
In this work, it was shown for the first time that NPG can also be prepared starting

from a bare Au electrode which can be specifically modified at higher voltages (in the HV electrolysis or aCGDE range). Details are provided in Chapter 5.1, Chapter 5.3 and Chapter 5.4. An advantage of the method presented in this work compared to the common production of NPG films by dealloying is that no special chemicals are required, thus representing a green chemistry approach. Furthermore, the resulting films are less susceptible to contamination, for example by foreign metals, due to the use of less chemicals and using only Au as a precursor material.
Finally, applying voltages in the range of HV electrolysis compared to applying voltages of only a few volts, reduces the preparation time significantly.[66, 99, 109, 169]

3.3.3.3 Restructuring during HV Electrolysis and CGDE

During HV electrolysis or under plasma conditions, the processes at the electrode can be partially changed compared to NE. Thereby, new possibilities to produce electrode structures by restructuring with or without the incorporation of additives from the electrolyte can open up, which were not yet accessible for the preparation of materials at lower voltages. Such structures can in turn be interesting for various applications, for example in the field of (electro)catalysis. In the following, electrode restructuring during HV electrolysis and the formation of nanomaterials, usually NPs, through electrode dissolution will be briefly discussed. The formation of NPs by reduction of ions in solution, which can originate from salts added to the electrolyte, is discussed in Section 3.4.2.
An example of electrode restructuring by aCGDE using additives is the formation of coral structures on a Cu electrode in KOH in the presence of SiO_2 NPs.[22] Moreover, it is also possible to modify PEO coatings by adding additives to the electrolyte.[170] More details about the processes occurring during PEO can be found in Section 3.3.1.3.
In some cases, concomitant to the restructuring of the electrode, the formation of NPs in solution takes place. NPs can thereby be produced either by the dissolution of the electrode or by the reduction of ions present in the solution by species formed during the plasma (for the latter see Section 3.4.2). Allagui *et al.* explained the formation of nanoparticles for both cases.[171] In the first case, the dissolution of the

electrode material for NP formation, applying a voltage, or generating a plasma at the electrode locally evaporates a part of the electrode material. Subsequent quenching in the electrolyte together with the aggregation of the evaporated electrode material results in the formation of NPs.[171] An example of this approach in the cCGDE range is the production of Ni and Pt NPs.[171] Another example are graphite sheets which can be prepared by both aCGDE and cCGDE in solution.[172] Depending on the polarization of the electrode the graphite sheets are flat (aCGDE) or have flakes on their surface (cCGDE).[172]
CGDE is mostly used to produce metallic or oxide nanoparticles. Mixed-composition nanomaterials are more difficult to prepare by CGDE because reactive species are quenched by the electrolyte.[14, 19, 20, 35, 171–175]
In addition, the formation of metallic or oxide nanoparticles can be influenced for example by protecting the tip of the smaller electrode (in the case of wire-type electrodes). By covering the tip of the wire, the electric field at the electrode is more homogeneous, favoring the formation of metallic nanoparticles. Without the protection of the tip, the electric fields at the tip are very high. Accordingly, the currents present there are also very high, favoring oxidation and thus the formation of oxidic nanomaterials.[19]
Compared to the formation of nanoparticles by a plasma in-liquid associated with the dissolution of the plasma electrode, the restructuring of electrodes by a plasma in-liquid has not yet received much attention. This means that often only the changes in solution are considered, but not those at the electrode. In this work, specifically, the restructuring of Pt, Au and Cu electrodes induced by HV electrolysis is considered in Chapter 5.1, Chapter 5.3, and Chapter 5.4.

3.3.3.4 Electropolishing

During electropolishing, the roughness of an electrode surface is minimized by applying a voltage that over time ablates and thus flattens the surface. The electrode is thus "polished".[79, 176] The electrode of interest for this process is the anode. The electrolyte is usually a relatively highly concentrated acid.[176]
The voltage used for electropolishing is ideally chosen in a way to limit the processes at the electrode either by the formation of a passive layer or by the removal of ions. This most suitable voltage range for electropolishing is therefore also re-

ferred to as the passive or material transport-limited range.[79, 176, 177] At these voltages, the electrolyte near the electrode is saturated with metal ions and the current flow at the electrode is therefore (diffusion-)limited. This voltage range offers the advantage that the surface is uniformly ablated regardless of the crystallographic orientation.[79, 176, 177]
If the electrode is not flat but rough, the currents at the peaks of the rough surface are larger than in the valleys. This can be explained by the concentration gradient (or by the voltage drop), being higher at the peaks of the rough surface compared to the valleys. As a consequence, the removal of the metal ions at the peaks of the rough surface and thus their ablation is favored.[176–178] The roughness of the electrode decreases exponentially with the electropolishing time.[79, 177]
A disadvantage of the voltage range ideally suited for electropolishing is that the processes at the electrode may become very slow due to the limited mass transport and the possible formation of a passive layer. Increasing the voltage can help in this regard since at higher voltages, which means at voltages at which the electrolyte decomposes (transpassive region), the mass removal is favored and thus the processes at the electrode are accelerated.[179] A disadvantage of the transpassive region is that the surface structure can also be affected by oxygen bubbles formed under these conditions, which can lead to pitting corrosion.[79]
At lower voltages than those normally used for electropolishing, the processes at the electrode are determined by the kinetics of the reactions taking place and can thus be strongly facet-dependent. Electropolishing is therefore usually not possible in this voltage range.[79, 177]

3.3.3.5 Plasma Electrolytic Polishing (PEP)

During plasma electrolytic polishing, the surface of an electrode is removed in the presence of a plasma, resulting in the flattening of the surface.[180]
While electropolishing, as described in Section 3.3.3.4, is preferably carried out in the passive or material transport-limited voltage range of the electrode, i.e., at a voltage at which electrolysis does not yet take place, electrolysis is unavoidable during PEP as significantly higher voltages are required for the formation of a plasma. Thus, during PEP, anodic dissolution of the electrode and plasma chemical processes occur simultaneously.[180–182] Nevertheless, defined removal rates can

also be set here.[180, 181, 183]
The advantages of PEP compared to electropolishing are usually the much shorter process time and the applicability to workpieces with complex shapes.[180, 182, 183] Additionally, dilute aqueous electrolytes are commonly used for PEP, which makes the method also interesting due to its environmental friendliness.[180–183]

3.4 Plasma – Electrolyte Interactions

If the potential of an electrode changes, e.g. by applying a voltage, various effects can occur in the electrolyte. On the one hand, the voltage drop in solution changes, on the other hand, products can form or product compositions can change and additionally, the temperature of the electrolyte can change. These aspects are applicable in the field of NE as well as during HV electrolysis or CGDE. Following, these aspects and methods for their determination will be discussed.
Voltage drops in the electrolyte can for example be determined by Ohmic microscopy, which is discussed in Section 3.4.1. First reports from the literature on the investigation of the voltage drop in the gas layer around the electrode during plasma will also be shown in Section 3.4.1.
Section 3.4.2 then provides more details on the products formed during HV electrolysis, as they can change the composition of the electrolyte, e.g., in terms of dissolved gases or the chemical composition. In a final step, differences in the product composition in the electrolyte in the plasma range compared to NE are addressed.

3.4.1 Voltage Drops

Applying a voltage between two electrodes induces a current flow in the electrolyte, which causes a voltage drop across the resistors in the system. Thereby, the voltage drops both at the electrodes and in the electrolyte. Voltage drops in the external circuit are considered to be negligible. In the case of aqueous systems and low voltages the resistance in the system is primarily determined by the resistance of the electrolyte and can be described by Ohm's law, since the electrolyte acts as an ohmic resistor.[2] At high voltages, other effects additionally come into play, such as bubbles or changes in temperature and concentration in the electrolyte, which

influence the resistances in the system and thus also the voltage drop.[2]
For the local *in situ* measurement of the voltage drop, in addition to the classical three electrodes for electrochemical measurements, two (micro)reference electrodes are required, between which the potential difference is measured.[184, 185] Depending on the positioning of the (micro)reference electrodes, the voltage drop of the solution $\Delta\ \varphi_{sol}$ is measured locally.
The voltage drop between two driving electrodes was studied in more detail by Forschner *et al.*, where I am also listed as co-author.[81] Briefly summarized, Forschner *et al.* have investigated the electric potential drop in 0.01 M KOH between two driving electrodes during HV electrolysis (in the NE region) both experimentally and theoretically using a COMSOL model. In addition, the potential of the two driving electrodes was determined. For this purpose, two reference electrodes (RHEs) were used besides the two driving electrodes. One RHE was placed outside the electric field and one movable RHE between the two plasma electrodes. The potential at any point in the electrolyte could thus be measured by varying the position of the movable RHE to this point and measuring the potential difference between the two RHEs.[81] More details regarding measuring of voltage drops in the electrolyte during HV electrolysis can be found in Ref. [81].

Ohmic Microscopy: Ohmic microscopy enables the local *in situ* measurement of the voltage drop in the electrolyte. One aim is to derive information about differences in the reactivity of an inhomogeneous surface from local changes in the voltage drop and resulting local potential differences.[184, 185] Differences between the behavior of different facets of a material, as well as various materials at the surface of the electrode (elemental composition) can be determined.[184, 186]
While Feng *et al.* were able to resolve on a Pt single crystal the characterisitic features of the Pt(111) facet with Ohmic microscopy[186] Chen *et al.* performed Ohmic microscopy on a WE consisting of Pt on one side and Au on the other. Depending on the position of the microreference electrodes, a characteristic Pt or Au CV was obtained or a CV that possessed contributions from both metals.[185]

Voltage Drop in the Plasma Sheath (liquid): At very high voltages and in the plasma region, the voltage drop at the electrode does not occur through an electrolyte layer on the electrode, in other words across a solid | liquid interface, but across a solid | gas interface.
The solid | gas interface was studied by Slovetskii and Terent'ev, with the aim of de-

termining various characteristic parameters, such as the thickness of the gas layer during the plasma, as well as the voltage drop in the gas layer.[88]
The authors chose an approach similar to Ohmic microscopy. Along the two electrodes used to generate a plasma in solution, two electric tungsten wire probes were employed. One probe had a fixed position, the other was moved stepwise. In this way, the voltage drop in the gas layer around the electrode was determined.[88]
In the case of aCGDE, a plasma ignites in the gas layer around the electrode only if the voltage drop in the gas layer is at least 100 V. At the same time, the current drops to one third of the previous current when the plasma ignites.[88]

3.4.2 Product Formation during HV Electrolysis

During electrolysis the electrolyte and eventually the components in the electrolyte react at or close to the electrode to form a product in the solution. Under normal electrolysis conditions (voltages of a few volts) electrolysis in aqueous environments probably represent the most common case. CGDE is also often performed in aqueous electrolytes. However, early plasma experiments were sometimes for example performed in molten electrolytes or liquid NH_3 and thus not in aqueous environments.[17, 187] The products formed primarily depend on the applied potential. The product formation at low voltages (OER / HER) is described in Section 3.2. Here we focus on aqueous electrolytes and the products formed during HV electrolysis, as well as under CGDE conditions.
A peculiarity at very high voltages, especially in the CGDE region, is that in addition to Faraday products, non-Faraday products are formed.[35, 188] Thus, in the region of aCGDE, H_2O_2 and H_2 are formed in addition to the expected product O_2 and can thus additionally lead to modifications of the electrode and/or the electrolyte (see Chapter 5.1 and Chapter 5.3).
Faraday's law represents a relationship between the charge Q, which is the current passed, the number of transferred electrons z per molecule and the amount of product of the species n in a reaction. F is the Faraday constant. Faraday's law is shown in equation 3.3.

$$Q = nzF = nzeN_A \tag{3.3}$$

By Faraday's law, all products formed in a electrochemical reaction or electrolysis reaction can be quantified.
Non-Faradayic products are not formed by the transfer of electrons through an external circuit. For example the formation of radicals and reactions with radicals cannot be described by Faraday's law.[54, 55, 67] Non-faradaic products can for example be formed with the help of H and OH radicals, which are formed by the electrolysis of water or by further reaction in solution.[18, 55, 67]
According to Sengupta *et al.* the formation of non-faradaic products begins with the onset of partial aCGDE. From this voltage to the onset of full aCGDE (at V_D), the non-faradaic product yields increase linearly with power. The non-faradaic products in this voltage range originate from the plasma zone around the electrode. Above the midpoint voltage, the yields are independent of the power. Here, the non-faradaic products originate both from the plasma zone around the electrode and from the electrolyte near the anode.[54]
Sengupta *et al.* attempted to quantify these by collecting the gases formed in an H-type electrochemical cell.[54, 67] This involved determining the amount of O_2 formed by absorption experiments, the amount of H_2 using combustion, and H_2O_2 using titration (often permanganometry).[18, 54, 67, 189–191] Other methods to detect H_2O_2 are for example Fourier-transform infrared spectroscopy (FTIR), where the H_2O_2 bands can be detected[192] or UV absorption spectroscopy (UVAS) measurements, with which optical depth spectra can be recorded.[193] In addition, luminol can be used to detect H_2O_2 as it glows in the presence of H_2O_2 due to chemiluminescence.[194]
In this work, we developed a five electrode setup that allows detecting H_2O_2 *operando* and *in situ*. Details to this proof of concept study can be found in Chapter 5.2. Compared to the common methods used for the detection of H_2O_2 just described, the advantage of the approach developed in this work is that the amount of non-faradaic products formed can not only be measured after the reaction but in principle also *operando*.
Another possibility to form products in solution is by reduction of ions in the electrolyte. This results in the formation of NPs and represents a second possibility in addition to the formation of NPs by dissolution of the electrode, which is described in Section 3.3.3.3. Species with reducing properties formed in the plasma, such as solvated electrons, hydrogen radicals, etc., are hereby responsible for the reduction of the ions and therefore the formation of NPs.[171]

In this way, for example, (multi-)metallic or oxidic nanoparticles can be produced.[14, 19, 20, 35, 173–175, 195]

4 Experimental

This Chapter provides a more detailed description of the experimental Sections presented in the original publications from Chapter 5. In addition, some results that led to these works are also shown here. Furthermore, all devices utilized for the purpose of this work are described in more detail.

4.1 Materials

All materials and chemicals used for this work are tabulated in Table 4.1. Milli-Q water (18.2 MΩ cm, TOC $\leq$ 3 ppb) was used to prepare aqueous solutions, such as KOH electrolyte. H_2O_2 solutions were prepared using H_2O_2 solution diluted to the desired concentration (wt.%) with 0.01 M KOH electrolyte. To prepare aqua regia, fuming HCl and 65 % HNO_3 were mixed in a 3:1 ratio.

4.2 POSC Growth

The Au POSCs used for the measurements in Chapter 5.4 were prepared by controlled-atmosphere flame fusion (CAFF).[196, 197] In this process, first, a Au wire (ø 1.0 mm) is melted in a H_2, O_2, Ar flame (0.7 H_2, 0.1 O_2, 1.0 Ar) until a Au ball of the desired size is formed at the lower end of the Au wire. The composition of the flame is controlled by three mass flow controllers (0.05 – 2.5 L min^{-1}, Bronkhorst, EL-FLOW Prestige, FG-201CV-RBD-22-V-DA-000), one for each gas. The size of the flame is defined by the selected gas flows and the diameter of the torch, which is in this case between 1 and 2 mm. To stabilize the flame, a quartz chamber is used, which is fixed with a metal ring.

Table 4.1: Summary of all materials, chemicals, and gases used in this work, including manufacturer and purity.

materials		
material	manufacturer	purity
Pt wire (ø 0.5 mm)	MaTecK	99.99 %
Au wire (ø 0.5 mm)	MaTecK	99.99 % or 99.995 %
Cu wire (ø 0.5 mm)	MaTecK	3N5
Au wire (ø 0.25 mm)	MaTecK	99.9 %
Au sheets (thickness: 0.127 mm)	MaTecK	99.99 %
Au wire (ø 1.0 mm)	MaTecK	5N
chemicals		
chemical	manufacturer	purity
KOH pellets	Sigma-Aldrich	99.99 %
30 % HCl	Merck	Suprapur
85 % phosphoric acid	Merck	Suprapur
50 wt.% H_2O_2 solution stabilised in water	Acros Organics	pure
fuming HCl (37 %)	Merck	for analysis
HNO_3 (65 %)	Merck	for analysis
gases		
gas	manufacturer	purity
H_2	Westfalen AG	5.0
O_2	MTI IndustrieGase AG	3.5
Ar	MTI IndustrieGase AG	4.6
N_2	MTI IndustrieGase AG	5.0
propane	MTI IndustrieGase AG	

Once the bead has reached the desired size, the bead is slowly cooled in a controlled manner by lowering the flame with a defined speed. Ideally, this yields a Au POSC single crystal.
The Au wire is mounted in a ceramic holder (BCE Special Ceramics, Al_2O_3/A-997) immobilized with a ceramic screw and inserted into the flame from above. After an initial manual alignment of the wire in the flame, the position of the torch, which is mounted on an xyz-stage (Newport, M-462-XYZ-M) connected to a z-stage (Newport, M-433), can be adjusted. For this, an actuator (xy: Newport, 860A-1, z: Newport, CONEX-LTA-HS, 0.1 µm s^{-1}-5 mm s^{-1}) and a motion controller (xy: Newport, Motion Controller 860-C2) are used. The temperature of the Au bead, as well as the location and orientation of the melting line within the Au bead, is controlled with two IR cameras (0.85-1.1 µm; 450-1800 °C, Optris, PI 1M) positioned in x- and y-direction (on the horizontal axes). By fine adjustment of the flame in the x, y, and z directions using the motion controller and the two actuators, the height and tilting of the melting line in the Au bead can be adjusted accordingly. If the melting line is straight and the Au bead has the desired size, cooling can be started. For this purpose, the flame is initially lowered with a velocity of 0.1 µm s^{-1}, which leads to cooling of the crystal. This very slow rate is necessary to ensure that the most thermodynamically stable facet prevails and that no bi- or tri-crystal is formed, but preferably a single crystal. Once the most critical part of the Au bead near the Au wire is cooled, the lowering of the flame can be increased to a speed of 0.2 – 0.5 µm s^{-1}. After complete cooling of the bead, the (single-)crystallinity of the bead can be checked by the arrangement of the facets on the bead with an optical microscope or an SEM.
If an as-received wire is melted during the growth of the POSC, impurities are liberated from the wire during the melting process, which settle at the top of the bead near the wire junction. After growing the POSC, these impurities must be removed to prevent the falsification of the subsequent measurements. For this, the POSC is etched in aqua regia for approximately 30 min. As mentioned above, this procedure is especially important after the first growth of the POSC. Since the etching also roughens the remaining surface of the POSC, the POSC must be regrown afterward.
Regrowth of the POSCs is also necessary after all experiments for which a noticeable roughening or restructuring of the surface is observed.

4.3 Sample Preparation

In order to create uniform starting conditions, the Pt, Au, and Cu samples were pretreated before the respective measurements. Depending on the shape of the sample (wire, sheet, or single crystal), the type of material, and the type of measurement, as well as the changes induced in the electrode structure during the previous measurement, the sample preparation differed. In the following, the sample preparations are divided depending on the material and partly also the shape of the material used.

4.3.1 Pt

The Pt wires utilized for the Pt measurements were used several times. For the investigations of the structural changes of the Pt electrodes at high voltages, the Pt wires were freshly prepared for each measurement by annealing them in a propane flame for 3 min. This was done both to remove impurities from the surface and to smooth out surface irregularities to some extent.
Since electrolysis at high positive voltages did not change the surface structure of the Pt electrodes measurably (compare Chapter 5.1), for the investigations of the influence of a plasma on an AE in solution (compare Chapter 5.2) both the Pt PWE and the Pt AE were only prepared once at the beginning of each measurement day.

4.3.2 Au

Wires: The Au wires were usually used several times. Before each measurement, they were annealed for 3 min in a propane flame.
When the Au wire appeared highly restructured after the measurement, i.e., its surface was not yet restored after 3 min annealing, it was additionally electropolished in 1 M HCl at 10 V vs. a graphite CE and then annealed again for 3 min in a propane flame.

Sheets: Some measurements required larger surfaces, i.e., for XPS, or samples without a curved surface, i.e., for FIB-SEM. For this reason, Au sheets were used

in addition to Au wires. These were cut accordingly before the respective measurements and then annealed for 3 min in a propane flame.
Repeated use of the Au sheets was not possible since (i) they were strongly restructured after the respective experiments and (ii) a significant amount of material (especially at the corners and edges) was removed during the attempt to restore the initial structural properties of the electrodes by electropolishing, meaning that the same initial structural properties of the electrodes could not be guaranteed when reusing the sheets.

POSCs: Au POSCs fabricated as described in Section 4.2 were annealed in a propane flame for 3 min before being used for a measurement, analogous to the Au wires and sheets. After the measurement, in most cases, their surface showed restructuring. If this was the case, they were regrown before the next measurement (as described in Section 4.2).

4.3.3 Cu

Due to the strong changes of the Cu wires under the investigated conditions (oxide formation and dissolution), a new Cu wire was used for each measurement. To create equal structural properties of the electrodes for all Cu measurements, the Cu wires were sonicated in 85 % phosphoric acid at room temperature for 1 min before each measurement. They were then washed thoroughly with Milli-Q water and dried in air. This procedure also ensured that the native Cu oxide layer was removed from the surface before each measurement.

4.4 Measurement Procedures

Throughout this work, the HV electrolysis and the electrochemical characterization of the PWE were always performed in two separate cells.
This is necessary because HV electrolysis can cause electrode dissolution and its material to accumulate in the electrolyte. O_2 formed during HV electrolysis dissolves and will also accumulate in the electrolyte. In addition to O_2, other products formed during HV electrolysis, such as H_2 and H_2O_2, and an elevated electrolyte temperature would also affect the subsequent electrochemical characterization and

thus falsify the results.
In the case of the AE experiments, the measurements were performed in an electrolysis cell. Experimental details of these measurements can be found in Section 4.4.3.
All experiments in this work were performed without stirring the electrolyte to avoid noise due to additional electrolyte movement. In addition, stirring the electrolyte can affect the formation and the subsequently formed plasma, as well as the electrode stability.

4.4.1 HV Electrolysis

4.4.1.1 Setup

Cell: The HV electrolysis experiments were performed in a beaker-type glass cell with a diameter of 6 cm. The cell was filled with 60 mL of 0.01 M KOH. The two electrodes, the plasma working electrode (PWE) and the plasma counter electrode (PCE) were placed at a distance of 2.5 cm from one another. A stainless steel plate with a size of 15 mm $\times$ 20 mm $\times$ 3.5 mm served as PCE in each measurement. A wire, a sheet, or a POSC made of Pt, Au, or Cu was used as PWE, depending on the measurement.
Power Supplies: The voltage required for HV electrolysis was applied for the majority of measurements using a TDK Lambda power supply (630 V / 1.365 A). This was controlled *via* a LabView software. The voltage range examined throughout this work is between 50 V and 580 V, with the most commonly studied voltages being 300 V (near the breakdown voltage V_B), 540 V (at the midpoint voltage V_D), and 580 V (in the aCGDE region). The formation of a plasma on the whole electrode surface exposed to the electrolyte could be observed at voltages of 540 V and above. The plasma is identified by a fluctuating purple color and an electrified hissing sound. The electrolysis time was often chosen as 30 s, although overall electrolysis times from 100 ms to 600 s were studied.
For the measurements in the millisecond range (some Au POSC measurements), a PlasmaTec power supply (PLASMATEC BIAS 1k015k NDCR1727F01002) was used instead. Here the current was measured and read out both directly with the PowerSupply and additionally with an oscilloscope (Tektronix) together with a cur-

rent probe (PICO TECHNOLOGY, TA189).
The comparison of the current density–time characteristic recorded with the two power supplies is shown in Fig. 4.1 for a Au wire electrode at a voltage of 540 V over a time of 30 s. The current density-time characteristic recorded with the TDK Lambda power supply is shown in red. In the case of the PlasmaTec power supply, the data was acquired both directly with the power supply (blue) and with the oscilloscope together with the current clamp (light cyan). Since the data recorded with the oscilloscope together with the current probe was very noisy, the data was smoothed by averaging 10 consecutive values at each time. The smoothed data is shown in cyan in Fig. 4.1.

As Fig. 4.1 shows, the obtained current density–voltage characteristics are identical for both power supplies, as well as for the different ways of recording the data. Minor differences can occur for example as a result of different data sampling rates or from experimental imprecision. The data sampling rate in the measurements shown in Fig. 4.1 is lower for the TDK Lambda power supply. However, the general progression of the current density–time characteristic and characteristic points within this curve, such as reaching a constant current density after about 12 s of HV electrolysis is the same in both cases. Therefore, there should be no influence of the used power supply on the results.

4.4.1.2 Samples

Wires:
Influence of Apex Protection: For some wire measurements, it was necessary to protect the tip of the wire with a polymer cap (Eppendorf pipette tip cap (0.1-10 µL)) to prevent it from melting under the prevailing conditions (high local temperatures and electric fields). For a more precise adjustment of the part of the wire exposed to the electrolyte, a second polymer cap was used in these cases to adjust the length of the wire in contact with the electrolyte. A photo of a Au wire after HV electrolysis with and without the use of protective caps as well as a photo of a molten Au wire is shown in Fig 4.2. If protection of the tip of the wire was not necessary under the given conditions, a cap was sometimes nevertheless used at the upper end of the wire for easier adjustment of the electrode surface exposed to the electrolyte. Any use of caps in wire measurements is noted in the appropriate sections or measure-

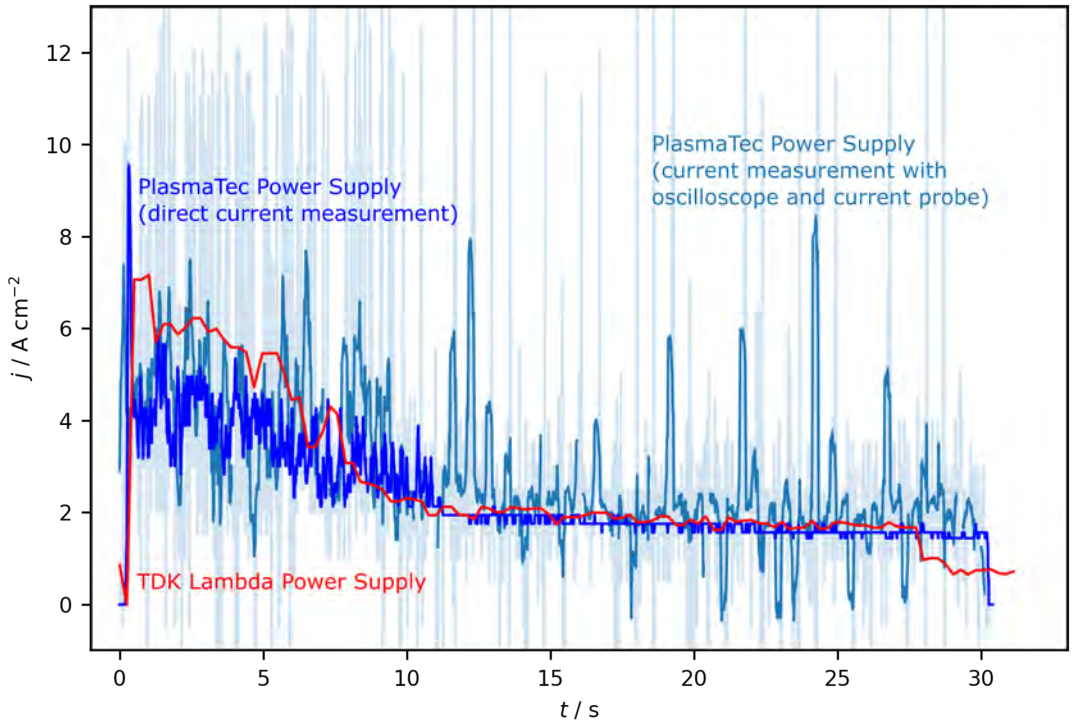

Figure 4.1: Current density-time characteristics of a Au wire electrode immersed 10 mm into the electrolyte during electrolysis at 540 V for 30 s in 0.01 M KOH. For the red curve, the voltage was applied with the TDK Lambda power supply, and the current was recorded *via* a LabView program. For the blue and cyan curves, the voltage was applied with the PlasmaTec power supply. In the case of the blue curve, the current was recorded directly with the PlasmaTec power supply, in that of the light cyan curve, with the oscilloscope together with the current probe. In the last case, the data was smoothed by averaging 10 data points at all measurement times. The smoothed data is shown in cyan.

ments.
Note that if the apex of the wire is not protected with a polymer cap, the electrolyte temperature will increase faster compared to measurements with a cap on the wire apex as a result of the high electric fields at the tip. This is illustrated in Fig. 4.2, which shows a staircase voltammetry (SCV) measurement of a Au wire electrode with an exposed wire length of 10 mm in 0.01 M KOH with (blue) and without (red) the use of caps. The voltage in this measurement was gradually increased here every 10 s by 20 V. As shown in Fig. 4.2, the SCV measurements with and without the use of caps are rather similar. Nevertheless, the current density up to V_B increases faster in the case of the Au wire electrode where the tip of the wire is not covered with a polymer cap (red curve). This can be attributed to a high electric field at the tip of the electrode and a resulting higher current flow per surface atom at the tip of the electrode. The higher current flow in turn causes more Joule heating which is why the temperature of the electrolyte and its conductivity increases compared to the measurements with a cap. Between 360 V and V_D (520 V), both curves are almost identical. Above V_D, the current density at the uncapped electrode increases faster again due to the higher electric field at the tip of the electrode. The electrode can become locally so hot in this area that melting occurs easily, especially if no caps are used.

Wire Length and Diameter: The length of the wire in contact with the electrolyte was usually 10 mm for investigations of the stability of Pt, Au, and Cu anodes in the HV electrolysis region, as well as in the aCGDE region and closer investigation of the NPG structure formation. Some Cu wire measurements were performed with a wire length of 4.5 cm. If a different wire length than 10 mm was used, this is marked at the appropriate points.
In the studies concerning the influence of a plasma on an AE in solution (see Chapter 5.2), a Pt wire electrode was used to generate a plasma. Its length in contact with the electrolyte was set to 2 mm by two caps for all measurements.
In isolated measurements, to investigate the influence of wire length exposed to the electrolyte and wire diameter on the current and current density, respectively, exposure lengths of 4 mm and 2 mm and a wire diameter of ø 0.25 mm besides the normally used diameter of ø 0.5 mm were also used. The influence of wire length and wire diameter on SCV measurements of Au wire electrodes in 0.01 M KOH can be seen in Fig. 4.3.

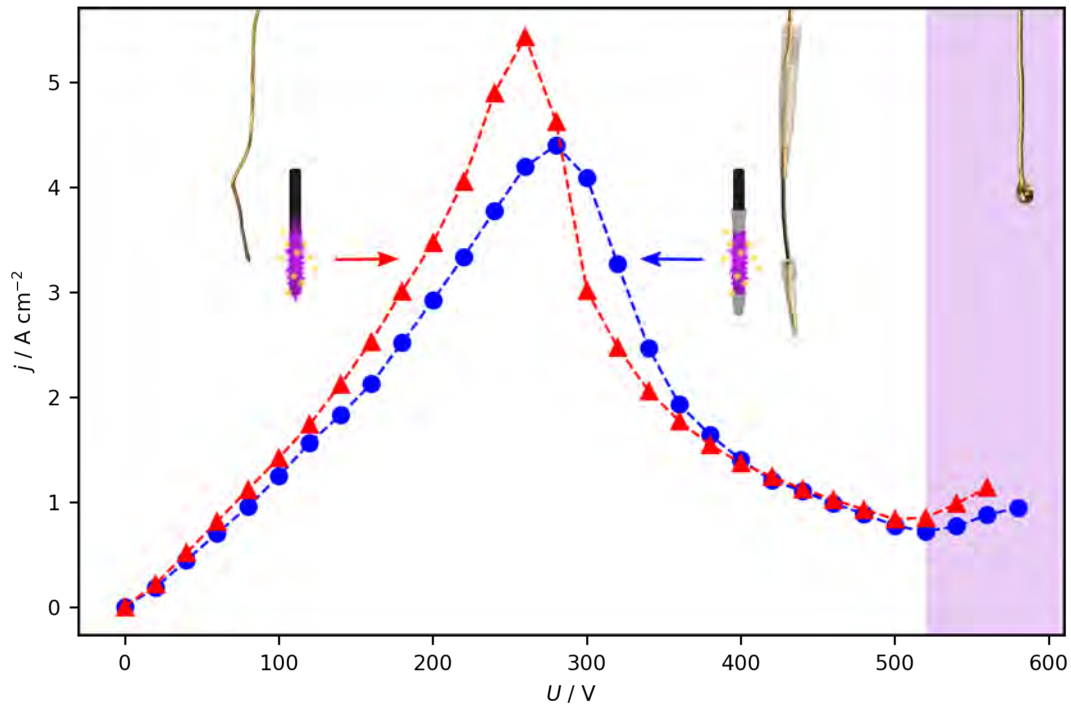

Figure 4.2: SCV measurements of a Au wire in 0.01 M KOH with and without protective polymer caps, photos of the Au wire electrode with and without protective caps and a Au wire melted at high voltages. The region where a plasma ignites is shaded purple. In both cases (with and without the use of protective caps) the wire length in contact with the electrolyte was 10 mm and each voltage was held for 10 s before the voltage was increased by 20 V.

Figure 4.3a illustrates that the current increases with wire length. This is in agreement with the behavior found in the literature (compare Section 3.2.1).[18, 57] Unlike for the wire length, the current density doubles, if the wire diameter is reduced from 0.5 mm to 0.25 mm. This is shown for a Au wire electrode with an exposed length of 10 mm in 0.01 M KOH in Fig. 4.3b. More details and literature on the influence of wire diameter on the resulting current density can be found in Section 3.2.1.

Sheet Measurements:

The Au sheets used for XPS and FIB-SEM measurements were cut in pieces of 2 mm $\times$ 12.5 mm and immersed either 4 mm or 10 mm into the electrolyte depending on the measurement.

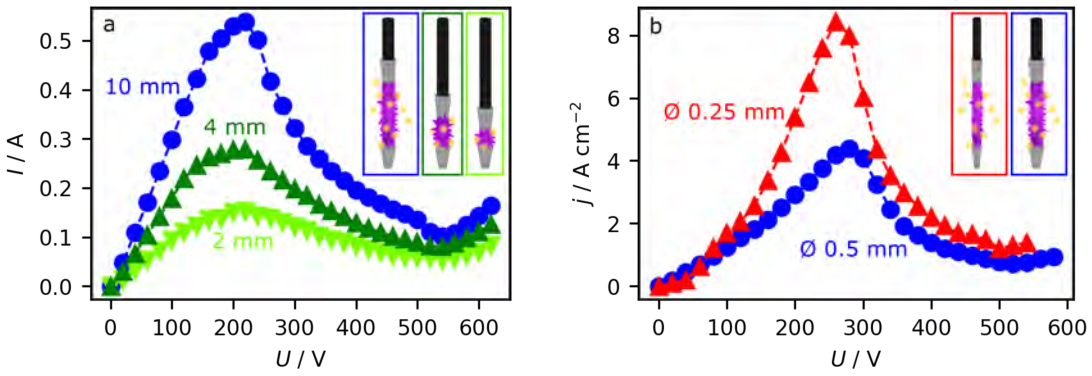

Figure 4.3: Influence of a) wire length exposed to the electrolyte and b) wire diameter on the current or current density in SCV measurements. The measurements were performed with Au wires in 0.01 M KOH. The voltage was gradually increased by 20 V every 10 s. The length of the wire in contact with the electrolyte was adjusted through caps. a) The wire length was 2 mm (light green), 4 mm (dark green) and 10 mm (blue) with a wire diameter of 0.5 mm. b) The length of the wire in contact with the electrolyte was 10 mm, the wire diameter was 0.5 mm (blue) or 0.25 mm (red).

POSC Experiments:

In contrast to most wire measurements, the measurements with POSCs were performed with a cap around the wire above the beads. The cap is necessary since due to acting capillary forces the electrolyte surface directly above the bead is not straight, but the electrolyte pulls itself upwards on the wire of the bead and thus also wets a part of the wire on which the bead is attached if no cap is used. By using a polymer cap above the bead, the bead can be immersed deeper into the electrolyte without having additional surface in contact with the electrolyte. The surface in contact with the electrolyte is thus precisely defined by the size of the POSC bead.

4.4.1.3 Influence of Electrolyte Temperature, Electrolysis Time and Electrolyte Concentration

Electrolyte Temperature: Since during high voltage electrolysis, high power is required, the electrolyte heats up strongly during the experiments. For this reason (and because the electrolyte composition also changes during the HV electrolysis),

fresh electrolyte was used for each HV electrolysis experiment.
The electrolyte temperature was measured before, as well as after each measurement. The initial temperature of the electrolyte was room temperature (24 °C) for most experiments. For some experiments, the electrolyte was heated to 40 °C, 46 °C, or 70 °C prior to the measurement. The increase in electrolyte temperature for a Au wire electrode after 10 s of electrolysis at voltages between 20 V and 540 V for different initial electrolyte temperatures is shown in Chapter 5.3 Fig. 5.44.
Changes of Current Density with Time: Note that the current at one voltage is high for small electrolysis times and decreases with longer electrolysis times, which can be explained by heating of the electrolyte (Joule heating). For long electrolysis times, the current has a relatively low, almost constant value. The changes in current density with electrolysis time are shown in Chapter 5.1 Fig. 5.13, and Chapter 5.3 Figs. 5.38a and 5.39.
The current density was determined by relating the measured current to the initial geometric surface area of the electrode (see also Section 4.5). The current density determined from a measurement over the entire electrolysis time at one voltage is called mean current density. The average mean current density at one voltage was determined by averaging the mean current density of several experiments performed under the same conditions. The standard deviation of this average mean current density over the entire electrolysis time was determined using the individual mean current densities determined from the individual experiments and is partially plotted as error bars in the *j*–*U* characteristics.
Electrolyte Concentration: Another aspect that has not yet been discussed in detail in this work is the choice of electrolyte concentration for the measurements performed within this work. For all measurements, 0.01 M KOH was used.
Nevertheless, in addition to measurements at an electrolyte concentration of 0.01 M KOH, measurements were also performed with 0.02 M and 0.05 M KOH. These concentrations correspond to pH values of 12.0, 12.3, and 12.7.
Measurements at these, higher electrolyte concentrations are shown in Fig. 4.4 for a Pt wire electrode with an immersed length of 4 mm. Two caps were used for these measurements to properly define the length of the wire in contact with the electrolyte.

The higher electrolyte concentration increases the conductivity of the electrolyte, which changes the *I*–*U* characteristic accordingly. The current at V_B increases with

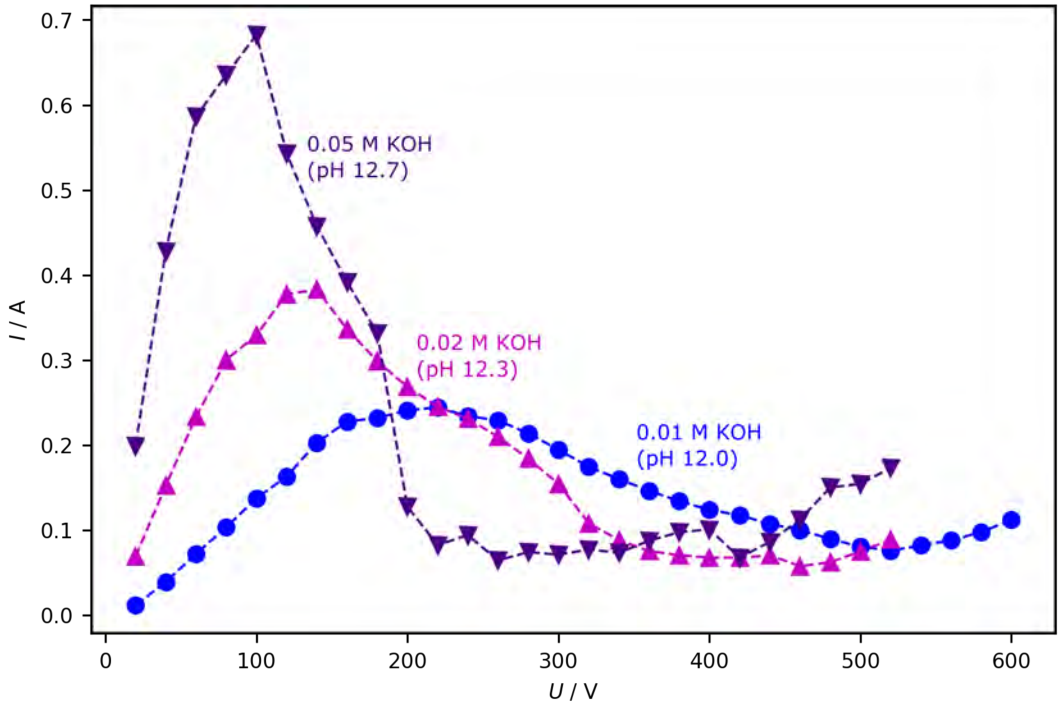

Figure 4.4: SCV measurements of a Pt wire electrode with a length of 4 mm in 0.01 M, 0.02 M, and 0.05 M KOH. Two caps were used to define the length of the wire in contact with the electrolyte. The voltage was gradually increased by 20 V every 10 s starting from 0 V.

the electrolyte concentration, while the voltage at which V_B appears, decreases in an exponential manner with increasing electrolyte concentration. This behavior is in agreement with the behavior reported in the literature.[56]
More detailed information on the influence of conductivity on the *I–U* characteristic can be found in Chapter 3 Section 3.2.1.

4.4.1.4 Measurement Procedure and Evaluation

SPST and SCV Measurements: Note that for this work, two different approaches were pursued to perform HV electrolysis experiments. In most cases, a new experiment was performed for each material–voltage–time combination to provide uniform starting conditions, i.e., each voltage was investigated in a separate experiment, and the same starting conditions were established before the next voltage was in-

vestigated. We denoted this type of experiment as single point single temperature (SPST) measurement, whereby the initial electrolyte temperature was identical for each voltage studied and only one data point could be obtained from each measurement to create a characteristic *I–U* plot.
In addition to these measurements, staircase voltammetry (SCV) measurements were performed such as in Figs. 4.2 and 4.3. Here, the voltage was increased stepwise. In these measurements, each voltage was usually held for 10 s and the voltage was then increased by 20 V and held again for 10 s until a final voltage was reached. In the SCV measurements, as in all other measurements, the electrolyte temperature increased with the measurement time. As a result, the starting conditions, such as the electrolyte temperature, are different for each voltage examined in the course of the SCV measurement. Additionally, the surface structure of the electrode may change during the SCV measurement, causing the next voltage to be investigated with an already restructured electrode, which in turn can also result in an altered measurement compared to the SPST measurements.
The comparison of a SPST measurement with a SCV measurement is shown in Chapter 5.1 in Fig 5.14 for a Au wire electrode.
The increasing electrolyte temperature and its influence on the *I–U* characteristic can also be seen when the voltage on the electrode is not gradually increased starting from low voltages (SCV measurements), but gradually decreased starting from high voltages (reversed staircase voltammetry (rSCV) measurements). In Fig. 4.5, SCV measurements (Fig. 4.5a), as well as rSCV measurements (Fig. 4.5b) of a Pt wire electrode at different initial electrolyte temperatures in 0.01 M KOH are shown. The length of the Pt wire in contact with the electrolyte was adjusted to 10 mm by two caps.
In the SCV measurements, the voltage was increased in 20 V steps starting from 0 V every 10 s, while in the rSCV measurements, the voltage was decreased by 20 V every 10 s starting from 600 V.

The *I–U* characteristic in Fig. 4.5 follows for both measuring procedures the behavior expected from literature and explained in Section 3.2. The influence of the initial electrolyte temperature on the SCV and rSCV measurements also follows the behavior known from the literature and is described in more detail in Section 3.2.1. The SCV measurements at different initial electrolyte temperatures show a similar behavior at high voltages since regardless of the initial electrolyte temperature, the

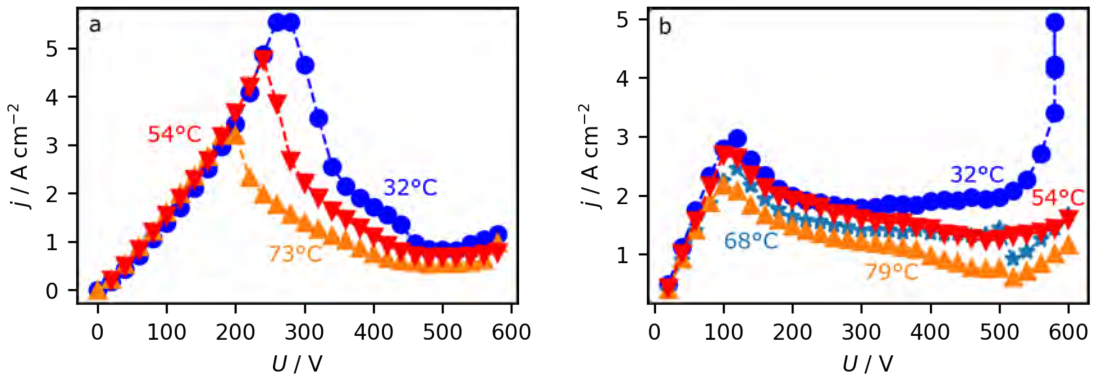

Figure 4.5: a) SCV and b) rSCV measurements of a Pt wire electrode in 0.01 M KOH at initial electrolyte temperatures between 30 °C and 79 °C. For both SCV, and rSCV measurements, the voltage was increased or decreased in 20 V steps. Each voltage was held for 10 s. For the SCV measurements the voltage was increased starting from 0 V, for the rSCV measurements the voltage was decreased starting from 600 V. The length of the Pt wire in contact with the electrolyte was 10 mm in all cases and adjusted with two caps at both ends of the wire.

electrolyte is strongly heated here through the course of the measurement and the electrolyte temperature is thus similar at the end of each measurement. In contrast, the rSCV measurements show the greatest differences at high voltages, while the curves are very similar at low voltages. Again, this can be attributed to similar electrolyte temperatures at lower voltages due to heating of the electrolyte during the course of the measurement.

However, the absolute shape of the *I–U* characteristic differs significantly between the SCV to the rSCV measurements, although the characteristic points are the same in both cases. More information on the effect of temperature on the *I–U* characteristic can be found in Section 3.2.1.

To create an *I–U* characteristic (for example, in Chapter 5.1 in Fig. 5.2 or Chapter 5.3 in Figs. 5.35 and 5.37), the data obtained for each material–voltage–time combination is evaluated as follows.

***I–U* Data Evaluation:** The current data obtained at each voltage was averaged in all cases over the entire electrolysis period at this voltage. In the case of the SPST measurements, this means over the complete measurement time, in the case of the SCV or rSCV measurements for each voltage at which the voltage was held for a predefined time over the whole holding time at this voltage (usually 10 s).

4.4.2 Electrochemical Characterization

For the electrochemical characterization of the electrodes, a distinction must be made between the experimental procedure for Pt and Au electrodes and the experimental procedure for Cu electrodes. The experimental procedure of Cu is different from the procedure of Pt and Au since these measurements were performed in a collaboration with Pramod V. Menezes (HV electrolysis of Cu) and Mohamed M. Elnagar (electrochemical characterization of Cu).
Therefore, in Section 4.4.2.1, first, all experimental details as well as the procedures for the Pt and Au measurements are explained, and next, in Section 4.4.2.2, the electrochemical characterization of Cu is described in more detail.

4.4.2.1 Electrochemical Characterization of Pt and Au

For the electrochemical characterization of the Pt and Au electrodes, a beaker cell with 6 cm diameter was used, which was filled with 150 mL 0.01 M KOH. In each case, the Pt or Au electrochemical working electrode (EWE) was freshly prepared in the manner described above (compare Section 4.3) or treated by HV electrolysis (compare Section 4.4.1). The electrochemical characterization of the Pt and Au electrodes was performed before and after HV electrolysis. The characterization of the electrodes after their preparation served also to control the consistency of the starting conditions, i.e., the presence of similar surface structures. A Pt-sheet of size 10 $\times$ 7.5 mm was always used as an electrochemical counter electrode (ECE). The reference electrode was a freshly prepared homemade reversible hydrogen electrode (RHE).
All potentials in this work are given on the RHE scale.
The potential during each measurement was controlled with a FHI ELAB potentiostat (FHI31 or FHI32). Since the electrodes that are used as working electrodes tend to roughen strongly during HV electrolysis, different current amplifier ranges are often required before and after HV electrolysis. Depending on the current amplifier range set, the measured current has a certain offset. The greater the current amplifier range, the greater this offset. Therefore, for each potentiostat, an offset calibration on a known system was carried out for all current amplifier ranges. Afterwards, the offset was determined for each current amplifier range and the measurement results were offset corrected accordingly. Figure 4.6 shows an offset

calibration for the FHI ELAB potentiostat FHI32. The calibration was performed on Pt wire electrodes in 0.01 M KOH.

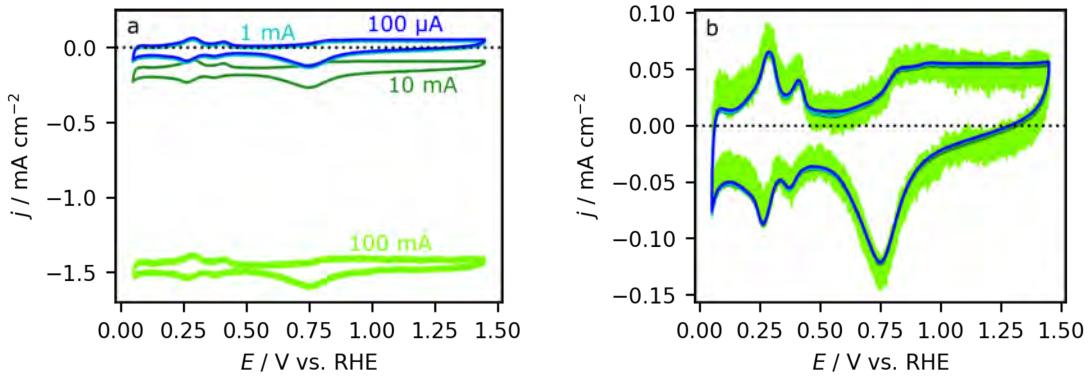

Figure 4.6: Calibration measurements with a 10 mm long Pt wire in 0.01 M KOH to determine the offset of different current amplifier ranges (100 µA, 1 mA, 10 mA and 100 mA) of the potentiostat (FHI32) used. The length of the Pt wire in contact with the electrolyte was adjusted by using polymer caps. a) Pt CVs as measured at different current amplifier ranges (without offset correction), b) the same Pt CVs offset corrected.

Figure 4.6a shows the CVs measured at different current amplifier ranges without offset correction, while Fig. 4.6b shows the same CVs after offset correction. To avoid influences on the electrochemical measurements by oxygen dissolved in the electrolyte, the electrolyte was deaerated with N_2 before the measurements, unless explicitly noted otherwise.

Pt

The initial potential of all Pt measurements was 0.95 V and thus at the open circuit potential. The potential was gradually decreased from the initial potential with a scan rate of 50 mV s^{-1} to a potential of 0.05 V. The upper potential limit was set to 1.45 V. After HV electrolysis, during the first cycles, scanning was only performed up to 1.00 V, to avoid potential-dependent restructuring of the electrode.[198] The lower potential limit remained unchanged. After a few scans, the upper potential limit was set back to 1.45 V, and thus the same scan range as prior to HV electrolysis was set again. This CV measurement allowed a direct comparison of the CV before and after HV electrolysis due to the same scan range.

Au

The initial potential for the electrochemical characterization of the Au electrodes was 1.1 V. With a scan rate of 50 mV s^{-1}, the potential was subsequently decreased and cycled in the potential window between 0.20 V and 1.69 V.
After the HV electrolysis experiments, an additional large reductive current appeared in several measurements of the Au samples. This reductive current, shown in Chapter 5.1 Fig. 5.7, resulted from the reduction of Au oxide formed during HV electrolysis. In order to be able to completely integrate the current resulting from the reduction of the Au oxide formed by HV electrolysis, an initial potential of 1.1 V, close to the OCP of Au (ca. 1.16 V), was necessary, since at a lower initial potential a negative current already flows at the initial potential and thus the current necessary for the reduction of the oxide cannot be completely integrated.
To determine the charge resulting from Au oxide reduction, the potential was cycled from the initial potential in the first cycle to 0.25 V and held there until the reductive current was negligible. More information on the evaluation of the flown charge or integration of the current can be found in Section 4.5.
After holding the potential at 0.25 V, the potential was further decreased to the lower potential limit of 0.20 V and then cycled in the potential window ranging from 0.20 V to 1.69 V.
If SEM images were taken after the electrochemical reduction, the Au electrodes were removed from the electrolyte after lowering the potential starting from 1.1 V and reducing the Au oxide at 0.25 V, and were not further cycled to prevent the surface structures formed by electrochemical reduction from changing due to potential cycling.
Due to technical reasons, for the Au sheets prepared for the FIB-SEM measurements, the total reduction of the Au oxide was performed at 0.25 V, i.e. the potential was not decreased from 1.1 V to 0.25 V. Furthermore, in most cases where a Au sheet or Au POSC was used, the electrolyte was not deaerated prior to the reduction of the Au oxide because the currents originating from the ORR of dissolved O_2 in the electrolyte were negligible compared to the additional reduction current in the CV, which was approximately 100 times larger. The current resulting from the reduction of Au oxide after 30 s HV electrolysis at different voltages is shown in Chapter 5.1 Fig. 5.7.

4.4.2.2 Electrochemical Characterization of Cu

The electrochemical characterization of the Cu electrodes performed in this work was carried out by Pramod V. Menezes and Mohamed M. Elnagar. For the sake of completeness, the experimental details are given below.
The Cu measurements were performed in a classical electrochemical glass cell. Cu wires were used as EWE, a graphite rod as ECE, and a Hg/HgO reference electrode (RE-61AP, ALS). All potentials were converted to the RHE scale. The potential for the Cu measurements was applied with a HEKA PG510 potentiostat. A calibration series was also created for this potentiostat to correct the offset of the current for different current amplifier ranges.
In contrast to the Pt and Au measurements, the Cu electrodes were not measured before (after preparation) and after HV electrolysis, but each electrode was measured either after preparation or HV electrolysis since they undergo structural changes during the electrochemical characterization. For this reason, the preparation of the Cu electrodes was only checked on some Cu electrodes to guarantee that the electrodes show similar structural properties.
All measurements for the electrochemical characterization of Cu were performed in 0.1 M KOH and without stirring the electrolyte. The initial potential was therefore set to 0.31 V. Starting from this potential with a scan rate of 50 mV s^{-1} the potential was decreased to the lower potential limit of -0.34 V and cycled in the potential window from -0.34 V to 0.41 V.
Similar to the Au electrodes, Cu oxide formed on the surface of the Cu electrodes during HV electrolysis (see Chapter 5.1 Fig. 5.11). To be able to quantify this more easily, the potential was lowered from the initial potential to a potential below $<$ -0.2 V and held at this potential in the first cycle until the additional reductive current in the CV, which indicated the reduction of the Cu oxide, was almost zero.

4.4.3 Auxiliary Electrode Experiments

To investigate the influence of an in-liquid plasma and changes in the electrolyte caused by the in-liquid plasma on an auxiliary electrode (AE) in solution, a setup with five electrodes was used. This five electrode setup combines a two electrode setup for electrolysis with a classical three electrode setup used in electrochemistry.

4.4.3.1 Setup

The five electrode setup, schematically shown in Fig. 4.7a and Chapter 5.2 Fig. 5.22, consists of the two plasma electrodes (PWE and PCE), analogous to the HV electrolysis experiments described above (Section 4.4.1), and a classical electrochemical three electrode setup (AE, ECE, REF).
All five electrodes were positioned in a large glass beaker with a diameter of 13.5 cm and a height of 7.5 cm, which was filled with 650 mL 0.01 M KOH. The distance between PWE and PCE was set between 1.2 cm and 1.5 cm, and the distance between the PWE and the AE was either set to 1.5 cm or 4.5 cm. The exact arrangement of all electrodes at both distances (PWE – AE) is illustrated in Figs. 4.7b and c.

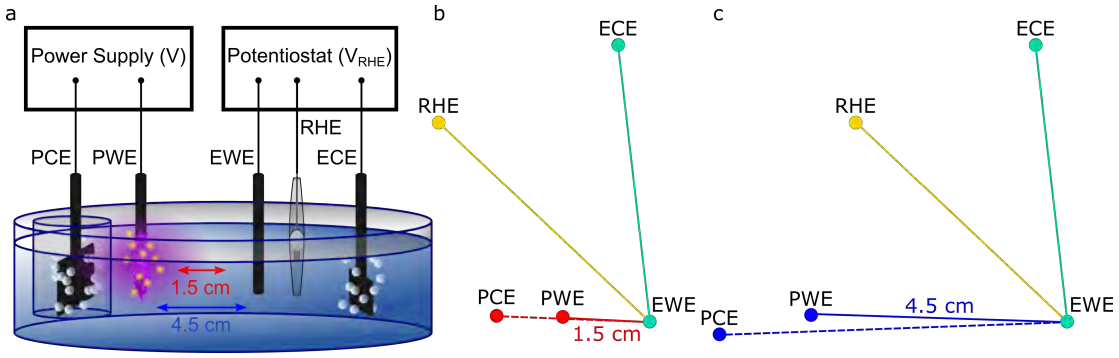

Figure 4.7: a) Schematic illustration of the five electrode setup.[199] Reprinted with permission from J. Vac. Sci. Technol. A, 40, E. Artmann *et al.*, "Using auxiliary electrochemical working electrodes as probe during contact glow discharge electrolysis: A proof of concept study", 053005, Copyright 2022, American Vacuum Society. Electrode configurations of the auxiliary electrode experiments in the five electrode setup with a distance between PWE and EWE of b) 1.5 cm and c) 4.5 cm. Each electrode position is indicated by a circle.

Since the results described in Chapter 5.1 indicated a high stability of Pt in the aCGDE region, a Pt wire was chosen as PWE.[66] Moreover since the electrochemical and electrocatalytic behavior of Pt electrodes is very well characterized, as Pt is also frequently used as a benchmark system, Pt electrodes were also used as AE.[58–63] Two polymer caps were used to better define the length of Pt PWE exposed to the electrolyte and to protect the tip from melting during aCGDE. The length of the wire exposed to the electrolyte was thereby limited to 2 mm (surface area of 0.031 cm^2). The Pt AE was also equipped with a polymer cap on the top

of the wire to limit the length of the wire exposed to the electrolyte to 10 mm (surface area of 0.159 cm^2). A Pt-sheet with a size of 10 $\times$ 7.5 mm served as ECE for all measurements, and a freshly prepared, home-made RHE served as reference electrode (analogous to the Pt and Au measurements in Chapter 4.4.2).
As for all HV electrolysis measurements described above (Chapter 4.4.1), a stainless steel plate of size 20 mm $\times$ 20 mm $\times$ 3.5 mm was used as PCE. To minimize or suppress the influence of products formed at the PCE (H_2) on the AE, a solid glass tube (outer diameter: 2.6 cm; inner diameter: 2.2 cm; wall thickness: 2 mm) was placed around the PCE to transport the products formed at the PCE to the electrolyte surface as efficiently as possible.[18] The glass tube was immersed in the electrolyte slightly deeper than the PCE. A schematic drawing of the experimental setup is shown in Chapter 5.2 in Fig. 5.22.
In some measurements, no glass tube was used around the PCE. If this was the case, it is noted at the appropriate location in the text (Chapter 5.2 Fig. 5.28). In those cases, only 500 mL of electrolyte instead of 650 mL were used.
The voltage between the two plasma electrodes was applied using a TDK Lambda power supply (630 V / 1.365 A) controlled *via* a LabView software. The applied voltage was usually 580 V (plasma power approximately 57 W) in order to ignite the plasma immediately and it was applied for an electrolysis time of 30 s. Some measurements were also performed at 550 V. If this was the case, it is noted at the specific point in the text.
The potential at the AE was controlled with an FHI ELAB potentiostat. The exact measurement procedure is described below. The applied potentials are also specified in this context.

4.4.3.2 Experimental Procedure

Before starting the first measurement of the day, all electrodes were prepared as described in Section 4.3. Based on the results of the investigations on the structural changes of the electrodes at high voltages (see Chapter 5.1), the electrodes were only re-prepared at the beginning of each measurement day and not after each measurement, since under the considered experimental conditions stable electrode surface structures could be assumed.
In contrast, the electrolyte was replaced after each measurement because its com-

position may change by species formed during the plasma, such as H_2, O_2, and H_2O_2.[18, 54, 67] All measurements were performed at an initial electrolyte temperature of 24 °C (room temperature). During the course of the measurement, the temperature of the electrolyte increased rapidly locally near the PWE. Since the electrolyte was not stirred for all measurements, an inhomogeneous temperature distribution is expected. The temperature of the electrolyte was checked both before and after each measurement using a thermometer inserted into the electrolyte and was found to be almost identical. The electrolyte was not deaerated before the respective measurements, since a lot of O_2 is formed anyway during the electrolysis. The structural properties of the electrodes were checked by CV measurements before each new measurement after exchanging the electrolyte to ensure that the structural properties of the electrodes were similar for each measurement. The reproducibility of the approach is shown in Chapter 5.2 in Fig. 5.25.
The measurements were always divided into 3 steps. In the first and third step (step A and C), the AE was characterized electrochemically. Starting from an initial potential of 1.00 V_{RHE} (close to the open circuit potential) the AE was cycled between 0.00 V_{RHE} and 1.05 V_{RHE} with a scan rate of 50 mV s^{-1} and an initial negative scan direction. After a few cycles, the second step B followed. For this, the potential of the AE was held at 1.00 V_{RHE} and, depending on the experimental procedure (see text in Chapter 5.2 for details), either a voltage was applied to the plasma electrodes (step B1) and/or the voltage was held at 1.00 V_{RHE} (step B2) for 15 min. Thereafter, CVs were measured again to elicit the changes caused by step B compared to step A.
For individual measurements, which are noted accordingly in the text, the upper potential limit was increased to 1.25 V_{RHE}. For these measurements, potential cycling was performed starting from an initial potential of 1.20 V_{RHE} and the potential was held at 1.20 V_{RHE} for 15 min after a few cycles. The rest of the procedure remained unchanged. In all measurements performed with this larger potential window, no plasma was ignited, only the potential was held at 1.20 V_{RHE} for 15 min.
When performing the measurements described in Chapter 5.2 Fig. 5.24c (step A-C) without waiting (step B1 only), the waiting time after plasma (step B1) or between the individual CV steps (step A and step C) was determined by measuring the time required for a CV in step C in Chapter 5.2 in Fig. 5.23 to return to its original state (comparison with the BCV in step A). Therefore, after performing step B1, the time was stopped until the final CV (in step C) almost matched the initial one. After this

time, it is assumed that all reactive species formed during the plasma have depleted in the electrolyte.
Since all stopped times are less than 15 min, we assumed that a waiting time of 15 min is well suited for comparing the different conditions. Comparison of the results after performing steps B1 and B2 (shown in Fig. 5.23f-g) with results after performing the same steps, but shortened waiting time in step B2 (stopped time until the final CV resembled the initial CV), showed similar results. Therefore, it could be concluded that the choice of waiting times is appropriate for the given experimental conditions here and does not affect the evolution of the CVs.
The resulting CVs in step C measured with shorter waiting times in step B2 are shown along with the 15 min waiting time measurements in step B2 in Fig. 4.8. However, to be more certain that the reactive species formed during plasma had reacted and for easier comparison of the individual measurements, a standard 15 min waiting period was maintained for all other measurements.

4.5 Surface Area

The surface areas of all samples were determined by calculating the geometric areas of the samples. If roughening of the sample occurred during the measurements, the current densities and charge densities were still related to the original geometric surface areas.
Wires: All wires were assumed to be cylinders. For the wire lengths and diameters used in this work, the use of caps had no effect on the resulting geometric surface areas because the area covered by the cap was too small to have a noticeable influence. With the normally used wire diameter of ø 0.5 mm and wire lengths in the solution of 2 mm, 4 mm and 10 mm, surface areas of 0.03 cm^2, 0.06 cm^2, and 0.16 cm^2 were obtained. For the Cu measurements with a wire diameter of ø 0.5 mm and a wire length of 4.5 cm, the resulting surface area was 0.07 cm^2. With a wire diameter of ø 0.25 mm and a wire length of 10 mm in solution, a surface area of 0.08 cm^2 results.
Sheets: The Au sheets used for some measurements had a size of 2 mm $\times$ 12.5 mm. Depending on the immersion depth, 4 mm or 10 mm, the resulting surface areas were 0.17 cm^2 or 0.43 cm^2.
POSCs: The most difficult task was to determine the surface area of the POSCs.

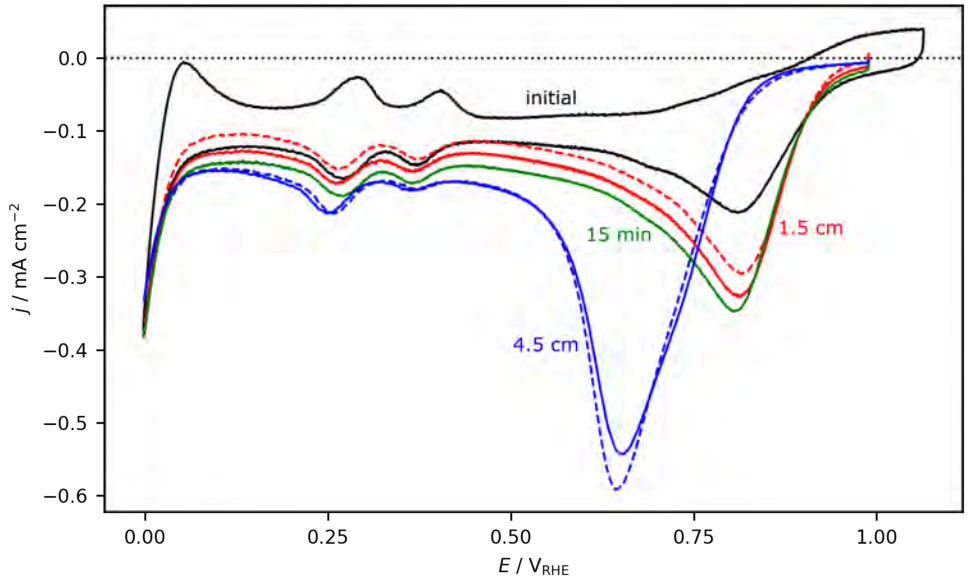

Figure 4.8: CVs of a Pt electrode in 0.01 M KOH at a scan rate of 50 mV s^{-1} before (black) and after 30 s at 580 V with subsequent waiting (steps: A, B1, B2, C) at a distance between PWE and AE of 1.5 cm (red) and 4.5 cm (blue), and a control measurement, without plasma (steps: A, B2, C) (green). In the case of the solid lines, the waiting time in B2 was 15 min; in the case of the dashed lines, a shorter, previously stopped time was used (see text for details). This was 5 min for a distance of 1.5 cm and 2 min 50 s for a distance of 4.5 cm. The potential of the AE during the steps B1 and B2 was held at 1.0 V_{RHE}. See text for details on steps A to C.

All POSCs have a drop-like shape. The larger the POSC, the stronger the deviation from a perfect sphere. For the determination of the surface area, the POSCs were nonetheless assumed to be ideally spherical. To keep the error resulting from the assumed spherical shape as small as possible, the diameter of each bead was determined from SEM images along the original wire and at a 90 °angle to it. The mean diameter, determined from these two diameters, was then used to determine the surface area of the POSC. The contact area between the bead and the wire was subsequently subtracted from the resulting surface area by subtracting the area of a circle with the wire diameter (0.7854 mm^2). The obtained surface areas of the POSCs were between 17.76 mm^2 and 32.21 mm^2.

Roughness Factor - RF: To quantify the roughening of the electrode surface due

to HV electrolysis, the electrochemical surface area (ECSA) before and after HV electrolysis, as well as their ratio before and after HV electrolysis, was determined from CV measurements. This ratio is referred to as the roughness factor (RF) in this work. The RF is a measure of roughness, although the RF does not correspond to the absolute roughness of the surface, but only to the change in the electrochemically active surface compared to the freshly prepared electrode.
The ECSA can be determined from the capacitive region in the CVs, i.e., at potentials where, both before and after HV electrolysis, neither Faraday reactions nor adsorption processes occur. In these double-layer regions, the current depends only on the size of the surface. Thus, the thicker the double-layer, the larger the ECSA.[200] Depending on the material or the system under consideration, the potential at which the ECSA can be determined differs.
In this work, the ECSA was determined for Pt at 0.50 V, for Au at 0.87 V, and for Cu at -0.24 V.
Note, that the absolute values of the RF are strongly dependent on the chosen potential. Therefore, all RF values of a material-electrolyte combination must be determined at the same potential in order to be able to compare different experimental conditions.
In the case of Au and Cu, it was not possible to determine the ECSA and consequently the RF directly after HV electrolysis because, as already described in Section 4.4.2, large negative currents are obtained in the first negative scan after HV electrolysis. These reductive currents can be attributed to the reduction of oxide formed on the surface of the electrode during HV electrolysis and had to be reduced first since the current resulting from the reduction of the oxide strongly overlapped with the double-layer region. For this reason, the roughening of the electrode could only be determined after the oxide had been completely reduced. Hence, the last recorded CV was used to determine the ECSA after HV electrolysis. As a reference for the roughness of the electrode before HV electrolysis, the last CV recorded directly before HV electrolysis was used in the case of Pt and Au. In the case of Cu, the last CV of a freshly prepared Cu electrode was used. All Cu measurements after HV electrolysis were referenced to the same CV before HV electrolysis.
Charge Density: The amount of charge that has passed on the electrode surface during electrochemical reduction can be determined by integrating the reduction current. Theoretically, the resulting charge or charge density should be proportional to the thickness of the oxide formed on the electrode surface, but, as shown in

Chapter 5.3 by FIB-SEM measurements, these values do not match. Nonetheless, the charge passed during the reduction allows to some extent to compare different voltages and thus different experimental conditions (compare Chapter 5.1 Fig. 5.2). As for the determination of the current density from the current passed during HV electrolysis through the initial geometric surface area of the different samples, the charge density was also determined through the charge and the initial geometric surface area of the different samples.

4.6 Structural Characterization

Various imaging methods were employed for the structural characterization of the electrodes. First, optical microscope images were acquired using a Leica S9i optical microscope from Thermo Scientific. Microscope images of a Au and Cu wire can be found in Chapter 5.1 Fig. 5.5 and Fig. 5.9, respectively. Microscope images of a Au sheet are shown in Chapter 5.3 Fig. 5.32 and of Au POSCs in Chapter 5.4. Scanning electron microscope (SEM) images were acquired using a Quattro S and a Scios2 from Thermo Scientific. Therefore, electrons were accelerated toward the sample under investigation. The acceleration voltage was 5 kV, 10 kV or 20 kV for all images. Through the incoming electrons, secondary electrons were released from the sample and always detected with an Everhart-Thornley Detector (ETD). After scanning the sample with the electron beam and subsequent position-dependent detection of the secondary electrons, an SEM image is obtained, which can be used to provide information about the topography of the sample. The additionally performed FIB-SEM measurements were acquired with the Scios2 also from Thermo Scientific by Mohammad Al-Shakran. A Ga source was used for milling the surface. SEM images of the resulting cross sections of the surfaces were taken at an acceleration voltage of 10 kV. A FIB-SEM image of a Au electrode can be found in Section 5.3 Fig. 5.32.
The composition of the surface and its oxidation state were determined by XPS measurements. The excitation was performed with monochromatic Al K_α (1486.6 eV) radiation. As a result of the incident photons on the sample, electrons are released from the inner shells of the atoms. The kinetic energy of these electrons is subsequently detected at a 45 °angle. With the help of the energy of the photons, the measured kinetic energy of the electrons, and the work function,

the binding energy of the electrons can then be calculated and conclusions about the composition and the oxidation state of the sample can be drawn. To thereby counteract possible charging effects, all samples were measured with a neutralizer although all samples were in contact with the ground. All XPS spectra measured within the scope of this work were performed by Konstantin M. Schüttler and can be found in Section 5.3 Fig. 5.32 and Fig.5.40.
The crystallographic orientation of the facets on the surface of the Au POSCs was partially determined using Laue XRD measurements. A Laue X-ray back-scattering camera from Multiwire Laboratories Ltd. was used for this purpose. The obtained diffraction patterns are specific for a particular crystallographic orientation.[196, 201]

5 Results and Discussion

In this Chapter, all results I have acquired during my thesis are shown. Chapter 5.1 to 5.3 are my first author publications. In Chapter 5.4 results published on a preprint server are shown.
The figures shown in Chapters 5.1 to 5.3 have been partially resized and formatted according to the layout of this thesis.
In addition, the numbering of the figures, as well as the numbering and style of the references, has been adjusted for the incorporation of the publications into this thesis.
The experimental parts of all results shown in Chapter 5.1 to 5.4 can be found summarized in Chapter 4. On the one hand, this avoids repetitions, on the other hand, some experimental aspects can be further elaborated.

5.1 Structural Evolution of Pt, Au, and Cu Anodes by Electrolysis up to Contact Glow Discharge Electrolysis in Alkaline Electrolytes

The results shown in this Section (5.1) were published in Chem. Phys. Chem.[66] Reprinted with permission from Chem. Phys. Chem., 22, E. Artmann *et al.*, "Structural Evolution of Pt, Au and Cu Anodes by Electrolysis up to Contact Glow Discharge Electrolysis in Alkaline Electrolytes", 2429-2441, Copyright 2021, John Wiley and Sons. "© 2021 The Authors. ChemPhysChem published by Wiley-VCH GmbH."
Most of the Pt and Au measurements were performed by myself. A few of these measurements were performed by Lukas Forschner in his project work with my instructions. All Cu measurements, except the Cu microscope image which was

taken by me, were performed by Pramod V. Menezes and Mohamed M. Elnagar in an internal collaboration.
The conceptualization of this publication, as well as the complete data analysis (analysis, visualization, validation), the preparation of all figures and writing of the original paper draft were done by myself.
As a summary of this Section, the graphical abstract of this work, already published in ChemPhysChem,[66] is included here.

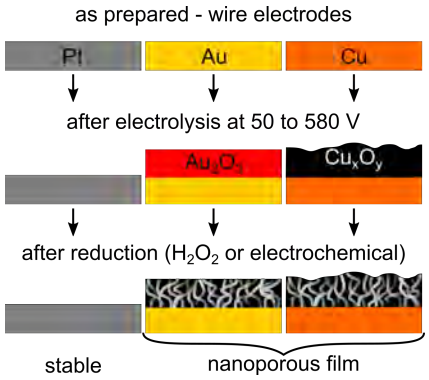

Figure 5.1: Graphical abstract of the publication titled "Structural Evolution of Pt, Au and Cu Anodes by Electrolysis up to Contact Glow Discharge Electrolysis in Alkaline Electrolytes".[66]

5.1.1 Abstract

Applying a voltage to metal electrodes in contact with aqueous electrolytes results in the electrolysis of water at low voltages and plasma formation in the electrolyte at high voltages referred to as contact glow discharge electrolysis (CGDE). While several studies explore parameters that lead to changes in the I–U characteristics in this voltage range, little is known about the evolution of the structural properties of the electrodes. Here we study this aspect on materials essential to electrocatalysis, namely Pt, Au, and Cu. The stationary I–U characteristics are almost identical for all electrodes. Detailed structural characterization by optical microscopy, scanning electron microscopy, and electrochemical approaches reveal that Pt is stable during electrolysis and CGDE, while Au and Cu exhibit a voltage-dependent oxide formation. More importantly, oxides are reduced when the Au and Cu electrodes are kept in the electrolysis solution. We suspect that H_2O_2 (formed during electrolysis) is

responsible for the oxide reduction. The reduced oxides (which are also accessible *via* electrochemical reduction) form a porous film, representing a possible new class of materials in energy storage and conversion studies.

5.1.2 Introduction

Applying a voltage to metal electrodes in contact with aqueous electrolytes is used to catalyze Faraday and non-Faraday reactions,[87, 202, 203] tailor surface properties of electrodes,[14, 69, 176, 182] form nanoparticles[19, 134] or alter the electrolyte composition,[14, 87] as well as to ignite plasmas in solution.[17, 18, 87] Depending on the application, a detailed understanding of the parameters that limit the electrode stability is decisive to prevent material degradation or to adjust the formation of specific structures. The electrode stability is highly dependent on the applied voltage and the processes occurring at the electrode surface, which change dramatically when the voltage is increased significantly. Focusing on gas-evolving working electrodes, the phenomena that are expected to occur at the solid | liquid interface can be summarized as follows. For low voltages, water electrolysis is observed (referred to as normal electrolysis - NE). Increasing the voltage leads to violent bubble formation until the so-called breakdown voltage, where a gas film (sheath) forms around the electrode. At even higher voltages, the formation of a homogeneous plasma is observed within this sheath, which is called contact glow discharge electrolysis (CGDE).[17, 18, 85, 87] The voltage at which CGDE is formed (minimum of the I-U curve) is called the midpoint voltage.

Since the discovery of CGDE in aqueous electrolytes by H. Kellog in 1950,[17] there have been several reports describing the shape of current-voltage (I–U) curves from NE to CGDE, exploring the impact of electrode material, electrolyte, temperature, pH, composition, electrode geometry, etc.[18, 19, 56, 82, 84–87] The most noteworthy observation for the present work is that during CGDE, the products formed at the interface are more diverse than those known from NE. For example, regardless of electrode polarity, both H_2 and O_2 may be formed simultaneously during CGDE. More importantly, in anodic CGDE, in addition significant amounts of H_2O_2 are also produced.[18, 67, 85] The origin of the formation of the product cocktail is caused by non-Faraday processes, where H_2O molecules decompose into highly reactive short-lived radicals and ions during CGDE, which react one with

another in the plasma phase or at the plasma | liquid interface.[65, 85, 87]

Less is known on the evolution of the structural properties of the electrode material with increasing voltage from the NE to the CGDE regime.[182] Instead, the structural properties for both limiting regions are usually studied separately, for different reasons which is illustrated by the following examples. For the NE region electrode stability is an important aspect in electrocatalysis. Stable electrodes during the reaction are desired since degradation of the catalyst often lowers the efficiency. Besides, anodizing electrodes in aqueous electrolytes is used to form oxide structures or to smooth or clean materials via electropolishing.[176, 177] When negative voltages are applied, the electrodes can undergo cathodic corrosion.[133, 134, 139, 140] This approach can produce nanoparticles, tune the surface crystallographic orientation for catalytic reactions or other applications.[133, 134, 139, 140] Regarding the high-voltage regime, where plasmas can be generated in liquid, is a growing area of research, aiming at a fundamental understanding of plasma formation, its interaction with the solid electrode and electrolyte, and to explore new fields of application.[14, 35, 65, 69, 182] Plasmas in liquid can be used to distinctly tailor the (near-)surface electrode properties, *i.e.*, to form durable oxide coatings on materials of complex sizes *via* plasma electrolytic oxidation (PEO)[25–27] or to remove irregularities from the workpiece *via* plasma electrolytic polishing (PEP).[181, 182] As with cathodic corrosion, the electrodes can also decompose into (multi-)metallic or oxidic nanoparticles.[14, 19, 20, 35, 171–175] Such particles can also be formed from metal ions present in the electrolyte during plasma electrolysis.[14, 195] Finally, another interesting and yet emerging field is the wastewater treatment by plasmas,[14, 34–37] where the stability of the prepared electrodes is detrimental to prevent any kind of metal contamination in the water. These examples and applications show the broad application of plasma treatment and the importance of having a clear picture of any kind of plasma-induced structure changes or formation processes. Overall, the examples also raise the questions if similar or other structures to those observed in the NE and CGDE regime, are accessible in the voltage regime in between.

This is subject of this work, which aims at providing (i) more detailed and systematic insights into possible changes in the structural properties of gas-evolving metal electrodes and (ii) new approaches for material design, covering the voltages range from NE to CGDE. Motivated by their importance in electrochemistry and electro-

catalysis, we restrict our investigations to processes at poly-crystalline Pt[28, 38–41], Au[29, 42, 43] and Cu[30, 52, 53] wire anodes. While various studies have addressed the structure of these electrodes at low potentials (NE regime), much less is known about their behavior during CGDE.[14, 17–19, 173, 174, 204] Au is the most noble metal and is used extensively as a model electrode in electrochemical surface science.[29, 42] Despite its nobility, Au was shown to form Au_2O_3 films on its surface for low potentials before and in the oxygen evolution reaction (OER) region.[43] These Au_2O_3 films are, however, unstable at room temperature.[117] Reports on the structural properties of Au beyond NE are rare,[18] and primarily focus on cCGDE, where Au nanoparticles are formed.[173, 174, 204] Cu raised a lot of interest in the electrocatalysis community over the last few decades as it is the only pure metal that converts CO_2 electrochemically into higher valuable hydrocarbons. This is an important process in the decarbonization of the society and closing the carbon cycle.[14, 30] There exists a plethora of different approaches to prepare Cu catalyst materials.[205] Among those, it was reported that nanostructured Cu electrode materials can be prepared via gas phase plasma oxidation.[53] A direct preparation of catalytically active surfaces via CGDE could provide an alternative approach for in situ preparation of the catalyst material. Similar to Au, Cu electrodes used under CGDE conditions were primarily studied for the purpose of nanoparticle formation.[14, 19] In our study, the electrodes are investigated by controlled–potential electrolysis at a set of voltages ranging from the NE region up to 580 V in 0.01 M KOH electrolyte. The resulting I–U behaviour is discussed based on the structural properties investigated after the electrolysis. The topography and microscopic changes of the electrodes are imaged with an optical microscope and by scanning electron microscopy (SEM). For the oxide-forming metals Au and Cu, the amount of oxide formed during electrolysis is determined after the electrolysis from chronoamperometric measurements performed at potentials below the reduction potential of the respective oxides. We demonstrate, that independent from the applied voltage during electrolysis (50 to 580 V), the Au and Cu oxides also reduce when kept in the electrolysis solution after the electrolysis. The effect of H_2O_2 on the oxide reduction is discussed. Finally, we demonstrate that the oxide reduction leads to the formation of highly porous nanostructures, determined from combined cyclic voltammetry and SEM experiments.

5.1.3 Results and Discussion

In the following, first the I–U behavior of the different investigated metals is discussed, followed by detailed analyses of their rather specific and divergent structural and electrochemical properties. The general observations for all systems are finally summarized in the conclusion. A detailed description of the experimental conditions is provided at the end of the manuscript and further details are provided in the supporting information (SI).

5.1.3.1 I–U Characteristics

Figure 5.2 shows stationary I–U characteristics of Pt, Au, and Cu wire electrodes (immersed 10 mm, diameter 0.5 mm) recorded for 30 s electrolysis in 0.01 M KOH where the averaged current values for each voltage were obtained with freshly prepared electrodes. The chronoamperometric curves for the individual values are provided in Fig. 5.13. Longer electrolysis times were avoided to prevent significant changes in electrolyte temperature, which can change the I–U behaviour significantly. For a similar reason, applying voltages above 580 V was avoided, where in addition the wire can easily melt. Details on the experimental approach, chronoamperometric measurements, data evaluation, and the effect of temperature are provided in the experimental section and the supporting information (Figs. 5.13 and 5.14).

The I–U behavior in Fig. 5.2 is characteristic for gas–evolving electrodes.[18, 82, 206] In the NE region from approximately 50 V up to the breakdown voltage (V_{B}) at ca. 350 V, the current increases linearly due to the limited conductivity of the electrolyte according to Ohm's law.[18, 85, 206] Note that at low overpotentials (few volts), electrolysis is limited by the activation of charge transfer that usually leads to an exponential increase of the current density.

At V_{B} the resistance increases due to gas film formation around the electrode, which leads to a break down of the NE concomitant with a decrease in current density. The effect becomes more pronounced with increasing voltage. Close to the midpoint voltage (V_{D}) at ca. 540 V, sparks are observed by visual inspection in the gas film forming around the electrode. At V_{D} the electrode is completely wrapped in a gas

sheath and a blue-violet fast fluctuating plasma with an electrifying, sharply hissing sound is observed within the sheath.

Overall, the I–U characteristics are very similar for all three electrode materials investigated, and the current densities at the characteristic voltages V_{B} and V_{D} are almost identical. This suggests that for a given electrolyte the I–U behaviour is almost independent of the examined electrode material and that the material properties (i) do not change, (ii) change in a similar fashion, or (iii) changes of the material properties are not important for the I–U curves.

A direct comparison of the current values at specific voltages, specifically the occurrence of characteristic voltages (V_{B} and V_{D}), with results from literature is, however, not straightforward. As mentioned above, in general the I–U behavior strongly depends on the experimental conditions, and furthermore the values of the characteristic voltages strongly depend on the cell and electrode geometry.[18, 19, 56, 82, 84–87, 92] Nevertheless, Hickling and Ingram investigated the I–U behavior of Pt, Au and Cu wire electrodes (among others), although in another electrolyte (0.05 M Na_2HP0_4). Their results showed that Au, Pd, and Pt show a very similar behavior during electrolysis at various voltages compared to W, Cu, or NiCr [18]. The authors suggested that on the latter metals oxide film formation and corrosion are at the origin of the different behavior compared to Au, Pd an Pt.[18] Our own results on the structural properties of the electrodes discussed below, will show that oxide formation occurs on Au and Cu electrodes. The fact that the I–U curves of Au and Cu are almost identical to that of Pt, suggests that the electron transport through the oxide film on Au and Cu is equally fast as for bare Pt electrodes, which is different for systems that form passive oxide films.[82]

5.1.3.2 Structure Formation

Further insights on the impact of the electrolysis on the structural properties of the electrodes is gained from optical microscopy, SEM, and detailed voltammetric studies of the electrodes, by comparing the data recorded before and after electrolysis. While the microscope images (optical and SEM) provide insights into the three-dimensional structural changes, from the cyclic voltammetry measurements we can additionally deduce (i) the amount of oxide formed during electrolysis, (ii) determine possible changes in the crystallographic orientation of the surface, and (iii) derive

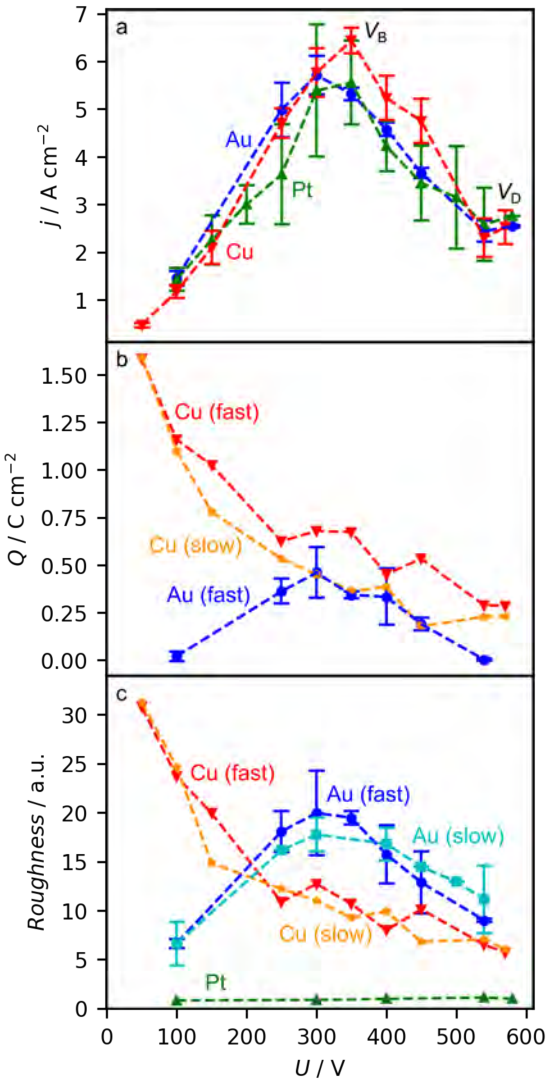

Figure 5.2: a) I–U characteristics, where each data point was recorded with a freshly prepared electrode for 30 s electrolysis in 0.01 M KOH. b) Cathodic charge density determined from the chronoamperometry measurements in Fig. 5.8 for Au, and for Cu, respectively, recorded after the electrolysis and subsequent electrochemical reduction. It is important to distinguish whether the electrode is removed immediately after the electrolysis from the solution (fast) or kept in the electrolysis solution for additional 60 s (slow). c) Change in roughness factor (RF) with respect to the as-prepared samples after the anodic polarization and subsequent electrochemical reduction determined from the CVs presented in Fig. 5.8 for Au, and Fig. 5.12 for Cu.[66]

changes in surface area.[200, 207] In the following, the electrode materials are discussed separately since the structural modifications of the investigated metals differ strongly one from another.

Pt

The SEM images of an as-prepared Pt wire and that after the electrolysis at 300 V for 30 s in 0.01 M KOH are depicted in Fig. 5.3. Further images obtained for other electrolysis voltages (100 and 580 V) are provided in Fig. 5.15. The SEM images suggest that the Pt surface does not restructure significantly during electrolysis at any applied voltage.

To substantiate this finding, we studied the electrodes by cyclic voltammetry. The cyclic voltammograms (CVs) recorded for the Pt electrodes in 0.01 M KOH at 50 mV s^{-1} before (black) and after electrolysis (blue & orange) are presented in Fig. 5.4. All potentials in the electrochemical experiments are on the reversible hydrogen electrode (RHE) scale unless otherwise mentioned. The CVs show the typical features for hydrogen ad-/desorption (between 0.05 and 0.55 V) and OH/O ad-/desorption (between 0.7 and 1.0 or 1.5 V) on Pt in alkaline electrolytes.[208] The downshift of the current in the hydrogen region is caused by residual oxygen in the cell. For the first voltammetric cycle recorded after the electrolysis (blue), the upper potential limit was fixed at 1.0 V to avoid significant surface restructuring which would occur by applying higher potentials.[209–212] The CV recorded with an upper potential limit of 1.45 V (orange) was subsequently recorded.

The peaks in the CV are located at almost the same potentials, and also the current densities at the peak maxima are rather similar, hence the crystallographic orientation of the surface did not change measurably. The small changes in the current density are within the limits of the experimental precision. This may be because the immersion depth of the wires cannot always be set precisely the same. Nevertheless, the almost similar current densities in CVs recorded before and after the electrolysis suggest that the surface area does not change significantly. Henceforth the change in electrochemical surface area is denoted as roughness factor (RF), which is described in detail in the experimental section. For Pt the RF remains almost at unity, as shown in Fig. 5.2 c (green triangles). Note that much more sensitive methods are needed to resolve possible restructuring processes on the atomic scale. For the high voltage region (CGDE), Pt was previously suggested to be sta-

ble in a wide range of electrolytes.[17, 18, 54–57] Interestingly, gas phase plasma treatment with oxygen also does not roughen the electrode surface, but leads to the formation of a Pt-oxide.[213] This is different in the OER region (onset of NE in the range of a few volts which was not investigated in this study), where surface restructuring has been suggested by Favaro *et al.*[62] Studying the oxygen evolution reaction (OER) on Pt electrodes in alkaline electrolytes, the authors observed a restructuring of the electrodes with *ex situ* atomic force microscopy (AFM) after the OER. They also observed the formation of a complex, several nm thick oxy-hydroxy film on the electrode surface, as elucidated by using ambient pressure X-ray photoelectron spectroscopy (APXPS).[62] Bulk oxide formation under these conditions was also suggested by theoretical studies to be thermodynamically favorable at high overpotentials for Pt nanoparticles.[214] From experiments the oxidation of Pt electrodes was, however, suggested to be kinetically limited and hence the formation of thick oxide films is slowed down due to the short electrolysis times.[110]

From studying the first negative potential scan of the CV starting from 0.95 V in our experiment, we did not observe any currents related to oxide reduction. Even though we cannot completely rule out that the surfaces reduce during the transfer from one electrochemical cell to another, based on our results we suggest that oxide formation might not occur during electrolysis at voltages above 100 V in alkaline electrolyte.

Au

After performing electrolysis at different voltages for 30 s in 0.01 M KOH (as in Fig. 5.2 a), inspection of the Au electrodes by the naked eye revealed a color change for all voltages. In addition, the intensity and color depends on the applied voltage and more importantly on the time of exposure of the electrode to the electrolyte after the electrolysis. This is demonstrated by the optical microscope image in Fig. 5.5 for a Au electrode on which 300 V were applied during electrolysis. If the electrode is immediately removed from the electrolyte after electrolysis the electrode is mostly red (Region 1), whereas the electrode part that was kept in the electrolysis solution turns black within a few seconds (Region 3). Respective microscope images taken after the electrolysis at different voltages are provided in Figs. 5.6 a to d (first column) along with selected SEM images recorded on the red region (1), transition region (2), and black region (3) in the second to the fourth column. Overall, the red

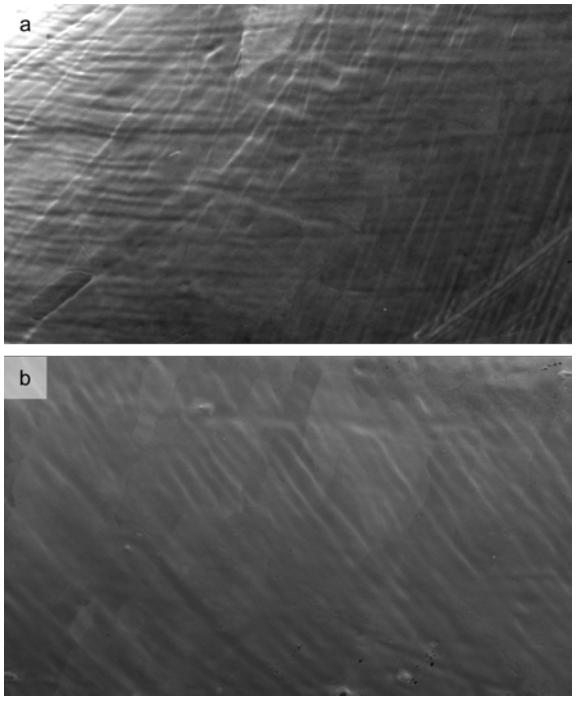

Figure 5.3: SEM images (250 µm × 150 µm) of a Pt wire electrode a) as-prepared and b) after electrolysis at 300 V for 30 s in 0.01 M KOH. Further SEM images are provided in Fig. 5.15. The images were improved by adjusting the contrast and brightness.[66]

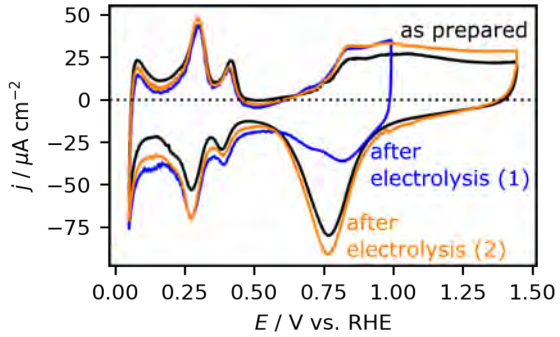

Figure 5.4: CVs recorded in 0.01 M KOH at 50 mV s^{-1} of an as-prepared Pt electrode (black curve) and the same electrode after the electrolysis at 300 V for 30 s in 0.01 M KOH. The first CV after the electrolysis was recorded with an upper potential limit of 1.0 V (blue). Subsequently, additional cycles were recorded with an upper potential limit of 1.45 V (orange).[66]

color of the Au wire suggests that a Au_2O_3 layer is formed during the electrolysis on the electrode. Considering that Au_2O_3 was also observed for oxygen plasma treated

Au electrodes,[215, 216] it is very likely that Au_2O_3 is formed especially in the CGDE region, where oxygen species are present in the plasma. For comparison with the initial surface structure of the Au electrode, a SEM image of the as-prepared Au electrode is provided in the SI (Fig. 5.16 a).

Figure 5.5: Microscope image of a Au wire after electrolysis at 300 V for 30 s in 0.01 M KOH. The left (golden) part shows the as-prepared Au wire, the middle (red) part (region 1) was immediately removed from the electrolyte after the electrolysis, and the right (black) part (region 3) was kept in the electrolysis solution for 60 s after switching the voltage off. Region 2 marks the transition between regions 1 and 3.[66]

Focusing on the red part (region 1), obtained by electrolysis and subsequently direct removal of the electrode from the electrolyte solution, we observe in the optical microscope images that the intensity of the red color varies with the applied voltage. At 300 and 400 V the red tone is rather intense, while at 100 and 540 V the red color is less pronounced and shows a touch of orange. Corresponding SEM images are provided in Figs. 5.6 e to h (second column). For all voltages, the surface shows large flat regions and several approximately 150 nm wide cracks. In some regions it seems as if the newly formed adlayer peels off from the Au wire substrate. While the origin of this process is unclear, we suggest that this can be caused by the emersion and immersion of the electrode during the transfer between the different electrochemical cells. The holes observed in the SEM images, especially in Figs. 5.6 e to g, are primarily induced by the electron beam of the SEM (see Fig. 5.17).

The amount of oxide formed during electrolysis was quantified by electrochemical reduction in 0.01 M KOH, as shown in Fig. 5.7. Here the potential was swept at 50 mV s^{-1} from an initial potential of 1.10 V to 0.25 V, where the potential was kept until the reduction current became insignificant (up to 50 s). The total charge passed during these chronoamperometry measurements is depicted in Fig. 5.2 b. The trend in charge density passed in each measurement follows the I–U behaviour

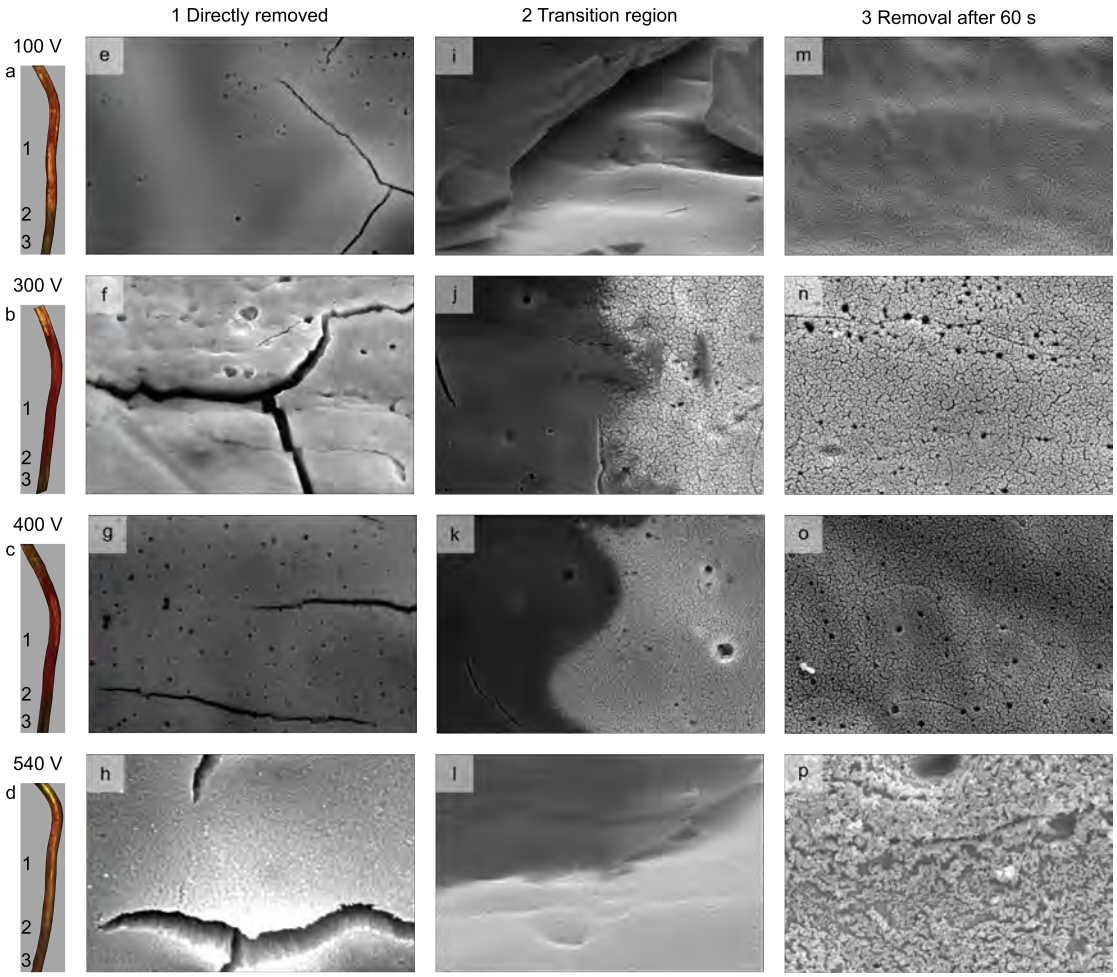

Figure 5.6: Left column: Optical microscope images of Au wires taken after electrolysis at the given voltages for 30 s in 0.01 M KOH. The numbers in the optical microscope images (a-d) illustrate the different regions in Fig. 5.5. The second to fourth column show from left to right SEM images of the regions 1-3 (12 µm $\times$ 8 µm), recorded after electrolysis at different voltages. A SEM image of an as-prepared electrode is provided in Fig. 5.16 a.[66]

in Fig. 5.2 a, where the largest charge density is obtained for electrolysis at 300 V with 460 mC cm^{-2}. For voltages around 100 V and 540 V the amount of oxide is significantly lower, with ca. 23 mC cm^{-2} at 100 V and 6 mC cm^{-2} at 540 V.

Considering that the charge density is related to the amount of oxide formed per cm^2, during 30 s of electrolysis the thickest oxide film is formed at around 300 V. Another important observation is that the initially red electrode turned black during the reduction process. SEM imaging of these reduced electrodes revealed a

highly porous structure which is depicted in Fig. 5.18. Such a change in color has been reported recently for the reduction of Au_2O_3 to metallic Au,[109] and the black color has been attributed to the ability of the nanostructured Au surface to absorb significantly the incident light from the visible spectrum.[158, 159]

Comparing the CV of an as-prepared Au wire electrode (Fig. 5.8 a) with those obtained after the electrolysis and subsequent electrochemical reduction in Fig. 5.8 b, overall higher current densities are observed for the latter electrodes. Note that all current densities are normalized to the initial geometric surface area of the wire. No additional peaks or changes in relative peak sizes are observed in the CVs, which would indicate a change of surface structure or crystallographic orientation.[133, 140] The shift of the oxidation (reduction) peaks to more positive (negative) potentials for higher current densities is presumably caused by internal resistance effects. The increase in Faraday current suggests a strong increase in surface area, especially for electrolysis at around 300 V, which is apparent from the change in RF shown in Fig. 5.2 c (labeled Au fast). The evolution of the RF after reduction of the Au_2O_3 phase formed during the electrolysis with increasing voltage follows the overall trend of the I–U and Q-U curves of Figs. 5.2 a and b, where the highest RF value is obtained at V_{B} (ca. 300 V). Interestingly, for electrolysis at 100 and 540 V, where the amount of surface oxide was low (Fig. 5.2 b), the increase in surface area is still significant but lower than at V_{B}. Possible reasons for the voltage-dependent growth rates are yet to be resolved.

A peculiar observation is that the Au electrodes also turn black when they are kept in the electrolysis solution for 60 s after the electrolysis (see region 3 in Fig. 5.5). Unlike for the red part (region 1), the intensity of the color is similar for all voltages. Corresponding SEM images are provided in Figs. 5.6 m to p (fourth column). Compared to the red part of the electrode, the surface is much more porous, with a sponge-like surface structure that looks very similar to that obtained after the electrochemical reduction of the Au_2O_3 above. For a better comparison between the structures, in Figs. 5.6 i to l (third column) we depict the transition region (region 2) between the red and black parts. In these images, the red Au_2O_3 region appears darker than the black nanoporous metallic Au region.

Inspection of the black region by cyclic voltammetry did not show any signs of surface or near-surface oxide reduction in the first negative-going scan in contrast to the red part of the Au wire. Instead, the CVs look almost identical to those ob-

tained after electrochemical reduction of the red electrodes shown in Fig. 5.8 b, and also the RF is almost identical to those obtained for the red electrodes polarized at similar voltages (Fig. 5.2 c – labelled Au slow).

To elucidate the origin of the color change of the Au electrodes kept in the electrolysis solution, we first stored electrodes directly removed from the electrolysis solution under ambient conditions or in a fresh 0.01 M KOH solution for 24 to 48 hours. This did not induce a color change, and hence, the structural change had to be caused by species present in the solution after electrolysis. For low voltages (NE), it is expected that mainly O_2 is formed from water splitting. At significantly high voltages, in the region of CGDE (in our case $> \ 540\ V$), it has been demonstrated that after the electrolysis in addition to O_2, also H_2 or H_2O_2 were detected.[18, 54, 67] In a further set of experiments, the Au electrodes that were removed immediately after electrolysis were dipped into KOH solutions saturated with H_2, O_2, or mixed with H_2O_2. We could only observe a color change from red to black in the H_2O_2 containing solution, hence it is reasonable to assume that the H_2O_2 is at the origin of the reduction process at least at high voltages. To what extent highly-reactive, short-living or excited radicals and ions, present during and shortly after CGDE, contribute to the reduction process after the electrolysis can not be deduced from our experiment. The origin of the oxide reduction at lower voltages in the electrolysis solution can only be speculated on, and further experiments are required to elucidate whether H_2O_2 possibly forms under these experimental conditions.

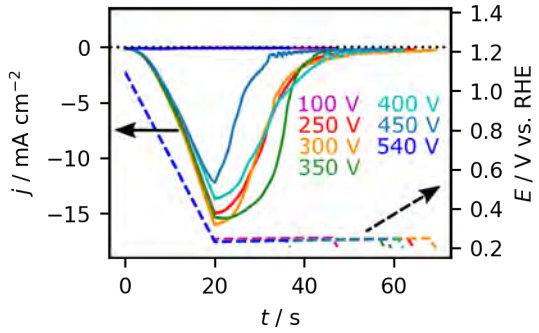

Figure 5.7: Characterization of the amount of oxide formed on Au wires after electrolysis in 0.01 M KOH at the given voltages. The potential was swept at 50 mV s^{-1} from the initial potential of 1.1 V to 0.25 V, where the potential was held until the reductive current became insignificant.[66]

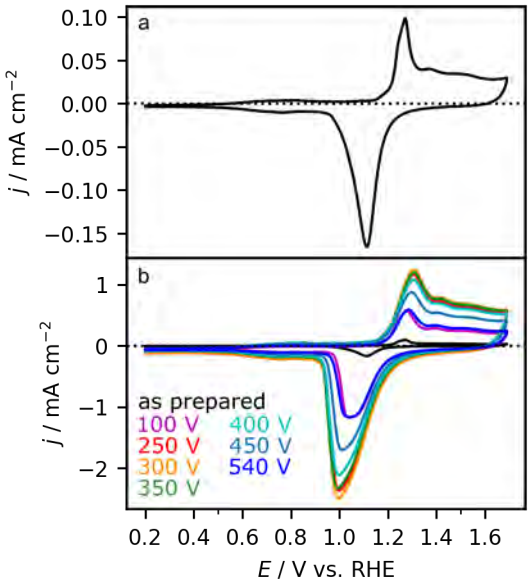

Figure 5.8: CVs of a) an as-prepared Au wire (black) and b) the same electrode in comparison to the electrochemically reduced electrodes in Fig. 5.7 (previously treated by electrolysis at the given voltages). The CVs were recorded at 50 mV s^{-1} in 0.01 M KOH.[66]

Cu

As in the case of Au, for Cu electrodes also the the impact of removing the electrodes immediately after the electrolysis from the electrolyte and after keeping the electrodes for additional 60 s in the electrolysis solution was investigated. Independent of the experimental procedure, the Cu electrodes turned black. Only with the optical microscope subtle color changes are observed on a wire treated by both approaches, as shown in Fig. 5.9. The color changes were independent of the applied voltage during electrolysis. The black color strongly implies that a Cu(II)-oxide (CuO) is formed. Note that Cu(I)-oxide (Cu_2O) is red. The formation of Cu oxides with different oxidation states was also shown previously for Cu electrodes prepared by oxygen plasma.[217] The origin of the two black regions is discussed below.

Figure 5.10 shows SEM images taken on regions of the Cu wires removed directly after the electrolysis (left column) and kept in the solution for additional 60 s (center column). In the supporting information, Fig. 5.19 shows additional SEM images depicting a larger surface area. SEM images of an as-prepared Cu electrode is provided in Fig. 5.16 b. The SEM images do not suggest distinct structural dif-

Figure 5.9: Microscope image of a Cu wire after electrolysis at 300 V for 30 s in 0.01 M KOH. The left part of the microscope image shows the as-prepared Cu wire. Region 1 shows the part of the wire which was immediately removed from the electrolyte after the electrolysis, where region 3 was obtained from keeping the electrode in the electrolyte for 60 s. Region 2 is the transition between region 1 and 3. The contrast and brightness of the image was visually improved for better visibility of the two regions.[66]

ferences between both experimental approaches, even though both regions show slightly different colors in the optical microscope (Fig. 5.9). Hence, the following description applies to both regions 1 and 3 depicted in Fig. 5.9. In contrast to Pt and Au, the SEM images of Cu (Fig. 5.10) demonstrate macroscopic surface structural changes as a function of the applied voltages. After electrolysis at low voltages (until 100 V), 3D flake-like structures are formed. Three-dimensional macroscopic structure formation for Cu electrodes in alkaline media is not uncommon.[124, 218, 219] Performing electrolysis at intermediate voltages (250 V) results in pitting of the surface. Performing electrolysis at high voltages, including the region for CGDE, the surface becomes more smooth.

As indicated above, the color change of the electrode during the electrolysis to black strongly implies that a CuO is formed. To quantify the amount of oxide, the electrodes were electrochemically reduced in 0.1 M KOH by sweeping the potential at 50 mV s^{-1} from 0.31 V to a potential beyond -0.2 V and kept at a potential lower than -0.2 V until the reduction current becomes insignificant (up to 40 s), as shown in Fig. 5.11. After this procedure the electrodes were completely reduced as confirmed by EDS measurements.[22] In principle, it is possible to determine the type of Cu oxide or hydroxide from the peak position in the negative-going scan direction of the CV.[124] However, in this case (see Fig. 5.11) the amount of oxide is rather high such that distinct well-separated reduction peaks could not be resolved and the contribution from the reduction of different Cu oxides/hydroxides overlap. Nevertheless, based on the work by Deng and coworkers, who studied the OER in alkaline electrolyte, CuO was identified along with $Cu^{III}O_2^-$ compounds by XANES and *in*

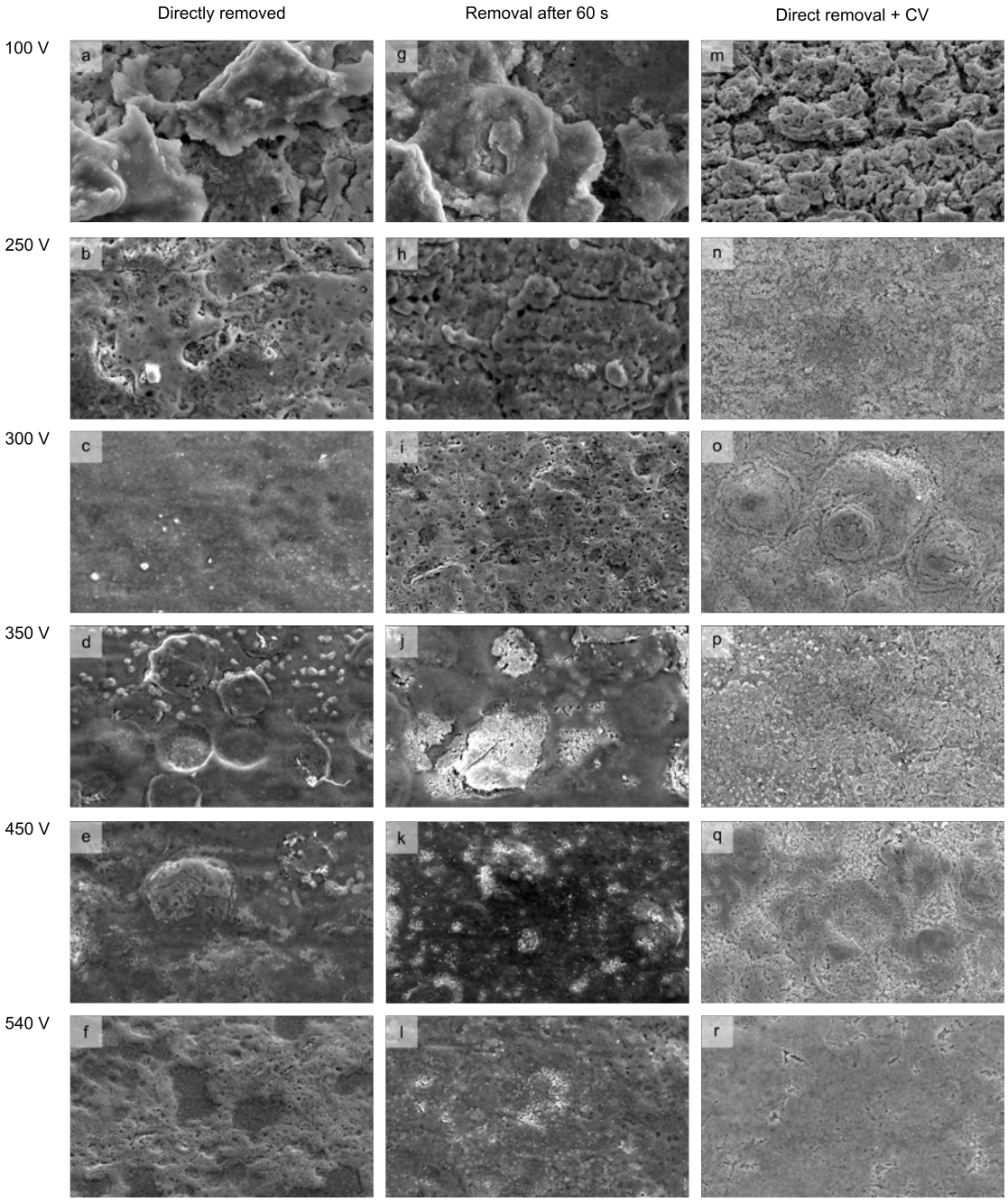

Figure 5.10: SEM images (50 µm × 30 µm) of Cu wire electrodes (length: 10 mm, diameter: 0.5 mm) after the electrolysis at the given voltages for 30 s in 0.01 M KOH. The first column (a-f) shows micrographs of the surface structures of the wires that were directly removed after the electrolysis, the second column (g-l) after keeping them in the electrolysis solution for 60 s , and the third column (m-r) after direct removal of the wires and subsequent electrochemical characterization.[66]

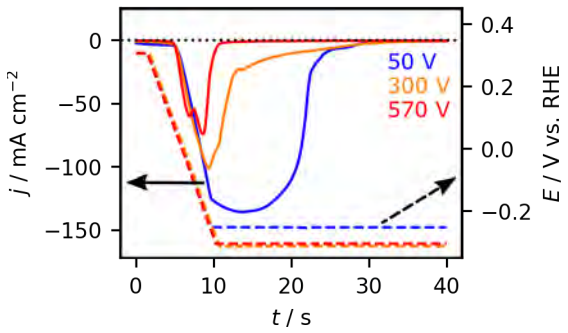

Figure 5.11: Characterization of the amount of oxide formed on Cu electrodes after the electrolysis at the given voltages, by sweeping the potential from 0.31 V to a potential beyond -0.2 V until the reductive current almost vanished.[66]

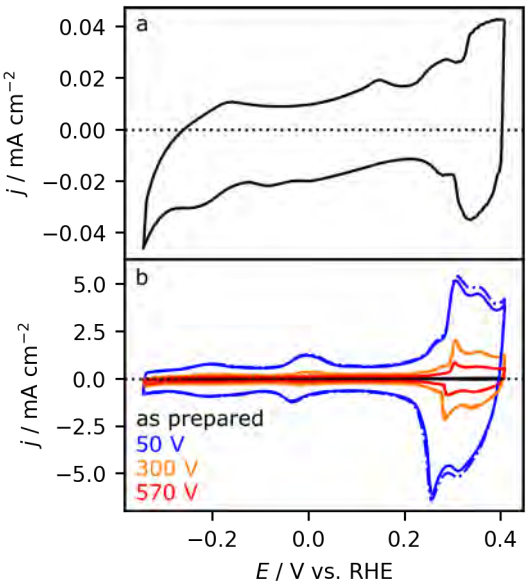

Figure 5.12: CVs of a) an as-prepared Cu wire (black) and b) the same electrode in comparison to the electrochemically reduced electrodes in Fig. 5.11 (previously treated by electrolysis at the given voltages). The CVs were recorded at 50 mV s^{-1} in 0.01 M KOH. The CVs presented in b) with solid lines were measured after direct removal of the electrodes from the electrolysis solution and subsequent electrochemical reduction in Fig. 5.11. In contrast, the CVs in dashed-dotted lines were recorded after keeping the electrodes in the electrolysis solution for 60 s and subsequent complete electrochemical reduction (reduction data not shown).[66]

situ Raman spectroscopy.[124] In combination with K^+ or Na^+, such cuprates have a bluish-black color. From visual inspection, these compounds cannot be discerned.

Electrochemically, it was suggested that the Cu(III) compounds could be reduced at potentials below 1.6 V and can be identified by a peak at potentials slightly below 1.6 V.[124] With our experimental approach, it is, however, not possible to identify the Cu(III) compounds since our starting potential (0.31 V) in the chronoamperometry measurements in Fig. 5.11 is already below 1.6 V. Nevertheless, it is very likely that both Cu(II) and Cu(III) compounds form during the electrolysis at high voltages. Additional experiments are, however, required to confirm this assumption and elucidate the nature of the surface oxides formed.

In contrast to Au, independent of the pre-treatment, *i.e.*, direct removal of the electrodes after the electrolysis (Cu fast) or keeping the electrode in the electrolysis solution (Cu slow), a reduction current is measured on all Cu electrodes. The corresponding charge density passed during the electrochemical reduction of the electrodes (Fig. 5.11) is depicted in Fig. 5.2 b for all investigated electrodes, along with the data obtained for Pt and Au. Overall, the charge density decreases almost exponentially with increasing applied voltage. In comparison to Au, the oxide formation is also still significant during CGDE.

For almost all electrolysis voltages in Fig. 5.2 c, it is apparent that the charge densities passed for the electrodes removed immediately after the electrolysis (Cu fast - red) are larger than those kept in the electrolysis solution (Cu slow - orange). Hence the electrodes are partially reduced when they are kept in the solution after electrolysis. Similar to the case of Au discussed above, we suggest that species in the electrolysis solution formed during the electrolysis, *i.e.*, H_2O_2, cause the reduction. Considering that Cu(III) compounds are formed during electrolysis (see above) and that these compounds are reduced at more positive potentials than the oxides that are reduced in the potential window of our electrochemical reduction experiment in Fig. 5.11, we suggest that Cu(III) compounds are reduced to Cu(II) compounds under these conditions. Since the difference in charge density is small for both experimental procedures, it further implies that the amount of Cu(III) compounds formed during electrolysis is comparatively low.

The structural changes induced by the electrolysis and subsequent electrochemical reduction of the electrodes were investigated by cyclic voltammetry. The CV of an as-prepared electrode is shown in Fig. 5.12 a and b (black), and these recorded after the electrolysis at 50, 300, and 570 V are shown in Fig. 5.12 b. In the latter, we also differentiate between electrodes, which were removed immediately from the

electrolysis solution (solid lines), and those which were kept for additional 60 s in the electrolyte (dash-dotted lines). In general, for Cu electrodes the peaks at potentials larger than 0.2 V can be attributed to the formation and reduction of Cu_2O. The peaks at potentials smaller than 0.2 V can be attributed to surface OH adsorption and desorption on different low index surfaces.[220–223] From the comparison of the CVs of the as-prepared electrode with those recorded after electrolysis and subsequent reduction, it is apparent that the voltammetric features in the CV change, indicating that the crystallographic orientation of the electrode surface changed.[220] Interestingly, the characteristic features of the voltammograms recorded after electrolysis at different voltages are very similar for all electrodes, indicating that all electrodes have a similar surface crystallographic orientation. In addition, the RF of Cu increased in comparison to the as-prepared Cu electrodes shown in Fig. 5.2 c and is independent from the experimental procedure (immediate removal of the electrode after electrolysis or keeping the electrode in the electrolysis solution).

In turn, the RF decreases exponentially from 50 to 570 V, following the voltage-dependent evolution of the charge density. Note that for electrolysis in the CGDE region, the electrodes still have a six times larger surface area than the as-prepared Cu wire. The change in surface area is, to some extent, also apparent in the SEM images in Fig. 5.10 m to r (right column), where the surfaces became smoother with increasing voltage. Comparing the SEM images taken directly after the electrolysis (Fig. 5.10 g to l - middle column) with those taken after the electrochemical reduction (Fig. 5.10 m to r - right column), shows that the more rough surfaces obtained after electrolysis at low voltages stay rough after the electrolysis (compare images in Figs. 5.10 a, g, m – first row). In a similar way the more flat surfaces obtained at high voltages also remain mostly flat after the electrochemical reduction (compare images in Figs. 5.10 f, l, r – last row). Furthermore, SEM images taken at higher magnification in Fig. 5.20 show, the formation of a porous structure after the electrochemical reduction. Overall, the structure formation of Cu is very similar to that observed for Au above, except that the oxide layer thickness and the porosity of the film shows a different voltage dependence.

5.1.4 Summary and Conclusions

In this work, we investigated the impact of electrolysis on the structural properties of Pt, Au, and Cu electrodes in a 0.01 M KOH solution in a voltage range from 50 to 580 V. We show that the I–U characteristics are mainly determined by the conductivity of the electrolyte or the gas film around the electrode at high voltages and that they are rather independent of the metal employed as well as the changes induced on the structural properties by the electrolysis. The difference in the structural properties has been explored by additional optical microscope, SEM, and electrochemical measurements. The following key observations were made, and questions remain:

1. Pt seems to be stable during electrolysis in agreement with previous studies in different electrolytes. Whether or not the electrodes are restructured at an atomic level or dissolve partially during electrolysis, cannot be deduced from our measurements and is the subject of further investigations.

2. During electrolysis, an oxide film is formed on the Au and Cu electrodes, where the rate of formation depends on the metal and the applied voltage. The red color of the Au wire suggests that Au_2O_3 is formed. In SEM images, the film appears rather flat and based on the charge density passed during the electrochemical reduction of the electrodes the oxide is thickest after electrolysis at the breakdown voltage of normal electrolysis (300 V). The black color of the Cu wire suggests that CuO is formed, which is rather textured (rough) and thickest for low voltages (50 V) and more flat and thinner in the CGDE region (540 V). Possible Cu(III) oxide formation, which was suggested to occur in the OER region under alkaline conditions, is very likely.[124] Further XPS measurements would be required to elucidate the oxidation state of the respective metals.

3. When the Au and Cu electrodes are kept for 30 s after the electrolysis in the electrolysis solution, their color changed from red to black for Au and from black to light black for Cu. Further electrochemical reduction measurements revealed that the Au oxide was completely and Cu oxide only partly reduced in the electrolysis solution. In the case of Cu we suggest that the partial reduction is attributed to the reduction of Cu(III) compounds. The content of which is low and less stable than CuO or Cu_2O.[124] Our preliminary results

to explain the reduction process on Au_2O_3 suggest that H_2O_2, present in the electrolysis solution after the electrolysis, is at the origin of the oxide reduction. While it is known that H_2O_2 is formed during CGDE,[18, 67] the formation at lower voltages has so far not been considered.

4. Reducing the oxides formed during electrolysis, either by keeping the electrodes in the electrolysis solution (for Au) or reducing the oxide electrochemically (for Au and Cu), leads to the formation of a high surface area nanoporous film. The change in electrochemical surface area to the as-prepared electrodes follows the same trend as the charge density determined from the reduction experiments. In the case of Au, the final porous structure is also independent of the reduction procedure.

Overall, performing electrolysis at high voltages on Au and Cu can be used to form thick oxide layers on the electrodes. Based on our findings, the oxide structure and film thickness differ significantly for the different metals, and the oxide structure also depends on the applied voltage. Similarly, the surface area of the porous films depends on the applied voltage during electrolysis. Hence, if this approach were used to prepare oxide or porous films with specific film thickness on other metals, a systematic study of the whole voltage range is inevitable. Reasons for the voltage-dependent oxide growth rates still have to be elucidated. Note that it is also mandatory to remove the electrodes swiftly from the electrolysis solution to assess properly the surface structures formed during electrolysis. Finally, such oxide-covered or highly-restructured materials with high surface area obtained from an initial electrolysis treatment could provide a new class of materials for possible applications as model electrodes in electrocatalysis, battery- and other energy-related research fields.

5.1.5 TOC Text

The structural changes of the catalytically relevant materials Pt, Au and Cu upon electrolysis at 50 to 580 V were studied in alkaline electrolytes. Pt is stable under all investigated electrolysis conditions, while Au and Cu form thick oxide films under the same conditions. The Au and Cu oxides can reduce spontaneously (partially for Cu) in the electrolysis solution or by electrochemical reduction, resulting in nanoporous film formation.

5.1.6 Appendix

5.1.6.1 S1: Temperature Effects on the I–U Characteristics

Figure 5.13 shows the chronoamperometric curves obtained for electrolysis on Pt in 0.01 M KOH for 30 s at the indicated voltages, where in a) the the applied voltage and in b) the resulting current is plotted *vs.* time. Overall, the applied voltages are very stable. The currents are also nearly constant when low voltages are applied to the electrode (up to 300 V). At about 300 V, the current increases slowly with time. At voltages higher than 300 V, the current density increases slowly at first (NE region). After some time, the current density breaks down, marking the moment when the plasma in solution is ignited.

The phenomena observed in the I–t behavior can be explained by the increase in electrolyte temperature due to Joule heating, which is more pronounced for higher voltages and current densities.[84, 87] The starting temperature is 22 °C. The temperatures after electrolysis are given next to the curves in Fig. 5.13 a. In the NE region the increase in current density is explained by the increase in conductivity of the 0.01 M KOH solution with increase temperature.[224] When the voltage is high enough and the temperature of the electrolyte near the electrode reaches a certain value, the current density breaks down. Therefore the breakdown occurs earlier for the higher voltages where Joule heating is more pronounced.

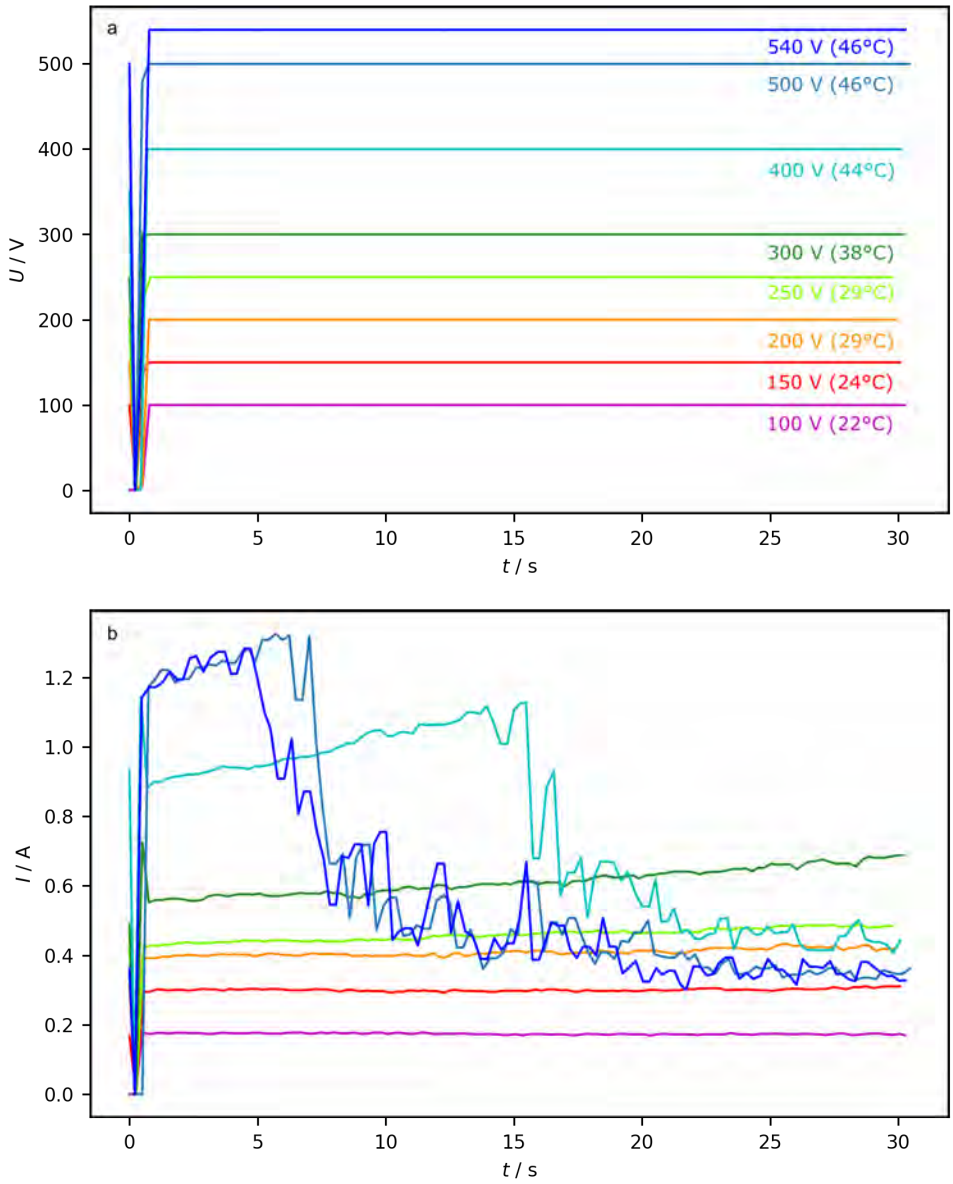

Figure 5.13: Chronoamperometry of a Pt wire electrode for 30 s in 0.01 M KOH at different voltages. The temperature in the brackets after the respective voltage is the temperature after electrolysis. a) applied voltages vs. time. b) Evolution of the current densities at the given voltages. Each measurement was performed with a freshly prepared wire and new electrolyte.[66]

The individual values in the I–U plot of Fig. 1 a) in the manuscript are obtained by averaging the current density values in Fig. 5.13 b) over the entire 30 s of electrolysis (see experimental section). Typically the I–U characteristics are studied by varying the applied voltage linearly with a specific constant scan rate (linear sweep voltammetry – LSV).[70, 84, 92] To mimic this situation, we also studied the electrodes by staircase voltammetry (SCV). Here the voltage was increased from 20 V every 10 s in 20 V steps until the desired final voltage of 540 V was reached. A comparison between the stationary I–U curve from Fig. 1 (blue dashed line) in the manuscript and the resulting SCV I–U curve (red solid line) is shown in Fig. 5.14. In the SCV plot, the individual points are average current density values recorded at the specific voltages. The temperatures of the electrolyte after electrolysis are given next to the corresponding data points in the figure.

Comparing both experimental approaches, the temperature effect does not play a significant role in the NE region (on the time scales of the experiment) since the curves are almost identical. The breakdown voltage of the electrolyte occurs at lower voltages in the SCV measurement. This can be rationalized by a higher electrolyte temperature, explained as follows. As already shown in Fig. 5.13, the increase of the electrolyte temperature near the electrode becomes significant at around 300 V. Furthermore, in the SCV experiment the electrolyte is continuously heated already before reaching 300 V, which presumably leads to overall higher electrolyte temperatures already at around 300 V, not only near the electrode. The effect of the different electrolyte temperatures in both experiments becomes apparent at high voltages, where at 540 V the temperature of the electrolyte after the SCV experiment is almost 40 K higher than in the chronoamperometry experiment. The difference in electrolyte temperature has an effect on the current density, which is lower in the SCV experiment than in the stationary current experiment. One explanation is that the higher electrolyte temperature makes it easier to bring the electrolyte near the electrode to the boiling point. This in turn means that less power is required to discharge the gas between the electrode and the electrolyte.[17, 18, 87, 92]

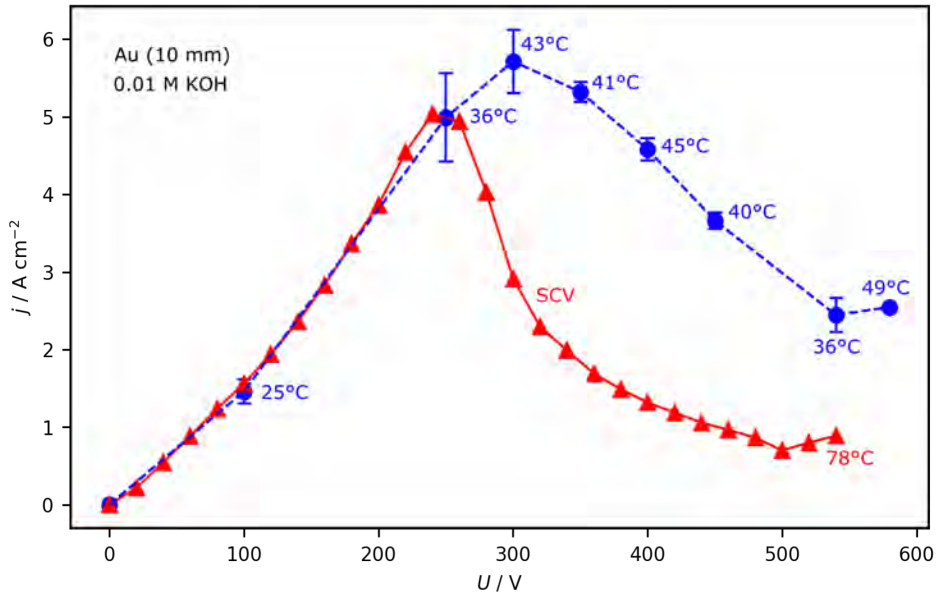

Figure 5.14: SCV recorded on a Au wire electrode in 0.01 M KOH between 0 and 560 V (20 V steps every 10 s) (red solid line) and stationary I-U curve from Fig. 1 a in the manuscript (blue dashed line and circles). The temperatures given next to the data points are the electrolyte temperatures recorded after the respective electrolysis experiments.[66]

5.1.6.2 S2: SEM Pt

Figure 5.15 shows SEM images of an as-prepared Pt electrode in a) as well as after 30 s electrolysis at 100, 300 and 580 V in b) to d). As already mentioned in the manuscript itself, no significant restructuring of the Pt electrode is observed after the electrolysis for all investigated electrolysis voltages.

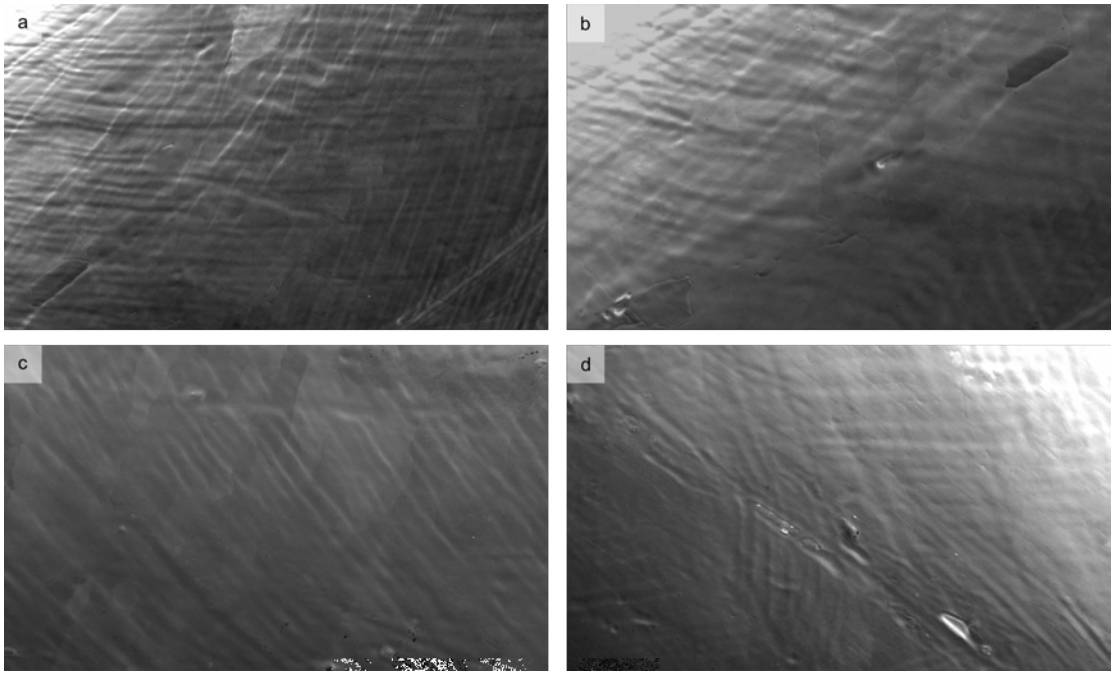

Figure 5.15: SEM images (250 µm × 150 µm) of a Pt wire electrode a) as-prepared and after electrolysis in 0.01 M KOH for 30 s at b) 100 V, c) 300 V and d) 580 V. The images were improved by adjusting the contrast and brightness.[66]

5.1.6.3 S3: SEM of as-prepared Au and Cu

Figure 5.16 shows SEM images of as-prepared Au and Cu wire electrodes.

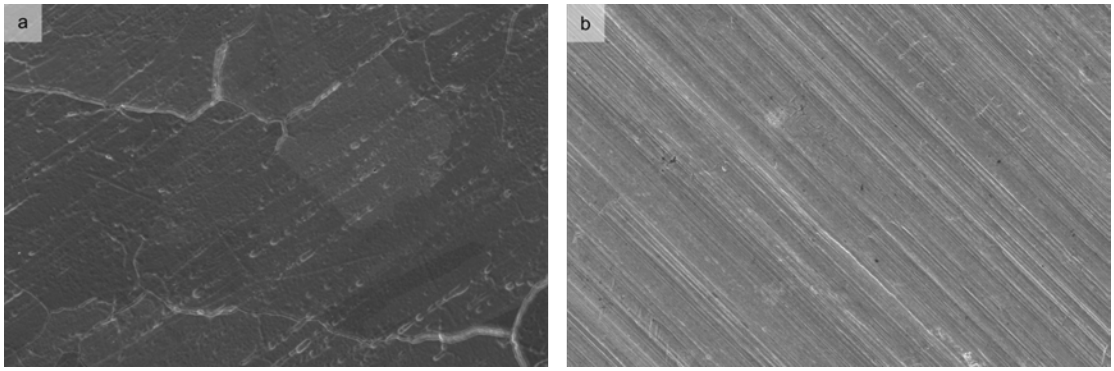

Figure 5.16: SEM images (120 µm × 80 µm) of as-prepared a) Au and b) Cu wire electrodes.[66]

5.1.6.4 S4: SEM Au

S4.1: Beam Damage

Figure 5.17 demonstrates the effect of electron beam damage during SEM on the Au_2O_3 structures formed by electrolysis at 300 V for 30 s in 0.01 M KOH and direct removal of the electrode from the electrolyte. In the SEM images taken successively at the same location in a) and b), the increase in number and formation of holes in the oxide layer can be seen. Also, when zooming out in c), the area scanned in a) and b) appears much brighter, indicating that the electronic structure of the electrode in this area changed.

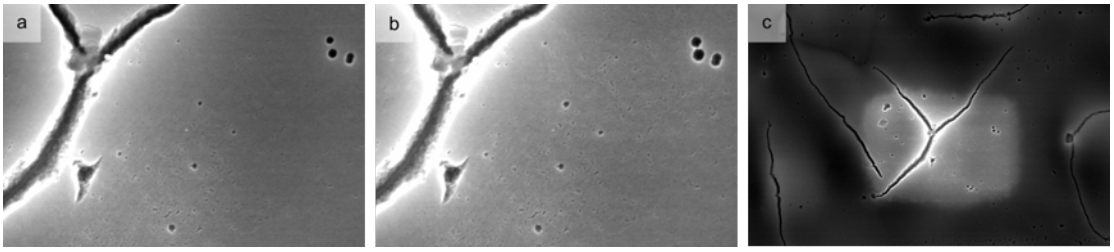

Figure 5.17: SEM image sequence of a particular spot of a Au wire after electrolysis at 300 V for 30 s in 0.01 M KOH and direct removal of the electrode from the electrolyte. Where a) and b) show images measured consecutively at the same location with identical image sizes and c) shows the next image after zoom out from the region depicted in a) and b). SEM image sizes are in a) and b) 6 µm $\times$ 4 µm and c) 24 µm $\times$ 16 µm.[66]

S4.2:Electrode structure after electrolysis and electrochemical reduction

Figure 5.18 a) shows an SEM image of a Au electrode after electrolysis at 300 V for 30 s and direct removal from the electrolysis solution. The surface consists of a solid Au_2O_3 film with cracks, as described in the manuscript. Figure 5.18 b) shows an SEM image of the same electrode but after electrochemical reduction (see main text for details). The formerly solid Au_2O_3 film transformed into a porous structure similar in appearance to that obtained by holding the electrode after the electrolysis for 60 s in the electrolysis solution, shown in Fig. 5 m) to p) in the manuscript. A more detailed description of the Au_2O_3 formation during electrolysis, the the porous

Au film formation during the subsequent reduction as well as the role of H_2O_2 in the reduction of the Au_2O_3 film, is given elsewhere.

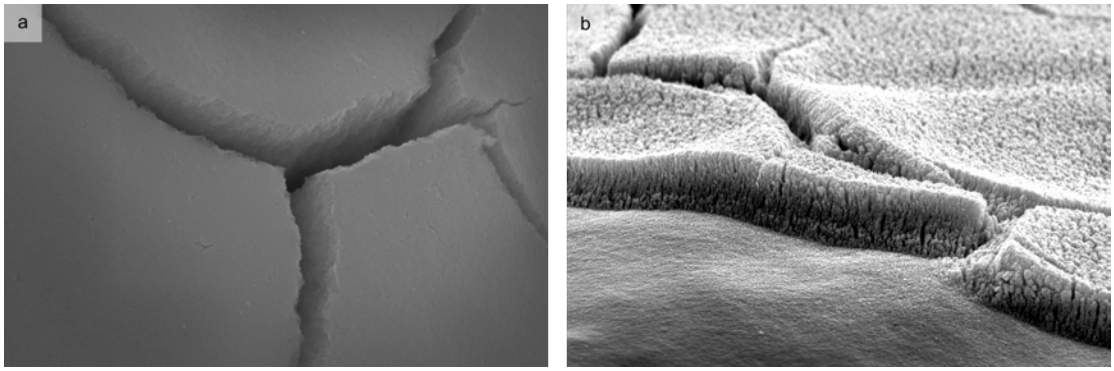

Figure 5.18: SEM images (6 µm × 4 µm) of a Au wire electrode a) after electrolysis at 300 V for 30 s in 0.01 M KOH and direct removal of the electrode from the electrolysis solution and b) the same electrode after electrochemical reduction.[66]

5.1.6.5 S5: SEM Cu

S5.1: Large area SEM images of Cu electrodes after electrolysis

From the SEM images in Fig. 5.19 taken on Cu electrodes removed immediately after the electrolysis and those left in the electrolysis solution, no clear differences in the structural properties can be seen.

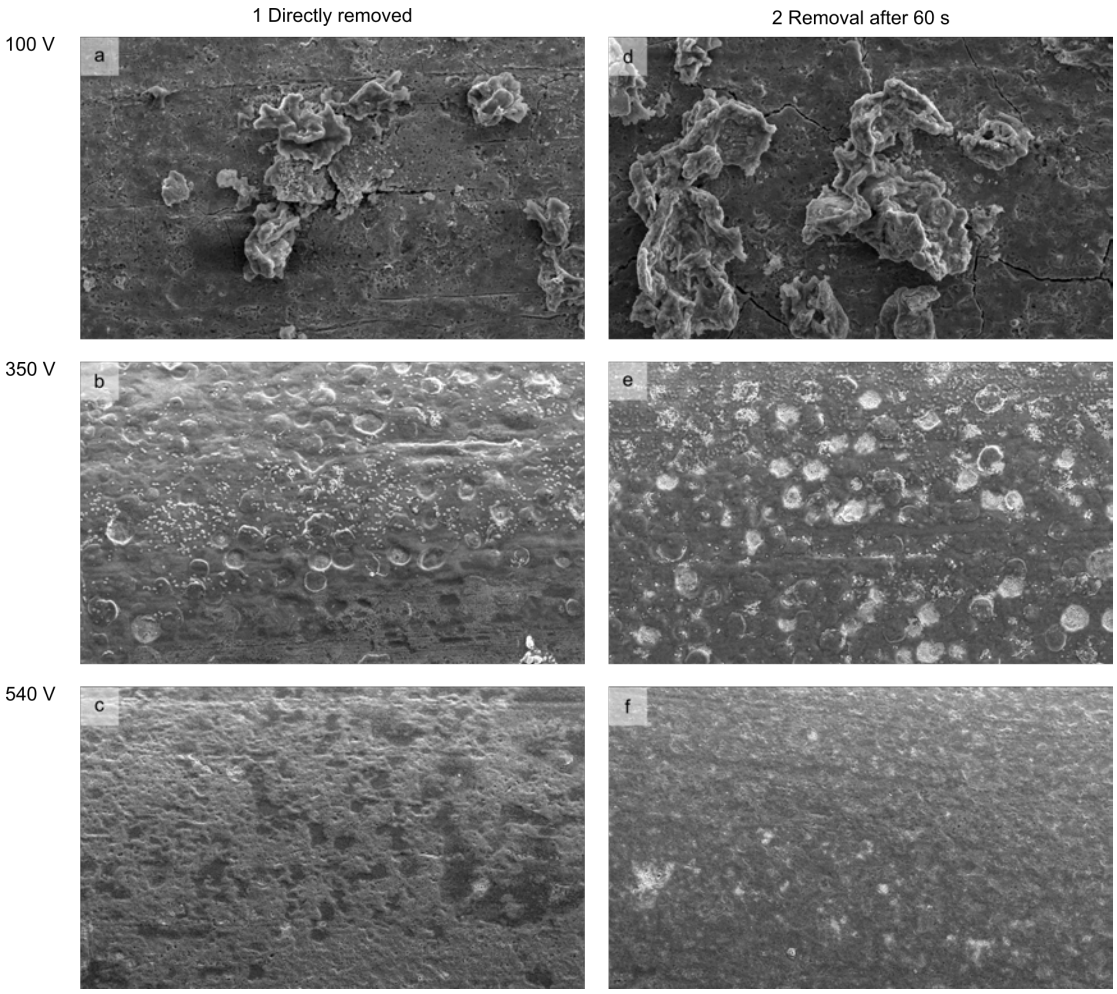

Figure 5.19: SEM images (250 µm × 150 µm) of Cu wire electrodes after electrolysis for 30 s in 0.01 M KOH at the voltages given in each row. The first column (a) to c)) shows the surface after direct removal of the electrodes from the electrolysis solution. The second column (d) to f)) shows electrodes which were treated in the same way but which were kept for additional 60 s in the electrolysis solution.[66]

S5.2: Electrode structure after electrolysis and electrochemical reduction

Fig. 5.20 demonstrates that Cu oxides formed by electrolysis turn into a porous film after electrochemical reduction. The effect is shown for an electrode which was removed immediately after the electrolysis and another electrode that was kept in the electrolysis solution for 60 s.

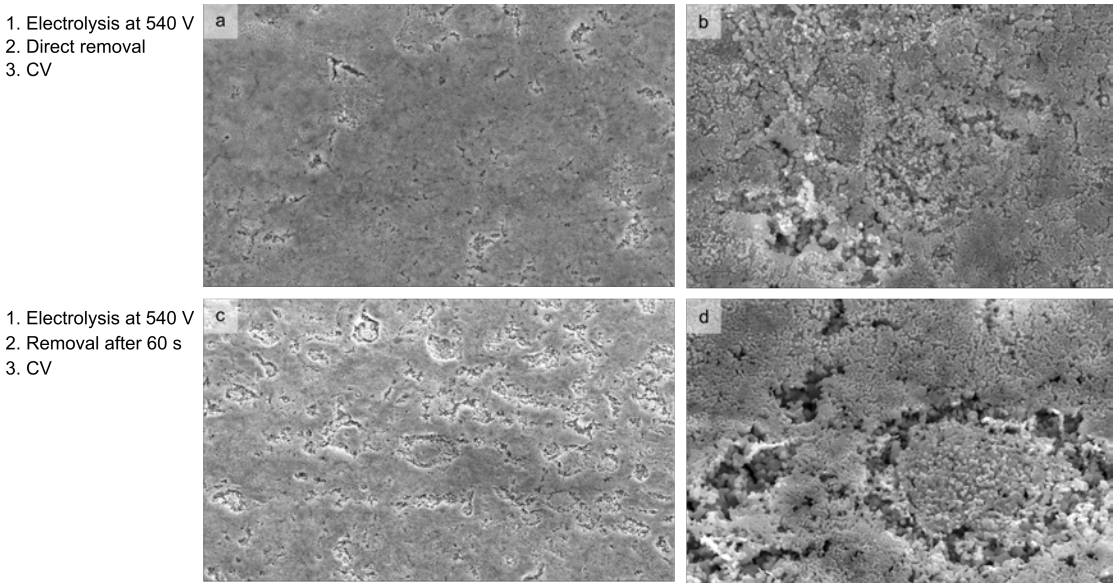

Figure 5.20: SEM images of Cu wire electrodes after electrolysis at 540 V for 30 s in 0.01 M KOH and subsequent electrochemical reduction. a) and b) show electrodes which were reduced electrochemically directly after removing the electrodes from the electrolysis solution. In c) and d) the electrodes were reduced after keeping the electrode for additional 60 s in the electrolysis solution. b) and d) are enlargement views of the structures in the images a) and c), respectively. Image size in a) and c) 50 µm $\times$ 30 µm and in b) and d) 6 µm $\times$ 4 µm.[66]

5.2 Using Auxiliary Electrochemical Working Electrodes as Probe during Contact Glow Discharge Electrolysis: A Proof of Concept Study

This Section (5.2) was published in a Special Topic Collection on "Atmospheric Plasma-Liquid Interfaces" in J. Vac. Sci. Technol. A.[199] Reprinted with permission from J. Vac. Sci. Technol. A, 40, E. Artmann *et al.*, "Using auxiliary electrochemical working electrodes as probe during contact glow discharge electrolysis: A proof of concept study", 053005, Copyright 2022, American Vacuum Society.
All measurements shown in Section 5.2 were performed and validated by me. Besides the full Investigation, all data analysis and evaluation, as well as the creation of all figures, and the visualization, was done by me. The concept of the paper and the original draft were done in close collaboration with Albert K. Engstfeld.
A graphical abstract published on a preprint server[225] (Reprinted from ChemRxiv, 10.26434/chemrxiv-2022-0v5sc, E. Artmann *et al.*, "Using auxiliary electrochemical working electrodes as probe during contact glow discharge electrolysis: A proof of concept study", "CC BY 4.0, https://creativecommons.org/licenses/by/4.0/") is included below as a summary of the results shown in this Section.

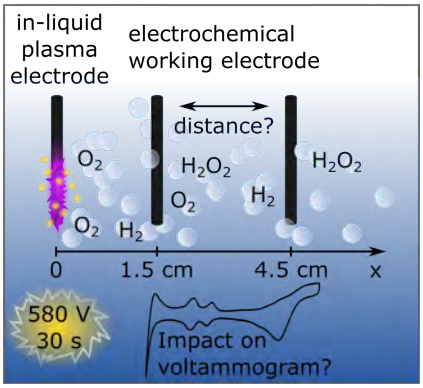

Figure 5.21: Graphical abstract of the publication titled "Using auxiliary electrochemical working electrodes as probe during contact glow discharge electrolysis: A proof of concept study" published on a preprint server.[225]

5.2.1 Abstract

Plasma in-liquid by means of anodic contact glow discharge electrolysis (aCGDE) is a growing research field allowing the selective modification of the electrode and the electrolyte. The aim of this proof of concept study is to demonstrate that auxiliary electrochemical electrodes placed in vicinity to the plasma electrode, can be modified by aCGDE (ignited at the anode by applying a DC voltage between the driving electrodes). Furthermore, we illustrate in how far such auxiliary electrodes can be used as a probe to detect products (in particular H_2, H_2O_2, and O_2) formed in the solution by aCGDE *via* electrochemical techniques. In this work aCGDE is achieved by applying a voltage of 580 V to a small Pt wire (plasma electrode) vs. a large stainless steel counter electrode. An auxiliary Pt electrochemical working electrode, operated in a three electrode configuration, is placed at different distances from the plasma working electrode. Depending on the distance, we find small changes in the electrode structure. More importantly, we will show that in principle the local H_2O_2 concentration in the electrolyte can be monitored *operando*. After aCGDE the concentration changes with time and depends on the distance from the plasma electrode.

5.2.2 Introduction

Studying plasma in-liquids has received increasing scientific interest over the last two decades for its possible application in, *e.g.*, wastewater treatment,[14, 35–37, 226] nanoparticle formation,[14, 19, 20, 35, 171–175, 195] catalyst material preparation,[22, 66] plasma electrolytic oxidation,[25–27] or plasma electrolytic polishing.[181, 182] These investigations provide information on the modification of the plasma electrode or changes induced within the electrolyte. Gas-phase plasma can be used in a similar way to modify the plasma electrode or the properties of a substrate placed close to the plasma source. Related to catalytic applications, the gas-phase plasma can also be used, *e.g.*, to change the mechanism of a catalytic reaction on the target (gas-phase plasma catalysis)[192, 193, 227] or to tailor the structural properties of the target, for example, to form catalyst materials with distinct (electro)catalytic properties.[53, 228–230] In contrast, much less is known about the effect of in-liquid plasma on target materials.

A better understanding of the impact of in-liquid plasma on an auxiliary target electrode placed in the same electrolyte in proximity to an in-liquid plasma electrode is of interest for the following applications. Firstly, in-liquid plasma could be used to prepare an electrocatalyst *in situ*. This approach would have the advantage that the electrodes do not have to be transferred after the plasma treatment from a gas-phase atmosphere into an electrochemical cell, avoiding contamination or uncontrolled restructuring of the electrode. Furthermore, the electrode potential of the auxiliary electrode can be changed during the preparation process, allowing for more specific tailoring of its structural properties. Secondly, an auxiliary electrode could be used as an electrochemical probe to determine the species formed by the plasma in the electrolyte, to measure the solution pH, or the voltage drop in the electrolyte.

Such fundamental aspects have, to the best of our knowledge, so far not been considered in the ongoing research, but are vital in the search of possible applications. The purpose of this work is to illustrate the influence of plasma in-liquid (ignited at the anode by applying a DC voltage between the driving electrodes) on the current–voltage behavior of an auxiliary electrode in solution placed in proximity of the plasma electrode and whether this auxiliary electrode can be used to determine products formed during the plasma. In general, plasma in-liquid can be generated by different approaches.[19, 69] Here, we focus on anodic contact glow discharge electrolysis (aCGDE), which is achieved by applying a high voltage between a gas evolving electrode and a significantly larger counter electrode.[17, 18, 71, 82, 87] Here, Pt is used as plasma working electrode (PWE), since it was suggested to be stable under these conditions,[17, 18, 54–57, 66] which means that neither the surface structure changes significantly nor nanoparticles are extruded from the electrodes as it is observed in other systems.[19, 171, 172] The auxiliary electrochemical working electrode (AE) is also made of Pt, which is an intensively studied electrochemical electrode material[58–63] and therefore an optimal benchmark system. Possible structural changes (if significant) can be inferred from changes in the *I-E* characteristics of the electrode.[58] The key products that form concomitantly during aCGDE are H_2, O_2 and H_2O_2,[18, 54, 67] the electrocatalytic reaction of these species with Pt electrodes in alkaline electrolyte are also described in detail in the literature.[231–236] It is also known that the electrode is well suited to detect the products, when the electrode is controlled with a potentiostat. A key aspect is

the detection of H_2O_2, which is usually determined after the electrolysis by means of titration.[18, 189–191] This approach does, however, not provide any information on the spatial distribution or temporal evolution of the H_2O_2 formed during aCGDE. Other methods are able to circumvent this issue to some extend.[192, 193] In total, knowing about local concentrations is for example important to understand possible structural changes of the working electrode induced by the H_2O_2 after aCGDE.[66] In electrocatalysis Pt is used as collector electrode, which oxidizes H_2O_2 selectively, i.e., during the oxygen reduction reaction (ORR).[237–239] As a proof of concept, in this work a Pt wire is placed as H_2O_2 probe at different distances from the PWE.

5.2.3 Results and Discussion

The experiments were performed in a large cylindrical glass cell (diameter: 13.5 cm, height: 7.5 cm) containing 0.01 M KOH. The two electrodes for aCGDE (PWE and plasma counter electrode - PCE) and the three electrochemical electrodes (auxiliary electrode - AE, reversible hydrogen electrode - RHE, and electrochemical counter electrode - ECE) are immersed in the cell as shown in the schematic illustration in Fig. 5.22. A glass tube (outer diameter: 2.6 cm; inner diameter: 2.2 cm; wall thickness: 2 mm) is placed around the plasma counter electrode to remove volatile products created at the PCE, an approach suggested by Hickling and Ingram.[18] Even though migration of species into the electrolyte can not be completely ruled out, most of the products contained in bubbles formed at the counter electrode during the aCGDE are believed to be transported to the electrolyte surface within the perimeter of the glass tube. The plasma was ignited at the anode by applying a DC voltage between the driving electrodes and was apparent by a distinct purple glow, confined in a gas sheath surrounding the Pt wire plasma electrode, as well as a sharp hissing noise. In our studies, the distance between the plasma working and counter electrode was between 1.2 cm and 1.5 cm, and the AE was placed at a distance of either 1.5 cm or 4.5 cm from the PWE. The applied voltage between the PWE and the PCE is given in V, while the potential at the AE is given on the RHE scale (V_{RHE}). A detailed description of the experimental set-up, materials used and experimental procedures is provided in the experimental section.

The effect of aCGDE on the AE was studied by comparing the variation of electrode potential (E) vs. time (t) (Fig. 5.23 top row) with the current density (j) vs. t

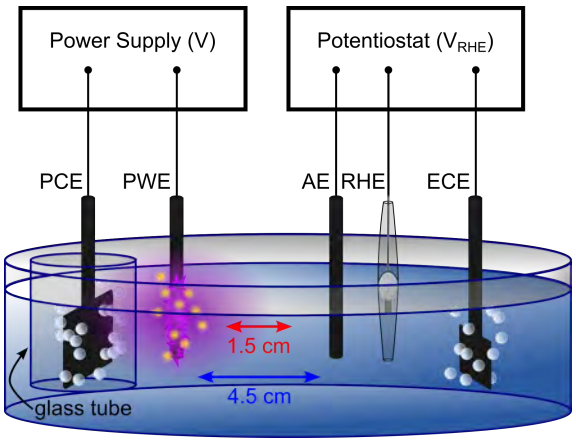

Figure 5.22: Schematic illustration of the electrochemical cell including the plasma electrodes (PWE and PCE) and the electrochemical electrodes (AE, ECE, and RHE). See text for details.[199]

(Fig. 5.23 middle and bottom row). Each experiment consists of a combination of the following experimental steps:

Step A: Cyclic voltammetry[5] (measuring the current response while applying a triangular wave potential) recorded at 50 mV s^{-1} between 0.0 and 1.05 V_{RHE} in the absence of aCGDE, followed by both or either one of the following steps B.

Step B1: Keeping the AE at 1.0 V_{RHE} (unless otherwise mentioned) during 30 s of aCGDE (PWE anode at 580 V vs. a stainless steel cathode, with a power of approximately 57 W).

Step B2: Keeping the AE at 1.0 V_{RHE} for 15 min in the absence of aCGDE.

Step C: Recording cyclic voltammograms (CVs) between 0.00 and 1.05 V_{RHE} in the absence of aCGDE.

Each column in Fig. 5.23 represents one of the experimental steps above. The time axis always counts from the beginning of each of these steps. The variation of the current density for an AE located 1.5 cm from the PWE (close to the PWE) is shown as a red curve and that for a distance of 4.5 cm as a blue curve (far from the PWE). The green curve represents the case where the AE was not exposed to aCGDE (no step B1), and was kept for 15 min at 1.0 V_{RHE} (in step B2). The same color scheme is used throughout the article. At 1.0 V_{RHE} H_2O_2 can be selectively

oxidized at a Pt electrode. Note that in literature H_2O_2 is usually reported to be detected at 1.2 V_{RHE},[63] however, at that potential Pt surface oxidation cannot be ruled out. After aCGDE, a waiting period of 15 min was applied to ensure that the species formed by the plasma have sufficient time to distribute evenly in the electrolyte. The waiting time was chosen based on continuous cyclic voltammetry measurements performed in the same voltage range as in step A. After 15 minutes the cyclic voltammogram looked identical to that recorded in step A.

Figs. 5.23e and i show the potential-dependent variation of the current density during cyclic voltammetry measurements. By applying a triangular wave potential in this voltage range, usually the current (density) shows electrode specific features. These are related to the capacitive charging of the surface and charge transfer reactions (ad-/desorption of ions) occuring at the electrode surface. The interpretation of these features is provided in the discussion to Fig. 5.24. Here it is important to note, that for all experiments the potential-dependent variation of current density vs. time in step A is almost identical (Figs. 5.23e and i), indicating that the experimental conditions at the start of each experiment are the same. This is even more apparent by comparing the current density vs. potential curves in the cyclic voltammograms described in Fig. 5.25. The voltammetric features apparent in these curves are discussed further below.

Performing aCGDE while applying a constant potential at an AE placed close to the PWE (step B1: Figs. 5.23f and j red curves), a large negative current density is recorded at the AE. The current density is several orders of magnitude larger compared to the redox currents obtained without aCGDE in step A. In contrast, much less negative current densities are recorded when the AE is placed far from the PWE (blue curves). Preliminary results indicate that the voltage drop between the PCE and PWE changes the electrolyte potential not only between the plasma electrodes but also further away from these electrodes in the electrochemical cell. Hence, depending on the position of the electrochemical electrodes, the potential at the AE cannot be controlled properly. Since we record a negative current at the AE during aCGDE it is likely that the AE potential shifts in the hydrogen evolution region. In addition, the currents recorded between the PWE and PCE are fluctuating strongly, which induces changes in the electric field and in turn induces a strong noise in the current densities recorded at the AE in step B1. Further measurements are required to clarify these assumptions. Note that the effect of electric

fields on auxiliary electrodes is not unknown and is for example explored in ohmic microscopy [79, 184–186] and bipolar electrochemistry.[240, 241] Overall, to derive a more meaningful conclusion, the effect of voltage drop on auxiliary electrodes will be discussed elsewhere using an electrochemical cell with a more defined geometry, which also allows a more precise positioning of the different electrodes.

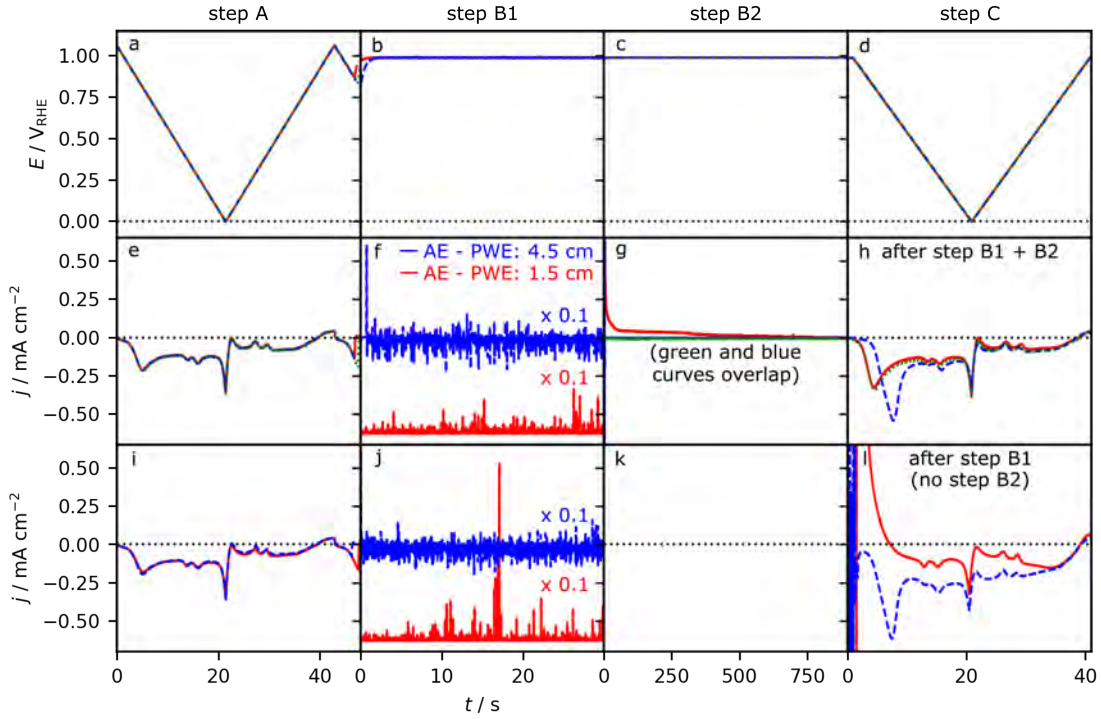

Figure 5.23: Effect of aCGDE on the AE by comparing the variation of the electrode potential (E) vs. time (t) (top row) on the current density (j) vs. t (middle and bottom row). The middle row shows the sequence of experimental steps A, B1, B2 and C, whereas the bottom row only comprises steps A, B1 and C. Each column represents the experimental steps described in the main text. Steps A, B2, and C are performed without aCGDE. In step B1, simultaneously aCGDE was performed at 580 V for 30 s. The red and blue curves show the measurements for AEs placed at a distance of 1.5 cm or 4.5 cm from the PWE, respectively. For comparison, the green curve shows the case where the AE was not exposed to aCGDE (no step B1).[199]

In step B2, the plasma was turned off and the AE potential was kept for 15 min at 1.0 V_{RHE} (Fig. 5.23g). When the AE is located far away from the PWE, the current density (blue curve) recorded at the AE is almost zero and remains constant for the rest of the waiting period. In the case where the AE is located close to the

PWE the current density (red curve) is high when the plasma is turned off. With time, the current density decreases and remains constant at slightly positive current densities during the entire waiting time. For comparison, keeping an AE at 1.0 V_{RHE} for 15 min without exposing it to aCGDE (no step B1 - green curve in Fig. 5.23g), the current density is almost zero. This difference in current densities recorded at the AE placed at different distances from the PWE, demonstrates that aCGDE certainly has an impact on the current time profiles recorded at auxiliary electrodes.

After the chronoamperometry steps (measuring the current density at a constant AE potential as a function of time - B1 and B2 or only B2), cyclic voltammetry was performed at the AE in step C (Figs. 5.23h and I). If the plasma, waiting time or species formed by the plasma had no effect on the current density profiles, we would expect the same behavior as in step A. The results, however, clearly show that especially in the first few seconds of the first cycle in step C, the evolution of current densities strongly depends on the waiting time as well as on the position of the AE with respect to the PWE during aCGDE. Possible changes of the pH should not play a significant role in the magnitude of the current density or the features in the CV. According to the Nernst equation this only shifts the features along the potential scale. Changes induced by variations in conductivity within the electrolyte might change the features. In order to draw detailed conclusions, more detailed studies are required, elucidating, e.g., the actual local OH^- concentrations.

As described above, the key products that form concomitantly during aCGDE are H_2, O_2 and H_2O_2,[18, 54, 67] whose electrocatalytic properties with Pt electrodes are well described in literature.[231–236] In order to assess whether or not the features observed in Figs. 5.23h and I are related to the presence of these species in solution after aCGDE, we performed a separate set of cyclic voltammetry measurements in electrolytes saturated with either one of the reactants possibly formed during aCGDE or N_2, shown in Fig. 5.24a. Even though N_2 is not a product during aCGDE it serves to remove residual O_2 from the electrolyte, which in turn allows studying surface specific redox processes. The grey curve shows the cyclic voltammogram (CV) of Pt recorded in N_2 saturated 0.01 M KOH, the light blue curve in O_2 saturated 0.01 M KOH, the pink curve in H_2 saturated 0.01 M KOH and the orange curve in 0.01 M KOH containing H_2O_2. Additional measurements with a larger upper potential limit are shown in Fig. 5.26. All CVs were recorded at a scan rate of 50 mV s^{-1}.

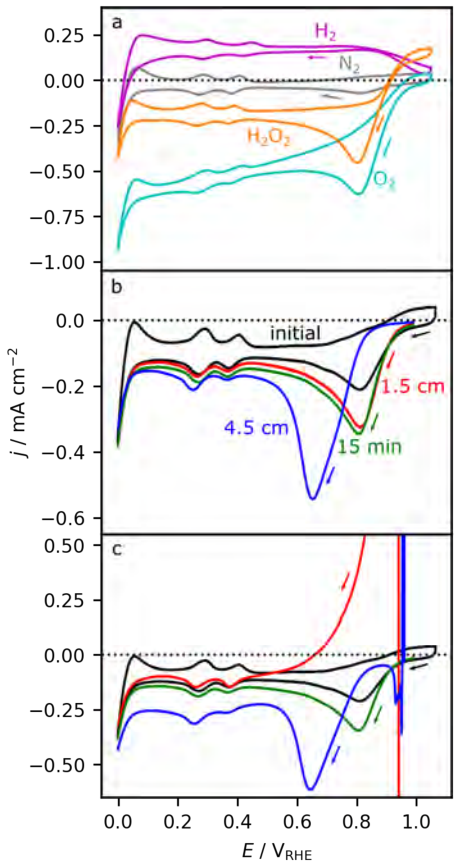

Figure 5.24: a) Cyclic voltammograms of a Pt wire recorded at 50 mV s^{-1} in 0.01 M KOH a) either saturated with N_2 (grey), H_2 (pink), O_2 (light blue) or after addition of H_2O_2 (orange). b) and c) shows the data from Figs. 5.23h and l (step C) with the same color code for the individual measurements. CVs recorded in non-deaerated electrolyte before (black) and after aCGDE for 30 s at 580 V (red and blue). The red curve shows the first half cycle after the plasma at a distance of 1.5 cm from the PWE and the one in blue at a distance of 4.5 cm, respectively. Panel b) shows the CVs obtained after performing the experimental steps B1 and B2 and c) after step B1 (no step B2). The green curve in b) and c) shows the current density voltage response after 15 min waiting at 1.00 V_{RHE}, without applying aCGDE before. The initial scan direction of all measurements was indicated with arrows.[199]

The features observed in the CVs recorded in different types of electrolytes are extensively discussed in the literature and can be interpreted as follows. The CV recorded in 0.01 M KOH (grey curve) deaerated with N_2 shows a negative current at $E < 0.05$ V_{RHE} which is related to the hydrogen evolution reaction (HER), where

water is spit to form H_2 and OH^- ($2H_2O + 2e^- \rightarrow H_2 + 2OH^-$). The features between 0.05 V_{RHE} and 0.5 V_{RHE} are related to the adsorption of hydrogen in the negative going scan and the desorption of adsorbed hydrogen in the positive going scan ($H_2O + * \rightleftharpoons H^* + 1\ e^- + OH^-$ with * being a free surface site). These features are sensitive to changes in surface crystallographic orientation. The features for $E > 0.8$ V_{RHE} are related to the adsorption of hydroxyl ($OH^- + * \rightarrow OH^* + 1e^-$) or the formation of surface oxygen (O*) from adsorbed OH ($OH^* + OH^- \rightarrow O^* + H_2O + 1e^-$) in the positive going scan.[62, 208] The slightly negative current densities for $E <$ ca. 0.95 V_{RHE} in this grey curve are caused by the reduction of residual O_2 in the electrolyte in the so called oxygen reduction reaction (ORR), where O_2 is reduced to water ($O_2 + 2H_2O + 4e^- \rightarrow 4OH^-$). Similar CVs to the grey curve are also obtained for all electrodes investigated before aCGDE in step A shown in Fig. 5.25.

In H_2-containing 0.01 M KOH (pink curve), the positive current density between 0.05 V_{RHE} and 1.0 V_{RHE} is attributed to the hydrogen oxidation reaction (HOR) whereby H_2 is oxidized to form water ($H_2 + 2OH^- \rightarrow 2H_2O + 2e^-$). The oxidation process is inhibited in the region of surface Pt oxide formation at around $E > 0.95$ V_{RHE}. In O_2-containing 0.01 M KOH (light blue curve) the negative current density at $E <$ ca. 0.95 V_{RHE} is related to the ORR. In H_2O_2-containing 0.01 M KOH (orange curve) the negative current density at around $E < 0.95$ V_{RHE} is related to the hydrogen peroxide reduction reaction (HPRR), where H_2O_2 is reduced to form hydroxid ions ($HO_2^- + 2e^- + H_2O \rightarrow 3OH^-$) and the positive current density at around $E > 0.95$ V_{RHE} is related to the hydrogen peroxide oxidation reaction (HPOR) ($HO_2^- + OH^- \rightarrow O_2 + H_2O + 2e^-$). In all cases, the ad-/desorption features observed in the CV recorded in 0.01 M KOH deaerated with N_2 (grey curve), overlap with the current density related to the electrocatalytic reactions (HOR, ORR, HPRR, and HPOR). In contrast to literature findings, the here reported current densities of the electrocatalytic reactions are low due to limited diffusion of the reactants to the electrode under stagnant electrolyte conditions.[231–236]

Figures 5.24b and c show the CVs from Figs. 5.23h and I (step C) recorded after aCGDE with and without waiting time, respectively. Similar results are also obtained when a lower voltage is applied between the PWE and the plasma counter electrode (550 V in Fig. 5.27), as well as with and without shielding the plasma counter electrode by a glass tube (Fig. 5.28). In addition, for comparison, a CV recorded in

step A (before the aCGDE treatment) is included in black and a CV recorded after 15 min waiting time without applying aCGDE in green.

Comparing the black and the green curves (before and after holding the potential at 1.0 V_{RHE} for 15 min) in Figs. 5.24b and c, a larger reduction current is apparent in the green curve in the first negative going scan at around 0.8 V_{RHE}. This feature is related to the degree of electrode oxidation at high potentials. In general, the size of the reduction peak depends on the upper potential limit of the CV as well as on the time and potential at which the electrode is kept (see also Fig. 5.29).[110] Hence, the larger reduction peak in the green curve is caused by holding the potential at 1.05 V_{RHE} for 15 min.

Cyclic voltammograms recorded on the AEs placed at different distances from the PWE, after aCGDE and subsequent waiting time at 1.0 V_{RHE} (steps B1 and B2) are shown in Fig. 5.24b. The CV recorded on an AE close to the PWE (red curve) is almost identical to the green curve (obtained without applying aCGDE). On the other hand, if the AE is placed further away from the PWE (blue curve), the size of the reduction peak in the first negative going scan is larger and shifted to more negative potentials (0.65 V_{RHE}) compared to the red and green curves. This implies that the electrode is significantly more oxidized. As mentioned above, such an effect would be expected for longer waiting times or if the upper potential limit was higher (see Fig. 5.29 and more details below).

Skipping the waiting time after aCGDE and recording CVs directly thereafter (only step B1) for AEs placed at different distances from the PWE are shown in Fig. 5.24c. For AEs close to the PWE (red curve), in the first negative going scan a large positive current density is observed at high potentials (0.8 – 0.95 V_{RHE}). The current density decreases at more negative potentials until at ca. 0.5 V_{RHE}, the curve follows the CV recorded before aCGDE (black curve). Compared to the CVs presented in Fig. 5.24a, this large positive current density can at least at high potentials ($>$ 0.95 V_{RHE}) be attributed to the oxidation of H_2O_2. Note that the HOR and the ORR are almost suppressed at these potentials, as shown in Fig. 5.24a and Fig. 5.26. The H_2O_2 oxidation current is also measured at higher potentials (above 0.95 V_{RHE}) in the following potential cycles, as shown in Fig. 5.30. The temporal decrease of the positive current density is more clearly seen in the potentiostatic measurements in Fig. 5.23g (red curve). The CVs and the potentiostatic experiments indicate that the H_2O_2 remains in the region around the AE for a certain time

until it dissipates into the electrolyte or reacts with the Pt PWE to decompose into O_2 and H_2O.[242, 243]

For AEs located farther from the PWE (blue curve), such a positive current density is not observed in the first negative going or subsequent scans, indicating that H_2O_2 is not measurably present in the electrolyte far away from the PWE. Similar to the blue curve in Fig. 5.24c, obtained directly after aCGDE, a large reduction peak is observed at around 0.65 V_{RHE} in the first negative going scan in Fig. 5.24b (steps B1 and B2). This large peak, which is observed in both experiments, suggests that the electrode surface oxidizes significantly during aCGDE. Interestingly this suggests, that the plasma or the species formed by the plasma only affect the structural properties of the Pt AE, when the AE is placed far away (4.5 cm) from the PWE. For the time being it is not clear if the increase in Pt oxide formation is induced (i) by the plasma (or plasma species) or whether it is related (ii) to changes in electrode potential induced by the electric fields during aCGDE, which could cause an uncontrolled oxidation of the electrode during aCGDE.

Overall, the CV measurements performed after aCGDE indicate that the plasma or the species formed by the plasma do not have a significant impact on the structural properties of the Pt AE. The additional current densities in the CVs, with respect to a CV recorded in N_2 saturated 0.01 M KOH (see black curves), are therefore attributed to the reaction of the Pt AE with the species formed by the plasma in the solution, where the reaction rates depend on the product distribution and its temporal evolution in the electrolyte. When the AE is located close (1.5 cm) to the PWE, significantly different current densities arise at the AE directly after aCGDE, which are tentatively attributed to the reaction of plasma created species (H_2, O_2, H_2O_2) with the Pt AE. In the CVs recorded right after aCGDE (step B1) and at potentials $<$ 0.65 V_{RHE}, a more significant negative current density is observed. Assigning these current densities to the reaction of different species with the Pt AEs is not straightforward, since the total current density is a sum of HOR current density (positive), ORR current density (negative), HPRR current density (negative) and surface redox processes. At high electrode potentials, especially 1.0 V_{RHE}, the situation is more clear. The observed positive current density can basically only be attributed to the oxidation of H_2O_2, with minor contributions from the oxidation of H_2. These positive current densities persist after multiple cycles (see Fig. 5.30). Finally, the different behavior of the j vs. E curve in the first negative going scan of

the CV recorded after aCGDE for AEs placed at different distances from the PWE suggests that the product distribution in the solution changes with the distance from the PWE. The change in current density in Fig. 5.23g during the waiting time after aCGDE also implies that the product distribution changes with time.

5.2.4 Conclusion

In this work we elucidated to what extend auxiliary electrochemical working electrodes can be used to determine by electrochemical methods the impact of aCGDE on (i) the structural properties of an auxiliary electrode and (ii) in how far such electrodes can be used as a probe to detect products formed during and after aCGDE. In both cases it was not yet possible to determine these properties during aCGDE. We suggested that changes in the electrode potential of the electrochemical electrodes might be responsible for this observation. This issue has to be addressed more specifically in a more detailed study where the electrode and electrochemical cell geometries are more defined.

After the aCGDE we did not observe any significant changes of the Pt auxiliary electrodes. Hence Pt is a suitable probe to detect H_2O_2. Even though the absolute local H_2O_2 concentration in the electrolyte is not accessible yet, we were able to measure relative changes of the concentration in the electrolyte which depends on the distance from the electrode as well as on the waiting time after electrolysis. This proof of concept study demonstrates that an electrochemical probe can indeed be used to detect H_2O_2 *operando* and also locally in the electrolyte, which is so far not accessible with other techniques. In order to gain more quantitative information, further studies elucidating local temperature changes or convection in the electrolyte are, however, required. Overall, such information is crucial for further studies aiming at a more detailed understanding of product formation during aCGDE, the composition of the plasma, the structure formation processes at the plasma electrode or the reaction of these intermediates with species in the electrolyte.

5.2.5 TOC Text

The influence of anodic contact glow discharge electrolysis on a Pt auxiliary electrode in alkaline electrolyte was investigated as a function of the distance between the electrodes and time. By studying the electrochemical properties of Pt before, during and after aCGDE by cyclic voltammetry, we demonstrate that the Pt auxiliary electrode can be used to monitor *operando* the formation of H_2O_2 by aCGDE in the electrolyte. The concentration depends on the distance of the electrodes to each other and the detection time.

5.2.6 Appendix

5.2.6.1 S1: Reproducibility of the Starting Conditions

Figure 5.25 shows a set of CVs of the Pt wire AE recorded in non deaerated 0.01 M KOH at a scan rate of 50 mV s^{-1} obtained in step A (see manuscript). Each curve represents a new measurement. All CVs look almost alike, indicating that the experimental conditions (structural properties of the electrodes and electrolyte purity) are similar in each experiment.

5.2.6.2 S2: Influence of Upper Potential Limit on Electrocatalytic Properties

As discussed in the manuscript, H_2, O_2, and H_2O_2 are formed during aCGDE. The electrocatalytic reactions of these species with Pt, are depicted in the CVs in Fig. 5.26. These were recorded in 0.01 M KOH solutions, which were saturated with the respective reactants. A similar plot with a lower upper potential limit is shown in Fig. 3a and discussed in the manuscript.

5.2.6.3 S3: Influence of the PWE Voltage on the CV Features Recorded at the AE (550 V vs. 580 V)

Figure 5.27 shows the CVs of Pt electrodes recorded in 0.01 M KOH at a scan rate of 50 mV s^{-1}, where Fig. 5.27a shows the CVs recorded directly after aCGDE

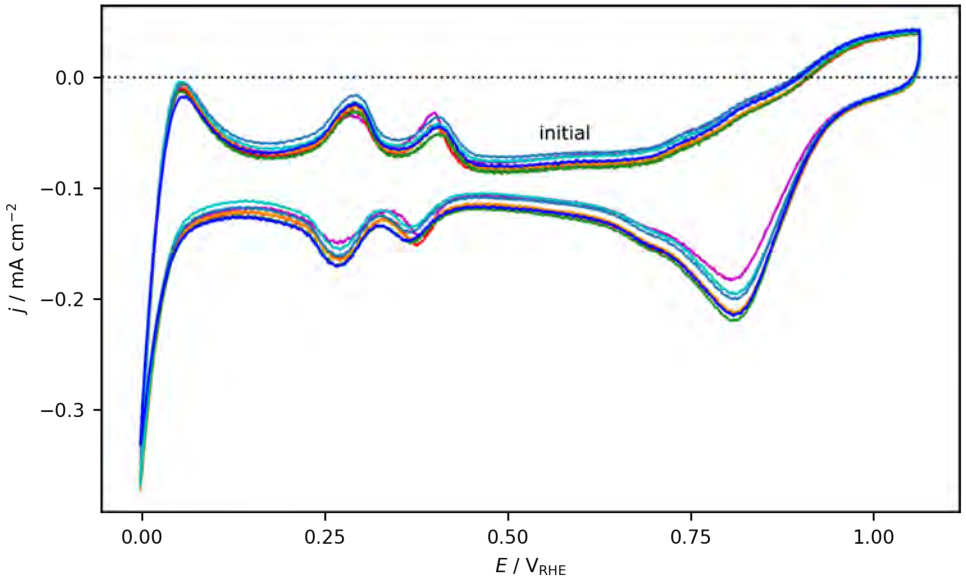

Figure 5.25: Set of CVs of Pt wire AEs recorded in 0.01 M KOH (not deaerated) at a scan rate of 50 mV s^{-1}, obtained in step A (see manuscript) for different experiments.[199]

(step B1) and in Fig. 5.27b after aCGDE and waiting for 15 min (steps B1 and B2). The solid lines correspond to the data obtained by applying 580 V at the PWE (as in the manuscript) and the dashed lines by applying 550 V. At this lower voltage the plasma ignites only after a few seconds. Overall the curves look rather similar. We suggest that the shifts of the current density profiles are attributed to different product ratios in the electrolyte obtained by applying different voltages at the plasma electrode.

5.2.6.4 S4: Influence of Tubes Around the Plasma Counter Electrode

During aCGDE, H_2 is evolved at the plasma counter electrode. In order to prevent that the H_2 diffuses far into the electrolyte, where it could oxidize the auxiliary electrochemical Pt electrode, a glass tube was placed around the plasma counter electrode. In this way, the H_2 bubbles are directed outside the electrolyte (see Fig. 1 in the manuscript). Figure 5.28a shows CVs recorded at the Pt AE in 0.01 M KOH at a scan rate of 50 mV s^{-1} directly after aCGDE (after step B1) and in Fig. 5.28b

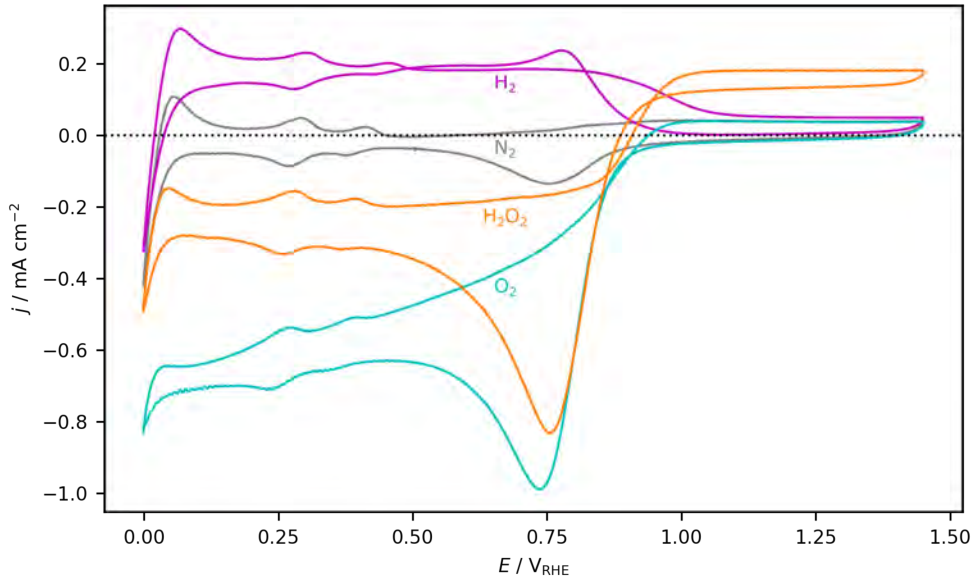

Figure 5.26: Pt CVs measured with a scan rate of 50 mV s^{-1} in 0.01 M KOH saturated with N_2 (grey curve), O_2 (light blue curve), H_2 (pink curve) and admixed with H_2O_2 (orange curve).[199]

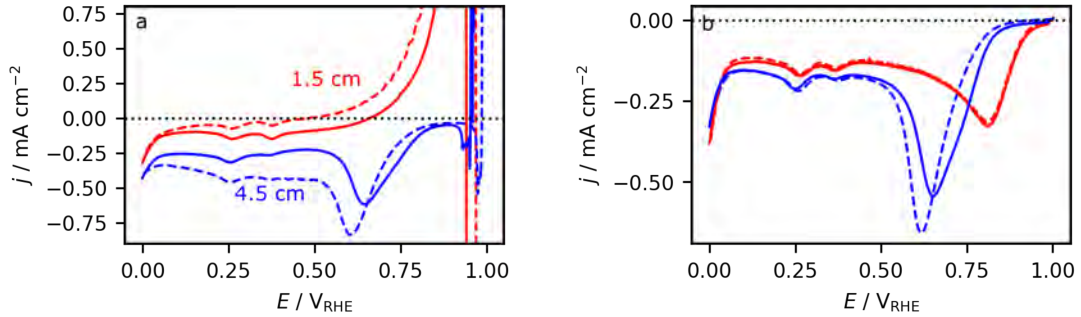

Figure 5.27: The first negative going scan of Pt CVs recorded in 0.01 M KOH at a scan rate of 50 mV s^{-1} after aCGDE (550 V or 580 V for 30 s) at the PWE. The red and blue lines indicate that the AE is placed at 1.5 cm or 4.5 cm from the PWE, respectively. The CVs in a) were recorded immediately after aCGDE (step B1) and those in b) after holding the potential for additional 15 min at 1.00 V_{RHE}. The dashed and solid CVs were measured after applying 550 V or 580 V at the PWE, respectively.[199]

after aCGDE and additional 15 min waiting time (after steps B1 and B2). Corresponding measurements in a setup without glass tube are presented by the dashed

curves. Overall the curves recorded with or without employing a glass tube look similar. Only when the AE is placed close to the PWE (1.5 cm) (red curves in Fig. 5.28a), the positive current density in the negative going scan in the potential region $>$ 0.60 V_{RHE} is larger when a glass tube was employed as if no glass tube was employed. As discussed in the manuscript, the positive current density was addressed to H_2O_2 oxidation. It appears as if the H_2 formed at the plasma counter electrode has an effect on the amount of H_2O_2 in the solution. The reason for this behavior remains, however, unknown.

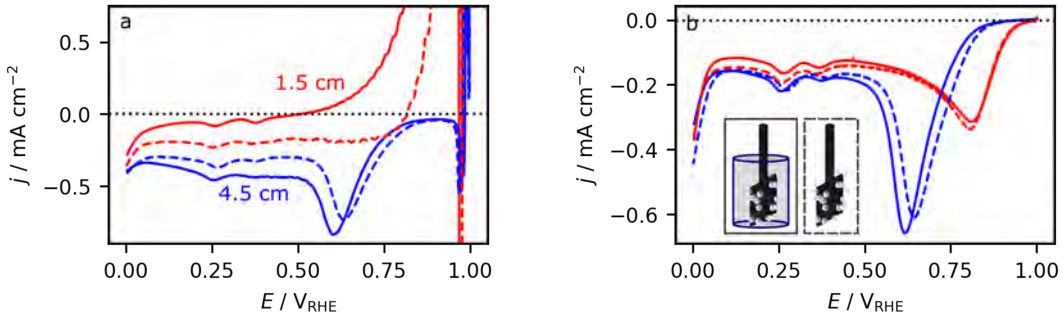

Figure 5.28: The first negative going scan of Pt CVs recorded in 0.01 M KOH at a scan rate of 50 mV s^{-1} after aCGDE (550 V for 30 s) at the PWE. The red and blue curves were obtained with Pt AEs placed at 1.5 cm and 4.5 cm from the PWE, respectively. The CVs were recorded a) directly after aCGDE and b) after waiting additional 15 min. In all cases, during the aCGDE and the subsequent waiting time, the potential of the AEs was kept at 1.00 V_{RHE}. The solid lines were recorded with a glass tube placed around the plasma counter electrode and the dashed lines without glass tube (see text for details).[199]

5.2.6.5 S5: Influence of the Upper Potential Limit on Pt Surface Oxidation

Fig. 5.29 shows the effect of applying higher upper potential limits (UPLs) on the CV of Pt recorded in 0.01 M KOH. The black solid line shows the CV with an UPL of 1.05 V_{RHE} and in green the CV after keeping the electrode at 1.0 V_{RHE} for 15 min (both in the manuscript with the same color code). Increasing the UPL to 1.25 V_{RHE} (black dashed curve), leads to an increase of the reduction peak at around 0.8 V_{RHE} in the negative going scan. The peak increases even more when the potential is kept at 1.20 V_{RHE} for 15 min (green dashed curve). As in case of the dashed black curve the UPL for the dashed green curve is also 1.25 V_{RHE}.

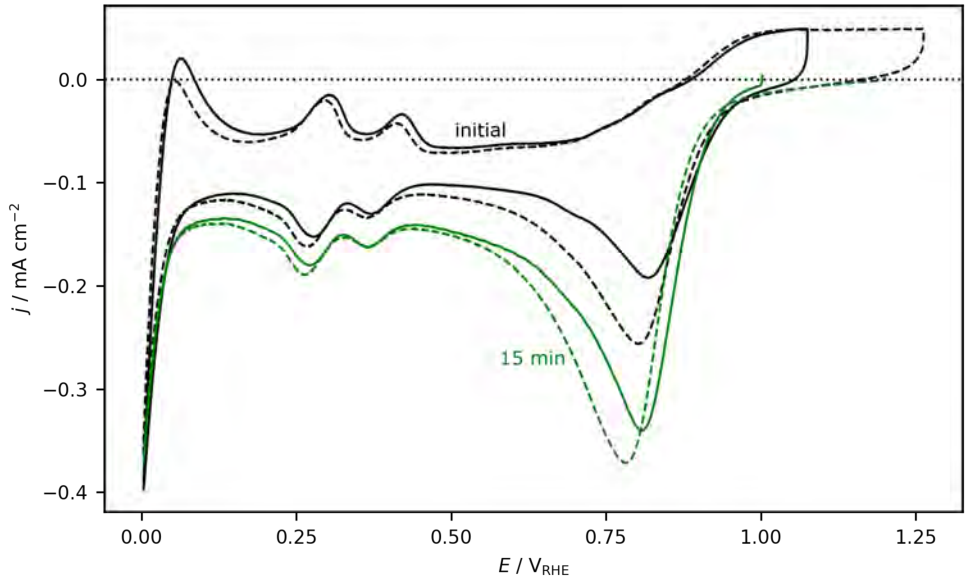

Figure 5.29: CVs of Pt electrodes recorded in 0.01 M KOH at a scan rate of 50 mV s^{-1}. The solid curve (black) shows the CV after cycling to an upper potential limit (UPL) of 1.05 V_{RHE} and the dashed black curves shows the CV after increasing the UPL to 1.25 V_{RHE}. The solid green curve was obtained by holding the potential at 1.0 V_{RHE} for 15 min and the dashed green curve after holding at 1.2 V_{RHE}.[199]

5.2.6.6 S6: Temporal Evolution of Cyclic Voltammograms after aCGDE

Fig. 5.30 shows the first and second cycles of the CVs recorded at a Pt AE directly after aCGDE (580 V for 30 s). For an AE placed at a distance of 4.5 cm from the PWE, in the first cycle (blue curve) a reduction peak is observed at around 0.6 V_{RHE} in the negative going scan (see manuscript). In the second cycle (light blue curve) the reduction peak is smaller and the maximum is located at 0.8 V_{RHE}, hence at a similar potential than what is observed in a CV recorded before the experiment (black curve). The current densities related to ORR (additional negative current density) also decreased significantly in the second scan. Placing the electrode at 1.5 cm from the PWE, a large positive current density is observed in the first negative going scan at potentials $>$ 0.65 V_{RHE} (red curve). In the second cycle, the positive current density associated with the hydrogen peroxide reduction is much lower, but still measurable. Overall the CV is slightly shifted to more negative

current densities for potentials < 0.65 V compared to the CV recorded before the experiment (black curve), which can be explained by the reduction of O_2 and H_2O_2 at the Pt electrode. In the first cycle (red curve), the CV is not as much shifted to lower current densities than in the second cycle (pink curve). This might be caused by an initially large H_2 concentration in the solution, which reacts with the Pt electrode giving rise to a positive current density which overlaps with negative current densities for ORR and HPRR. More importantly, a positive current density is still apparent at potentials > 0.95 V_{RHE}. This indicates that H_2O_2 is still present in the solution, which is oxidized at these potentials. The concentration is, however, much lower compared to the first cycle.

Continuous cycling reveals, that when the Pt electrode is placed at a distance of 1.5 cm from the PWE, it takes ca. 5 min until the CV looks almost identical to that recorded before the experiment, whereas when the electrode is placed at a distance of 4.5 cm from the PWE, it only takes ca. 3 min.

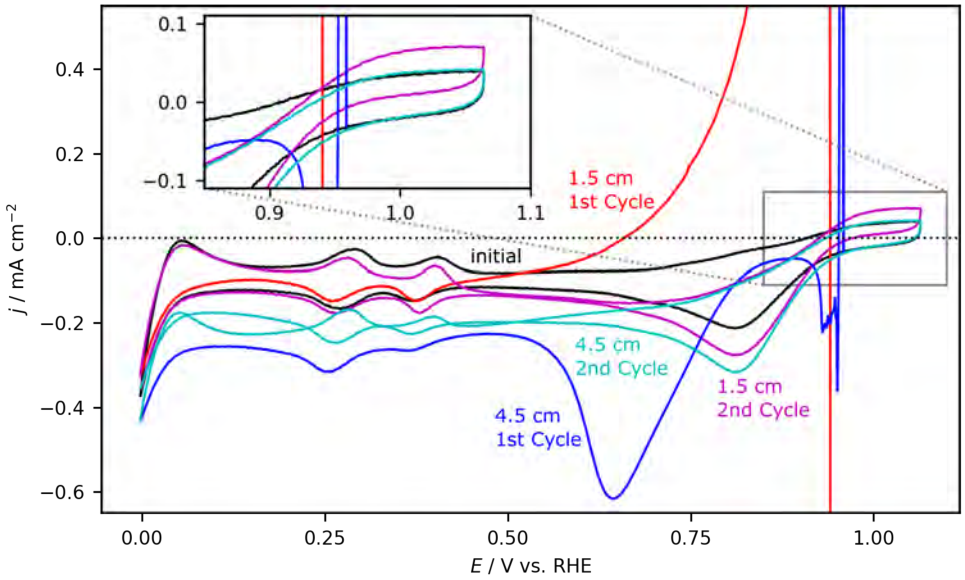

Figure 5.30: CVs recorded at a Pt AE in 0.01 M KOH with a scan rate of 50 mV s^{-1}. The CV recorded before performing aCGDE (580 V for 30 s) is shown in black. The first two cycles recorded directly after aCGDE of an electrode placed at a distance of (i) 1.5 cm from the PWE are shown in red (1st Cycle) and pink (2nd Cycle) or (ii) of 4.5 cm from the PWE in blue (1st Cycle) and light blue (2nd Cycle). The inset shows a magnification of the the potential range from 0.85 V_{RHE} to 1.10 V_{RHE}.[199]

5.3 Nanoporous Au Formation on Au Substrates via High Voltage Electrolysis

The results shown in this Section (5.3) were published in Chem. Phys. Chem.[169] Reprinted with permission from Chem. Phys. Chem., 24, E. Artmann *et al.*, "Nanoporous Au Formation on Au Substrates via High Voltage Electrolysis", e202200645, Copyright 2022, John Wiley and Sons. "© 2022 The Authors. ChemPhysChem published by Wiley-VCH GmbH."
The investigation was performed by me together with three of my co-authors. The XPS measurements as well as the FIB-SEM measurements were performed as service measurements by Konstantin M. Schüttler and Mohammad Al-Shakran, respectively. The H_2O_2 concentration and temperature dependancy experiments were measured by Lukas Forschner in his project work under my instructions. All other experiments, especially those on temperature and time dependence, were carried out by me. The concept of this paper, the complete data analysis and evaluation, the validation and visualization of all results and the preparation of all figures of this paper, as well as the original draft of this paper were prepared by me. The graphical abstract shown here, serving as a summary of this Section, was also published in Chem. Phys. Chem.[169]

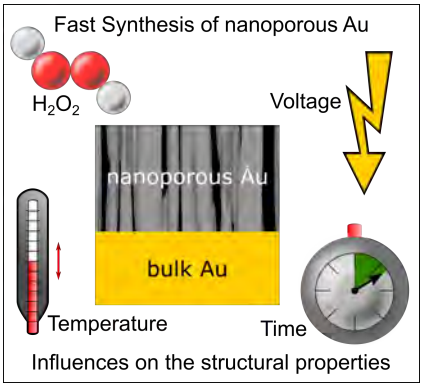

Figure 5.31: Graphical abstract of the publication with the title "Nanoporous Au Formation on Au Substrates via High Voltage Electrolysis".[169]

5.3.1 Abstract

Nanoporous Au (NPG) films have promising properties, making them suitable for various applications in (electro)catalysis or (bio)sensing. Tuning the structural properties, such as the pore size or the surface-to-volume ratio, often requires complex starting materials such as alloys, multiple synthesis steps, lengthy preparation procedures or a combination of these factors. Here we present an approach that circumvents these difficulties, enabling for a rapid and controlled preparation of NPG films starting from a bare Au electrode. In a first approach a Au oxide film is prepared by high voltage (HV) electrolysis in a KOH solution, which is then reduced either electrochemically or in the presence of H_2O_2. The resulting NPG structures and their electrochemically active surface areas strongly depend on the reduction procedure, the concentration and temperature of the H_2O_2-containing KOH solution, as well as the applied voltage and temperature during HV electrolysis. Secondly, the NPG film can be prepared directly by applying voltages that result in anodic contact glow discharge electrolysis (aCGDE). By carefully adjusting the corresponding parameters, the surface area of the final NPG film can be specifically controlled. The structural properties of the electrodes are investigated by means of XPS, SEM and electrochemical methods.

5.3.2 Introduction

Nanoporous metals show distinct physico-chemical properties that often differ from those of the bulk materials.[45–47, 244] These materials typically have pores in the range of 50 to 200 nm interconnected with ligaments of the bulk material. A rather intensively studied systems during the last years is nanoporous Au (NPG), for its possible application as, *i.e.*, (bio)sensor,[45, 49–51, 152, 245] in biomedicine[51], as actuator [246], heterogeneous catalyst material[44, 50, 155, 247], electrocatalyst,[45, 46, 148, 149, 151, 248, 249] or material in battery systems.[45, 46]

A large number of approaches exist to prepare NPG, either free standing or on a support material.[45, 46, 49, 50, 150] The most common method discussed to synthesize nanoporous structures in general is dealloying, which is not limited to Au but is successfully employed for example to create nanoporous Ni (Raney-Ni).[46, 250] Within this approach, an alloy is used as precursor, which can for example be

fabricated by electrodeposition of one metal on another followed by alloying both elements. In a subsequent electrochemical dealloying step, the less noble metal is dissolved (electro)chemically and a nanoporous structure of the more noble metal remains.[44, 156] This method is, however, mostly limited to noble metals.[46] To prepare NPG, the precursor alloy usually consists of a mixture of Ag and Au.[149, 151–155]

Another frequently used method is the reduction of precursor molecules such as metal salts, *e.g.*, $HAuCl_4$, in solution.[107] The reduction of the precursor molecules can, for example, be achieved by igniting a plasma above a liquid,[251–253] or by using another molecule that acts as a reducing agent.[254, 255] By combining different preparation methods, not only NPG films but also nanoporous Au nanoparticles can be produced.[48]

NPG films can also be prepared by anodizing a Au substrate in aqueous solutions at potentials in the oxygen evolution region (for example 2.0 V *vs.* Ag/AgCl) and subsequent electrochemical reduction.[99, 109] This approach bears the advantage that no additional chemicals or multimetallic precursors have to be used. Other groups also report on combining electrodeposition with subsequent anodization.[159] Overall, most of these common processes for producing nanoporous substrates are relatively complex, time-consuming, and require different, potentially harmful chemicals, which can also lead to the incorporation of impurities in the nanoporous film (in case of alloy precursors or salts). Impurities in particular can be problematic in further (electro)catalytic studies, where trace impurities can have a significant impact on the reaction rates such as for the CO oxidation.[167, 168] To scale up material production it is necessary that the production process is cheap, fast, reliable and preferentially does not pose any environmental hazards.
Recently, we demonstrated that NPG films can be prepared by anodization of a Au electrode in aqueous alkaline electrolyte at high voltages (between 100 and 540 V) leading to the formation of a Au oxide film, which upon subsequent electrochemical reduction turns into a NPG film.[66] NPG films with similar structures were also obtained by keeping the Au oxide after electrolysis in the electrolysis solution. We suggested that the Au oxide is reduced by H_2O_2 which forms during anodic contact glow discharge electrolysis (aCGDE).[18, 54, 67, 199] Our results also indicate that H_2O_2 might also form at lower voltages (still in the range of a few 100 V) in the normal electrolysis region, as suggested previously.[87] This approach allows

preparing samples within a few minutes. In addition, this method is also comparably environmental friendly since an alkaline KOH solution is the only chemical used in the preparation process.

In this work we systematically investigate the formation of NPG on bare Au wire and sheet electrodes. The experimental approach is based on our previous study, whereby a Au electrode is oxidized during electrolysis at high voltage (HV) in 0.01 M KOH and subsequently reduced either electrochemically or in a H_2O_2-containing 0.01 M KOH solution. The conclusions on the composition of the electrodes after this procedure by electrochemical measurements in the previous work are here confirmed by XPS measurements. Furthermore, with cross sectional SEM analyses we show that the Au oxide, obtained after HV electrolysis, as well as the NPG film, obtained after reducing the Au oxide, forms a several micrometer thick layer. In order to tune the NPG film, we systematically explore the possibility to reduce the Au oxide with H_2O_2 solutions with different concentration and temperature. The final NPG structures are compared to those obtained by electrochemical reduction. We also demonstrate that the thickness (or surface area) of the NPG film can be controlled by varying the electrolysis time, the electrolyte temperature and the voltage applied during electrolysis. The structural properties are investigated primarily by SEM imaging and electrochemical measurements.

5.3.3 Results and Discussion

The results and discussion section is separated in four parts. Based on our previous study, first we provide further complementary information on the structural properties of Au oxide structures obtained by HV electrolysis as well as the NPG films obtained by subsequent electrochemical reduction. Second we discuss the impact of H_2O_2 concentration (in 0.01 M KOH) and temperature on the reduction of Au oxide films formed by HV electrolysis at 300 V. Third we show the impact of the electrolysis voltage and the electrolyte temperature on the change in surface area of the NPG films after electrochemical reduction. Finally we discuss the impact of the electrolysis time on the change in electrolyte temperature and more importantly on the structure formation.

5.3.3.1 Structural Properties

The structural properties of Au electrodes after HV electrolysis were investigated on wire and sheet Au anodes. The choice of the electrode type depends on the analytical approaches employed (see experimental section). In this section we studied Au sheet electrodes modified by HV electrolysis at 300 V for 290 s, which were (i) directly removed from the electrolysis solution or (ii) subsequently reduced electrochemically, as reported previously.[66] At 300 V the structural changes are most significant, compared to lower voltages or voltages in the aCGDE region. Nevertheless, the following observations are also representative for other voltages in the range of 100 to 540 V.

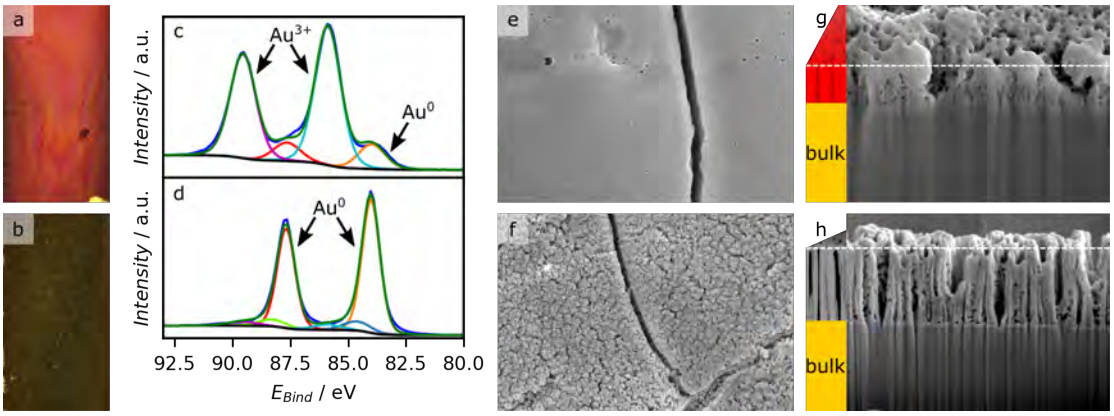

Figure 5.32: Top row: Structural properties of a Au sheet electrode after electrolysis at 300 V for 290 s in 0.01 M KOH. Bottom row: A Au sheet electrode which was reduced electrochemically after HV electrolysis. a) and b) show corresponding optical microscope images. c) and d) show XPS spectra of the Au 4*f* region, including the peaks fitted to Au^0 and Au^{3+}. e) and f) show top-view SEM images with image sizes of 6 µm $\times$ 4 µm. g) and h) show cross sectional SEM images of the surfaces in e) and f) with image sizes of 4 µm $\times$ 3 µm and 8 µm $\times$ 6 µm. The schematic illustration next to the cross sectional SEM images show the color of the sheets and the viewing angle during the image acquisition.[169]

Upon direct removal of the Au electrode from the electrolysis solution the electrodes color is red, while the reduced electrode is black as illustrated in the optical microscope images in Figs. 5.32a and b. Previously, we suggested that the red color is related to the formation of a Au_2O_3 film. This assumption is confirmed by XPS measurements of the Au 4*f* region shown in Fig. 5.32c. The spectrum clearly shows features related to Au^0 (binding energies - BE: 84.0 eV and 87.7 eV [256–259]) and

Au^{3+} (BE: 85.8 eV and 89.5 eV [256, 257]), where the latter is significantly more pronounced. A contribution from Au^{+}, which should appear between the features of Au^{0} and Au^{3+}, is not measurable. Au^{+} would possibly be related to Au_2O, which is considered to be a metastable intermediate during the reduction of Au_2O_3.[118, 119] The Au^{0} feature in the Au 4*f* region can be attributed to areas that are not covered with Au oxide, resulting from the detachment of the Au oxide film from the Au substrate during the transfer (compare Fig. 5.32a lower right edge). Plausibly, the Au oxide also decomposes during the XPS measurement due to beam damage.[260] In the O 1*s* region (see Fig. 5.40) a typical oxidic oxygen state is observed as main feature, which is most likely related to Au_2O_3.[261, 262] The peak is, however, relatively broad compared to pure metal oxides, which, in general, is indicative for defects in the oxide. A second feature visible in the O 1*s* region can be ascribed to OH species.

The black color of the reduced electrodes was suggested to originate from a nanoporous Au (NPG) structure.[99, 109, 156, 158, 159] A corresponding XPS spectrum of the Au 4*f* region is shown in Fig. 5.32d. The spectrum clearly shows that the electrode consists primarily of metallic Au^{0}. Minor contributions from oxidic Au^{+}- and Au^{3+}-species are also present. The corresponding O 1*s* peak, has a much lower intensity than that of the oxidic sample. Nevertheless, the peak still consists of two features, which were ascribed to oxidic oxygen and OH (as discussed above and described along with Fig. 5.40).

Corresponding SEM images of both electrodes are shown in Figs. 5.32e and f. The image taken on the red electrode shows a relatively flat surface with some large cracks, while images of the black electrodes (after electrochemical reduction) exhibit in addition to the large cracks a more patterned structure. Further SEM images of Au electrodes formed by HV electrolysis at 300 V are provided in Fig. 5.41. Cross sectional SEM images of both the red and black electrodes in Figs. 5.32g and h, provide further information on the film thickness and structure. The schematic illustration shows the different regions of the cross section, where the part above the dashed line shows the surface. The cross section of the Au_2O_3 film (Fig. 5.32g) shows a several 100 nm thick porous film. Note, however, that cutting the sample with an ion beam could also damage the structures and lead to the formation of porous structures observed in the Au oxide. The NPG film obtained by electrochemical reduction depicted in Fig. 5.32h shows a more ordered porous structure,

with mostly vertically aligned pores. To be able to estimate the pore and ligament size of the NPG structures formed in this work more precisely, SEM images of the NPG structures with high resolution and magnification after 30 s at 300 V, as well as 540 V are shown in Section 5.3.6.3.

5.3.3.2 H_2O_2 Concentration and Temperature Dependence

As described above, the Au oxide formed during HV electrolysis is reduced when the electrode is kept in the electrolysis solution after HV electrolysis. It was suggested that the reduction process is caused by H_2O_2 in the electrolyte[66, 199] which forms during HV electrolysis.[18, 67, 87] The general ability of H_2O_2 to reduce Au cations is already known in literature and can be explained by using the standard electrochemical potentials.[251–253, 255] Therefore, we suggest the following reactions.

Reduction:

$$Au_2O_3 + 3H_2O + 6e^- \rightarrow 2Au + 6OH^- \tag{5.1}$$

Oxidation:

$$H_2O_2 + 2OH^- \rightarrow 2H_2O + 2e^- + O_2 \tag{5.2}$$

Overall reaction:

$$Au_2O_3 + 3H_2O_2 \rightarrow 2Au + 3O_2 + 3H_2O \tag{5.3}$$

To illustrate the role of H_2O_2 in the reduction of the Au oxide, we investigated changes in the surface structure induced by i) H_2O_2-containing KOH solutions of different concentration at constant temperature and ii) by varying the H_2O_2 solution temperature for a constant H_2O_2 concentration. In the following a "H_2O_2 solution" refers to a "H_2O_2-containing 0.01 M KOH solution". All H_2O_2 concentrations are referred to weigth%. Table 5.1 summarizes the following experimental conditions, observations, and evaluated RF.

For these investigations, the Au oxide films were prepared on Au wire electrodes in 0.01 M KOH at 300 V for 30 s. The electrodes were directly removed from the electrolysis solution to minimize the reducing effect from the H_2O_2 in the electrolysis solution.

The concentration dependence was studied by immersing the Au oxide-covered electrodes at room temperature for 60 s in H_2O_2-containing KOH solutions with concentrations of 0.007 %, 0.08 % and 0.8 %. Upon removal from a 0.007 % H_2O_2-containing 0.01 M KOH solution, the electrode still appears red, whereas in a 0.08 % and 0.8 % H_2O_2-containing 0.01 M KOH solution, the electrodes turn black within 60 s.
Corresponding SEM images of the electrodes are shown in Fig. 5.33 with large scale images in the top row and regions with higher magnification of these surfaces in the bottom row. It is apparent that the structure formation strongly depends on the H_2O_2 concentration. The electrodes surface upon removal from the 0.007 % H_2O_2 solution (Figs. 5.33a and b) still appears rather smooth and is only restructured in certain regions. Interestingly, it seems that the restructuring process starts in random regions on the surface, which are separated by about 0.5 µm. For electrodes immersed in a 0.08 % H_2O_2 solution (Figs. 5.33c and d) the entire surface is nanostructured. Increasing the concentration further by an order of magnitude (0.8 % H_2O_2 - Figs. 5.33e and f), large cracks appear on the surface. In some regions the surface even peels off (Fig. 5.33e), in others large protrusions form on the surface (Fig. 5.33f). The amount of oxide remaining on the electrode after removal from a H_2O_2 solution was determined by electrochemical reduction of the electrodes. The electrodes removed from low concentrated H_2O_2 solutions still show a current density related to oxide reduction. This current density is significantly lower compared to that recorded on electrodes reduced electrochemically directly after the HV electrolysis. The electrode immersed in 0.8 % H_2O_2 solution is completely reduced after 60 s.

Even though H_2O_2 seems to play a critical role in the reduction of the Au oxide, the structures obtained after HV electrolysis and subsequent electrochemical reduction (compare with Fig. 5.32f) do not resemble those observed upon immersion of the Au oxide in H_2O_2 solutions. Possible reasons for this discrepancy are that after HV electrolysis the H_2O_2 concentration will be high in the region around the electrode and will decrease with increasing time, as shown elsewhere.[199] Furthermore, during HV electrolysis the temperature of the electrolyte will increase,[17, 18, 84, 87] which could also be a decisive factor for the structure formation.

To separate the effect of temperature and H_2O_2 concentration on the structure formation, Au oxide electrodes prepared by HV electrolysis at 300 V were immersed

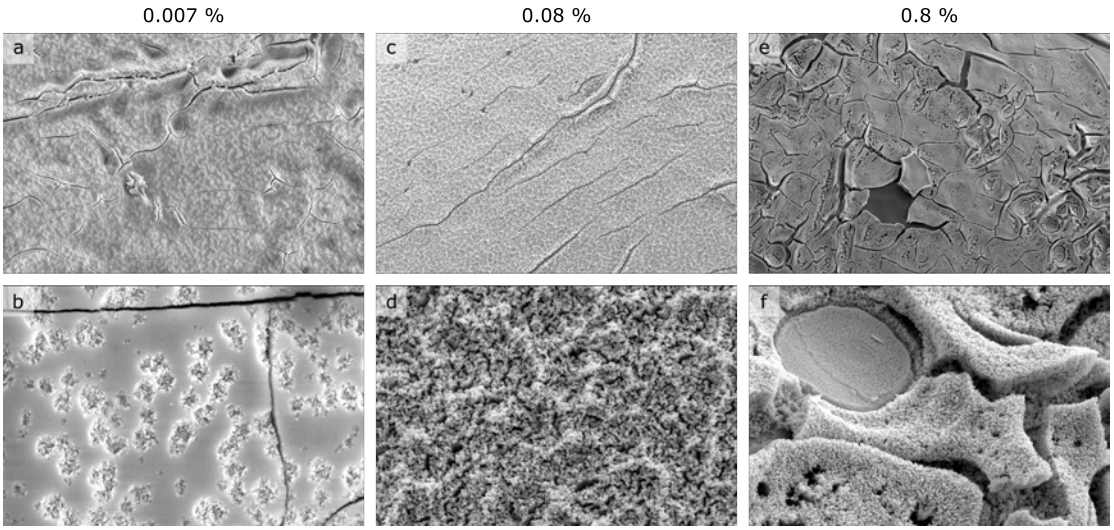

Figure 5.33: SEM images recorded on Au wire electrodes after electrolysis at 300 V for 30 s, direct removal from the electrolysis solution and subsequent reduction for 60 s in H_2O_2-containing 0.01 M KOH solutions (room temperature). The amount of H_2O_2 is given above the respective columns. The top row images show regions with sizes of 120 $\times$ 80 µm and the bottom row 12 $\times$ 8 µm.[169]

for 60 s in a freshly prepared 0.01 M KOH solution heated to 70 °C. Afterwards, the electrodes color was still red, indicating that the Au oxide is stable at this temperature in pure 0.01 M KOH. This result is in line with the findings by Tsai *et. al.* who studied the kinetics of dissociation of Au_2O_3 at different temperatures.[117] Hence, we can exclude that temperature alone has an effect on the transformation of Au oxide to pure Au or other structural changes of the electrode.

To study the influence of the combined effect of temperature and H_2O_2 on the NPG structure formation, Au oxide electrodes were immersed for 60 s in 0.007 % H_2O_2 solutions with electrolyte temperatures of 24, 40, and 70 °C. Au oxide electrodes immersed in a 0.007 % H_2O_2 solution at 24 °C or 40 °C remained red. At 70 °C, the color of the electrodes turned black with a touch of red. In all three cases, additional electrochemical reduction of the electrodes revealed that the electrodes still contain a significant amount of Au oxide. Hence, under these conditions the electrodes do not reduce completely.

Corresponding SEM images of the resulting electrode surfaces are shown in Fig. 5.34 with large scale images in the top row and magnified regions of these surfaces in the bottom row. The conditions in Figs. 5.34a and b are identical to

those in Figs. 5.33a and b and are only shown for comparison. The main observation is that the restructuring becomes more pronounced with higher temperature and that the number of cracks, observed already at room temperature, increases. Despite the significant restructuring, the surface structure is not identical to that obtained by HV electrolysis at 300 V and subsequent electrochemical reduction (see Figs. 5.36a to d) or reduction in the electrolyte.

Overall, these results show that the H_2O_2 concentration and temperature play a major role in structure formation. This is an important aspect, since these parameters change dynamically and in an uncontrolled way when the electrodes are kept in the electrolysis solution after HV electrolysis, *i.e.*, the H_2O_2 concentration will probably decrease due to dissipation in the electrolyte[199] and the local temperature will also decrease due to heat dissipation into the surrounding electrolyte.

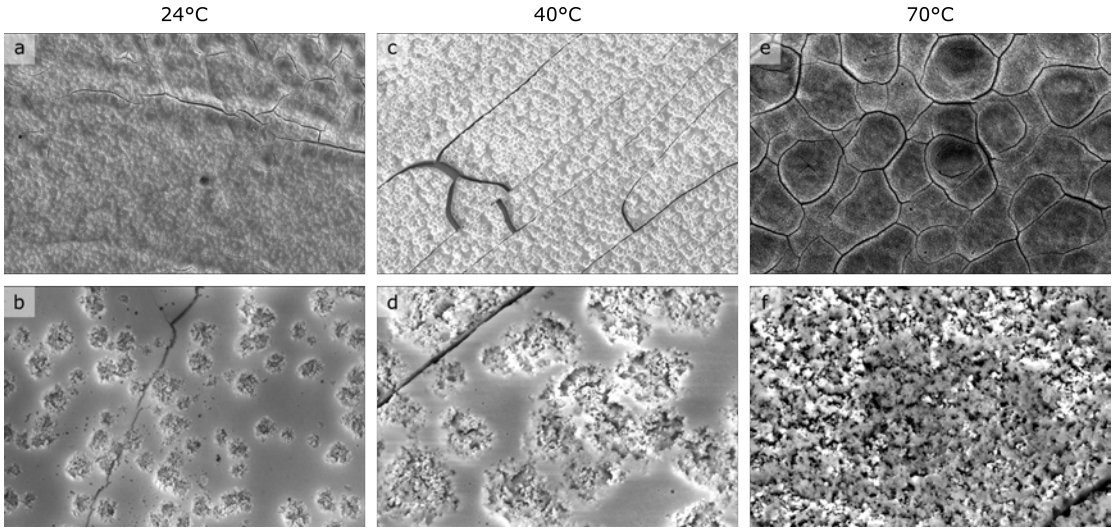

Figure 5.34: SEM images of Au wires after HV electrolysis at 300 V for 30 s and direct removal from the electrolysis solution with subsequent reduction through immersion in 0.01 M KOH solutions with a H_2O_2 concentration of 0.007 % for 60 s and temperatures of a) and b) 24 °C (room temperature), c) and d) 40 °C and e) and f) 70 °C. The image size of a), c) and e) is 120 $\times$ 80 µm, from b), d) and f) 12 $\times$ 8 µm.[169]

5.3.3.3 Effect of HV Electrolysis Parameters - Voltage and Temperature

In the following, we demonstrate and discuss how the surface area of the NPG film can be controlled by tuning the electrolysis voltage and electrolyte temperature. In

our previous work we demonstrated that independent of the applied voltage during HV electrolysis the resulting Au oxide surface structures appear rather similar, as well as the fully-reduced Au oxide structures (also shown in an additional set of SEM images in Fig. 5.43). The change in surface area, here discussed based on the roughness factor (RF – see experimental section), of the NPG film, however, depends on the electrolysis voltage and correlates with the average current density during HV electrolysis.[66] A corresponding j–U curve (dark blue solid line) is shown along with the RF (dark blue dashed line) in Fig. 5.35. Note that each point in the plot represents an individual measurement on a freshly-prepared Au wire, where the voltage was applied for 30 s and the electrode was subsequently reduced electrochemically. Overall, the j–U characteristic is described in the literature.[18, 56, 82, 84, 86, 244] Thus, only the most important aspects are briefly introduced here.

For gas-evolving electrodes, the j–U curve can be divided into different regions. First, the current increases linearly with increasing voltage (Ohmic behavior) up to a certain breakdown voltage (V_B). Here, bubble formation becomes significant and a gas sheath starts to form around the electrode, which increases the resistance at the electrode | electrolyte interface and hence leads to a decrease in current density. With increasing voltage, the gas film becomes more stable showing partial ionization of the gas in the sheath (partial aCGDE). At the midpoint voltage (V_D, here ca. 540 V), full aCGDE is observed.

First, to demonstrate possible differences between the electrochemical reduction and reduction by H_2O_2 on the RF, Au oxide samples were prepared at different voltages as described above and were reduced in an 0.8 % H_2O_2 solution. At this H_2O_2 concentration the reduction process was suggested to be complete. The corresponding j–U curve (cyan solid line) resulting from the electrolysis of the Au electrodes is shown in Fig. 5.35, which shows a similar behavior to the curve in dark blue (illustrating the reproducibility of the approach). The RF of the Au oxide films reduced in the H_2O_2 solution is shown by the cyan dashed curve in Fig. 5.35.

Comparing the RF of the Au oxide reduced electrochemically with that reduced in a H_2O_2 solution (dashed blue and cyan curves in Fig. 5.35), the values are rather similar for Au electrodes treated by low and high electrolysis voltages. For intermediate electrolysis voltages around V_B, the Au oxides reduced in H_2O_2 have a larger RF than the electrochemically reduced Au oxides. This is also apparent from SEM

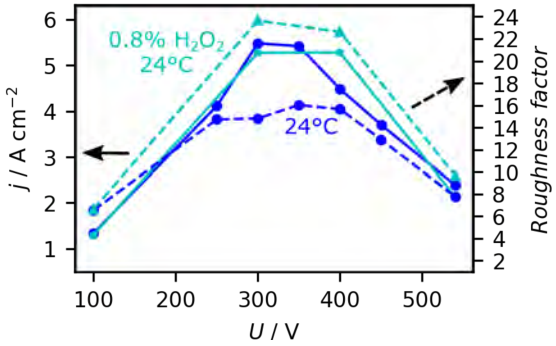

Figure 5.35: HV electrolysis of a Au wire electrode for 30 s at different voltages and an initial electrolyte temperature of 24 °C in 0.01 M KOH and subsequent electrochemical reduction (dark blue), as well as reduction by immersion of the electrode for 60 s in a 0.8 % H_2O_2-containing 0.01 M KOH solution at 24 °C (cyan). The average current densities during HV electrolysis are shown by the points linked by solid lines, the roughness factors of the electrode after HV electrolysis and following reduction are shown by the points linked by dashed lines.[169]

images, where the NPG film formed by reducing Au oxide in a 0.8 % H_2O_2 solution shown in Fig 5.36e–h is much more inhomogeneous than the electrochemically reduced film in Fig. 5.36a–d.

The effect of the electrolysis solution temperature on the RF of NPG films after the electrochemical reduction of Au oxide films is illustrated in Fig. 5.37 by the dashed lines (24 °C - blue, 46 °C - orange and 70 °C - red). The corresponding j–U curves are shown by the solid lines. At higher initial electrolyte temperatures the breakdown voltage (V_B) shifts to lower voltages. This shift can be explained by the fact that the boiling point of the electrolyte is reached on a shorter timescale at a higher initial electrolyte temperature.[17, 18, 70, 85] In addition, the average current densities at low voltages increase due to an increase in ion conductivity in the electrolyte, whereas at high voltages the current densities decrease with the temperature due to more facile gas sheath formation. More detailed information on the effect of the initial electrolyte temperature on the j–U curves can be found elsewhere.[17, 18, 70, 85, 92] Further information on the increase in electrolyte temperature at different initial electrolyte temperatures during HV electrolysis is explained along with Fig. 5.44.

More importantly, after the electrochemical reduction the evolution of the RF with applied voltage follows the evolution of the average current density for all temper-

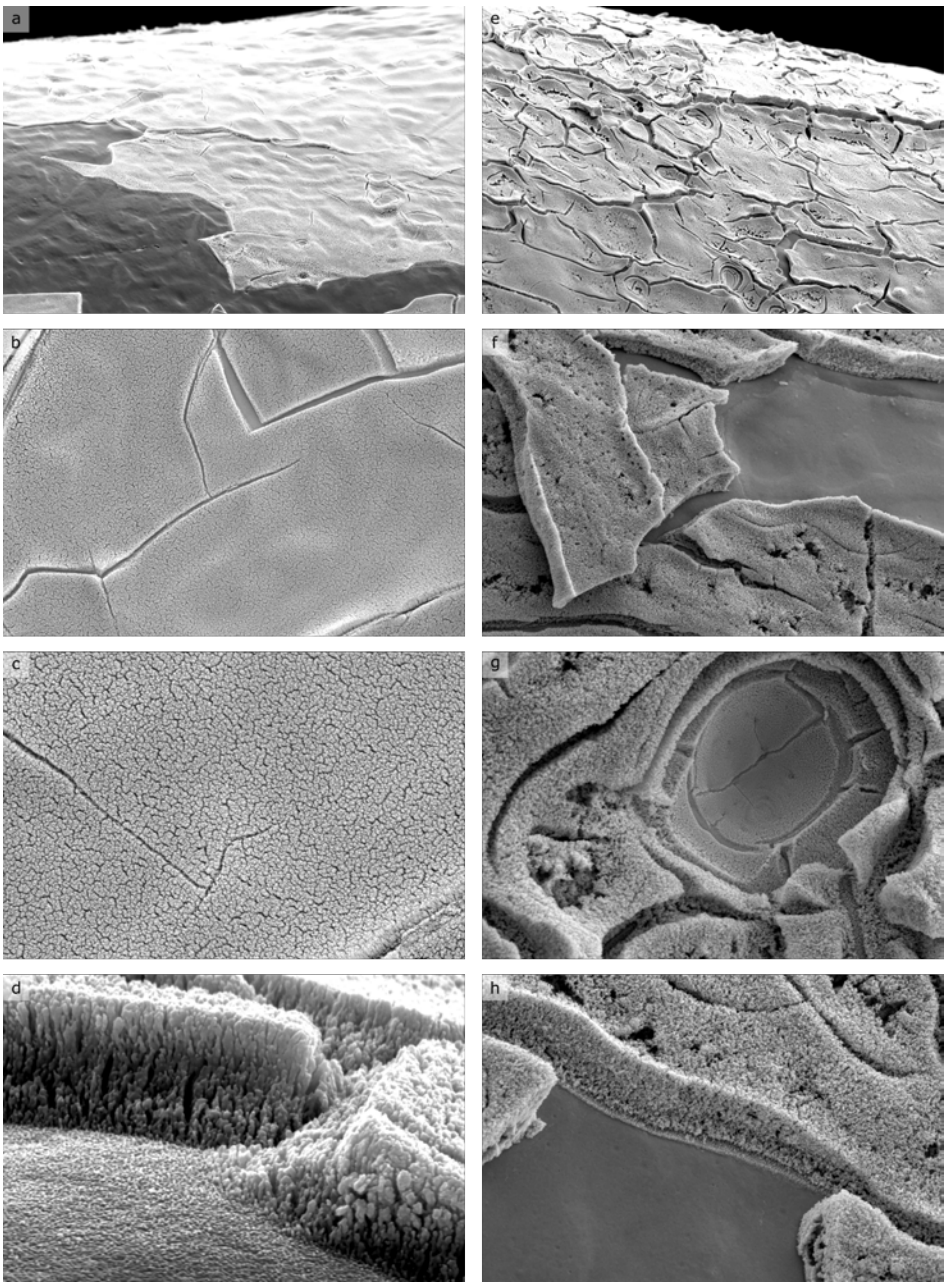

Figure 5.36: SEM images of Au wire electrodes after HV electrolysis at 300 V for 30 s and a) to d) subsequent electrochemical reduction, or e) to h) reduction in a 0.8 % H_2O_2-containing 0.01 M KOH solution. The image size in a) and e) is 120 µm $\times$ 80 µm, b) and f) 30 µm $\times$ 20 µm, c) g) and h) 12 µm $\times$ 8 µm and d) 3 µm $\times$ 2 µm.[169]

atures and applied voltages. The largest increase in surface area is observed for low initial electrolyte temperatures and voltages in the range of V_B. For low and high voltages the differences in RF at different initial electrolyte temperatures is less significant. In addition, for high voltages in the aCGDE region ($\geq$ 450 V), the RF does not increase significantly compared to bare Au electrodes at higher initial electrolyte temperatures. Therefore, NPG films with high surface area are achieved for low initial electrolyte temperatures.

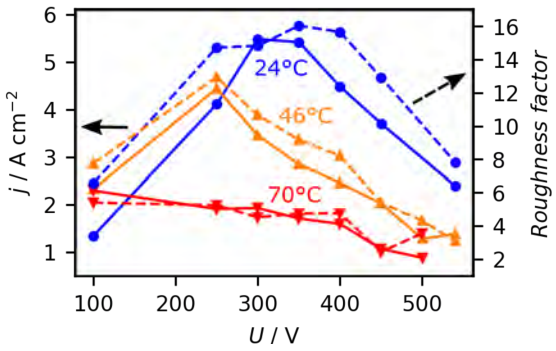

Figure 5.37: HV electrolysis of a Au wire electrode for 30 s at different voltages and initial electrolyte temperatures (24 °C - blue, 46 °C - orange and 70 °C - red) in 0.01 M KOH. The j–U traces are connected with solid lines, while the corresponding RF after electrochemical reduction are connected with dashed lines. Each data point marks an individual measurement. The current densities are averaged over 30 s (see experimental section). The lines only serve as a guide to the eye.[169]

5.3.3.4 Time Dependence

To illustrate the impact of electrolysis time on the Au oxide formation and the RF of the final NPG film, we performed electrolysis experiments at 300 V and 540 V for different times ranging from 10 to 600 s. The 300 V experiments were also performed at 46 °C and 70 °C. Since the 300 V measurements could not be performed without complications (see below), we first discuss the results obtained for 540 V.

Figure 5.38a shows the evolution of the current density during 600 s electrolysis at 540 V (black line). The curves for shorter electrolysis times are not shown, but look very similar and follow the same trend. At the start of the measurement the current density rises sharply, reaching a maximum within a second (see inset in Fig. 5.38a). Immediately, strong bubble formation is observed, followed by the for-

mation of a dynamic gas layer around the electrode. Furthermore, at this voltage a plasma develops in the resulting gas layer between the electrode surface and the electrolyte. With increasing time the current drops, until it becomes almost constant for longer electrolysis times (ca. 100 s).

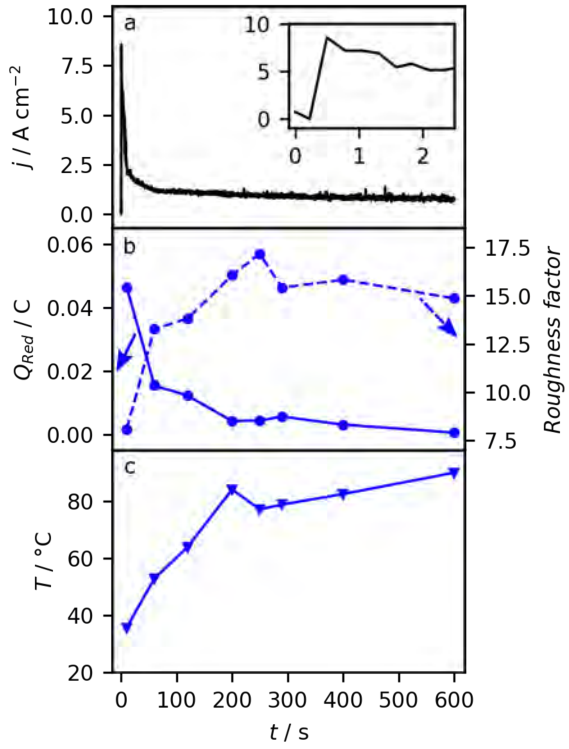

Figure 5.38: Time dependence of HV electrolysis on a Au wire electrode at 540 V in 0.01 M KOH. a) Current density during HV electrolysis. b) Amount of Au_2O_3 formed after different HV electrolysis times determined by electrochemical reduction (solid line) and RF (dashed line) of the NPG film. c) Electrolyte temperature after HV electrolysis (initial electrolyte temperature: 24 ℃).[169]

The evolution of the structural properties was determined from several experiments with different electrolysis times, on freshly prepared electrodes. For each sample, Figs. 5.38b and c show (i) the amount of Au oxide formed during HV electrolysis (Fig. 5.38b - solid), (ii) the RF of the electrodes after electrochemical reduction (Fig. 5.38b - dashed), and (iii) the electrolyte temperature after electrolysis (Fig. 5.38c). The starting electrolyte temperature was in each case room temperature. For short electrolysis times (10 s) the amount of Au oxide is high (Fig. 5.38b - solid), which decreases with longer electrolysis times exponentially. From approxi-

mately 200 s onward, the amount of Au oxide on the surface is very low and almost negligible at 600 s. In turn, the RF follows an opposite trend, whereby in the first 30 to 60 s, the RF of the NPG electrodes increases sharply. For longer electrolysis times the increase in RF becomes smaller, reaching a plateau after approximately 200 s where the surface area is 15 times larger compared to that of the bare Au electrode. With increasing electrolysis time, the temperature rises up to ca. 80 °C within 200 s and increases only slightly within the next 400 s. By comparing all measurements in Fig. 5.38, it is apparent that the amount of Au_2O_3 is not directly correlated with the increase in surface area obtained after the electrochemical reduction. Thus it seems that the Au oxide is reduced automatically, as discussed further below. More importantly, this set of measurements suggest, that the formation of NPG films via HV electrolysis does not necessarily require an additional step to reduce a Au oxide, but it can be formed directly via HV electrolysis, when the electrolysis time is sufficiently long.

While a full explanation for the observed behavior is still missing, the following aspects can be excluded or considered to be at the origin. First, we often observed (also in previous measurements) that parts of the newly formed films (Au oxide or NPG) peeled of from the substrate surface during HV electrolysis. If this effect would be significant, especially at long electrolysis times, we would not only expect that the amount of Au oxide on the surfaces decreases, but also the roughness factor will decrease (or both should be correlated with one another). Hence this aspect can be ruled out. Second, with increasing electrolysis time, the amount of H_2O_2 in the solution will increase, which in turn would increase the probability to reduce the Au oxide. However, performing electrolysis at 540 V leads to the formation of a gas sheath around the electrode, and hence the contact area between the electrode and electrolyte can be considered to be negligible. Whether or not H_2, which also forms under these conditions and might be present in the sheath,[85, 87, 263] plays a role is questionable. Based on separate experiments, where we immersed a Au oxide electrode in a H_2-containing 0.01 M KOH solution, we did not observe reduction of the Au oxide. Third, during the electrolysis not only the electrolyte temperature increases, but most likely also that of the electrode. Under certain circumstances, the electrodes might even melt during aCGDE conditions.[17, 18] Considering that the decomposition temperature of Au_2O_3 is only approximately 150 °C,[117, 118, 261] it is likely that the Au oxide decomposes

to Au due to the high local electrode temperature. Overall, we suggest that this is presumably the most likely scenario.

We performed a similar set of experiments at an electrolysis voltage of 300 V and in electrolytes initially at room temperature. In contrast to electrolysis at 540 V, the averaged current densities during HV electrolysis are much higher and the electrode is still to some extend in contact with the electrolyte, despite vivid bubble formation. The amount of H_2O_2 formed at this voltage may also differ from that formed at 540 V, since the literature only reports H_2O_2 formation above the midpoint voltage. However, we were recently able to show that H_2O_2 is most likely also formed at lower voltages and at 300 V.[66] The temporal evolution of the current density recorded at 300 V is shown in red in Fig. 5.39 together with that recorded at 540 V in black. The inset shows the increase in current density at the beginning of the HV electrolysis.

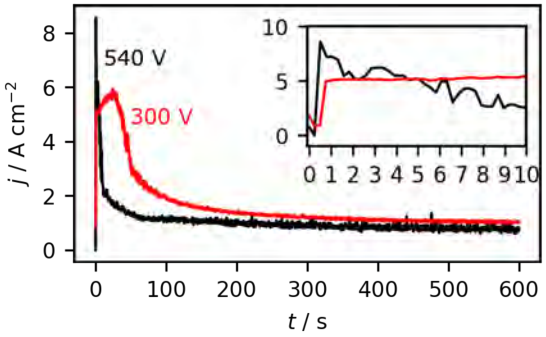

Figure 5.39: Evolution of the current density with time during HV electrolysis at 540 V (black) and 300 V (red) in 0.01 M KOH.[169]

A key issue in the experiments performed at 300 V was that for longer electrolysis times, the films formed on the surface significantly peeled off. Therefore, we limit ourselves to a more qualitative description. After 120 s of HV electrolysis the electrode exhibits a red color, indicating that the electrode is covered with a Au oxide film. After the electrochemical reduction the RF of the NPG electrode is larger compared to the bare Au electrode. From visual inspection it is apparent that for longer electrolysis times (290 s up to 600 s) the Au oxide or NPG film significantly pealed off from the electrode and the electrode appears mostly golden. The RF determined after the electrochemical reduction is very low compared to the electrode which was treated by electrolysis for only 120 s. But since the resulting film seemed to peel off, this result is not very meaningful, except that it

underlines that no Au oxide or NPG can be formed under these conditions, *i.e.* at long electrolysis times. To what extend the rise of the electrolyte temperature up to 80 °C or the vivid bubble formation plays a role in the removal of the films is unclear. Hence, at high current densities and during HV electrolysis with bubble formation, short time scales are required to form a stable Au oxide film, which can then be reduced in a second step to form a NPG film.

5.3.4 Conclusion

In this work, we demonstrated that NPG can be prepared by a simple and fast method, namely by (i) HV electrolysis alone or followed by (ii) electrochemical reduction or (iii) reduction in an H_2O_2-containing KOH solution. The thickness of the NPG film and surface structure can be controlled by several parameters:

1. the voltage applied during HV electrolysis.

2. the initial electrolyte temperature before HV electrolysis. The lower the initial electrolyte temperature, the greater is the surface area of the resulting NPG film, when the current densities during HV electrolysis are higher at low initial electrolyte temperatures.

3. The electrolysis time in the region of aCGDE. With short electrolysis times, the surface area increases sharply within a very short time period (30 to 60 s), while for longer electrolysis times the surface area remains almost constant.

Reduction of the Au_2O_3 films previously formed by HV electrolysis on the electrode surfaces in H_2O_2 solutions of different concentrations and temperatures additionally leads to different surface areas and surface structures. Depending on the application, these differences in surface structure and surface area should be considered during the preparation of NPG films in order to asses its impact for possible applications. HV electrolysis thus represents a suitable "green chemistry"-approach to produce well adaptable NPG films in a fast and efficient way.

5.3.5 TOC Text

High voltage electrolysis (100–540 V) in alkaline electrolyte can produce Au oxide films, which can be reduced to nanoporous Au in various ways. By varying the parameters of voltage, temperature, time and the amount of H_2O_2 to reduce the Au oxide, the subsequent nanoporous structure of the Au electrode can be tailored. The choice of the individual high voltage electrolysis and reduction parameters has a sensitive influence on the final surface structure of the Au electrode.

5.3.6 Appendix

5.3.6.1 S1: XPS Spectra of the O 1s Region

Fig. 5.40 shows the O 1*s* signals recorded on a) a Au electrode covered by a Au oxide film obtained by high voltage (HV) electrolysis at 300 V for 290 s, as well as b) a sample with a NPG film formed after electrochemical reduction of the Au oxide. In both cases, the signal consists of two peaks. We ascribe the lower BE peak to the oxidic oxygen species and the higher BE peak to hydroxyls. On the Au oxide electrode (Fig. 5.40a) the oxide peak appears at 530.1 eV, which is typically reported for Au_2O_3 [261, 262] and the hydroxyl peak is located at 531.6 eV. For the NPG film (Fig. 5.40b) the intensity of O 1*s* is much smaller, which is expected after reducing the Au oxide. The results also agree with the different oxidation state of Au concluded from the analysis of the Au 4*f* signals. Here, the oxide peak appears at 531.2 eV and the hydroxyl peak is found at 533.0 eV. The signals significantly shift to higher BE compared to the Au oxide. The reason for this shift is currently unclear. Note that the fitted oxidic signal is rather broad compared to pure Au oxides in both cases, which is in general an indication for defects in the oxide film.[264]

5.3.6.2 S2: SEM Images of Modified Au Wire Electrodes

Fig. 5.41 shows SEM images of a) a Au oxide film on a Au wire electrode prepared by HV electrolysis at 300 V for 30 s and direct removal from the electrolyte solution, and b) a NPG film obtained by keeping the Au oxide electrode additional 60 s in the electrolysis solution after HV electrolyis.

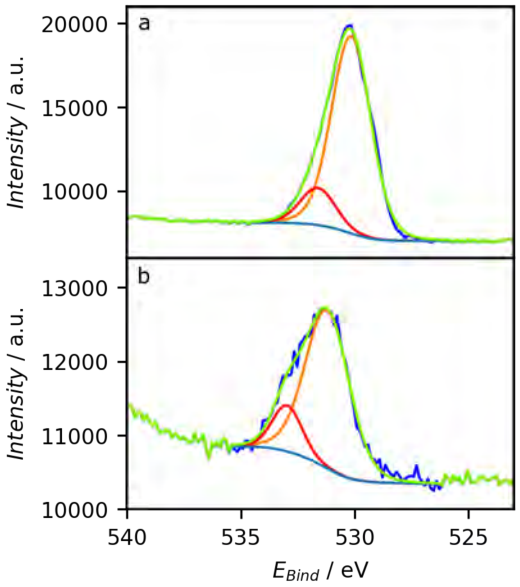

Figure 5.40: O 1*s* region of XPS spectra of a) a Au oxide film on Au obtained by HV electrolysis for 290 s at 300 V in 0.01 M KOH and b) a NPG film obtained by electrochemical reduction of the Au oxide.[169]

Images with higher magnification were shown elsewhere[66]. These also show relatively smooth surface structure with some cracks for the Au oxide electrodes and a rather nanoporous structure for the NPG electrode.

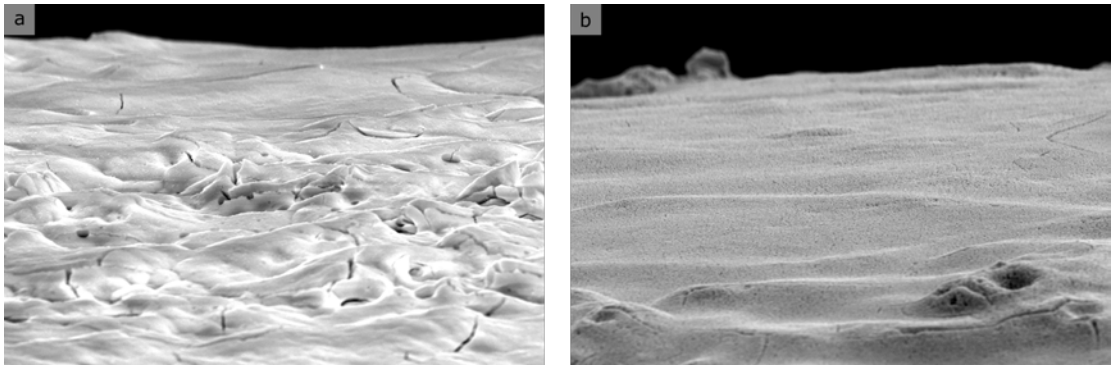

Figure 5.41: SEM images (30 µm × 20 µm) of Au wire electrodes covered with a) a Au oxide film prepared by HV electrolysis at 300 V for 30 s and b) a reduced Au oxide film which was kept in the electrolysis solution for additional 60 s.[169]

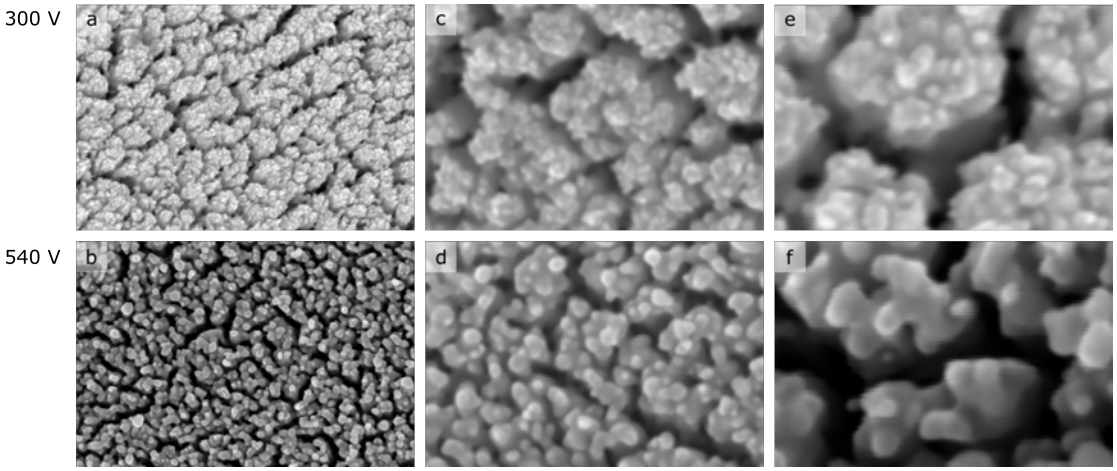

Figure 5.42: SEM images of Au electrodes after HV electrolysis and subsequent electrochemical reduction at 300 V (a), c) and e)) and 540 V (b), d) and f)). The image size in a) and b) is 1500 $\times$ 1000 nm, in c) and d) 600 $\times$ 400 nm and in e) and f) 300 $\times$ 200 nm.[169]

5.3.6.3 S3: SEM Images of NPG with High Resolution and Magnification

Fig. 5.42 shows SEM images after 30 s HV electrolysis at 300 V (upper row) and 540 V (lower row) followed by electrochemical reduction with higher resolution and magnification than those reported in the main manuscript. The magnification increases from left to right. Comparing the SEM images at both voltages shows that the NPG structures at 300 V form additional nanostructures on top of the NPG, while the nanoporous structures formed at 540 V appear to be smoother. The pore size estimated from the SEM images (Figs. 5.42e and f) is about 30 nm in both cases, whereas the ligament size is significantly larger at 300 V compared to 540 V. At 300 V the ligament size is about 140 nm, while at 540 V it is about 70 nm.

5.3.6.4 S4: RF after Reduction in 0.01 M KOH Containing H_2O_2

Table 5.1: Electrode color and RF of electrodes after 30 s at 300 V and subsequent reduction in H_2O_2-containing 0.01 M KOH solutions of various concentrations and temperatures.[169]

voltage / V	time / s	H_2O_2 concentration / %	solution temperature	Roughness factor	electrode color
300	30	0.007	24	24	darker red
300	30	0.007	40	17	darker red, parts golden
300	30	0.007	70	17	black with touch of red
300	30	0.08	24	14	black
300	30	0.8	24	24	black

5.3.6.5 S5: SEM Images of Au Oxide Films Prepared by HV Electrolysis at Different Voltages

To get an overview of the surface structures formed on a Au wire electrode after 30 s of HV electrolysis between 100 V and 540 V, Fig. 5.43 shows in the left column SEM images of Au oxide films on wire electrodes prepared by HV electrolysis at different voltages in 0.01 M KOH for 30 s (Figs. 5.43a to d), and in the right column electrodes which were kept additional 60 s in the electrolysis solution after the HV electrolysis (Fig. 5.43e to h). After both procedures, the electrodes surface structure differ from that of an as prepared Au electrode, but are similar for all voltages.

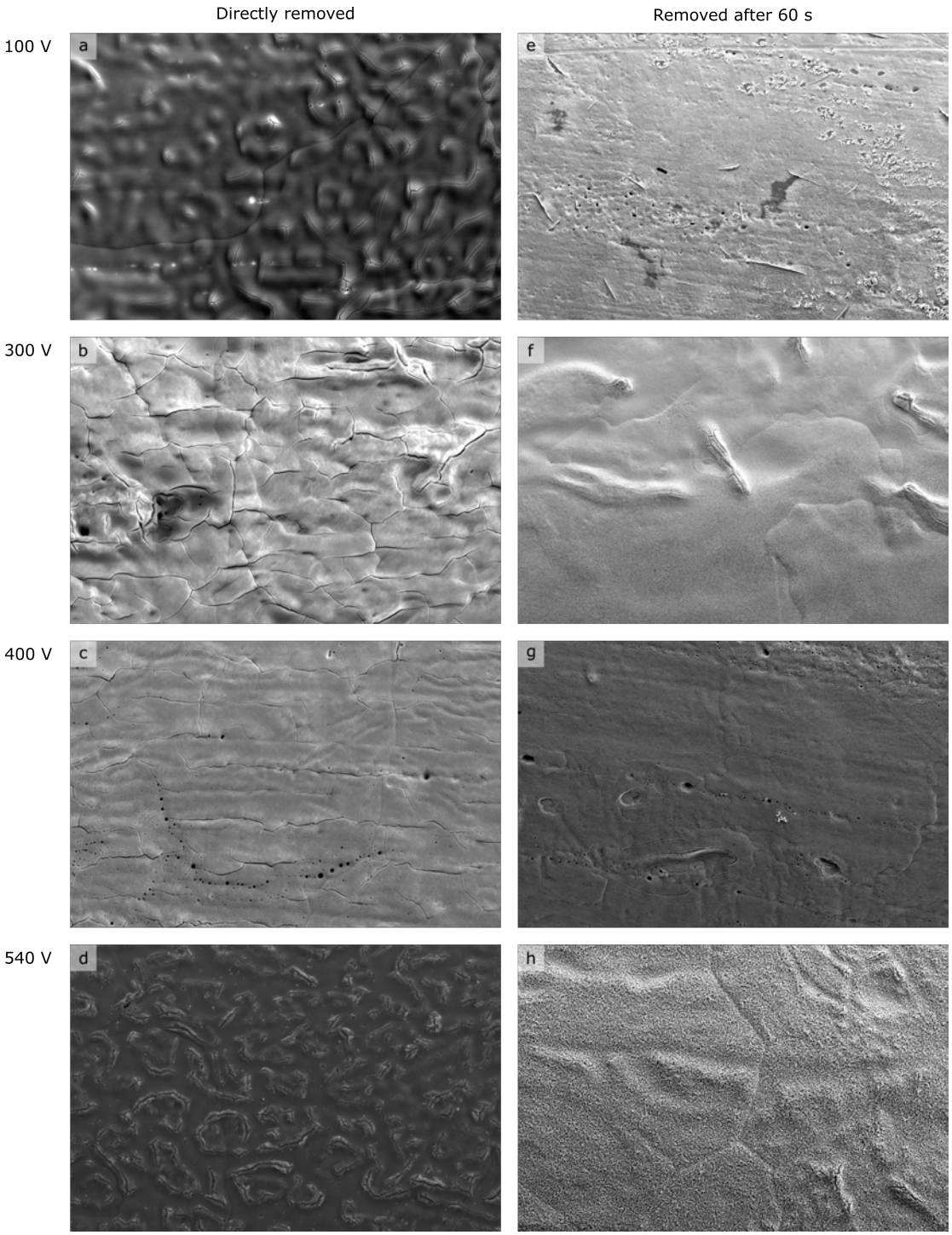

Figure 5.43: SEM images (120 µm × 80 µm) of a) to d) a Au oxide film on a Au wire electrode prepared by HV electrolysis at different voltages for 30 s and direct removal from the electrolysis solution and e) to h) of a Au oxide electrode kept for additional 60 s in the electrolysis solution after the electrolysis. The voltages are given next to the SEM images.[169]

5.3.6.6 S6: Electrolyte Temperatures before and after HV Electrolysis

Fig. 5.44 shows both the averaged current densities during HV electrolysis (10 s in 0.01 M KOH) of Au wire electrodes at different voltages (blue solid lines), and the initial electrolyte temperature (orange dashed lines), final electrolyte temperature (red dashed lines), and the temperature rise of the electrolyte during HV electrolysis (blue dashed lines). The change in electrolyte temperature was investigated for different initial electrolyte temperatures with a) 24 °C, b) 46 °C, and c) 70 °C. Note that for these measurements, the length of the Au wire in the electrolyte (10 mm) was adjusted using two Eppendorf pipette tip caps at both ends of the wire to (i) prevent melting of the Au electrode at the apex of the wire and (ii) to define the length of the wire.
The temperature rise (blue dashed curve) during the HV electrolysis correlates with the averaged current densities (blue solid curve). The higher the initial electrolyte temperatures (46.3 °C or 70.0 °C), the temperature rise of the electrolyte caused by HV electrolysis becomes much smaller. At 70 °C initial electrolyte temperature, the temperature does not increase significantly during the electrolysis (Fig. 5.44c).

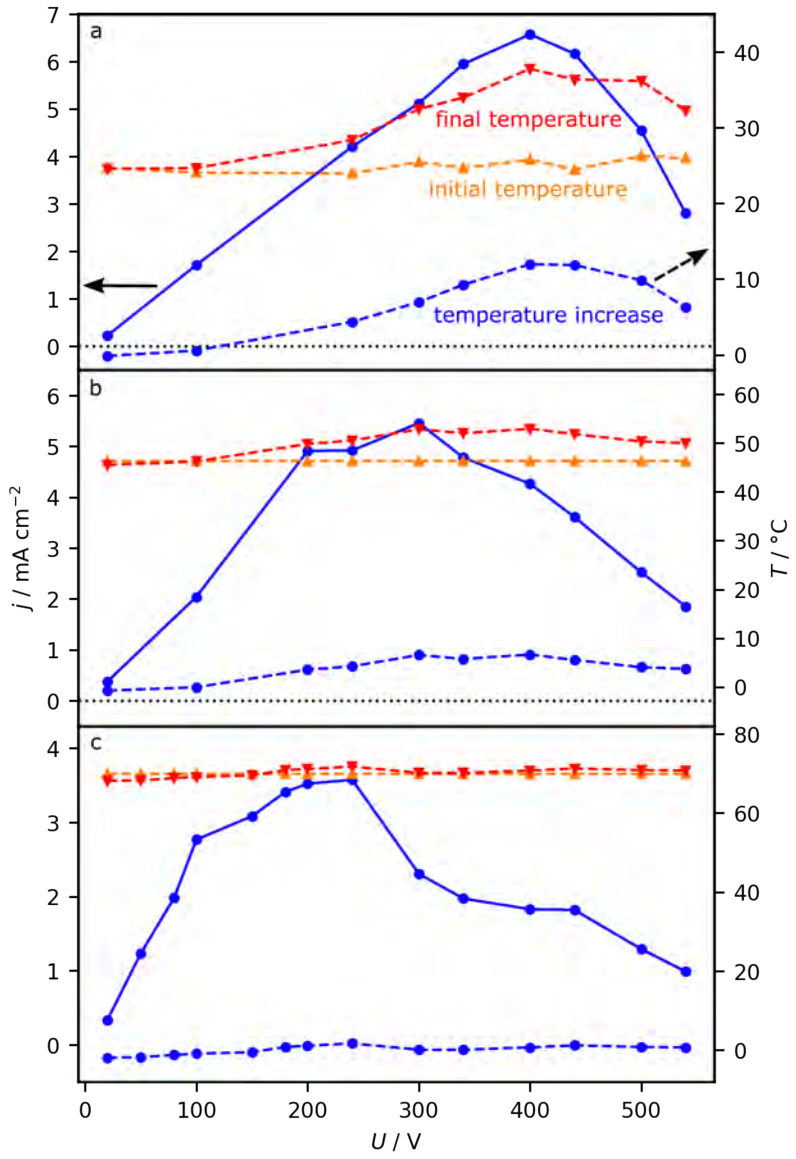

Figure 5.44: Current density (solid line) and temperature before (dashed orange) and after (dashed red) as well as the temperature rise of the electrolyte (dashed blue) before, and after HV electrolysis of a Au wire electrode for 10 s at different voltages in 0.01 M KOH.[169]

5.3.6.7 S7: Au CV in KOH

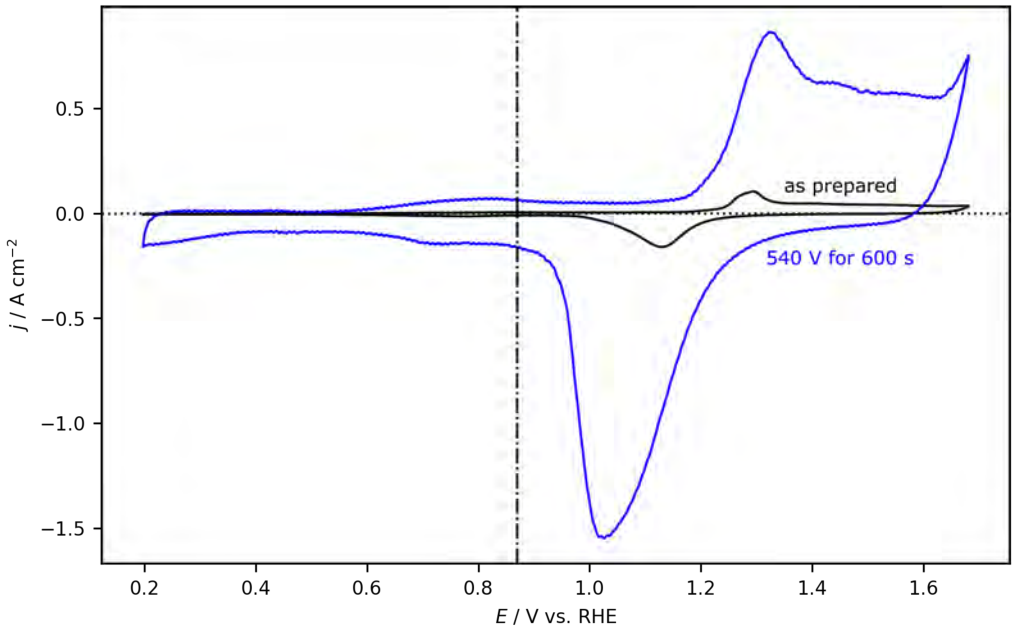

Figure 5.45: Cyclic voltammogram (CV) recorded on an as prepared Au wire (black), as well as a CV of a NPG electrode prepared by HV electrolysis at 540 V for 600 s in 0.01 M KOH and subsequent electrochemical reduction (blue) in 0.01 M KOH. The CVs were recorded at 50 mV s^{-1} in 0.01 M KOH. The roughness factor was determined at a potential of 0.87 V indicated by the dashed dotted line.[169]

5.4 Facet-Dependent Formation and Adhesion of Au Oxide and Nanoporous Au on Poly-Oriented Au Single Crystals

In this Section (5.4) results published on a preprint server[265] on structural changes of Au POSCs as a function of crystallographic orientation under HV electrolytic conditions are shown. Reprinted from ChemRxiv, doi: 10.26434/chemrxiv-2023-nf7v3, E. Artmann *et al.*, "Facet-Dependent Formation and Adhesion of Au Oxide and Nanoporous Au on Poly-Oriented Au Single Crystals", "CC BY 4.0, https://creativecommons.org/licenses/by/4.0/".
All measurements at 540 V were performed by me, while the measurements at 300 V were performed by Tobias Schmider in his project work under my instruction. The concept of this Section, the written working paper draft, the data analysis and evaluation, the visualization of the results, as well as the preparation of all figures and the validation of the results was done by me.

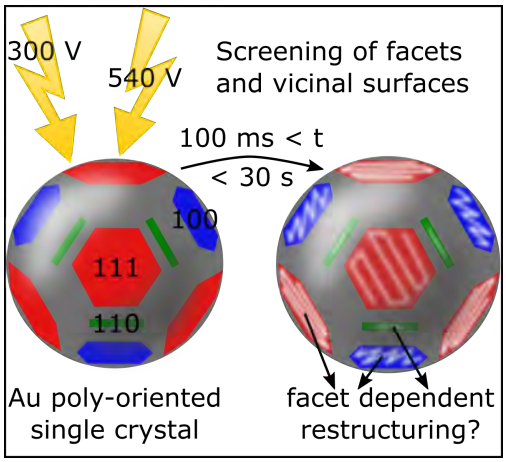

Figure 5.46: Graphical abstract of the publication with the title "Facet-Dependent Formation and Adhesion of Au Oxide and Nanoporous Au on Poly-Oriented Au Single Crystals" published on a preprint server.[265]

5.4.1 Abstract

Nanoporous Au has different properties compared to bulk Au, making it an interesting material for numerous applications. Depending on the preparation procedure, the porosity, thickness, and homogeneity of the NPG films can be tuned. To modify the structure of NPG films in a targeted manner and thus adapt them to specific applications, a fundamental understanding of the structure formation is essential. In this work, we focus on NPG prepared from Au oxide formed during high voltage electrolysis in an alkaline electrolyte on a poly-oriented Au single crystal electrode. These poly-oriented single crystals consist of a single crystalline metal bead, with faces with different crystallographic orientations. Consequently, these POSCs allow screening of the influence of the crystallographic orientation on the structure formation of the Au oxide formed during high voltage electrolysis and the NPG film formed via electrochemical reduction of the Au oxide for different facets in a single experiment. The high voltage electrolysis is performed at current densities between 2.70 and 3.76 A·cm^{-2} (300 V) and between 0.24 and 6.39 A·cm^{-2} (540 V) with electrolysis times ranging from 100 ms to 30 s. The amount of Au oxide formed is determined by electrochemical measurements and the structural properties are investigated by scanning electron microscopy and optical microscopy. We show that the Au oxide formation is mostly independent of the crystallographic orientation except for thick Au oxide layers. In turn, the macroscopic structure of the NPG films depend on the experimental parameters, the thickness of the Au oxide precursor thickness, and the crystallographic orientation of the substrate. Possible reasons for the frequently observed exfoliation of the NPG films are discussed.

5.4.2 Introduction

Nanoporous Au (NPG) has a porous, sponge-like structure whose pores are connected by Au ligaments.[47, 49] The sponge-like structure often shows different properties compared to the bulk material. Possible applications for NPG films are in the fields of (bio)sensing,[45, 49–51, 152, 245] (electro)catalysis,[45, 46, 148, 149, 151, 248, 249] or in heterogeneous catalysis.[44, 50, 155, 247]
Typically, NPG films are prepared by chemical dealloying, mostly of a Ag-Au alloy. In this process, the less noble metal is dissolved, *e.g.*, Ag, by using a HNO_3

solution.[50, 149, 151, 153, 154] Alternatively, the dealloying process can also be induced electrochemically.[152] A disadvantage of these dealloying processes is that Ag residues can remain in the resulting NPG film. Such trace impurities can play a significant role for example in catalytic processes.[50, 167, 168] Recently it has been shown that NPG films can also be prepared by anodization (Au oxide formation at a Au anode set to a potential of a few volts versus a fixed reference with current densities of approximately 0.035 $A \cdot cm^{-2}$) and subsequent electrochemical reduction.[99, 109] Similarly, recently we have shown that NPG films can be produced by (electro)chemically reducing Au oxide films formed during high voltage (HV) electrolysis and anodic contact glow discharge electrolysis (aCGDE). The latter phenomenon refers to a plasma that forms in a gas sheath around the working electrode at high voltages.[17, 18, 87] In both cases, the voltages can reach several hundreds of volts and the current densities are in the range of 1 to 10 $A \cdot cm^{-2}$.[66, 81, 169] Advantages of this high voltage (current density) approach are that the preparation times are significantly shorter and only an (alkaline) electrolyte is required.[169] Furthermore, we demonstrated that the final structure of the NPG film depends on the method used to reduce the Au oxide, *i.e.*, electrochemically or in the presence of H_2O_2.[169] For long electrolysis times, it is even possible to form a NPG film *in-situ* in a single step.[169]

To further tune the formation of the NPG film, it is beneficial to understand both the growth and the interaction of the Au oxide films as well as the NPG films with the Au substrate. Within that context, Henkelmann *et al.* studied, for example, the densification/detachment of NPG films from Au substrates and found that the substrate's curvature and, thus, the surface morphology of the Au substrate plays an important role.[166] Khristosov *et al.* demonstrated that NPG single crystals can be grown on a SiO_2 substrate up to a size of several hundred micrometers.[266] For this purpose, a eutectic melt of Au and Ge is first prepared, which is then solidified. The Ge is subsequently removed by wet etching, NPG single crystals remain.[266]

In this work, we study the influence of the crystallographic orientation of the substrate on the formation of the Au oxide during HV electrolysis and the structure of the NPG film formed by electrochemical reduction. Such aspects can be investigated by using oriented single-crystal electrodes, an approach widely used in surface science and electrochemistry. For example, the facet-dependent oxide formation has been studied on noble metals such as Pt,[267] Au,[268] and on non-noble metals

such as Al,[269, 270] Ni,[271] Fe,[272] or Cu[218, 273]. Conway and Jerkiewicz, for example, found that oxide formation occurs at different rates on the Pt(111) and the Pt(100) facets.[267] Vvedenskii *et al.* studied the influence of different Cu low-indexed crystallographic orientations regarding the Cu(I) and Cu(II) oxide formation.[218] Scholten *et al.* were able to show that O_2 plasma pre-treatment leads to the formation of CuO on the Cu(111) surface, while on Cu(100) primarily Cu_2O is formed after the same experimental procedure. Also, the surface morphology in both cases differed significantly.[273] The different structures obtained on the different facets during the pre-treatment can have a significant impact on the catalytic activity.[53] A caveat of using such oriented single crystals is that several differently oriented single crystals are required, to study the facet-dependent properties, which is a rather time-consuming task. In recent years, poly-oriented single crystals (POSCs) have been exploited to screen processes occurring at facets with different crystallographic orientations in a single experiment.[139, 274, 275] Such POSCs are created by melting the end of a metal wire, which leads to the formation of a liquid bead. This bead is then slowly cooled in a controlled atmosphere, resulting in a single crystal with facets exhibiting different crystallographic orientations.[196, 197, 201, 276–279] Note that the distribution and size of these facets can vary depending on the metal used in the process and the size of the POSC.[196] These electrodes were used to determine the facet-dependent restructuring of Pt electrodes during oxidation and reduction cylces[275] or cathodic corrosion of Au and Pt.[139, 274]
In this work, we study the growth of Au oxide on Au POSCs, prepared by HV electrolysis at a voltage close to the breakdown voltage (300 V / current density between 2.70 and 3.76 A·cm^{-2}) and in the region of aCGDE (540 V / current density between 0.24 and 6.39 A·cm^{-2}) for different electrolysis times (a few 100 ms up to 30 s) in 0.01 M KOH. The amount of Au oxide is inferred from the electrochemical reduction of the Au oxide film. In the second step, the Au oxide film is reduced electrochemically to form a NPG film on the Au POSC. The structural properties of the resulting Au oxides and the NPG films are investigated by optical microscopy and scanning electron microscopy (SEM). Aside from the overall structure of the entire POSC, we focus on the low-index regions, *i.e.*, Au(111) and Au(100), and the regions vicinal to those surfaces, which consist of extended Au(111) and Au(100) terraces.

5.4.3 Results and Discussion

Each measurement in this work was performed on a freshly-prepared Au POSC, shown in an SEM image in Fig. 5.47a. A detailed description of the preparation procedure, verification of the quality, and the size of the crystals can be found in the experimental section. From Laue X-ray diffraction (XRD) measurements, we determined the position of the low-index facets, *i.e.*, Au(111), Au(110), and Au(100). Typical Laue XRD patterns of all three low-index facets of a Au POSC can be found in the SI (Section 5.4.6.1). Once these regions were characterized, the Au(111) and the Au(100) facets can also be discerned by visual inspection of the POSC. Other facets, such as the Au(110), can then be inferred from their relative position to the other low-index facets. A magnification of the Au(111) and Au(100) facets is shown in the SEM images in Figs. 5.47b and d. The images in Figs. 5.47c and e show the region vicinal to the Au(111) and the Au(100) facets, which are referred to as Au(111*) and Au(100*) regions throughout this work. These regions have a significant amount of steps. We suggest that the crystallographic orientation in these regions is, however, predominately that of the adjacent low-index facet.

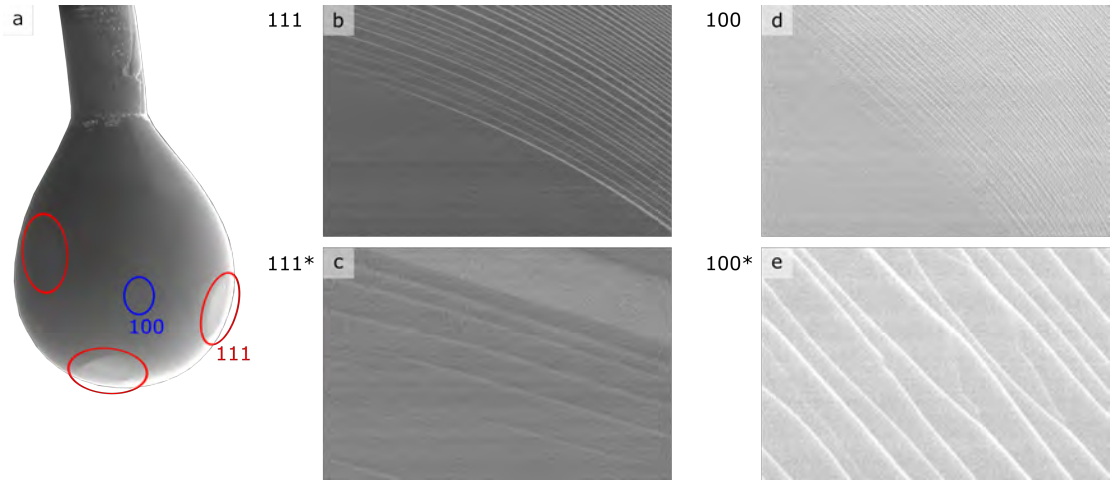

Figure 5.47: a) SEM image of an as-prepared Au POSC, and SEM images of b) the Au(111) facet, c) the surface vicinal to the Au(111) facet (Au(111*)), d) the Au(100) facet and e) the surface vicinal to the Au(100) facet (Au(100*)), respectively. The size of the POSC in a) can be estimated from the diameter of the wire, which is 1 mm. The image size in b) is 150 µm $\times$ 100 µm, in d) 30 µm $\times$ 20 µm and in c) and e) 3 µm $\times$ 2 µm.[265]

5.4.3.1 Au Oxide Film Formation

During HV electrolysis, a Au oxide film forms on the Au POSCs. This Au oxide film acts as a precursor for the formation of a NPG film via electrochemical reduction discussed below. We study the Au oxide growth at 300 V (before the breakdown of NE – average current density between 2.70 and 3.76 A·cm^{-2}) and at 540 V (in the aCGDE region – average current density between 0.24 and 6.39 A·cm^{-2}) for different electrolysis times.[66, 169] Note, for the Au oxide formation, the current density is a more meaningful parameter since the applied voltage strongly depends on the electrodes' geometry, electrodes position, and the cell geometry.[81] Nevertheless, in this article we use the voltages to discern between the NE and aCGDE region. During the Au oxide growth at 300 V, vivid bubble formation is observed, and hence the electrode is only partially in contact with the electrolyte. The current is slightly increasing with increasing electrolysis time (see the red curve in Fig. 5.59). This is related to an increase in electrolyte temperature, which increases the electrolytes' conductivity. At 540 V the electrode is surrounded by a gas sheath in which a plasma can be ignited.[66, 169] During HV electrolysis at 540 V the current is high and almost constant for short times until it breaks down to a lower constant value (see blue curve in Fig. 5.59). This marks the point when a plasma is formed within the gas sheath. Note that for short electrolysis times, the plasma is not always perfectly discernable by the naked eye.

In general, the amount of Au oxide formed can be determined from the charge which passed during the electrochemical reduction of the Au oxide.[268] The experiment is performed in an electrochemical cell in 0.01 M KOH. The electrode potential is decreased starting from 1.1 V_{RHE} (vs. the reversible hydrogen electrode) with a scan rate of 50 mV s^{-1} and kept at 0.25 V_{RHE} until the measured current was negligible. A more detailed description can be found in the Experimental Section and elsewhere.[66, 169] Figure 5.48 shows the evolution of the charge density during electrochemical reduction of the Au oxide formed on the Au POSCs for different HV electrolysis times at 300 V (red curve) and 540 V (blue curve). In both cases, the charge density increases in a linear way with increasing electrolysis time, indicating that the Au oxide film thickness increases with increasing electrolysis time up to 30 s. Note that POSCs modified with the same HV electrolysis treatment but with different bead sizes will show similar charge densities upon electrochemical

reduction, although the size distribution of the facets on the crystal may change with the size of the bead. For short electrolysis times, the Au oxide film thickness is similar for electrodes prepared by HV electrolysis at 540 V and 300 V. For long electrolysis times, the Au oxide films are thicker at 300 V than at 540 V. This can be rationalized by the difference in current density for different times and applied voltages. The current density at 540 V is higher for short electrolysis times and lower for long electrolysis times. Moreover, the charge densities obtained after 30 s HV electrolysis are very similar to those reported previously for wire electrodes.[66]

Following we discuss the structural properties of the Au oxide films grown during HV electrolysis at both voltages and different electrolysis times, starting with electrodes prepared at 540 V.

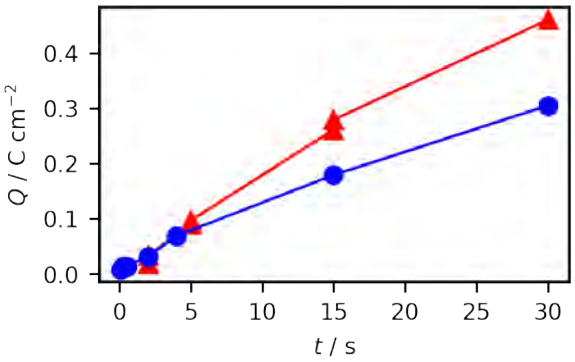

Figure 5.48: Charge densities inferred from electrochemical reduction of Au oxide formed after different HV electrolysis times on Au POSCs at 300 V between 2 s and 30 s (red) and 540 V between 100 ms and 30 s (blue) in 0.01 M KOH.[265]

Au Oxide Formation during aCGDE

Optical microscope and SEM images of Au POSCs taken after HV electrolysis at 250 ms, 2 s, and 30 s at 540 V are shown in Fig. 5.49. Additional optical microscope images for other electrolysis times can be found in the SI in Section 5.4.6.3. After 30 s the Au POSC is red, clearly indicating Au oxide formation.[66, 99, 109, 169] For shorter electrolysis times, the red color is not as clearly apparent in the optical microscope images.From visual inspection, the red color is clearly apparent for electrolysis times longer than 2 s.The electrochemical characterization above (see Fig. 5.48) suggests that Au oxide also forms at shorter electrolysis times. Thus, the Au oxide films at electrolysis times shorter than two seconds are presumably too thin to be apparent by the red color by the naked eye. More detailed insights on the

structural properties and the integrity of the Au oxide films are visualized by SEM images of the entire POSCs after all electrolysis times in Fig. 5.61. A magnification of the Au(111*) and Au(100*) regions can also be found in Fig. 5.61.

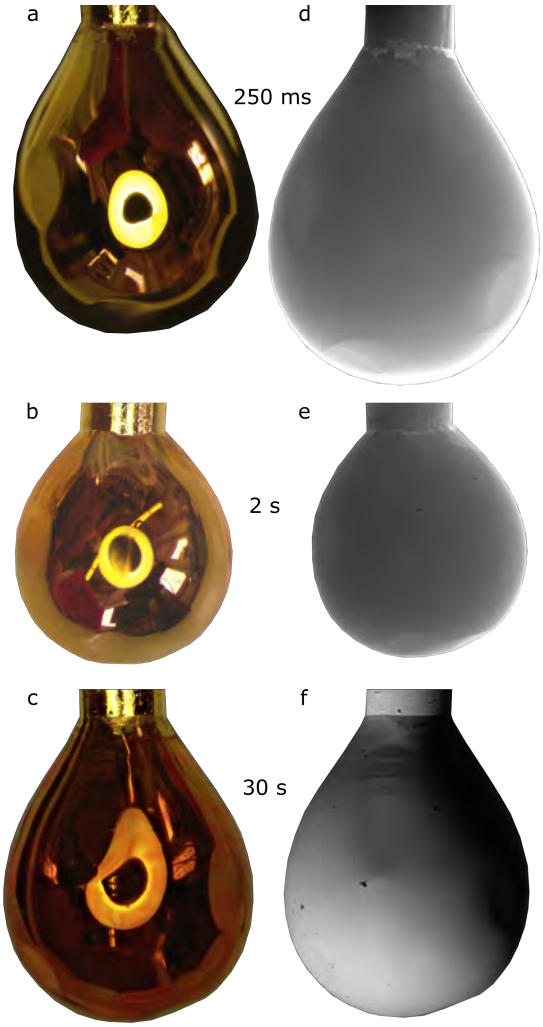

Figure 5.49: Optical microscope and SEM images of Au POSCs after HV electrolysis for 250 ms, 2 s and 30 s at 540 V in 0.01 M KOH. Optical microscope images after additional electrolysis times after HV electrolysis at 540 V can be found in Fig. 5.60 and SEM images of the whole POSCs, as well as magnifications of the Au(111*) and Au(100*) facets after the same conditions can be found in Fig. 5.61. The size of the beads can be estimated from the wire diameter, which is 1 mm.[265]

From the SEM images of the entire Au POSC no apparent structural changes were observed, indicating that the Au oxide film grows homogeneous on the entire surface independent from the crystallographic orientation or the electrolysis time (up

to 30 s). From a closer look at both the Au(111*) and the Au(100*) (see Figs. 5.61h and o), no clear structural changes of the surface are observed after HV electrolysis for 100 ms at 540 V. After 250 ms, in some of the images of the Au(111*) region, minor changes in the form of elongated ripples at the step edges, are observed (marked by arrows in Fig. 5.61i). These features could be considered to be an artifact. Further below, we will indeed show that these features play a role in the NPG film formation. After 500 ms, a slight roughening of the Au(111*) surface is apparent (indicated by an arrow). The Au(100*) surface seems to change to a smaller extent compared to the Au(111*) surface (see Figs. 5.61j and q). On Au(100*), hardly any changes can be seen up to a HV electrolysis time of 500 ms. A distinct roughening of the surface can be seen after 2 s and longer electrolysis times (up to 30 s) on the Au(111*) and Au(100*) facets (see Figs. 5.61k-n and Figs. 5.61r-u). The morphology of the Au oxide and the degree of roughening for the different facets observed in the SEM images are hereby similar for all electrolysis times considered.

Au Oxide Formation during NE

From visual inspection and optical microscope images of Au POSCs after HV electrolysis at 300 V, the distinct red color for the formation of a Au oxide is visible after 2 s and becomes more clear after 15 s (see Figs. 5.63a and b and Fig. 5.62). Here, also additional electrochemical measurements clearly indicate Au oxide formation for all electrolysis times (see Fig. 5.48 red curve). SEM images of the resulting electrodes are shown in Fig. 5.63c and d. Additional SEM images of the whole Au POSCs at all electrolysis times studied at 300 V, including a magnification of the Au(111*) region are shown in the SI in Fig. 5.63.

Up to 15 s the SEM images of the entire Au POSC in Fig. 5.63 do not suggest any kind of restructuring of the Au oxide. A closer inspection of, for example, the Au(111*) facet shows a slightly roughened surface in the range from 2 s to 15 s. The surface structures look similar to those observed at 540 V (compare Figs. 5.63e to g and Figs. 5.61k to m). After 30 s the formation of cracks within the Au oxide film is observed (see Fig. 5.63 or Figs. 5.51a and b).

Comparing the SEM images of the Au oxide taken on different regions of the POSC after 30 s HV electrolysis at 300 V in Figs. 5.51a to d, we observe distinctly different structural properties. First, it seems that the Au oxide film does not form a uniform film on smooth surfaces, namely the Au(111) and the Au(100) facets (Figs. 5.51a

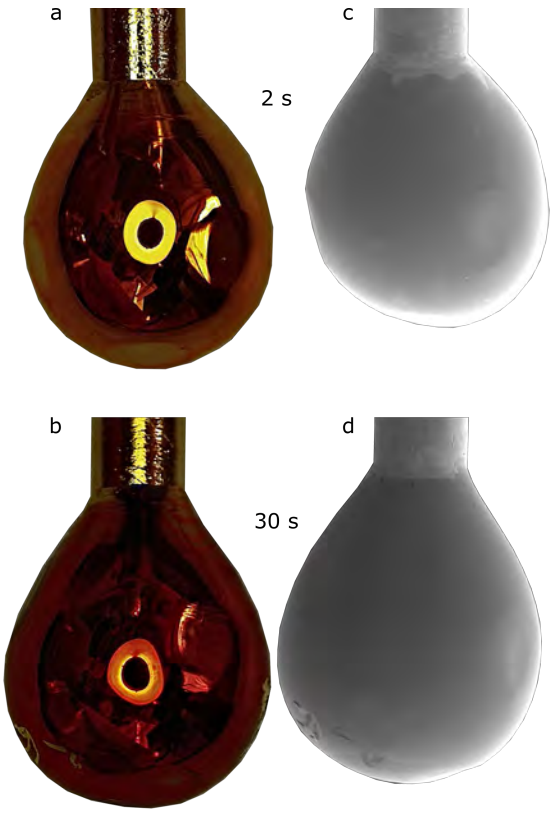

Figure 5.50: Optical microscope (left column) and SEM images (right column) of Au POSCs after HV electrolysis at 300 V for 2 s in a) and c) and 30 s in b) and d). More microscope and SEM images after other electrolysis times at 300 V can be found in Section 5.4.6.5 and 5.4.6.6, respectively. Additional SEM images of the Au(111*) facet can be found in Fig. 5.63. Based on the wire diameter of the POSCs (1 mm), the size of the Au POSCs can be estimated.[265]

and c). In these regions, the Au oxide film contains many cracks and even seems to exfoliate from the surface. Interestingly, the Au oxide film also exfoliates on the Au(111*) facet (see Figs. 5.63b and d, Figs. 5.51a and b and Fig. 5.63). On the Au(100*) facet the Au oxide film is still rather smooth and does not show pronounced crack formation (Figs. 5.51c and d. The region marked with an arrow in Fig. 5.51c is magnified in Fig. 5.51d). For comparison with our previous experiments on polycrystalline (poly) Au wire electrodes, we included SEM images in Figs. 5.51e and f. These electrodes show significant restructuring and crack formation on the entire surface. Intuitively, one could assume that the cracks might be related to grain boundaries present on the polycrystalline samples. In order to elucidate the impact of grain boundaries, we investigated the Au oxide growth on different POSCs con-

taining one or more grain boundaries (see Fig. 5.52 and Fig. 5.64). Fig. 5.52 shows a region with a grain boundary after HV electrolysis at 300 V for 30 s. It is apparent that along the grain boundary merely some defects are observed. The cracks only appear on one side of the boundary. Hence the crack formation seems to depend on the adhesion to the substrate and therefore mainly on the crystallographic orientation of the underlying substrate and not the grains itself.

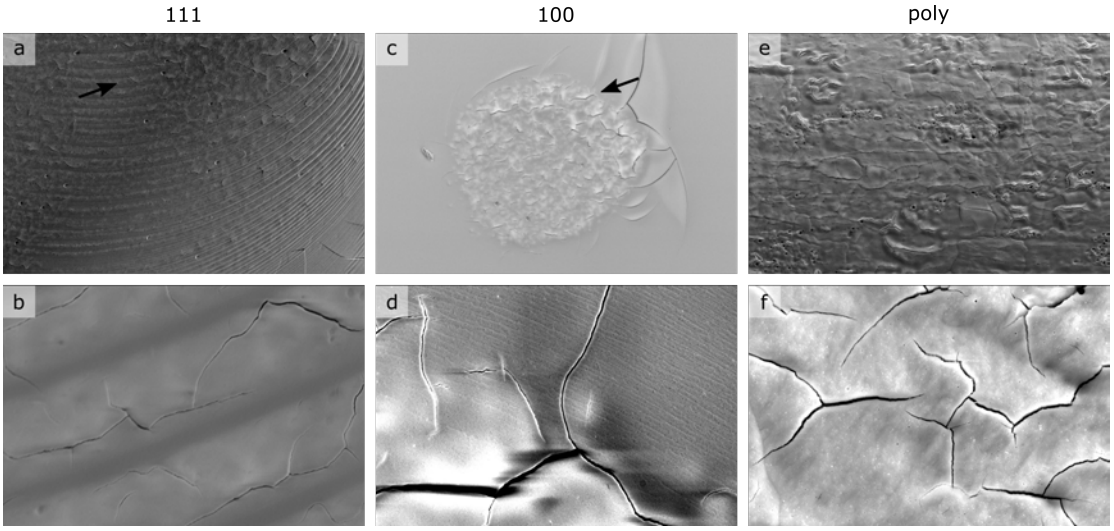

Figure 5.51: SEM images of a) and b) the Au(111), c) and d) the Au(100) facet, and e) and f) Au(poly) after HV electrolysis at 300 V for 30 s. The positions where the image magnifications in b) and d) were taken are marked with an arrow in a) and c). The size of the images in the top row are 300 µm $\times$ 200 µm and in the bottom row 30 µm $\times$ 20 µm. The contrast and brightness in a) and d) have been adjusted for better visibility.[265]

In total, for both electrolysis voltages, a homogeneous Au oxide film is formed on the entire Au POSC. Only for 30 s HV electrolysis at 300 V, the Au oxide film is less homogeneous or exfoliates from the flat Au(111) and Au(100) regions as well as in the Au(111*) region. The origin of the crack formation can at this point not be explained. Possible reasons could be the difference in Au oxide thickness obtained for long electrolysis times or the differences in processes occurring at the electrodes at both voltages (electrolysis with bubble formation or plasma). It is also possible that the thick Au oxide film formed after 30 s HV electrolysis is disrupted upon emersion of the electrode from the electrolysis solution.

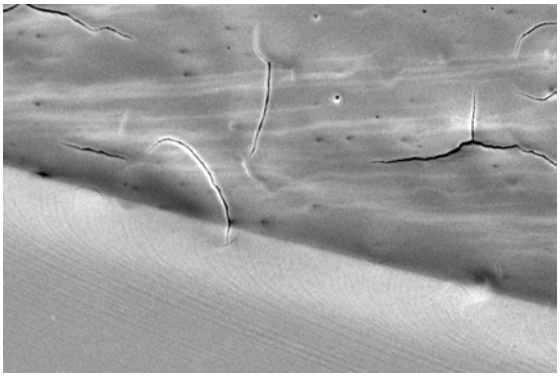

Figure 5.52: SEM image of a grain boundary adjacent to a Au(111) facet and its influence on the structure formation of Au oxide on the Au POSC after HV electrolysis for 30 s at 300 V. The image size is 30 µm $\times$ 20 µm.[265]

5.4.3.2 NPG Film Formation

NPG films were prepared by electrochemically reducing similar Au oxide electrodes to those presented in the previous section. Here, we also first focus on electrodes prepared by HV electrolysis at 540 V. Optical microscope and SEM images of electrochemically reduced Au POSCs after 250 ms, 15 s and 30 s are shown in Fig. 5.53. Additional optical microscope and SEM images for different electrolysis times are provided in Fig. 5.65. Although the Au POSCs in the optical microscope images tend to appear golden to some extent, they exhibit a black coloration, especially at electrolysis times longer than 500 ms. The black color is distinct for the formation of a NPG film.[66, 99, 109, 156, 158, 159, 169]
From the optical microscope and SEM images of the entire Au POSC in Fig. 5.53 and Fig. 5.65 it is apparent that after HV electrolysis at 540 V for 15 s (and more) and subsequent electrochemical reduction, the resulting NPG film randomly exfoliates from the surface. In some cases, exfoliation is also observed to some degree in the SEM images of the entire POSC in experiments with 2 s and 4 s electrolysis time.

For short electrolysis times (in the range of milliseconds), the optical microscope and the SEM images of the entire POSC do not show macroscopic exfoliation of the NPG film (Figs. 5.53a and d and Fig. 5.65). Small changes are, however, observed after different electrolysis times and in different regions of the Au POSC.This is illustrated with SEM images of the NPG films formed on the Au(111*) and the

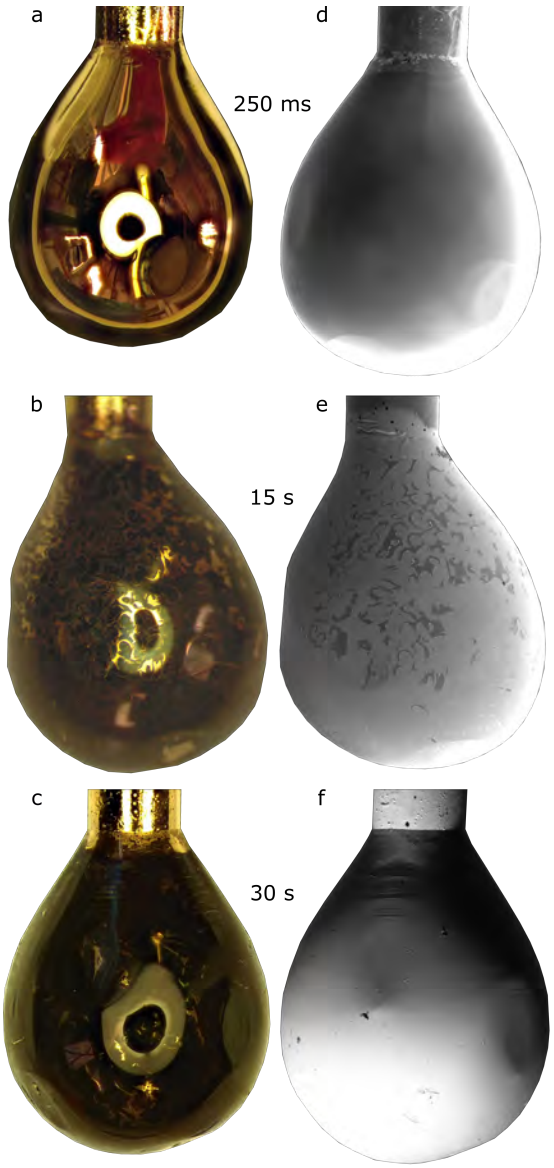

Figure 5.53: Optical microscope (a) to c)) and SEM images (d to f)) of Au POSCs after HV electrolysis at 540 V for a) and d) 250 ms, b) and e) 15 s, and c) and f) 30 s followed by electrochemical reduction of the POSCs. Optical microscope images, as well as SEM images after all studied electrolysis times at 540 V and subsequent electrochemical reduction can be found in Fig. 5.65. The size of the Au POSCs can be estimated based on the wire diameter of the POSCS which is 1 mm.[265]

Au(100*) facets after 100 ms and 250 ms in Fig. 5.66. After 100ms, the NPG film is rather homogeneous on all facets, as the Au oxide film formed after 100 ms on the POSC (see Figs. 5.61a, h, o). After 250 ms small ripples were observed in the Au

Table 5.2: Exfoliation of the NPG film formed after electrochemical reduction (✓) or intact NPG film (-) after treatment of the Au POSCs at 540 V between 100 ms and 30 s. A bracket indicates the tendency of the film in terms of its stability, but its behavior is not as clear as in the cases without brackets.[265]

	100 ms	250 ms	500 ms	2 s	4 s	15 s	30 s
111	-	-	✓	✓	(✓)	✓	✓
111*	-	-	✓	✓	(✓)	✓	✓
100	-	-	✓	-	-	(✓)	✓
100*	-	-	(✓)	-	-	(✓)	✓

oxide film grown on the Au(111*) facet in Fig. 5.61i, which are also observed in the NPG film after electrochemical reduction in Fig. 5.66c. Thus, in the regions where a homogeneous Au oxide film was observed, also a homogeneous NPG film was formed (at least for short electrolysis times up to 250 ms).

The NPG film formed on the different facets after 500 ms is shown in Fig. 5.54, where Figs. 5.54a and b show the regions vicinal to the Au(111) and Au(100) facets and Figs. 5.54c to f the flat Au(111) and Au(100) regions (low index regions). According to Fig. 5.54a the NPG film starts to exfoliate from the Au(111*) facet, while on the Au(100*) facet in Fig. 5.54b the NPG film tends to be more stable/homogeneous with a small number of defects, such as the one in the center of the image. The NPG film on the Au(111) and Au(100) facets also exfoliates strongly, as shown in Figs. 5.54c to f. Overall, on the Au(100) facet, the exfoliation is more pronounced in certain regions than others. This aspect might be due to an inhomogeneity in the local atomic structure on the (100) facets. However, such detailed atomic insights can not be inferred from SEM imaging and require further studies on oriented single crystals.

For longer electrolysis times (2 to 30 s), the NPG film formed on the Au(111) facet always exfoliates significantly (Fig. 5.67), while it is rather stable on the Au(100) facet (Fig. 5.68). On the regions vicinal to the low index facets the situation is more complex. SEM images of these regions are provided in Fig. 5.55. The observations are briefly summarized and subsequently discussed.

After 2 s the NPG film strongly exfoliates in certain measurements and regions of the Au(111*) facet from the substrate, as shown in Fig. 5.55a, indicating that the adhesion of the film to the substrate is rather weak in these regions. Figures 5.55b'

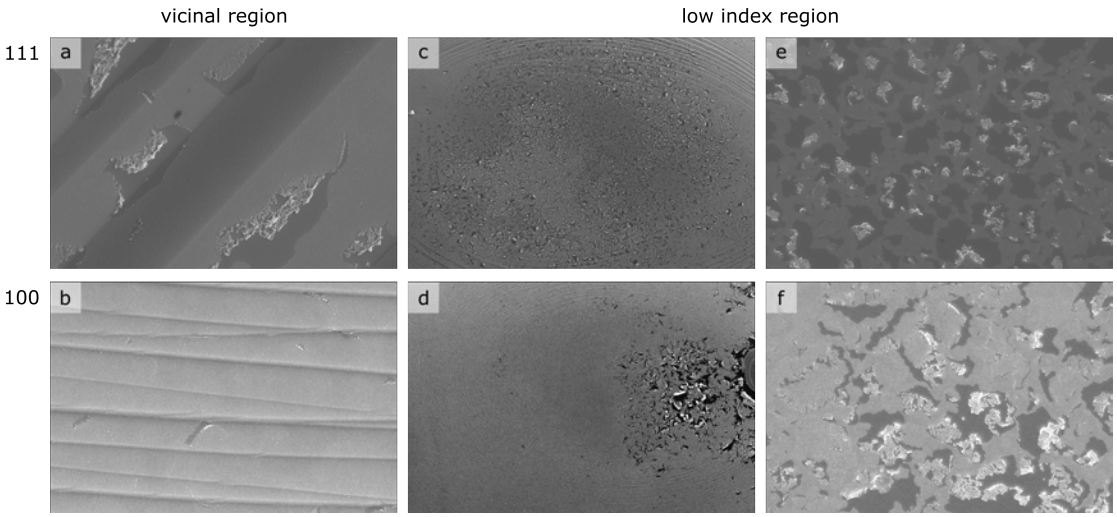

Figure 5.54: SEM image of the Au(111) and the Au(100) facet after HV electrolysis at 540 V for 500 ms and subsequent electrochemical reduction. a) and b) show the regions vicinal to the Au(111) and Au(100) facets. The image size in both cases is 9 µm $\times$ 6 µm. c) and d) show the entire facets with images sizes of 600 µm $\times$ 400 µm and 300 µm $\times$ 200 µm. The brightness and contrast were adjusted in both images. e) and f) show the same region with higher magnification (30 µm $\times$ 20 µm).[265]

and b", show a magnification of the region where the film exfoliated and a region where the film appears mostly homogeneous. (regions are marked with arrows in Fig. 5.55a). In the region where the film exfoliated (Fig. 5.55b'), the surface seems significantly restructured. In Fig. 5.55b", where the film is still more or less intact, the porosity of the NPG film is very much different on the Au(111) terraces (bright region) than in the region which connects these terraces (dark region). In the Au(100*) region in Figs. 5.55c and d, exfoliation of the film is usually not observed. However, here we also observe a difference in the NPG film structure depending on the region on the Au(100*) facet. Unlike the Au(111*) facet, the NPG film structure is not different for the Au(100) terraces and the adjacent step edges, but the NPG film breaks up randomly between them. In the brighter areas, the NPG film is less dense or seems slightly torn apart. Figure 5.55d' shows a magnification of the homogeneous NPG region in Fig. 5.55c, *i.e.*, of the region where the NPG film is rather compact. Figure 5.55d" shows a region of the NPG film that is less compact. The two regions in Figs. 5.55d' and d" are marked in Fig. 5.55c. Overall, the NPG film obtained on the Au(100*) facet is clearly more homogeneous than the one formed

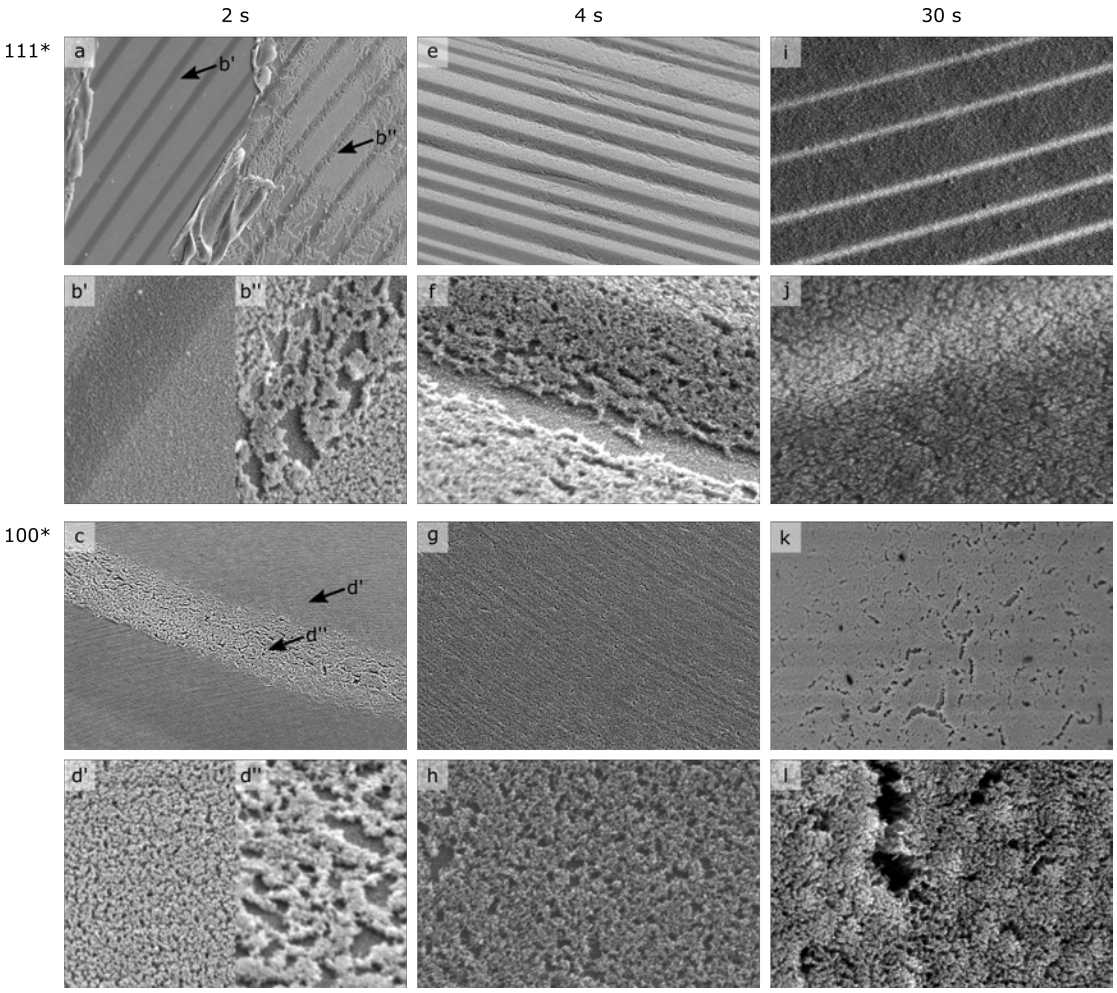

Figure 5.55: SEM images of the Au(111*) (first two rows) and the Au(100*) facet (third and fourth row) after 540 V for 2 s (a–d), 4 s (e–h) and 30 s (i–l) followed by electrochemical reduction. The images in the first and third rows have a size of 30 µm × 20 µm, and those in the second and fourth rows have a size of 3 µm × 2 µm. The contrast and brightness were adjusted in images c, g, and i.[265]

on the Au(111*) facet. As in the case of Au oxide formation, grain boundaries have no influence on the structural properties of the NPG films at 540 V as illustrated in Fig. 5.64b. The structure of the NPG film formed after 4 s on the Au(111*) facet in Figs. 5.55e and f, is very similar to that obtained after 2 s. Thus, a homogeneous NPG film forms on the Au(111) terraces, which is torn apart in the regions between these terraces apparent from Fig. 5.55f. On the Au(100*) facet in Figs. 5.55g and h, the NPG film is still homogeneous, showing similar structures on the terraces and

the regions in between. Only in a few cases, we observed that the film was slightly torn apart at the regions vicinal to the Au(100) facet, as shown in Fig. 5.69. After 15 s and 30 s, from the microscopy and SEM images (see Fig. 5.53 and Fig. 5.65), the NPG film on the Au surface is rather irregular and inhomogeneous on the entire bead. After both electrolysis times, the NPG film significantly exfoliates from the Au(111) facet as shown in Figs. 5.67b and c. Interestingly, from a closer inspection of the individual facets shown in Figs. 5.55i to l, one observes that the NPG film on the Au(111*) facet is rather homogeneous in contrast to shorter electrolysis times, where the NPG films are much thinner (according to the electrochemical data presented in Fig. 5.48). On the Au(100*) facet, the situation is different (see Figs. 5.55k and l). After 30 s, the NPG film is torn apart, though it does not exfoliate. This suggests strong interaction of the NPG film with the substrate. On the Au(100) facet, the NPG film is homogeneous, and almost no cracks were observed within the film (see Fig. 5.68).

We deduce the following from the findings for NPG film formation from electrochemically reducing Au oxides formed during HV electrolysis at 540 V and different times. First, even though the precursor Au oxide layer is homogeneous on the entire bead, it was observed that the resulting NPG film exfoliates for some of the samples from the surface. Since the Au oxide is homogeneous, we suggest that the exfoliation either occurs during the electrochemical reduction or the emersion of the electrodes from the electrolyte after the electrochemical reduction. From our experiment, we can not distinguish which experimental step is at the origin of the exfoliation process. Focusing on a region where the NPG film exfoliated in Fig. 5.55a, we observed that the underlying Au surface was rather inhomogeneous. We suggest that the inhomogeneity is due to residues or pinning points of the exfoliated NPG film. For short electrolysis times, after 500 ms, exfoliation primarily occurs in regions with Au(111) and Au(111*) orientation and to a certain extent also on the Au(100) facet, but not on the Au(100*) facet. More homogeneous NPG films are formed on the Au(111*) facet for longer electrolysis times, while it still exfoliates from the Au(111) facet. On the Au(100*) and the Au(100) facets, more homogeneous NPG films are formed. Between 2 and 30 s no exfoliation occurs on the Au(100) facet. Nonetheless, for electrolysis times longer than 15 s significant film exfoliation is observed on the entire POSC, making it difficult to assign a facet-dependent growth of the film to any region on the POSC. The reason for the exfoliation can be found in the thick-

ness of the Au oxide film formed on the Au POSC, which increases with increasing electrolysis time (see Fig 5.48). Assuming that the film thickness is identical on all facets after the HV electrolysis, we suggest that the thin NPG films tend to exfoliate more easily than thick NPG films. The observed facet-dependent exfoliation for short electrolysis times might be related to the adhesion of the NPG film in some regions and/or the lateral interaction of the NPG film. For longer electrolysis times which produce thicker Au oxide films, exfoliation becomes less pronounced due to possible stronger lateral interactions within the formed NPG film. Further experimental and theoretical investigations on single crystals with preferential orientation are required to substantiate these assumptions.

300 V 2-30 s: Next, we focus on NPG films formed by the electrochemical reduction of Au oxide films, which were formed by HV electrolysis at 300 V at different times. Optical microscope images of the resulting POSCs are shown in the first row in Fig. 5.56. After 2 s the POSC still appears golden, and the distinctive black color for a NPG film is not observed. Electrochemical measurements (Fig. 5.48 red curve), however, clearly indicate that a Au oxide film covered the surface. Hence, the film is presumably too thin to change the optical properties of the POSC surface (at least from visual inspection). Electrodes prepared by electrolysis times longer than 5 s clearly show a distinct black color. These electrodes also show already by visual inspection clearly significant exfoliation of the NPG film from the surface. For comparison, the stability of NPG films at 300 V is also shown in Table 5.3. Note that grain boundaries also do not influence the NPG formation, which is shown in Fig. 5.64d (2 s HV electrolysis at 300 V), as in the case of the Au oxide and also for the NPG film formed at 540 V. SEM images of the POSCs are also shown in Fig. 5.56. Homogeneous NPG films are observed for electrodes prepared by HV electrolysis at 300 V up to 15 s. After 30 s, the NPG film randomly exfoliates from different surface regions. A closer inspection of, for example, the Au(111*) region shows rather compact NPG structures up to electrolysis times of 15 s (Figs. 5.56c, f and i), while the NPG film after 30 s HV electrolysis is rather inhomogeneous (Fig. 5.56l). This aligns with the fact that the Au oxide film formed at 300 V and 30 s electrolysis time is not smooth (see Figs. 5.51a and b and Figs. 5.63d and h), but shows cracks and regions with exfoliated Au oxide.

From a closer inspection of the regions where the NPG film exfoliated in Fig. 5.57, we observe that the bare Au surface is no longer smooth. Compared to the NPG

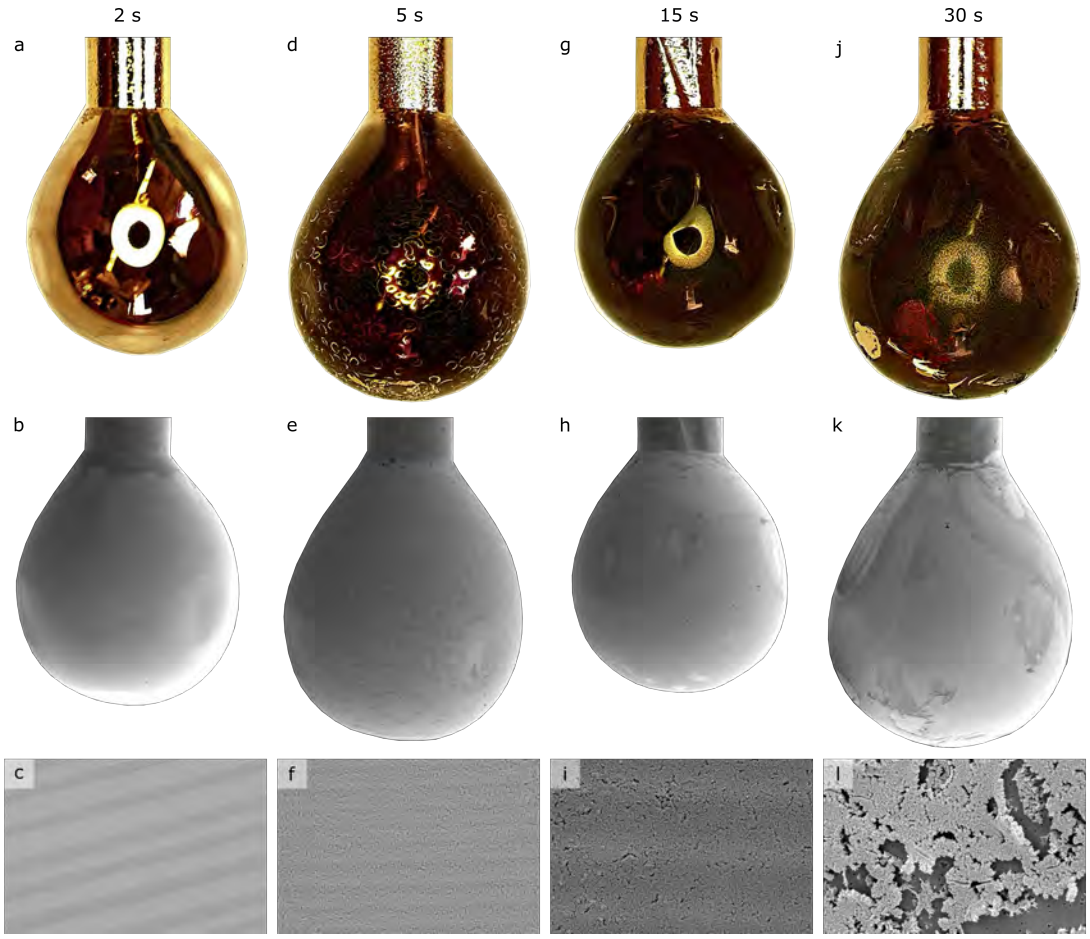

Figure 5.56: Optical microscope (first row) and SEM images (second row) of Au POSCs and the NPG film formed on Au(111*) (bottom row) after HV electrolysis at 300 V followed by electrochemical reduction. The electrolysis time was 2 s in images a to c, 5 s in images d to f, 15 s in images g to i, and 30 s in images j to l. The size of the POSCs can be estimated based on the diameter of the Au wire on which they are grown, which is 1 mm. The images in the bottom row have a size of 15 µm $\times$ 10 µm.[265]

film formed from Au oxide prepared at 540 V and 30 s where the NPG structure was randomly torn apart, we find here instead randomly distributed holes within the underlying Au substrate. More specifically, from the SEM images with higher magnification in Fig. 5.57, it is apparent that the holes on the Au(111*) facet have a triangular shape, while those on the Au(100*) facet have a square/rectangular shape.[139]. The shape of the holes is hereby directly related to the crystallographic orientation of the substrate, substantiating our assignment of the different regions

Table 5.3: Intact NPG films (-) or NPG films with exfoliated areas (✓) after HV electrolysis at 300 V for 2 to 30 s followed by electrochemical reduction. In the case of a bracket, the behavior of the NPG film in terms of stability is not entirely clear, which is why the tendency is given in brackets.[265]

	2 s	5 s	15 s	30 s
111	-	(✓)	-	✓
111*	-	(✓)	✓	✓
100	-	(✓)	(-)	✓
100*	-	(✓)	(-)	✓

to specific crystallographic orientations.

Overall, more homogeneous NPG films are formed from Au oxides prepared by HV electrolysis at 300 V compared to 540 V. Exfoliation of the Au oxide only occurs after 30 s electrolysis time at 300 V, where the Au oxide is thicker than that formed at 540 V, but is also less homogeneous. This suggests that thick Au oxide films might not adhere as well to the substrate as thin Au oxide films. Whether the Au oxide film exfoliates during the HV electrolysis or the emersion of the electrode from the electrolysis solution can not be deduced from our experiment. Why the structural properties of the Au substrate in the regions where the NPG film exfoliated are different for the preparation procedures at both voltages is currently unclear. Finally, the question remains, why NPG films formed from Au oxide films prepared by HV electrolysis at 300 V between times of 2 s to 15 s are more stable than those formed from Au oxides prepared by HV electrolysis at 540 V at the same times? Specifically, since for such short electrolysis times as at 2 s, no plasma was yet ignited around the POSC, but instead, normal electrolysis takes place according to the *j*–*t* curves in Fig. 5.59. Thus, the Au oxide film formed under these different conditions must have some distinctly different structural properties, such as adhesion to the substrate in general or lateral interactions within the NPG film.

5.4.4 Conclusion

In this work, we systematically investigated the formation of Au oxide on Au POSCs by HV electrolysis and the subsequent formation of a NPG film formed by electrochemical reduction of the Au oxide. The HV electrolysis was performed in the

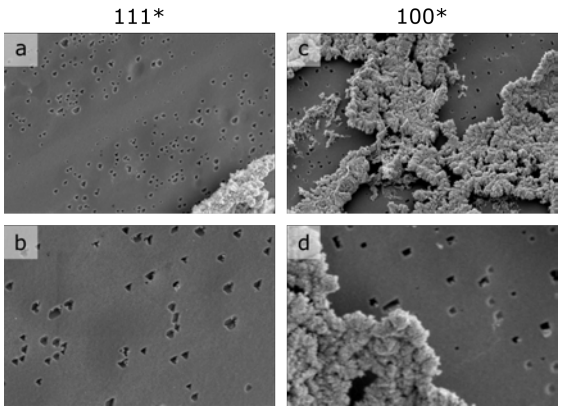

Figure 5.57: SEM images of the Au(111*) and the Au(100*) facet on a Au POSC after 30 s HV electrolysis at 300 V followed by electrochemical reduction of regions where the NPG film exfoliated. The size of the images in a) and c) is 15 µm × 10 µm and in b) and d) 6 µm × 4 µm.[265]

normal electrolysis region (at 300 V) and in the aCGDE region (at 540 V) for different times (100 ms to 30 s.) From electrochemical measurements, we infer that for both conditions the thickness of the Au oxide film increases with increasing electrolysis time, with a stronger increase for electrodes prepared at 300 V. Overall, the Au oxide films are mostly homogeneous on the POSCs for all conditions, except for HV electrolysis at 300 V for 30 s. In that case, the Au oxide shows different structures depending on the crystallographic orientation of the substrate and adhesion seems to be weakest on the low-index facets, *i.e.*, Au(111) and Au(100). Grain boundaries were found to play no role in the quality of the Au oxide or NPG films. In regions where the Au oxide film is inhomogeneous or exfoliated, also inhomogeneous or exfoliated NPG films are obtained. The NPG film formed from Au oxides prepared by HV electrolysis at 300 V is mostly homogenous on all facets up to 15 s electrolysis time. In turn, NPG films obtained from thin Au oxides prepared by HV electrolysis at 540 V tend to exfoliate even though the Au oxide film is homogeneous. This process seems to be facet-dependent and films are less stable on Au(111) or Au(111*) facets than on Au(100) or Au(100*) regions. The stability increases with increasing Au oxide thickness (longer electrolysis times). From our experiments, we cannot deduce whether the NPG film exfoliates during the electrochemical reduction of the Au oxide or during the emersion of the electrode from the electrolyte. Gaining more fundamental insights into the exfoliation process could be beneficial to either find ways to systematically exfoliate NPG from a bare Au substrate or to form stable

NPG films on a bare Au substrate.

5.4.5 TOC Text

The adhesion of Au oxide and NPG films on a Au substrate was investigated at high voltages with respect to the crystallographic orientation. While the Au oxide films formed are homogeneous in most cases, the NPG films show a strong dependence on the crystallographic orientation. Both very thin and thick NPG films tend to exfoliate.

5.4.6 Appendix

5.4.6.1 S1: Laue XRD Pattern of Au POSC low-indices Facets

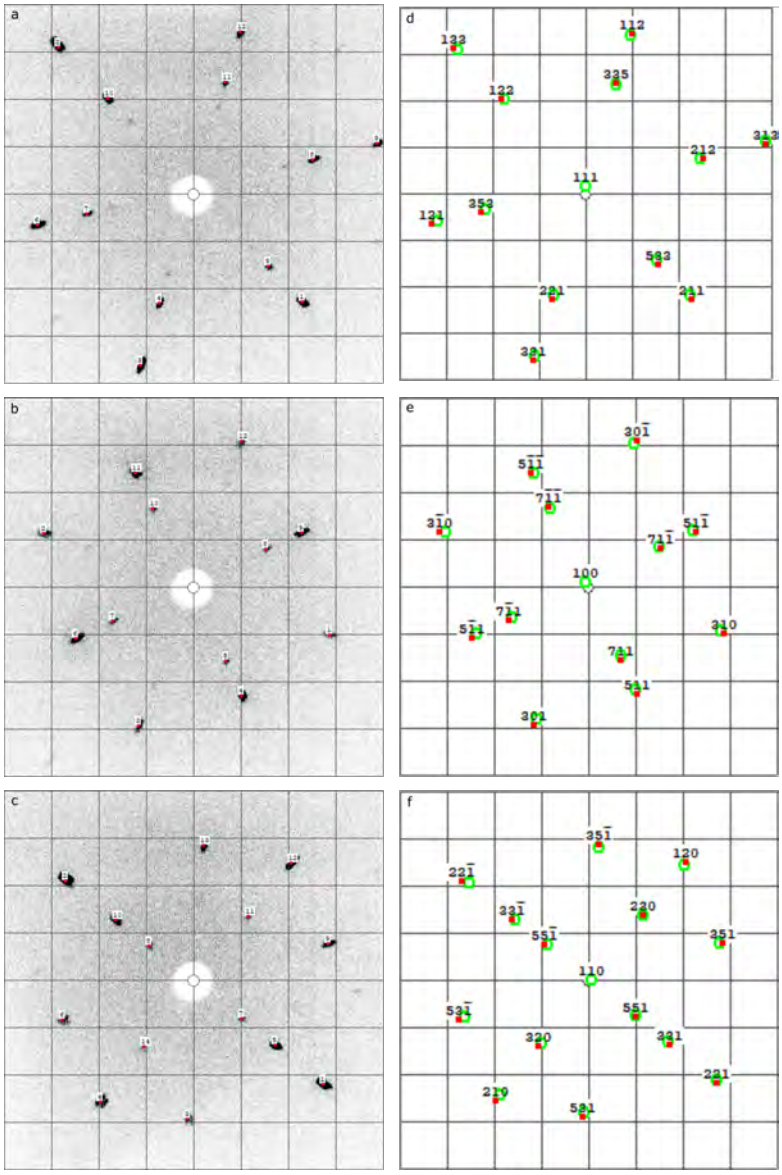

Figure 5.58: Laue XRD patterns of the a) Au(111), b) Au(100), and c) Au(110) facets of a Au POSC. d) to f) are the calculated stereographic solution for each Laue XRD measurement.[265]

5.4.6.2 S2: *j* vs. *t* Curves Recorded at 300 V and 540 V

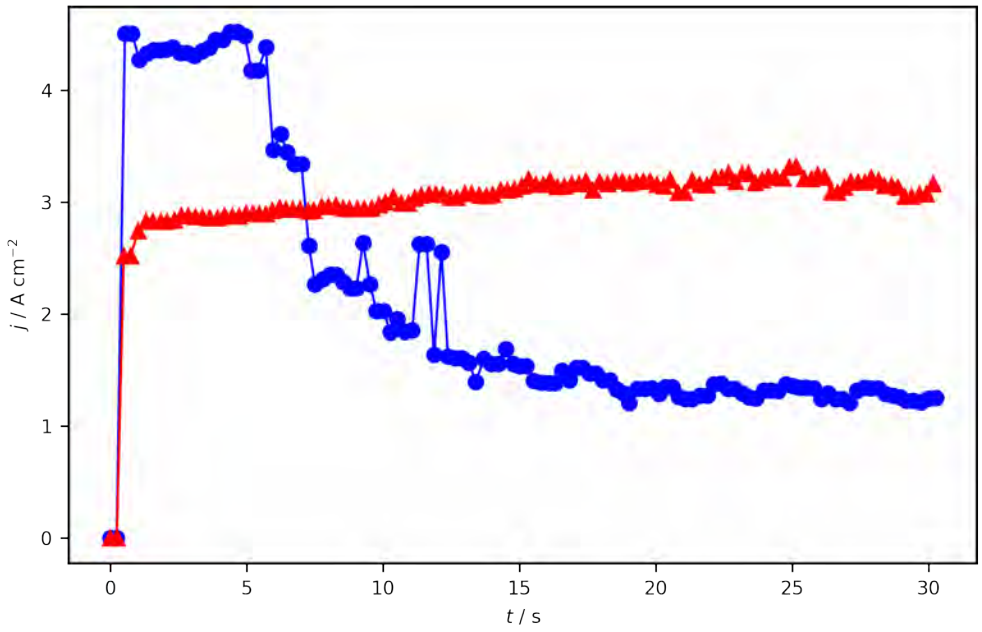

Figure 5.59: Temporal evolution of the current density during HV electrolysis at 300 V (red) or 540 V (blue) for 30 s with a Au POSC working electrode in 0.01 M KOH.[265]

5.4.6.3 S3: Optical Microscope Images of Au Oxide Formed During HV Electrolysis at 540 V

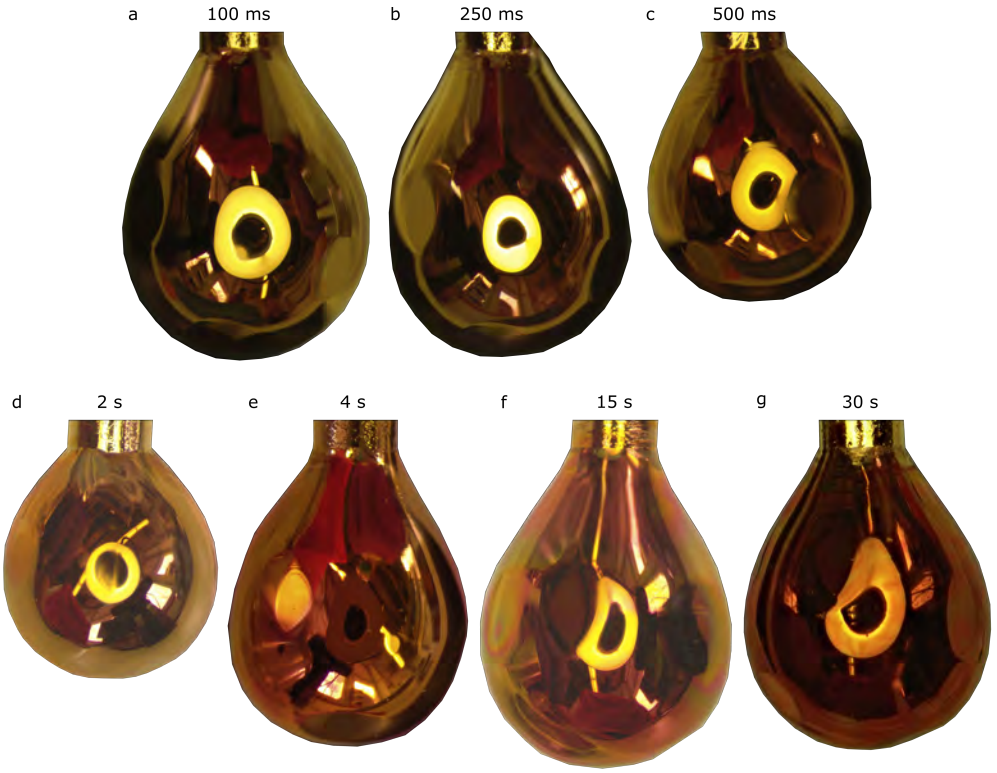

Figure 5.60: Optical microscope images of Au POSCs after HV electrolysis at 540 V between 100 ms and 30 s. The POSCs were grown on a Au wire with 1 mm diameter, from which their size can be estimated.[265]

5.4.6.4 S4: SEM Images of the Au Oxide Formed During HV Electrolysis at 540 V

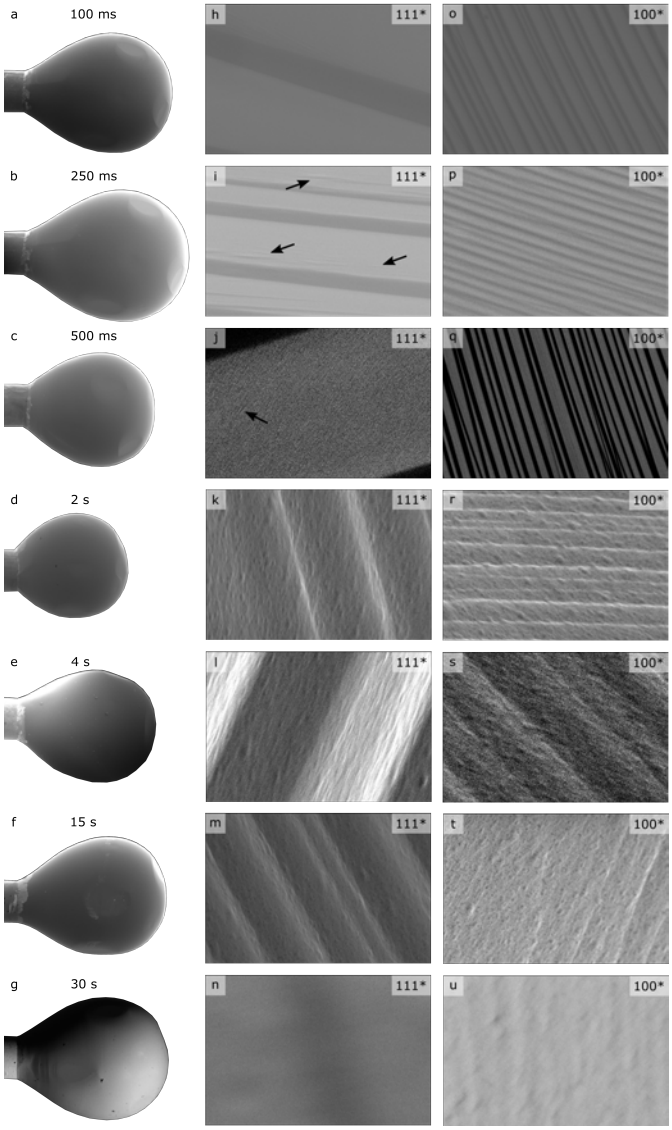

Figure 5.61: SEM images of the entire Au POSCs (left column) and a magnification of the Au(111*) (middle column) and the Au(100*) (right column) facets after 100 ms, 250 ms, 500 ms, 2 s, 4 s, 15 s and 30 s HV electrolysis at 540 V. The size of the POSCs in the left column can be estimated using the Au wire diameter on which the POSCs were grown, which is 1 mm. The image size in h)-j) and o)-q) is 9 µm $\times$ 6 µm and in k)-n) and r)-u) 3 µm $\times$ 2 µm. The brightness and contrast of the SEM images in j), q) and s) have been adjusted.[265]

5.4.6.5 S5: Oxide Formation between 2 s and 300 s after HV Electrolysis at 300 V

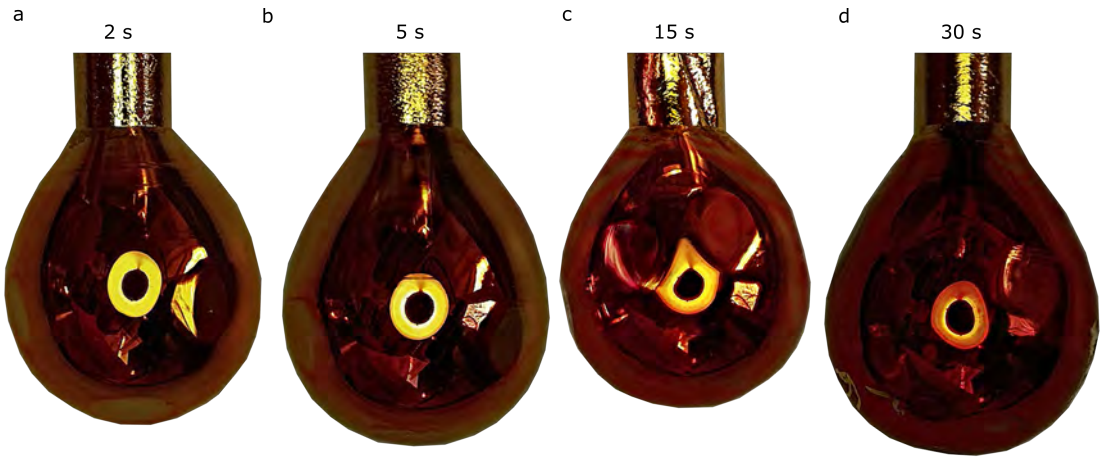

Figure 5.62: Optical microscope images of Au POSCs after HV electrolysis for 2 s to 30 s at 300 V. The size of the beads can be estimated from the diameter of the Au wire on which they are grown, which is 1 mm.[265]

5.4.6.6 S6: SEM Images of Au Oxide Formation During HV Electrolysis at 300 V

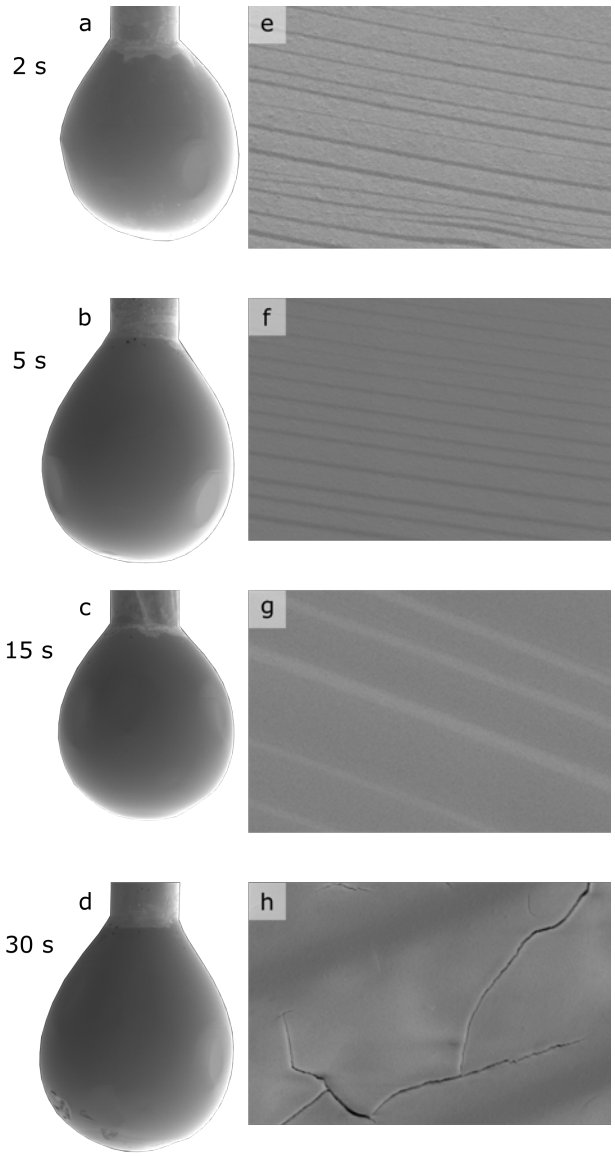

Figure 5.63: SEM images of a)-d) the entire Au POSCs with an oxide layer after HV electrolysis at 300 V and e)-h) magnifications of the Au(111*) facet. The electrolysis time was 2 s in a) and e), 5 s in b) and f), 15 s in c) and g), and 30 s in d) and h). The size of the POSCs in the left column can be estimated using the diameter of the Au wire they are grown on, which is 1 mm in each case. The SEM images in e)-h) have a size of 15 µm $\times$ 10 µm.[265]

5.4.6.7 S7: Influence of Grain Boundaries on the Au Oxide and NPG Film Formation

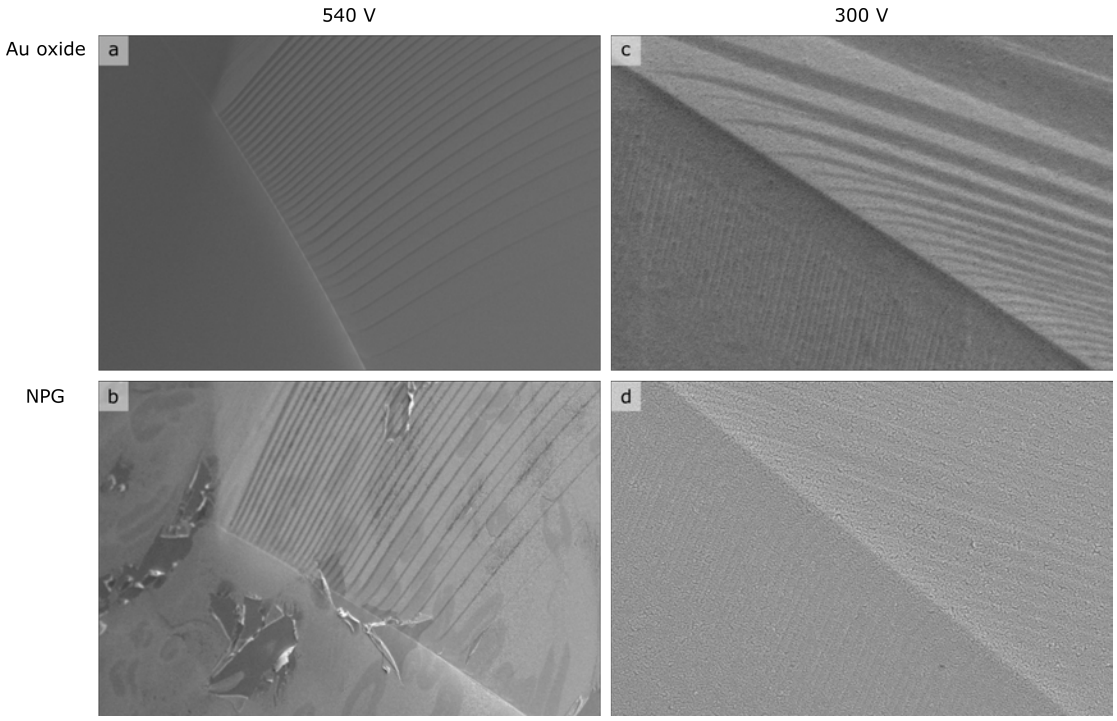

Figure 5.64: Effect of a grain boundary after 2 s HV electrolysis at a) and b) 540 V and c) and d) 300 V. The upper row shows the influence on Au oxide formation, and the lower one on the NPG film formation (being prepared by electrochemically reducing a Au oxide layer formed by HV electrolysis at b) 540 V and d) 300 V). The image size in a) and b) is 150 µm $\times$ 100 µm in c) and d) 15 µm $\times$ 10 µm.[265]

5.4.6.8 S8: Optical Microscope and SEM Images of NPG Formed by HV Electrolysis at 540 V and Subsequent Electrochemical Reduction

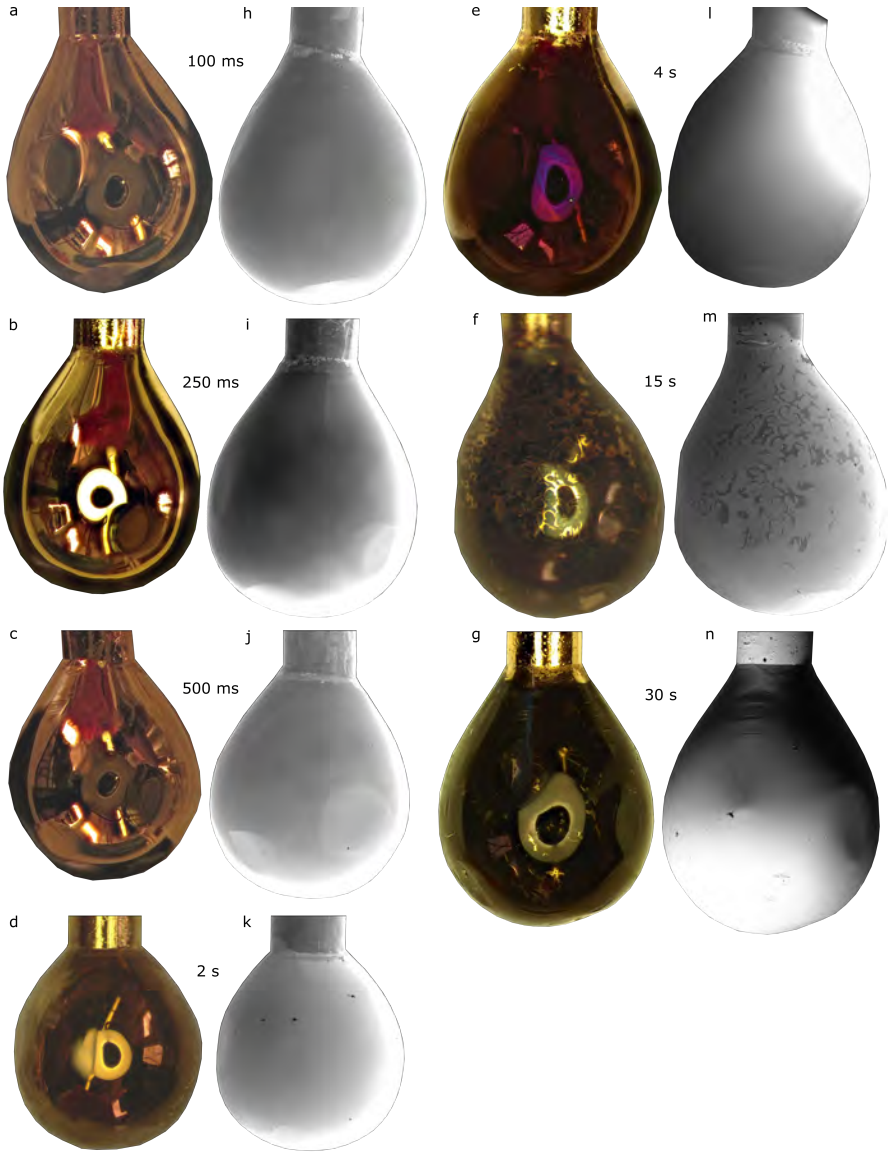

Figure 5.65: Optical microscope (left column) and SEM images (right column) of Au POSCs after the electrochemical reduction of a Au oxide layer prepared by HV electrolysis at 540 V for a) and h) 100 ms, b) and i) 250 ms, c) and j) 500 ms, d) and k) 2 s, e) and l) 4 s, f) and m) 15 s, and g) and n) 30 s. The size of the POSCs can be estimated using the diameter of the Au wire they were grown on, which is always 1 mm.[265]

5.4.6.9 S9: NPG Film Formation after HV Electrolysis at 540 V and Subsequent Electrochemical Reduction

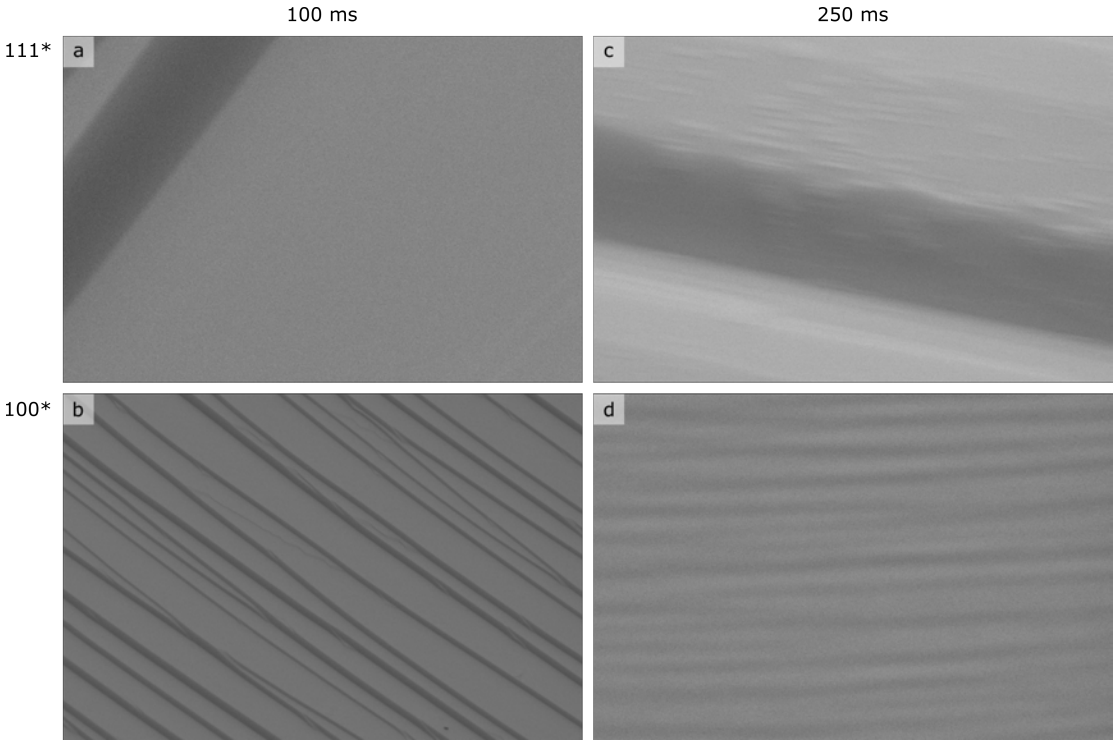

Figure 5.66: Restructuring of a Au POSC after HV electrolysis at 540 V for a) and b) 100 ms and c) and d) 250 ms and subsequent electrochemical reduction. The image size of all images is 9 µm $\times$ 6 µm.[265]

5.4.6.10 S10: Exfoliation of NPG From a Au(111) Facet, Formed From HV Electrolysis at 540 V and Subsequent Electrochemical Reduction

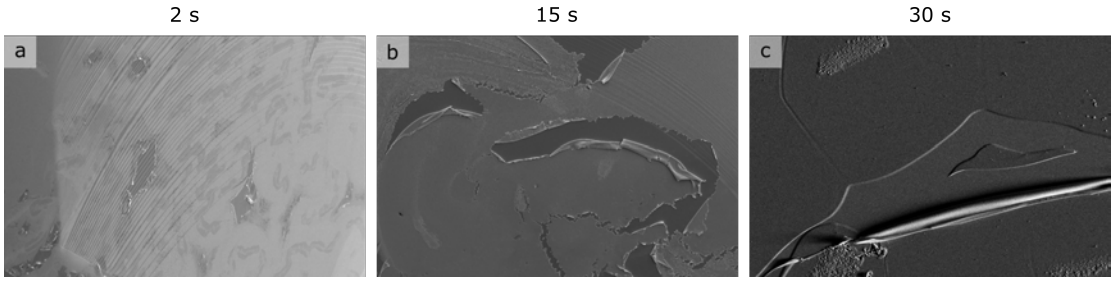

Figure 5.67: SEM images showing exfoliation of NPG from a Au(111) facet after HV electrolysis at 540 V (for 2, 15, and 30 s) followed by electrochemical reduction. The region depicted in the SEM image has a size of 300 µm × 200 µm.[265]

5.4.6.11 S11: NPG Film on the Au(100) Facet Obtained by HV Electrolysis at 540 V and Subsequent Electrochemical Reduction

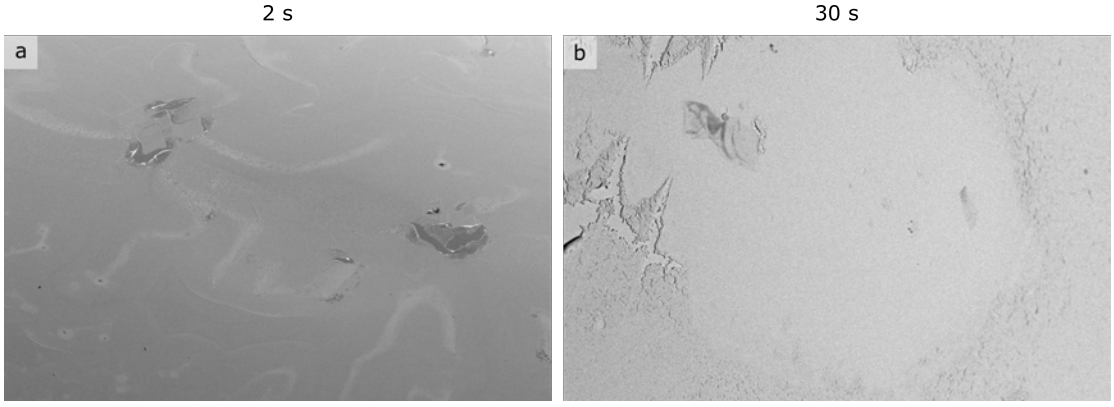

Figure 5.68: SEM images of the NPG film on the Au(100) facet, obtained by HV electrolysis at 540 V (for 2 and 30 s) followed by electrochemical reduction. The region depicted in the SEM image has a size of 300 µm × 200 µm.[265]

5.4.6.12 S12: Stability of the NPG Film on the Au(100*) after HV Electrolysis at 540 V for 4 s and Subsequent Electrochemical Reduction of the Oxide

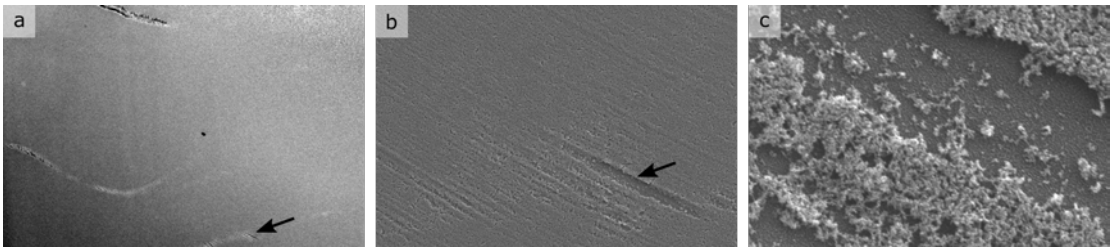

Figure 5.69: a) SEM image of the Au(100) facet and the adjacent step edges after HV electrolysis at 540 V for 4 s and subsequent electrochemical reduction. b) and c) represent magnifications of the step edges, at locations where the NPG film is torn apart. The arrow indicates the magnified region shown in the image to the right. The regions depicted in the SEM images have a size of 300 µm $\times$ 200 µm, in b 30 µm $\times$ 20 µm and in c 3 µm $\times$ 2 µm. The contrast and brightness in a) have been adjusted for better visibility.[265]

6 Summary

In this work, the behavior and stability of the (electro)catalytically relevant metals Pt, Au, and Cu in the field of HV electrolysis at voltages between 50 V and 580 V were investigated and differences in their behavior were elaborated. Further investigations of influencing parameters during HV electrolysis on the structure formation of the electrodes were then performed for Au electrodes in order to gain a more comprehensive understanding of the restructuring of the electrodes and thus to be able to control the electrode structure in a targeted manner in a final step. Parameters such as the electrolysis voltage, the initial electrolyte temperature, the electrolysis time, and the reduction method of a (possible) oxide film formed during HV electrolysis were addressed. In addition to the significantly increased production rate of NPG films at high voltages, the aim was to clarify whether there are conditions in the HV electrolysis range that may achieve a similar or better result than the conditions at a few volts or in the range of aCGDE and whether HV electrolysis is thus more suitable than aCGDE for the production of certain electrode structures.
In a further step, the influence of the crystallographic orientation of Au on the structure formation of the Au oxide during HV electrolysis and the subsequently formed NPG film was addressed.
Finally, the influence of the current induced by the applied voltage or rather a plasma on the electrolyte was investigated, since at high voltages also the electrolyte properties change, e.g., the electrolyte temperature, which in turn can influence the formation of structures on the electrode. For this purpose, the changes induced during plasma treatment in the electrolyte, especially formed H_2O_2, were monitored at an additional electrode in solution in a time- and space-dependent manner.
The key results of this work are summarized conclusively as follows.

Stability and Structure Formation on Different Electrode Materials and Parameters Influencing the Resulting Structures: Upon systematically studying Pt, Au, and Cu anodes in the range from 50 V to 580 V, it has been shown that the *I*–

U characteristic is very similar for all three electrode materials. Nevertheless, the stability of the different materials differs strongly under the conditions. This is the first study covering the structural changes of electrodes not only caused by NE or aCGDE, but in the complete HV electrolysis range.
While Pt showed no measurable structural changes after 30 s of HV electrolysis in the entire voltage range, thick oxide films developed on the Au and Cu anodes after the same time. The increase in electrochemical surface area (ECSA) due to HV electrolysis was determined for all three electrode materials after the reduction of the formed oxide.
The roughness factor (RF) for Au determined after 30 s of HV electrolysis is proportional to the current density during HV electrolysis, i.e., the maximum RF is obtained for Au after 30 s of electrolysis at average voltages around V_B. However, a general proportionality between current density and RF is not given for Au at all electrolysis times, since the roughness of the Au electrode increases sharply at small electrolysis times, while the RF reaches a plateau at longer electrolysis times (see Chapter 5.3). However, regardless of the applied voltage and electrolysis time, NPG films on Au form after HV electrolysis and subsequent reduction. Hence, this work demonstrates for the first time that nanoporous Au structures can be fabricated not only, as reported earlier, in the NE region but also very efficiently by the formation of Au oxide at voltages between 100 V and 540 V and subsequent reduction or direct reduction during HV electrolysis at longer electrolysis times (see Chapter 5.1, Chapter 5.3 and Chapter 5.4).
The largest roughening for Cu after 30 s of HV electrolysis is observed at the smallest applied voltage (50 V). With increasing applied voltage, the roughness of the electrode apparently decreases. Overall, the structure of the Cu electrode, both after electrolysis and electrochemical reduction depends strongly on the HV electrolysis voltage.
Another key finding of this study was that the oxide films formed on the Au and Cu electrodes during HV electrolysis can be reduced after HV electrolysis not only by subsequent electrochemical reduction but also by H_2O_2 formed during HV electrolysis. H_2O_2 represents a non-faradaic product that is formed at high positive voltages in addition to O_2. If the oxide film-covered electrode is not immediately removed from the electrolyte after HV electrolysis, the oxide film is reduced by H_2O_2 present in the electrolysis solution. This behavior was observed for all voltages studied in this work. H_2O_2 is, therefore, able to significantly influence the resulting electrode

structures (see Chapter 5.1 and Chapter 5.3). The surface structures obtained for Au after reduction by H_2O_2 in the electrolyte are similar to those after electrochemical reduction.
According to the literature, the formation of H_2O_2 is only observed for voltages above partial aCGDE. The results of this work suggest, however, that H_2O_2 can eventually also be formed at lower voltages. Proof, as well as quantification of the H_2O_2 formed, will be part of a future study.

Designing Nanostructures: The method shown in this work for the preparation of NPG films by applying a high voltage and subsequently reducing the formed Au oxide films is a simple, fast, and environmentally friendly approach, since apart from an aqueous KOH electrolyte no other chemicals are required. Additionally, the preparation method described here has the advantage that no foreign metal impurities remain in the NPG film, which could play a decisive role in following catalytic studies, e.g., in (electro)catalysis. Foreign metal impurities due to alloying metals are a common problem encountered during dealloying, which is the main method used for the production of NPG films. A detailed comparison between the NPG films formed by different methods is subject of future works.
In order to specifically tune the NPG films prepared by HV electrolysis, the parameters applied voltage, reduction method (electrochemical or by H_2O_2), temperature, and time, as well as their influence on the resulting nanoporous Au structures, were further elucidated.
If the Au oxide films formed during HV electrolysis are reduced by H_2O_2, the final NPG surface structures differ strongly depending on the electrolyte temperature and concentration of the H_2O_2-containing 0.01 M KOH solution. At a H_2O_2 concentration of 0.8 %, significantly rougher surfaces can be obtained compared to electrodes that were electrochemically reduced. The difference between the RF after reduction in 0.8 % H_2O_2-containing 0.01 M KOH solution compared to the RF after electrochemical reduction is largest at medium voltages, where the current density is highest during HV electrolysis. At low (100 V) and high voltages (540 V), there is almost no difference in the RF with respect to the reduction method.
Moreover, the higher the initial electrolyte temperature, the lower the current densities during HV electrolysis, and the earlier V_B appears. This can be explained by reaching the boiling point of the electrolyte sooner, which enables the formation of a gas layer around the electrode more easily.

If the electrolysis time is varied, it was observed that in the range of aCGDE (at 540 V) the roughness of the electrode increases strongly for short electrolysis times up to approximately 60 s, while it reaches a constant value for long electrolysis times. If the electrolysis times are sufficiently long, the resulting Au oxide is reduced directly in the solution and does not have to be reduced electrochemically in a second step. But if the current density during HV electrolysis is very high, parts of the Au oxide film may dissolve during longer electrolysis times, which means that homogeneous NPG films can no longer be obtained.
Although attempts were made in this work to quantify the dissolution of the electrode material, the amount of metal ions in the solution was always close to the detection limit of the ICP-AES instrument used (performed in collaboration with Margit Lang – Institute of Analytical and Bioanalytical Chemistry). Thus, at the moment, it can only be stated that the Cu electrode dissolves the most of all three metals investigated (Pt, Au, and Cu) during HV electrolysis, which is also apparent by a change in electrolyte color, while no signs of dissolution could be found for Pt.

Influence of Crystallographic Orientation on Electrode Restructuring: To study the influence of the crystallographic orientation on the structure formation of the Au oxide and the NPG film formed by HV electrolysis in the range of NE (300 V) and aCGDE (540 V), HV electrolysis was performed on Au POSC electrodes. These electrodes allow simultaneous screening of different facets on the surface of the POSC. The focus herein was on the Au(111) and Au(100) facets.
Regardless of the voltage considered (300 V or 540 V), there were no structural differences in the oxide structures of the two facets for electrolysis times at which no cracks had yet formed on the surface (up to 15 s). The similar oxide structures can be explained by the amorphous character of the Au oxide film formed.
The structures of the NPG film, on the other hand, seemed to depend on the facet on which the oxide film was grown. For the considered electrolysis times from 100 ms to 30 s at 540 V, it was shown that homogeneous NPG films cannot be prepared on the Au(111*) facet at short electrolysis times, while they are homogeneous when they were formed from oxides created during 30 s of HV electrolysis. The * denotes the step edges adjacent to the Au(111) facet. Strong exfoliation from the crystal was observed for longer electrolysis times randomly on the entire crystal, especially on the Au(111) facet. On the Au(100*) surface, however, relatively homogeneous structures can be produced at 540 V between 500 ms and 2 s of HV

electrolysis treatment and almost no exfoliation occurs on the Au(100) facet even for long electrolysis times. At 300 V on both the Au(111*) and the Au(100*) facet homogeneous NPG films can be obtained in a broad window of electrolysis times (2 to 15 s). Exfoliation of the NPG film starts here on the Au(111*) facet after 30 s. Grain boundaries have no influence at both considered voltages on the structure formation of the Au oxide and NPG films.

Time- and spatial-dependent Distribution of aCGDE Products in the Electrolyte: Since products formed during HV electrolysis or during aCGDE can critically affect the composition of the electrolyte and in turn, the electrodes, specifically H_2O_2, a proof of concept study in the aCGDE region was performed with the aim of tracking changes in the electrolyte. For a better estimation of the amount of H_2O_2 formed during aCGDE, as well as its local and temporal evolution in the electrolyte, H_2O_2 was detected *operando* in a five-electrode setup. This presents the first attempt to detect H_2O_2 during aCGDE. Since Pt exhibits high stability at the prevailing conditions, both in the aCGDE region and at potentials where H_2O_2 can be detected, Pt electrodes were used both as PWE and AE.
It was shown that immediately after aCGDE, H_2O_2 is only present very close to the PWE and that the H_2O_2 distributes fairly quickly in the electrolyte. Changes in the electrolyte due to H_2O_2 formed during HV electrolysis thus decay rather fast. Detection of H_2O_2 during aCGDE and quantification of the amount of H_2O_2 formed in the electrolyte, both in the NE and aCGDE region, was not yet possible and will be part of future work, for which the cornerstone has been laid in this work.
In order to gain a more detailed understanding of the influence of the products formed during aCGDE on the electrolyte in the future, the influence of existing electric fields must be better taken into account and the removal of bubbles has to be optimized. By designing a new cell in which the existing electric fields are more homogeneous and thus better defined, the effect of an electric field can be disentangled. The design and first measurements of the voltage drop in such a cell during HV electrolysis below aCGDE were performed in the context of a master thesis. More information on this topic can be found in Ref. [81], where I am listed as a coauthor.

6.1 Scientific Value

In this work, the complete voltage range between NE and aCGDE was investigated for the first time and the influences of voltage and if present a plasma on (i) the electrode structure and (ii) the electrolyte.
It was shown that the restructuring of the electrode under the aforementioned conditions is strongly dependent on the electrode material, as well as products formed during HV electrolysis, in particular H_2O_2, having a significant influence on the restructuring of the electrode. Different electrode structures were not necessarily obtained with and without plasma. Thus, if a material needs to be treated at high voltages, in the future it is recommended to investigate the entire voltage range in order to find optimal conditions for the formation of the desired electrode structure. Moreover, the workpiece should be removed from the electrolyte as soon as possible after HV electrolysis to avoid undesirable side effects due to formed products accumulated in the electrolyte.
Furthermore, currently the nanostructuring of electrode materials for catalytic processes, as well as "green chemistry", is becoming more and more important. The fabrication of NPG films on Au substrates by HV electrolysis or under aCGDE conditions, as shown in this work, represents a simple, fast, and environmentally friendly method in terms of sustainability. Moreover, compared to the mainly used method of dealloying, it offers the advantage that no alloy formation and thus no foreign metal is required for the preparation of the NPG film, which after its possibly incomplete dissolution from the alloy may still contaminate the formed NPG film and thus may alter the catalytic activity of the resulting NPG film. In general, these findings can be considered a proof of concept for further studies on other electrode materials.
The dependence of restructuring on the crystallographic orientation using Au POSCs as an example represented a first attempt to combine plasma in-liquid and single crystal research. Since single crystals represent very well-characterized model systems, these initial investigations represent a first step towards a better understanding of structure formation under plasma conditions and lay the cornerstone for future works.
The detection of H_2O_2 formed during aCGDE was for the first time evidenced *operando* in the electrolyte in a proof of concept study. Further development of *operando* detection of products formed during aCGDE should also be part of future studies. Such information is for example very valuable for studies related to

modeling reactions in the region of the HV working electrode.

7 Zusammenfassung

In dieser Arbeit wurden das Verhalten und die Stabilität der (elektro)katalytisch relevanten Metalle Pt, Au und Cu im Bereich der HV Elektrolyse bei Spannungen zwischen 50 V und 580 V untersucht und Unterschiede in ihrem Verhalten herausgearbeitet. Weitere Untersuchungen der Einflussparameter bei der HV Elektrolyse auf die Strukturbildung der Elektroden wurden anschließend für Au Elektroden durchgeführt, um ein umfassenderes Verständnis für die Restrukturierung der Elektroden zu erhalten und damit in einem letzten Schritt die Elektrodenstruktur gezielt steuern zu können. Dabei wurden Parameter wie die Elektrolysespannung, die anfängliche Elektrolyttemperatur, die Elektrolysezeit und die Methode zur Reduktion einer (möglichen) Oxidschicht, die sich während der HV Elektrolyse bildet, untersucht. Neben der deutlich gesteigerten Produktionsrate von NPG Filmen bei hohen Spannungen sollte geklärt werden, ob es im Bereich der HV Elektrolyse Bedingungen gibt, die ein ähnliches oder besseres Ergebnis erzielen können als die Bedingungen bei wenigen Volt oder im Bereich der aCGDE und ob die HV Elektrolyse damit für die Herstellung bestimmter Elektrodenstrukturen besser geeignet ist als die aCGDE.
In einem weiteren Schritt wurde der Einfluss der kristallographischen Orientierung von Au auf die Struktur des während der HV Elektrolyse gebildeten Au Oxids und dem anschließend gebildeten NPG Film untersucht.
Schließlich wurde der Einfluss des durch die angelegte Spannung bzw. eines Plasmas induzierten Stroms auf den Elektrolyten untersucht, da sich bei den hohen Spannungen auch die Elektrolyteigenschaften verändern, z.B. die Elektrolyttemperatur, welche wiederum die Strukturbildung der Elektrode beeinflussen können. Dafür wurden die durch die Plasmabehandlung induzierten Veränderungen im Elektrolyten, insbesondere gebildetes H_2O_2, an einer zusätzlichen Elektrode in Lösung zeit- und ortsabhängig verfolgt.
Die wichtigsten Ergebnisse dieser Arbeit lassen sich abschließend wie folgt zusam-

menfassen.

Stabilität und Strukturbildung auf verschiedenen Elektrodenmaterialien und Einflussparameter auf die resultierenden Strukturen: Duch die systematische Untersuchung von Pt, Au und Cu Anoden im Bereich von 50 V bis 580 V hat sich gezeigt, dass die *I–U* Kennlinie für alle drei Elektrodenmaterialien sehr ähnlich ist. Dennoch unterscheidet sich die Stabilität der verschiedenen Materialien unter den gegebenen Bedingungen stark. Dies ist die erste Studie, die die strukturellen Veränderungen von Elektroden nicht nur durch NE oder aCGDE, sondern im gesamten HV Elektrolysebereich abdeckt.
Während Pt nach 30 s HV Elektrolyse im gesamten Spannungsbereich keine messbaren strukturellen Veränderungen zeigte, entwickelten sich auf den Au und Cu Anoden nach der gleichen Zeit dicke Oxidfilme. Die Zunahme der elektrochemischen Oberfläche (ECSA) aufgrund der HV Elektrolyse wurde für alle drei Elektrodenmaterialien nach der Reduktion des gebildeten Oxids bestimmt.
Der nach 30 s HV Elektrolyse ermittelte Rauigkeitsfaktor (RF) für Au ist proportional zur Stromdichte während der HV Elektrolyse, d.h. der maximale RF wird für Au nach 30 s Elektrolyse bei mittleren Spannungen um V_B erreicht. Eine allgemeine Proportionalität zwischen Stromdichte und RF ist für Au jedoch nicht bei allen Elektrolysezeiten gegeben, da die Rauigkeit der Au Elektrode bei kleinen Elektrolysezeiten stark zunimmt, während der RF bei längeren Elektrolysezeiten ein Plateau erreicht (siehe Kapitel 5.3). Unabhängig von der angelegten Spannung und der Elektrolysezeit bilden sich jedoch NPG Filme auf Au nach der HV Elektrolyse und der anschließenden Reduktion. Diese Arbeit zeigt somit zum ersten Mal, dass nanoporöse Au Strukturen nicht, wie bereits berichtet, nur im NE Bereich, sondern auch sehr effizient durch die Bildung von Au Oxid bei Spannungen zwischen 100 V und 540 V und anschließender Reduktion oder direkter Reduktion während der HV Elektrolyse bei längeren Elektrolysezeiten hergestellt werden können (siehe Kapitel 5.1, Kapitel 5.3 und Kapitel 5.4).
Die stärkste Aufrauung für Cu nach 30 s HV Elektrolyse wird bei der kleinsten angelegten Spannung (50 V) beobachtet. Mit zunehmender angelegter Spannung nimmt die Rauigkeit der Elektrode offensichtlich ab. Insgesamt hängt die Struktur der Cu Elektrode sowohl nach der Elektrolyse als auch nach der elektrochemischen Reduktion stark von der HV Elektrolysespannung ab.
Eine weitere zentrale Erkenntnis dieser Untersuchung war, dass die während der

HV Elektrolyse auf den Au und Cu Elektroden gebildeten Oxidfilme nach der HV Elektrolyse nicht nur durch die anschließende elektrochemische Reduktion, sondern auch durch während der HV Elektrolyse gebildetes H_2O_2 reduziert werden können. H_2O_2 stellt ein nicht-faradaysches Produkt dar, das bei hohen positiven Spannungen zusätzlich zu O_2 gebildet wird. Wird die mit einem Oxidfilm bedeckte Elektrode nach der HV Elektrolyse nicht sofort aus dem Elektrolyten entfernt, wird der Oxidfilm durch das in der Elektrolyselösung vorhandene H_2O_2 reduziert. Dieses Verhalten wurde bei allen in dieser Arbeit untersuchten Spannungen beobachtet. H_2O_2 kann daher die resultierenden Elektrodenstrukturen erheblich beeinflussen (siehe Kapitel 5.1 und Kapitel 5.3). Die für Au nach der Reduktion durch H_2O_2 im Elektrolyten erhaltenen Oberflächenstrukturen ähneln hierbei denen nach der elektrochemischen Reduktion.
In der Literatur wird die Bildung von H_2O_2 nur bei Spannungen oberhalb partieller aCGDE beobachtet. Die Ergebnisse dieser Arbeit deuten jedoch darauf hin, dass H_2O_2 eventuell auch bei niedrigeren Spannungen gebildet werden kann. Der Nachweis sowie die Quantifizierung des gebildeten H_2O_2 werden Teil einer zukünftigen Studie sein.

Entwurf von Nanostrukturen: Die in dieser Arbeit gezeigte Methode zur Herstellung von NPG Filmen durch Anlegen einer hohen Spannung und anschließende Reduktion der gebildeten Au Oxid Filme ist ein einfacher, schneller und umweltfreundlicher Ansatz, da außer einem wässrigen KOH Elektrolyten keine weiteren Chemikalien benötigt werden. Zudem hat die hier beschriebene Präparationsmethode den Vorteil, dass keine Fremdmetallverunreinigungen im NPG Film verbleiben, die bei nachfolgenden katalytischen Untersuchungen, z.B. in der (Elektro-)Katalyse, eine entscheidende Rolle spielen könnten. Fremdmetallverunreinigungen durch Legierungsmetalle sind ein häufiges Problem beim Entlegieren, dem Hauptverfahren zur Herstellung von NPG Filmen. Ein detaillierter Vergleich zwischen den mit verschiedenen Methoden hergestellten NPG Filmen ist Gegenstand künftiger Arbeiten.
Um die durch HV Elektrolyse hergestellten NPG Filme gezielt modifizieren zu können, wurden die Parameter angelegte Spannung, Reduktionsmethode (elektrochemisch oder durch H_2O_2), Temperatur und Zeit sowie ihr Einfluss auf die resultierenden nanoporösen Au Strukturen nochmals näher beleuchtet.
Werden die während der HV Elektrolyse gebildeten Au Oxidfilme durch H_2O_2 re-

duziert, unterscheiden sich die endgültigen NPG Oberflächenstrukturen stark in Abhängigkeit von der Elektrolyttemperatur und der Konzentration der H_2O_2-haltigen 0,01 M KOH Lösung. Bei einer H_2O_2 Konzentration von 0,8 % lassen sich im Vergleich zu elektrochemisch reduzierten Elektroden deutlich rauere Oberflächen erzielen. Der Unterschied zwischen dem RF nach der Reduktion in 0,8 %iger H_2O_2-haltiger 0,01 M KOH Lösung im Vergleich zum RF nach elektrochemischer Reduktion ist bei mittleren Spannungen am größten, da hier die Stromdichte während der HV Elektrolyse am höchsten ist. Bei niedrigen (100 V) und hohen Spannungen (540 V) ist nahezu kein Unterschied im RF in Bezug auf die Reduktionsmethode vorhanden.
Je höher die Anfangstemperatur des Elektrolyten ist, desto geringer sind die Stromdichten während der HV Elektrolyse und desto früher tritt V_B auf. Dies lässt sich dadurch erklären, dass der Siedepunkt des Elektrolyten früher erreicht wird, wodurch sich leichter eine Gasschicht um die Elektrode ausbilden kann.
Wird die Elektrolysezeit variiert, so zeigt sich, dass im Bereich der aCGDE (bei 540 V) die Rauigkeit der Elektrode bei kurzen Elektrolysezeiten bis etwa 60 s stark zunimmt, während sie bei langen Elektrolysezeiten einen konstanten Wert erreicht. Sind die Elektrolysezeiten ausreichend lang, wird das entstehende Au Oxid direkt in der Lösung reduziert und muss nicht in einem zweiten Schritt elektrochemisch reduziert werden. Ist die Stromdichte bei der HV Elektrolyse jedoch sehr hoch, können sich bei längeren Elektrolysezeiten Teile des Au Oxid Films lösen, so dass keine homogenen NPG Filme mehr erhalten werden können.
Obwohl in dieser Arbeit versucht wurde, die Auflösung des Elektrodenmaterials zu quantifizieren, lag die Menge der Metallionen in der Lösung immer nahe an der Nachweisgrenze des verwendeten ICP-AES-Geräts (durchgeführt in Zusammenarbeit mit Margit Lang – Institut für Analytische und Bioanalytische Chemie). Somit kann derzeit nur festgehalten werden, dass sich die Cu Elektrode von allen drei untersuchten Metallen (Pt, Au und Cu) während der HV Elektrolyse am stärksten auflöst, was sich auch durch eine Änderung der Elektrolytfarbe bemerkbar macht, während für Pt keine Anzeichen für eine Auflösung gefunden werden konnten.

Einfluss der kristallographischen Orientierung auf die Elektrodenrestrukturierung: Zur Untersuchung des Einflusses der kristallografischen Orientierung auf die Strukturbildung des Au Oxids und des NPG Films, der durch HV Elektrolyse im Bereich von NE (300 V) und aCGDE (540 V) gebildet wird, wurde die HV Elek-

trolyse mit Au POSC Elektroden durchgeführt. Diese Elektroden ermöglichen die gleichzeitige Untersuchung verschiedener Facetten auf der Oberfläche des POSC. Der Schwerpunkt lag dabei auf den Au(111) und Au(100) Facetten.
Unabhängig von der betrachteten Spannung (300 V oder 540 V) gab es keine strukturellen Unterschiede in den Oxidstrukturen der beiden Facetten bei Elektrolysezeiten, bei denen sich noch keine Risse auf der Oberfläche gebildet hatten (bis zu 15 s). Die ähnlichen Oxidstrukturen lassen sich durch den amorphen Charakter der gebildeten Au Oxidschicht erklären.
Die Strukturen des NPG Films hingegen scheinen von der Fläche abzuhängen, auf der der Oxidfilm gewachsen ist. Für die betrachteten Elektrolysezeiten von 100 ms bis 30 s bei 540 V wurde gezeigt, dass bei kurzen Elektrolysezeiten keine homogenen NPG Filme auf der Au(111*) Facette hergestellt werden können, während sie homogen sind, wenn sie aus Oxiden gebildet wurden, die durch 30 s HV Elektrolyse entstanden sind. Das * kennzeichnet hierbei die Stufenkanten an der Au(111) Facette. Bei längeren Elektrolysezeiten wurde auf dem gesamten Kristall, insbesondere auf der Au(111) Facette, ein starkes Abblättern beobachtet. Auf der Au(100*) Oberfläche hingegen können bei 540 V zwischen 500 ms und 2 s HV Elektrolyse relativ homogene Strukturen erzeugt werden, und auf der Au(100) Facette tritt selbst bei langen Elektrolysezeiten fast kein Abblättern auf. Bei 300 V können sowohl auf der Au(111*) als auch auf der Au(100*) Facette homogene NPG Filme in einem breiten Fenster von Elektrolysezeiten (2 bis 15 s) erhalten werden. Das Abblättern des NPG Films beginnt hier auf der Au(111*) Fläche nach 30 s. Korngrenzen haben bei beiden betrachteten Spannungen keinen Einfluss auf die Strukturbildung der Au Oxid und NPG Filme.

Zeit- und ortsabhängige Verteilung von aCGDE Produkten im Elektrolyten: Da während der HV Elektrolyse bzw. der aCGDE gebildete Produkte die Zusammensetzung des Elektrolyten und damit auch die Elektroden beeinflussen können, insbesondere H_2O_2, wurde eine Machbarkeitsstudie im aCGDE Bereich durchgeführt, um Veränderungen im Elektrolyten zu verfolgen. Für eine bessere Abschätzung der während aCGDE gebildeten Menge an H_2O_2, sowie seiner lokalen und zeitlichen Entwicklung im Elektrolyten, wurde H_2O_2 in einem Fünf-Elektroden Setup *operando* nachgewiesen. Dies ist der erste Versuch, H_2O_2 während aCGDE nachzuweisen. Da Pt unter den vorherrschenden Bedingungen eine hohe Stabilität aufweist, sowohl im aCGDE Bereich als auch bei Potentialen, bei denen H_2O_2

nachgewiesen werden kann, wurden Pt Elektroden sowohl als PWE als auch als AE verwendet.
Es wurde gezeigt, dass unmittelbar nach aCGDE H_2O_2 nur in unmittelbarer Nähe der PWE vorhanden ist und dass sich das H_2O_2 relativ schnell im Elektrolyten verteilt. Veränderungen im Elektrolyten durch H_2O_2, das während der HV Elektrolyse entsteht, klingen daher relativ schnell ab. Ein Nachweis von H_2O_2 während aCGDE und eine Quantifizierung der im Elektrolyten gebildeten H_2O_2 Menge, sowohl in der NE als auch in der aCGDE Region, war bisher nicht möglich und wird Teil zukünftiger Arbeiten sein, für die in dieser Arbeit der Grundstein gelegt wurde.
Um zukünftig ein detaillierteres Verständnis des Einflusses der bei der aCGDE gebildeten Produkte auf den Elektrolyten zu erlangen, muss der Einfluss vorhandener elektrischer Felder besser berücksichtigt und der Abtransport von Blasen optimiert werden. Durch den Entwurf einer neuen Zelle, in der die vorhandenen elektrischen Felder homogener und damit besser definiert sind, kann der Einfluss eines elektrischen Feldes bestimmt werden. Der Aufbau und erste Messungen des Spannungsabfalls in einer solchen Zelle bei der HV Elektrolyse unterhalb aCGDE wurden im Rahmen einer Masterarbeit durchgeführt. Weitere Informationen zu diesem Thema finden sich in Ref. [81], bei der ich als Mitautor aufgeführt bin.

7.1 Wissenschaftlicher Mehrwert

In dieser Arbeit wurde zum ersten Mal der gesamte Spannungsbereich zwischen NE und aCGDE untersucht und die Einflüsse der Spannung und des gegebenenfalls vorhandenen Plasmas auf (i) die Elektrodenstruktur und (ii) den Elektrolyten betrachtet.
Dabei konnte gezeigt werden, dass die Restrukturierung der Elektrode unter den oben genannten Bedingungen stark vom Elektrodenmaterial abhängt und dass die bei der HV Elektrolyse gebildeten Produkte, insbesondere H_2O_2, einen erheblichen Einfluss auf die Restrukturierung der Elektrode haben. Hierbei werden mit und ohne Plasma nicht unbedingt unterschiedliche Elektrodenstrukturen erhalten. Es empfiehlt sich somit, zukünftig den gesamten Spannungsbereich zu untersuchen, sollte ein Werkstoff bei hohen Spannungen behandelt werden, um optimale Bedingungen für die Ausbildung der gewünschten Elektrodenstruktur zu finden. Darüber

hinaus sollte das Werkstück nach der HV Elektrolyse so schnell wie möglich aus dem Elektrolyten entfernt werden, um unerwünschte Nebeneffekte aufgrund von im Elektrolyten angesammelten gebildeten Produkten zu vermeiden.
Aktuell kommt zudem der Nanostrukturierung von Elektrodenmaterialien für katalytische Prozesse sowie für der "grüne Chemie" immer mehr Bedeutung zu. Die in dieser Arbeit gezeigte Herstellung von NPG Filmen auf Au Substraten durch HV Elektrolyse oder unter aCGDE Bedingungen stellt eine einfache, schnelle und umweltfreundliche Methode im Sinne der Nachhaltigkeit dar. Darüber hinaus bietet sie im Vergleich zu der hauptsächlich verwendeten Methode des Entlegierens den Vorteil, dass keine Legierungsbildung und damit kein Fremdmetall für die Herstellung des NPG Films erforderlich ist, das nach seiner möglicherweise unvollständigen Herauslösung aus der Legierung den gebildeten NPG Film verunreinigen und damit die katalytische Aktivität des resultierenden NPG Films verändern kann. Generell können diese Ergebnisse als Machbarkeitsnachweis für weitere Untersuchungen an anderen Elektrodenmaterialien angesehen werden.
Die Abhängigkeit der Restrukturierung von der kristallographischen Orientierung am Beispiel von Au POSCs stellte einen ersten Versuch dar, Plasma in Lösung und Einkristallforschung zu verbinden. Da Einkristalle sehr gut charakterisierte Modellsysteme darstellen, sind diese ersten Untersuchungen ein erster Schritt zu einem besseren Verständnis der Strukturbildung unter Plasmabedingungen und legen den Grundstein für zukünftige Arbeiten.
Der Nachweis von H_2O_2, das während aCGDE gebildet wird, wurde zum ersten Mal *operando* im Elektrolyten in einer Machbarkeitsstudie nachgewiesen. Die Weiterentwicklung des *operando* Nachweises von Produkten, die während aCGDE gebildet werden, sollte ebenfalls Teil zukünftiger Studien sein. Solche Informationen sind zum Beispiel sehr wertvoll für Studien zur Modellierung von Reaktionen im Bereich der HV Arbeitselektrode.

8 Danksagung

An dieser Stelle möchte ich all denjenigen Danken, die mich während meiner Promotion unterstützt haben oder diese Promotion erst möglich gemacht haben.
Zunächst danke ich Prof. Dr. Timo Jacob, dass er mir die Anfertigung dieser Arbeit am Institut für Elektrochemie ermöglicht hat. Zudem möchte ich PD Dr. Joachim Bansmann für das Erstellen eines Gutachtens und allen weiteren Prüfern danken.
Desweiteren danke ich dem "Stiftung Stipendien-Fonds des Verbandes der Chemischen Industrie (VCI)" für seine finanzielle Unterstützung in Form eines Kekulé Stipendiums.
Darüberhinaus danke ich Dr. A. K. E. für seine wissenschaftlichen Anregungen zu allen Zeitpunkten der Promotion und L. F. für weiteren thematischen Austausch und das Korrekturlesen meiner Arbeit. Ein weiterer Dank geht an alle Mitglieder des Instituts für Elektrochemie für die angenehme Arbeitsatmosphäre während meiner Zeit am Institut, insbesondere an meine Laborkollegen und meinen Bürokollegen M. U. für seine zahlreichen Aufheiterungsversuche, oft verbunden mit erhöhtem Süßigkeitenkonsum. Darüberhinaus danke ich meinen Kaffeetrinkgefährten H. B. und C. F. für die unzähligen Kaffees während allen Höhen und Tiefen der Promotion und die unzähligen damit verbundenen Gespräche. Ein ganz besonderer Dank geht auch an S. F. für seine Unterstützung, besonders in der Endphase meiner Promotion und seine zahlreichen Aufmunterungs- und Ablenkungsversuche z.B. in Form von Käsefondues.
Zuletzt geht auch ein großer Dank an meine Familie für die Unterstützung während meines gesamten Studiums und der Promotion, insbesondere an J. A.

9 Lebenslauf

Persönliche Daten

Name	Evelyn Artmann
Geburtsjahr	1995
Geburtsort	Ulm
Staatsangehörigkeit	deutsch

Schulausbildung

2005-2013	Allgemeine Hochschulreife, St. Hildegard Gymnasium Ulm

Hochschulausbildung und Promotion

2013-2016	Bachelor Chemie, Universität Ulm
2016-2018	Master Chemie, Universität Ulm
2018-2019	Wissenschaftliche Mitarbeiterin, Institut für Oberflächenchemie und Katalyse, Universität Ulm
2019-2023	Promotion, Institut für Elektrochemie, Universität Ulm

10 Publikationen, Konferenzbeiträge und Projekttreffen

10.1 Artikel

1. **Evelyn Artmann**, Pramod V. Menezes, Lukas Forschner, Mohamed M. Elnagar, Ludwig A. Kibler, Timo Jacob, Albert K. Engstfeld, *Chem. Phys. Chem.* **22**, 2429 (2021), "Structural Evolution of Pt, Au and Cu Anodes by Electrolysis up to Contact Glow Discharge Electrolysis in Alkaline Electrolytes".
2. **Evelyn Artmann**, Lukas Forschner, Timo Jacob, Albert K. Engstfeld, *J. Vac. Sci. Technol. A* **40**, 053005, (2022), "Using auxiliary electrochemical working electrodes as probe during contact glow discharge electrolysis: a proof of concept study".
3. **Evelyn Artmann**, Lukas Forschner, Konstantin M. Schüttler, Mohammad Al-Shakran, Timo Jacob, Albert K. Engstfeld, *Chem. Phys. Chem.* **24**, e202200645, (2022), "Nanoporous Au Formation on Au Substrates via High Voltage Electrolysis".
4. Lukas Forschner, **Evelyn Artmann**, Timo Jacob, Albert K. Engstfeld, *J. Phys. Chem. C* **127**, 4387, (2023), "Electric Potential Distribution Inside the Electrolyte During High Voltage Electrolysis".

10.2 Vorträge

1. **Evelyn Artmann**, Pramod V. Menezes, Timo Jacob, Albert K. Engstfeld: "Influence of electrode materials and pH on in-liquid plasma" *Regional FCI Meet-*

ing, Ulm, 25.02.2020.

2. Albert K. Engstfeld, **Evelyn Artmann**, Pramod V. Menezes, Ludwig A. Kibler, Timo Jacob: "Influence of (above liquid and) in liquid plasma on the redox processes and structure of electrocatalyst materials" *SFB1316 Meeting*, Virtual Ulm/Bochum/Berlin, 01.04.2020.

3. Albert K. Engstfeld, **Evelyn Artmann**, Pramod V. Menezes, Ludwig A. Kibler, Timo Jacob: "(Contact) Glow Discharge Electrolysis and electrochemistry" *SFB1316 Meeting*, Virtual Ulm/Bochum/Berlin, 30.06.2020.

4. **Evelyn Artmann**, Pramod V. Menezes, Timo Jacob, Albert K. Engstfeld: "Anodic Contact Glow Discharge Electrolysis (aCGDE) Electrodes in Alkaline Media" *Institutsseminar*, Virtual Ulm, 16.07.2020.

5. Albert K. Engstfeld, **Evelyn Artmann**, Pramod V. Menezes, Mohamed M. Elnagar, Lukas Forschner, Ludwig A. Kibler, Timo Jacob: "Influence of in liquid plasma on the redox processes and structure of electrocatalyst materials: Structure formation" *SFB1316 Meeting*, Virtual Ulm/Bochum/Berlin, 16.11.2020.

6. Albert K. Engstfeld, **Evelyn Artmann**, Pramod V. Menezes, Mohamed M. Elnagar, Lukas Forschner, Fabian Schütt, Ludwig A. Kibler, Timo Jacob: "B12: Impact of plasma in liquid on electrode structure and solution properties" *SFB1316 Meeting*, Virtual Ulm/Bochum/Berlin, 19.02.2021.

7. **Evelyn Artmann**, Lukas Forschner, Pramod V. Menezes, Mohamed M. Elnagar, Ludwig A. Kibler, Timo Jacob, Albert K. Engstfeld: "Anodic Polarization of Electrodes at High Voltages in Alkaline Electrolytes" *MGK Kolloquium SFB1316*, Virtual Ulm/Bochum/Berlin, 21.04.2021.

8. **Evelyn Artmann**, Lukas Forschner, Pramod V. Menezes, Mohamed M. Elnagar, Ludwig A. Kibler, Timo Jacob, Albert K. Engstfeld: "High voltage polarization of metal electrodes: surface and electrolyte effects" *Institutsseminar*, Virtual Ulm, 08.07.2021.

9. **Evelyn Artmann**, Lukas Forschner, Tobias Schmider, Pramod V. Menezes, Mohamed M. Elnagar, Fabian Schütt, Ludwig A. Kibler, Timo Jacob, Albert K. Engstfeld: "B12: Impact of plasma in liquid on electrode structure and solution properties" *SFB1316 Meeting*, Virtual Ulm/Bochum/Berlin, 12.07.2021.

10. **Evelyn Artmann**, Lukas Forschner, Pramod V. Menezes, Mohamed M. Elnagar, Ludwig A. Kibler, Timo Jacob, Albert K. Engstfeld "Electrode stability at high voltages in alkaline electrolyte" *72nd Annual ISE Meeting*, Virtual Jeju (Südkorea)/Ulm, 29.08.2021-03.09.2021.
11. **Evelyn Artmann**, Lukas Forschner, Tobias Schmider, Pramod V. Menezes, Timo Jacob, Albert K. Engstfeld: "Impact of plasma in liquid on electrode structure and solution properties" *SFB1316 Meeting*, Virtual Ulm/Bochum/Berlin, 09.12.2021.
12. **Evelyn Artmann**, Lukas Forschner, Tobias Schmider, Vincent P. Menezes, Timo Jacob, Albert K. Engstfeld: "Impact of high voltage electrolysis and plasma in-liquid on the electrode structure" *Seminarday Institut of Electrochemistry*, Ulm, 22.09.2022.
13. **Evelyn Artmann**, Lukas Forschner, Tobias Schmider, Konstantin M. Schüttler, Mohammad Al-Shakran, Timo Jacob, Albert K. Engstfeld: "B12: Nanoporous Au Film Formation: From macro to micro Restructuring and Influence of Surface Orientation" *SFB1316 Meeting*, Bochum, 16.11.2022.
14. **Evelyn Artmann**, Lukas Forschner, Konstantin M. Schüttler, Mohammad Al-Shakran, Timo Jacob, Albert K. Engstfeld: "Nanoporous Au Film Formation in Alkaline Electrolyte by High Voltage Electrolysis" *Symposium Nano-BW*, Bad Herrenalb, 05.12.2022.
15. **Evelyn Artmann**, Lukas Forschner, Konstantin M. Schüttler, Mohammad Al-Shakran, Timo Jacob, Albert K. Engstfeld: "Electrode Restructuring by HV Electrolysis and aCGDE" *Institutsseminar*, Ulm, 02.02.2023.
16. **Evelyn Artmann**, Lukas Forschner, Konstantin M. Schüttler, Mohammad Al-Shakran, Timo Jacob, Albert K. Engstfeld: "Tuning Nanoporous Au Film Formation via High Voltage Electrolysis" *DPG Spring Meeting*, Dresden, 26.-31.03.2023.

10.3 Poster

1. **Evelyn Artmann**, Lukas Forschner, Pramod V. Menezes, Mohamed M. Elnagar, Ludwig A. Kibler, Timo Jacob, Albert K. Engstfeld: "Anodic Polarization

of Electrodes at High Voltages in Alkaline Electrolyte" *DPG Spring Meeting*, Virtual, 01-04.03.2021.

2. **Evelyn Artmann**, Lukas Forschner, Konstantin M. Schüttler, Mohammad Al-Shakran, Timo Jacob, Albert K. Engstfeld: "High Voltage Synthesis of nanoporous Au Films in Alkaline Electrolyte: Influence of H_2O_2, Voltage, Temperature and Time" *MGK Kolloquium SFB1316*, Virtual Ulm/Bochum/Berlin, 07.03.2022.

3. **Evelyn Artmann**, Lukas Forschner, Tobias Schmider, Konstantin M. Schüttler, Mohammad Al-Shakran, Timo Jacob, Albert K. Engstfeld: "B12: Nanoporous Au Film Formation in Alkaline Electrolyte: Influence of H_2O_2 and Surface Orientation on Restructuring" *SFB1316 Meeting*, Bad Honnef, 12.07.2022.

4. **Evelyn Artmann**, Lukas Forschner, Tobias Schmider, Konstantin M. Schüttler, Mohammad Al-Shakran, Timo Jacob, Albert K. Engstfeld: "B12: Nanoporous Au Film Formation: From macro to micro Restructuring and Influence of Surface Orientation" *SFB1316 Meeting*, Bochum, 16.11.2022.

5. **Evelyn Artmann**, Tobias Schmider, Timo Jacob, Albert K. Engstfeld: "B12: Influence of Surface Orientation on the Au Oxide and Nanoporous Au Film Formation on Au" *MGK Kolloquium SFB1316*, Blaustein, 01-04.03.2023.

11 Appendix

11.1 Appendix 1

This appendix contains my first author publication titled "Structural Evolution of Pt, Au and Cu Anodes by Electrolysis up to Contact Glow Discharge Electrolysis in Alkaline Electrolytes" as published in Chem. Phys. Chem.[66]

Structural Evolution of Pt, Au and Cu Anodes by Electrolysis up to Contact Glow Discharge Electrolysis in Alkaline Electrolytes**

Evelyn Artmann,[a] Pramod V. Menezes,[a] Lukas Forschner,[a] Mohamed M. Elnagar,[a] Ludwig A. Kibler,[a] Timo Jacob,*[a] and Albert K. Engstfeld*[a]

Applying a voltage to metal electrodes in contact with aqueous electrolytes results in the electrolysis of water at voltages above the decomposition voltage and plasma formation in the electrolyte at much higher voltages referred to as contact glow discharge electrolysis (CGDE). While several studies explore parameters that lead to changes in the *I–U* characteristics in this voltage range, little is known about the evolution of the structural properties of the electrodes. Here we study this aspect on materials essential to electrocatalysis, namely Pt, Au, and Cu. The stationary *I–U* characteristics are almost identical for all electrodes. Detailed structural characterization by optical microscopy, scanning electron microscopy, and electrochemical approaches reveal that Pt is stable during electrolysis and CGDE, while Au and Cu exhibit a voltage-dependent oxide formation. More importantly, oxides are reduced when the Au and Cu electrodes are kept in the electrolysis solution after electrolysis. We suspect that H_2O_2 (formed during electrolysis) is responsible for the oxide reduction. The reduced oxides (which are also accessible *via* electrochemical reduction) form a porous film, representing a possible new class of materials in energy storage and conversion studies.

1. Introduction

Applying a voltage to metal electrodes in contact with aqueous electrolytes is used to catalyze Faraday and non-Faraday reactions,[1–3] tailor surface properties of electrodes,[4–7] form nanoparticles[8,9] or alter the electrolyte composition,[1,7] as well as to ignite plasmas in solution.[1,10,11] Depending on the application, a detailed understanding of the parameters that limit the electrode stability is decisive to prevent material degradation or to adjust the formation of specific structures. The electrode stability is highly dependent on the applied voltage and the processes occurring at the electrode surface, which change dramatically when the voltage is increased significantly. Focusing on gas-evolving working electrodes, the phenomena that are expected to occur at the solid|liquid interface can be summarized as follows. For voltages above the decomposition voltage of water (low voltages), water electrolysis is observed (referred to as normal electrolysis – NE). Increasing the voltage leads to violent bubble formation until the so-called breakdown voltage (V_B), where a gas film (sheath) forms around the electrode. At even higher voltages, the formation of a homogeneous plasma is observed within this sheath, which is called contact glow discharge electrolysis (CGDE).[1,10–12] The voltage at which CGDE is formed (minimum of the *I–U* curve) is called the midpoint voltage (V_D).

Since the discovery of CGDE in aqueous electrolytes by H. Kellog in 1950,[10] there have been several reports describing the shape of current-voltage (*I–U*) curves from NE to CGDE, exploring the impact of electrode material, electrolyte, temperature, pH, composition, electrode geometry, etc.[1,9,11–16] The most noteworthy observation for the present work is that during CGDE, the products formed at the interface are more diverse than those known from NE. For example, regardless of electrode polarity, both H_2 and O_2 may be formed simultaneously during CGDE. More importantly, in anodic CGDE, in addition significant amounts of H_2O_2 are also produced.[11,12,17] The origin of the formation of the product cocktail is caused by non-Faraday processes, where H_2O molecules decompose into highly reactive short-lived radicals and ions during CGDE, which react one with another in the plasma phase or at the plasma|liquid interface.[1,12,18]

Less is known on the evolution of the structural properties of the electrode material with increasing voltage from the NE to the CGDE regime.[6] Instead, the structural properties for both limiting regions are usually studied separately, for different reasons which is illustrated by the following examples. For the NE region electrode stability is an important aspect in electrocatalysis. Stable electrodes during the reaction are desired since degradation of the catalyst often lowers the efficiency. Besides, anodizing electrodes in aqueous electrolytes is used to form

[a] E. Artmann, Dr. P. V. Menezes, L. Forschner, M. M. Elnagar, Dr. L. A. Kibler, Prof. Dr. T. Jacob, Dr. A. K. Engstfeld
Institute of Electrochemistry, Ulm University, D-89081 Ulm, Germany
Phone: +49 (0)731 25401, Fax: +49 (0)731 25409
E-mail: timo.jacob@uni-ulm.de
albert.engstfeld@uni-ulm.de

[**] *A previous version of this manuscript has been deposited on a preprintserver (https://doi.org/10.26434/chemrxiv.14721111.v1)*

Supporting information for this article is available on the WWW under https://doi.org/10.1002/cphc.202100433

oxide structures or to smooth or clean materials *via* electropolishing.[4,19] Strong negative polarization in turn can lead to corrosion of the cathode.[8,20–22] This approach can produce nanoparticles, tune the surface crystallographic orientation for catalytic reactions or other applications.[8,20–22] Investigating the high-voltage regime, where plasmas can be generated in liquid is a growing area of research, aiming at a fundamental understanding of plasma formation, its interaction with the solid electrode and the electrolyte, as well as exploring new fields of application.[5–7,18,23] Plasmas in liquid can be used to distinctly tailor the (near-)surface electrode properties, *i.e.*, to form durable oxide coatings on materials of complex sizes *via* plasma electrolytic oxidation (PEO)[24–26] or to remove irregularities from the workpiece *via* plasma electrolytic polishing (PEP).[6,27] As with cathodic corrosion, the electrodes can also decompose into (multi-)metallic or oxidic nanoparticles.[7,9,23,28–33] Such particles can also be formed from metal ions present in the electrolyte during plasma electrolysis.[7,34] Finally, another interesting and yet emerging field is the wastewater treatment by plasmas,[7,23,35–37] where the stability of the prepared electrodes is detrimental to prevent any kind of metal contamination in the water. These examples and applications show the broad application of plasma treatment and the importance of having a clear picture of any kind of plasma-induced structure changes or formation processes. Overall, the examples also raise the question if similar or other structures to those observed in the NE and CGDE regime, are accessible in the voltage regime in between.

This is subject of this work, which aims at providing (i) more detailed and systematic insights into possible changes in the structural properties of gas-evolving metal electrodes and (ii) new approaches for material design, covering the voltage range from NE to CGDE. Motivated by their importance in electrochemistry and electrocatalysis, we restrict our investigations to processes at poly-crystalline Pt,[38–42] Au[43–45] and Cu[46–48] wire anodes. While various studies have addressed the structure of these electrodes at low potentials (NE regime), much less is known about their behavior during CGDE.[7,9–11,31,32,49] Au is the most noble metal and is used extensively as a model electrode in electrochemical surface science.[43,44] Despite its nobility, Au was shown to form Au_2O_3 films on its surface for low potentials before and in the oxygen evolution reaction (OER) region.[45] These Au_2O_3 films are, however, chemically unstable at room temperature.[50] Reports on the structural properties of Au beyond NE are rare,[11] and primarily focus on cathodic CGDE, where Au nanoparticles are formed.[31,32,49] Cu raised a lot of interest in the electrocatalysis community during recent decades as it is the only pure metal that converts CO_2 electrochemically into higher valuable hydrocarbons. This is an important process in the decarbonization of society and closing the carbon cycle.[7,48] There exists a plethora of different approaches to prepare Cu catalyst materials.[51] Among those, it was reported that nanostructured Cu electrode materials can be prepared *via* gas phase plasma oxidation.[47] A direct preparation of catalytically active surfaces *via* CGDE could provide an alternative approach for *in situ* preparation of the catalyst material. Similar to Au, Cu electrodes used under CGDE conditions were primarily studied for the purpose of nanoparticle formation.[7,9] In our study, the electrodes are investigated by potentiostatic electrolysis at a set of voltages ranging from the NE region up to 580 V in 0.01 M KOH electrolyte. The resulting *I–U* behavior is discussed based on the structural properties investigated after the electrolysis. The topography and microscopic changes of the electrodes are imaged with an optical microscope and by scanning electron microscopy (SEM). For the oxide-forming metals Au and Cu, the amount of oxide formed during electrolysis is subsequently determined from chronoamperometric measurements performed at potentials below the reduction potential of the respective oxides. We demonstrate, that independent of the applied voltage during electrolysis (50 to 580 V), the Au and Cu oxides are also reduced when kept in the electrolysis solution after the electrolysis. The effect of H_2O_2 on the oxide reduction is discussed. Finally, we demonstrate that the oxide reduction leads to the formation of highly porous nanostructures, determined from combined cyclic voltammetry and SEM experiments.

2. Results and Discussion

In the following, first the *I–U* behavior of the different investigated metals is discussed, followed by detailed analysis of their rather specific and divergent structural and electrochemical properties. The general observations for all systems are finally summarized in the conclusion. A detailed description of the experimental conditions is provided at the end of the manuscript and further details are provided in the supporting information (SI).

2.1. *I–U* Characteristics

Figure 1 shows stationary *I–U* characteristics of Pt, Au, and Cu wire electrodes (immersed length 10 mm, diameter 0.5 mm) recorded for 30 s electrolysis in 0.01 M KOH where the averaged current density values for each voltage were obtained with freshly prepared electrodes. The chronoamperometric curves for the individual values are provided in Figure S1. Longer electrolysis times were avoided to prevent significant changes in electrolyte temperature, which can change the *I–U* behavior significantly. For a similar reason, applying voltages above 580 V was avoided, where in addition the wire can easily melt. Details on the experimental approach, chronoamperometric measurements, data evaluation, and the effect of temperature are provided in the experimental section and the supporting information (Figures S1 and S2).

The *I–U* behavior in Figure 1 is characteristic for gas–evolving electrodes.[11,15,52] In the NE region from approximately 50 V up to V_B at ca. 350 V, the current increases linearly due to the limited conductivity of the electrolyte according to Ohm's law.[11,12,52] Note that at low overpotentials (few volts), electrolysis is limited by the activation of charge transfer that usually leads to an exponential increase of the current density.

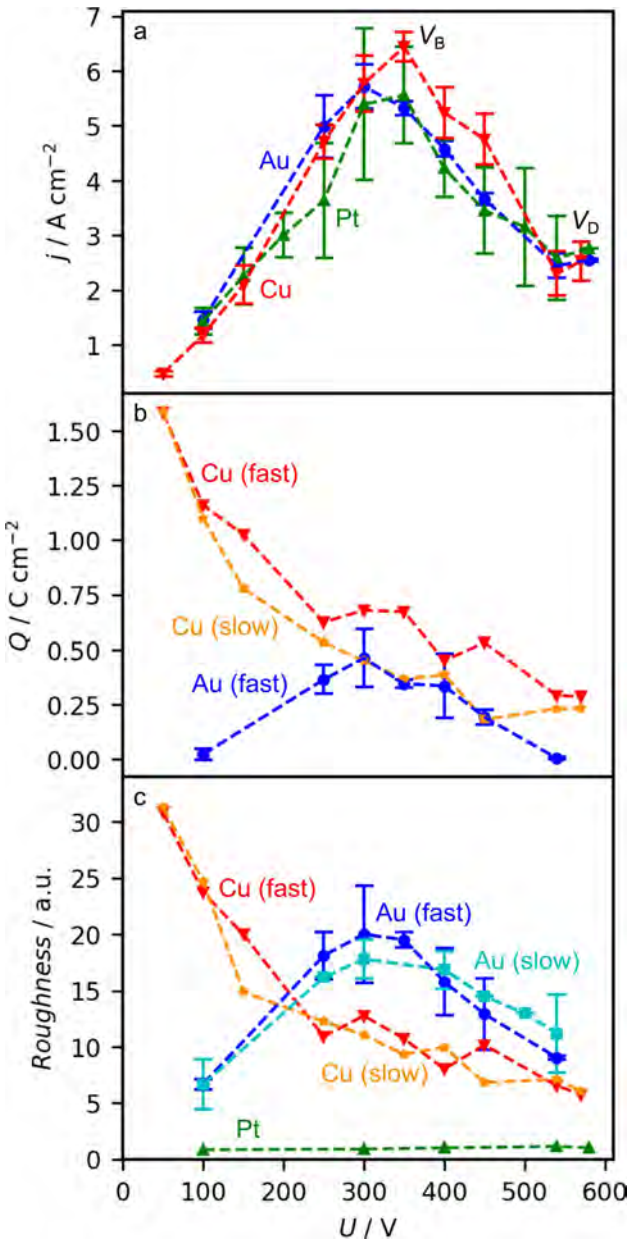

Figure 1. a) *I–U* characteristics, where each data point was recorded with a freshly prepared electrode for 30 s electrolysis in 0.01 M KOH. b) Cathodic charge density determined from the chronoamperometry measurements in Figure 6 and Figure 10 for Au and for Cu, respectively, recorded after the electrolysis and subsequent electrochemical reduction. It is important to distinguish whether the electrode is removed immediately after the electrolysis from the solution (fast) or kept in the electrolysis solution for additional 60 s (slow). c) Change in roughness factor (RF) with respect to the as-prepared samples after the anodic polarization and subsequent electrochemical reduction determined from the CVs presented in Figure 7 for Au, and Figure 11 for Cu.

At V_B the resistance increases due to gas film formation around the electrode, which leads to a breakdown of the NE concomitant with a decrease in current density. The effect becomes more pronounced with increasing voltage. Close to V_D at ca. 540 V, sparks are observed by visual inspection in the gas film forming around the electrode. At V_D the electrode is completely wrapped in a gas sheath and a blue–violet fast fluctuating plasma with an electrifying, sharply hissing sound is observed within the sheath.

Overall, the *I–U* characteristics are very similar for all three electrode materials investigated, and the current densities at the characteristic voltages V_B and V_D are almost identical. This suggests that for a given electrolyte the *I–U* behavior is almost independent of the examined electrode material and that the material properties (i) do not change, (ii) change in a similar fashion, or (iii) changes of the material properties are not important for the *I–U* curves.

A direct comparison of the current values at specific voltages, specifically the occurrence of characteristic voltages (V_B and V_D), with results from literature is, however, not straightforward. As mentioned above, in general the *I–U* behavior strongly depends on the experimental conditions, and furthermore the values of the characteristic voltages strongly depend on the cell and electrode geometry.[1,9,11–16,53] Nevertheless, Hickling and Ingram investigated the *I–U* behavior of Pt, Au and Cu wire electrodes (among others), although in another electrolyte (0.05 M Na_2HPO_4). These results showed that Au, Pd, and Pt show a very similar behavior during electrolysis at various voltages compared to W, Cu, or NiCr.[11] The authors suggested that on the latter metals oxide film formation and corrosion are at the origin of the different behavior compared to Au, Pd an Pt.[11] Our results on the structural properties of the electrodes discussed below, will show that oxide formation occurs on Au and Cu electrodes. The fact that the *I–U* curves of Au and Cu are almost identical to that of Pt, suggests that the electron transport through the oxide film on Au and Cu is equally fast as for bare Pt electrodes, which is different for systems that form passive oxide films.[15]

2.2. Structure Formation

Further insights on the impact of the electrolysis on the structural properties of the electrodes are gained from optical microscopy, SEM, and detailed voltammetric studies of the electrodes, by comparing the data recorded before and after electrolysis. While the microscope images (optical and SEM) provide insights into the three-dimensional structural changes, from the cyclic voltammetry measurements we can additionally deduce (i) the amount of oxide formed during electrolysis, (ii) determine possible changes in the crystallographic orientation of the surface, and (iii) derive changes in surface area.[54,55] In the following, the electrode materials are discussed separately since the structural modifications of the investigated metals differ strongly one from another.

2.2.1. Platinum

The SEM images of an as-prepared Pt wire and that after the electrolysis at 300 V for 30 s in 0.01 M KOH are depicted in Figure 2. Further images obtained for other electrolysis voltages (100 and 580 V) are provided in Figure S3. The SEM images

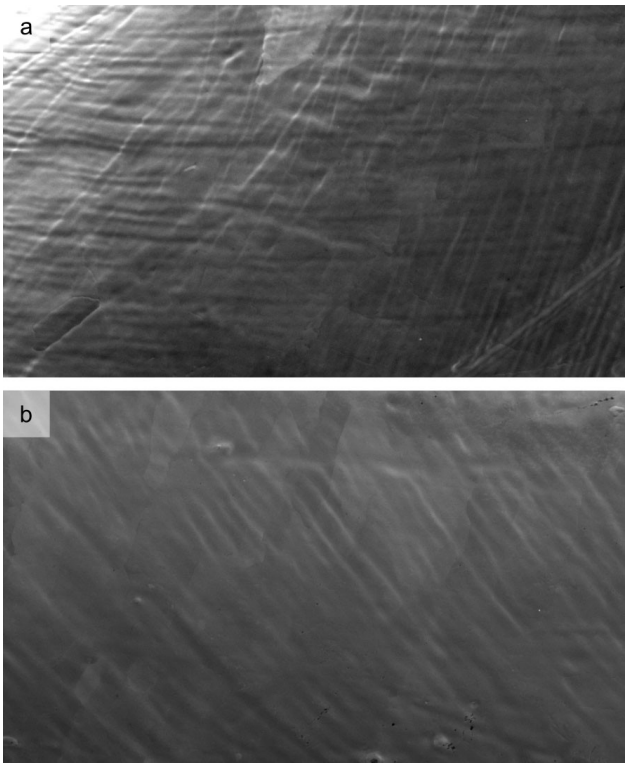

Figure 2. SEM images (250 µm × 150 µm) of a Pt wire electrode a) as-prepared and b) after electrolysis at 300 V for 30 s in 0.01 M KOH. Further SEM images are provided in Figure S3. The images were improved by adjusting the contrast and brightness.

suggest that the Pt surface does not restructure significantly during electrolysis at any applied voltage.

To substantiate this finding, we studied the electrodes by cyclic voltammetry. The cyclic voltammograms (CVs) recorded for the Pt electrodes in 0.01 M KOH at 50 mV s^{-1} before (black) and after electrolysis (blue & orange) are presented in Figure 3. All potentials in the electrochemical experiments are on the reversible hydrogen electrode (RHE) scale unless otherwise mentioned. The CVs show the typical features for hydrogen ad-/desorption (between 0.05 and 0.55 V) and OH/O ad-/desorption (between 0.7 and 1.0 or 1.5 V) on Pt in alkaline electrolytes.[56] The downshift of the current density in the hydrogen region is caused by residual oxygen in the cell. For the first voltammetric cycle recorded after the electrolysis (blue), the upper potential limit was fixed at 1.0 V to avoid significant surface restructuring which would occur by applying higher potentials.[57–60] The CV recorded with an upper potential limit of 1.45 V (orange) was subsequently recorded.

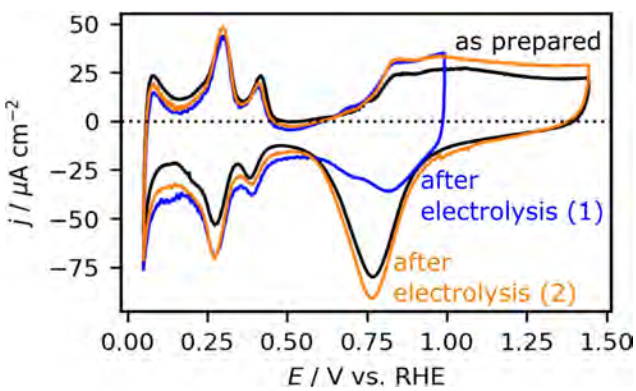

Figure 3. CVs of an as-prepared Pt electrode recorded in 0.01 M KOH at 50 mV s^{-1} (black curve) and the same electrode after the electrolysis at 300 V for 30 s in 0.01 M KOH. The first CV after the electrolysis was recorded with an upper potential limit of 1.0 V (blue). Subsequently, additional cycles were recorded with an upper potential limit of 1.45 V (orange).

The voltammetric peaks are located at almost the same potentials, and also the current densities at the peak maxima are rather similar, hence the crystallographic orientation of the surface did not change measurably. The small changes in the current density are within the limits of the experimental precision. This may be because the immersion depth of the wires cannot always be set precisely the same. Nevertheless, the almost identical current-potential profiles in the CVs recorded before and after the electrolysis suggest that the surface area does not change significantly. Henceforth, the change in electrochemical surface area is denoted as roughness factor (RF), which is described in detail in the experimental section. For Pt the RF remains almost at unity, as shown in Figure 1c (green triangles). Note that much more sensitive methods are needed to resolve possible restructuring processes on the atomic scale. For the high voltage region (CGDE), Pt was previously suggested to be stable in a wide range of electrolytes.[10,11,13,61–63] Interestingly, gas phase plasma treatment with oxygen also does not roughen the electrode surface, but leads to the formation of a Pt-oxide.[64] This is different in the OER region (onset of NE in the range of a few volts which was not investigated in this study), where surface restructuring has been suggested by Favaro *et al.*[65] Studying the OER on Pt electrodes in alkaline electrolytes, the authors observed a restructuring of the electrodes with *ex situ* atomic force microscopy (AFM) after the OER. They also observed the formation of a complex, several nm thick oxy–hydroxy film on the electrode surface, as elucidated by using ambient pressure X-ray photoelectron spectroscopy (APXPS).[65] Bulk oxide formation under these conditions was also suggested by theoretical studies to be thermodynamically favorable at high overpotentials for Pt nanoparticles.[66] From experiments the oxidation of Pt electrodes was, however, suggested to be kinetically limited and hence the formation of thick oxide films is slowed down due to the short electrolysis times.[67]

From studying the first negative potential scan of the CV starting from 0.95 V in our experiment, we did not observe any currents related to oxide reduction. Even though we cannot completely rule out that the surfaces reduce during the transfer from one cell to another, we suggest that in our experiment oxide formation does not occur during electrolysis at voltages above 100 V in alkaline electrolyte.

2.2.2. Gold

After performing electrolysis at different voltages for 30 s in 0.01 M KOH (as in Figure 1a), inspection of the Au electrodes by the naked eye revealed a color change for all voltages. In addition, the intensity and color depends on the applied voltage and more importantly on the time of exposure of the electrode to the electrolyte after the electrolysis. This is demonstrated by the optical microscope image in Figure 4 for a Au electrode on which 300 V were applied during electrolysis. If the electrode is immediately removed from the electrolyte after electrolysis the electrode is red (region 1), whereas the electrode part that was kept in the electrolysis solution turns black within a few seconds (region 3). Respective microscope images taken after the electrolysis at different voltages are provided in Figures 5a to d (first column) along with selected SEM images recorded on the red region (1), transition region (2), and black region (3) in the second to the fourth column. Overall, the red color of the Au wire suggests that a Au_2O_3 layer is formed during the electrolysis on the electrode. Considering that Au_2O_3 was also observed for oxygen plasma treated Au electrodes,[68,69] it is very likely that Au_2O_3 is formed especially in the CGDE region, where oxygen species are present in the plasma. For comparison with the initial surface structure of the Au electrode, a SEM image of the as-prepared Au electrode is provided in the SI (Figure S4a).

Focusing on the red part (region 1), obtained by electrolysis and subsequently direct removal of the electrode from the electrolyte solution, we observe in the optical microscope images that the intensity of the red color varies with the applied voltage. At 300 and 400 V the red tone is rather intense, while at 100 and 540 V the red color is less pronounced and shows a touch of orange. Corresponding SEM images are provided in Figures 5e to h (second column). For all voltages, the surface shows large flat regions and several approximately 150 nm wide cracks. In some regions, it seems as if the newly formed adlayer peels off from the Au wire substrate. While the origin of this process is unclear, we suggest that this can be caused by the emersion and immersion of the electrode during the transfer between the different electrochemical cells. The holes observed in the SEM images, especially in Figures 5e–g, are primarily induced by the electron beam of the SEM (see Figure S5).

The amount of oxide formed during electrolysis was quantified by electrochemical reduction in 0.01 M KOH, as shown in Figure 6. Here the potential was swept at 50 $mV\,s^{-1}$ from an initial potential of 1.10 V to 0.25 V, where the potential was kept until the reduction current became insignificant (up to 50 s). The total charge passed during these chronoamperometry measurements is depicted in Figure 1b. The trend in charge density passed in each measurement follows the *I–U* behavior in Figure 1a, where the largest charge density is obtained for electrolysis at 300 V with 460 $mC\,cm^{-2}$. For voltages around 100 V and 540 V the amount of oxide is significantly lower, with ca. 23 $mC\,cm^{-2}$ at 100 V and 6 $mC\,cm^{-2}$ at 540 V.

Considering that the charge density is related to the amount of oxide formed per cm^2 during 30 s of electrolysis, the thickest oxide film is formed at around 300 V. Another important observation is that the initially red electrode turned black during the reduction process. SEM imaging of these reduced electrodes revealed a highly porous structure which is depicted in Figure S6. Such a change in color has been reported recently for the reduction of Au_2O_3 to metallic Au,[70] and the black color has been attributed to the ability of the nanostructured Au surface to absorb significantly the incident light from the visible spectrum.[71,72]

Comparing the CV of an as-prepared Au wire electrode (Figure 7a) with those obtained after the electrolysis and subsequent electrochemical reduction in Figure 7b, overall higher current densities are observed for the latter electrodes. Note that all current densities are normalized to the initial geometric surface area of the wire. No additional peaks or changes in relative peak sizes are observed in the CVs, which would indicate a change of surface structure or crystallographic orientation.[21,22] The shift of the oxidation (reduction) peaks to more positive (negative) potentials for higher current densities is presumably caused by internal resistance effects. The increase in Faraday current suggests a strong increase in surface area, especially for electrolysis at around 300 V, which is apparent from the change in RF shown in Figure 1c (labeled Au fast). The evolution of the RF after reduction of the Au_2O_3 phase formed during the electrolysis with increasing voltage follows the overall trend of the *I–U* and *Q–U* curves of Figures 1a and b, where the highest RF value is obtained at V_B (ca. 300 V). Interestingly, for electrolysis at 100 and 540 V, where the amount of surface oxide was low (Figure 1b), the increase in surface area is still significant but lower than at V_B. Possible

Figure 4. Microscope image of a Au wire after electrolysis at 300 V for 30 s in 0.01 M KOH. The left (golden) part shows the as-prepared Au wire, the middle (red) part (region 1) was immediately removed from the electrolyte after the electrolysis, and the right (black) part (region 3) was kept in the electrolysis solution for 60 s after switching the voltage off. Region 2 marks the transition between regions 1 and 3.

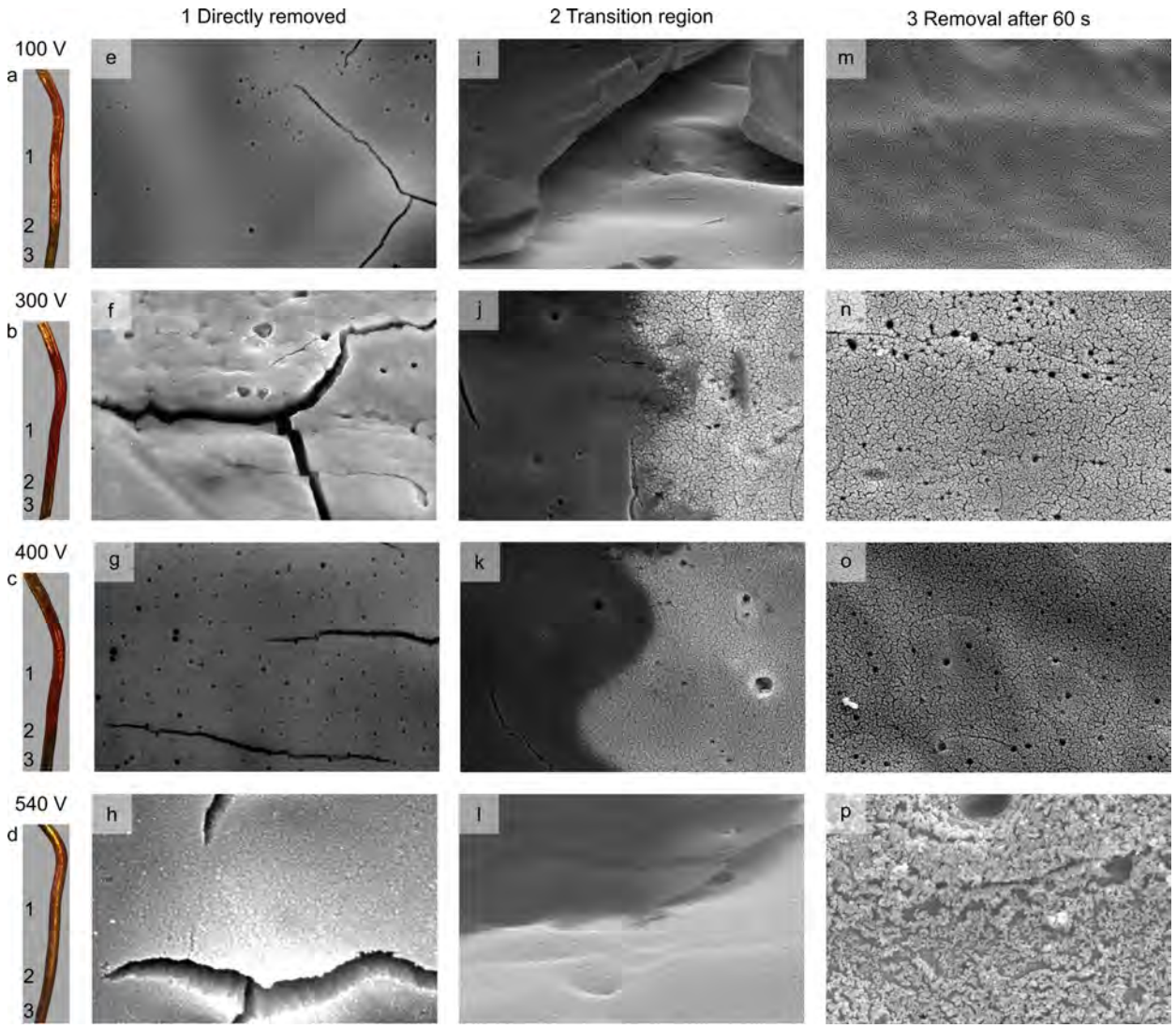

Figure 5. Left column: Optical microscope images of Au wires taken after electrolysis at the given voltages for 30 s in 0.01 M KOH. The numbers in the optical microscope images (a–d) illustrate the different regions in Figure 4. The second to fourth column show from left to right SEM images of the regions 1–3 (12 μm × 8 μm), recorded after electrolysis at different voltages. A SEM image of an as-prepared electrode is provided in Figure S4a.

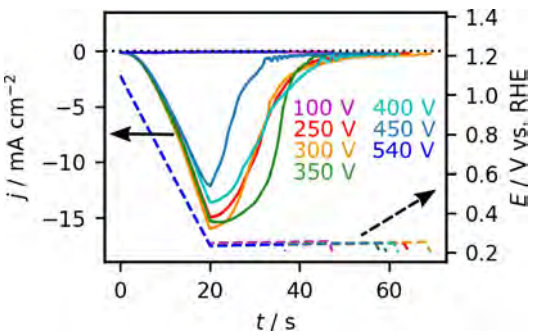

Figure 6. Characterization of the amount of oxide formed on Au wires after electrolysis in 0.01 M KOH at the given voltages. The potential was swept at 50 mV s^{-1} from the initial potential of 1.1 V to 0.25 V, where the potential was held until the cathodic current became insignificant.

reasons for the voltage-dependent growth rates are yet to be resolved.

A peculiar observation is that the Au electrodes also turn black when they are kept in the electrolysis solution for 60 s after the electrolysis (see region 3 in Figure 4). Unlike for the red part (region 1), the intensity of the color is similar for all voltages. Corresponding SEM images are provided in Figures 5m–p (fourth column). Compared to the red part of the electrode, the surface is much more porous, with a sponge-like surface structure that looks very similar to that obtained after the electrochemical reduction of the Au_2O_3. For a better comparison between the structures, in Figures 5i–l (third column) we depict the transition region (region 2) between the red and black parts. In these images, the red Au_2O_3 region appears darker than the black nanoporous metallic Au region.

Inspection of the black region by cyclic voltammetry did not show any signs of surface or near-surface oxide reduction in the

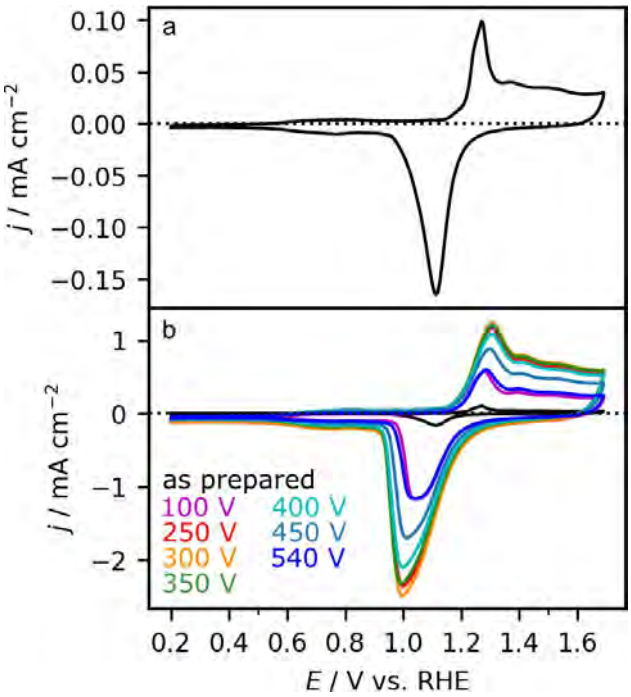

Figure 7. CVs of a) an as-prepared Au wire in 0.01 M KOH (black) and b) the same electrode in comparison to the electrochemically reduced electrodes in Figure 6 (previously treated by electrolysis at the given voltages). The CVs were recorded at 50 mV s^{-1}.

first negative-going scan in contrast to the red part of the Au wire. Instead, the CVs look almost identical to those obtained after electrochemical reduction of the red electrodes shown in Figure 7b, and also the RF is almost identical to those obtained for the red electrodes polarized at similar voltages (Figure 1c – labelled Au slow).

To elucidate the origin of the color change of the Au electrodes kept in the electrolysis solution, we first stored electrodes directly removed from the electrolysis solution under ambient conditions or in a fresh 0.01 M KOH solution for 24 to 48 hours. This did not induce a color change, and hence, the structural change had to be caused by species present in the solution after electrolysis. For low voltages (NE), it is expected that mainly O_2 is formed from water splitting. At significantly high voltages, in the region of CGDE (in our case $>$540 V), it has been demonstrated that after the electrolysis in addition to O_2, also H_2 and H_2O_2 are present in the electrolyte.[11,17,61] In a further set of experiments, the Au electrodes that were removed immediately after electrolysis, were dipped into KOH solutions saturated with H_2, O_2, or mixed with H_2O_2. We could only observe a color change from red to black in the H_2O_2 containing solution. Hence it is reasonable to assume that the H_2O_2 is at the origin of the reduction process at least at high voltages. To what extent highly-reactive, short-living or excited radicals and ions, present during and shortly after CGDE, contribute to the reduction process after the electrolysis can not be deduced from our experiments. The origin of the oxide reduction at lower voltages in the electrolysis solution can only be speculated on, and further experiments are required to elucidate whether H_2O_2 possibly forms under these experimental conditions.

2.2.3. Copper

As in the case of Au, for Cu electrodes also the impact of removing the electrodes immediately after the electrolysis from the electrolyte and after keeping the electrodes for additional 60 s in the electrolysis solution was investigated. Independent of the experimental procedure, the Cu electrodes turned black. Only with the optical microscope subtle color changes are observed on a wire treated by both approaches, as shown in Figure 8. The color changes were independent of the applied voltage during electrolysis. The black color strongly implies that a Cu(II)-oxide (CuO) is formed. Note that Cu(I)-oxide (Cu_2O) is red. The formation of Cu oxides with different oxidation states was also shown previously for Cu electrodes prepared by oxygen plasma.[73] The origin of the two black regions is discussed below.

Figure 9 shows SEM images taken on regions of the Cu wires removed directly after the electrolysis (left column) and kept in the solution for additional 60 s (center column). Figure S7 shows additional SEM images depicting a larger surface area. An SEM image of an as-prepared Cu electrode is provided in Figure S4b. The SEM images do not suggest distinct structural differences between both experimental approaches, even though both regions show slightly different colors in the optical microscope (Figure 8). Hence, the following description applies to both regions 1 and 3 depicted in Figure 8. In contrast to Pt and Au, the SEM images of Cu (Figure 9) demonstrate macroscopic surface structural changes as a function of the applied voltages. After electrolysis at low voltages (up to 100 V),

Figure 8. Microscope image of a Cu wire after electrolysis at 300 V for 30 s in 0.01 M KOH. The left part of the microscope image shows the as-prepared Cu wire. Region 1 shows the part of the wire which was immediately removed from the electrolyte after the electrolysis, where region 3 was obtained from keeping the electrode in the electrolyte for 60 s. Region 2 is the transition between region 1 and 3. The contrast and brightness of the image was visually improved for better visibility of the two regions.

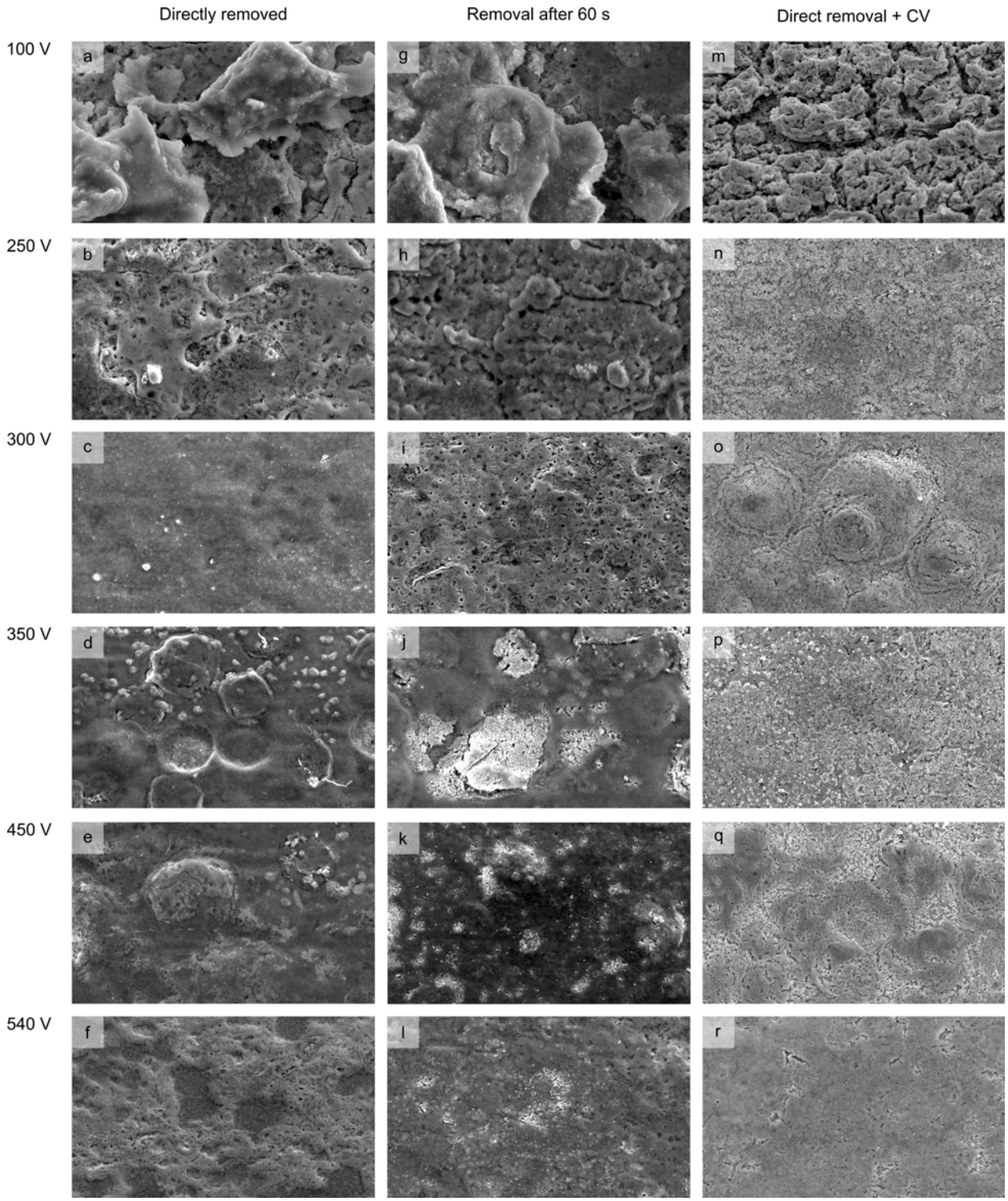

Figure 9. SEM images (50 μm × 30 μm) of Cu wire electrodes (length: 10 mm, diameter: 0.5 mm) after electrolysis at the given voltages for 30 s in 0.01 M KOH. The first column (a–f) shows micrographs of the surface structures of the wires that were directly removed after the electrolysis, the second column (g–l) after keeping them in the electrolysis solution for 60 s, and the third column (m–r) after direct removal of the wires and subsequent electrochemical characterization.

3D flake-like structures are formed. Three-dimensional macroscopic structure formation for Cu electrodes in alkaline media is not uncommon.[74–76] Performing electrolysis at intermediate voltages (250 V) results in pitting of the surface. Performing electrolysis at high voltages, including the region for CGDE, the surface becomes more smooth.

As indicated above, the color change of the electrode during the electrolysis to black strongly implies that a CuO is formed. To quantify the amount of oxide, the electrodes were electrochemically reduced in 0.1 M KOH by sweeping the potential at 50 mV s^{-1} from 0.31 V to a potential beyond −0.2 V and kept at a potential lower than −0.2 V until the reduction current becomes insignificant (up to 40 s), as shown in Figure 10. After this procedure, the electrodes were completely reduced as confirmed by EDS measurements.[77] In principle, it is possible to determine the type of Cu oxide or hydroxide from the peak position in the negative-going scan direction of the CV.[76] However, in this case (see Figure 10) the amount of oxide is rather high such that distinct well-separated reduction peaks could not be resolved and the contribution from the reduction of different Cu oxides/hydroxides overlap. Nevertheless, based on the work by Deng and coworkers, who studied the OER in alkaline electrolyte, CuO was identified along with $Cu^{III}O_2^-$ compounds by XANES and *in situ* Raman spectroscopy.[76] In combination with K^+ or Na^+, such cuprates have a bluish-black color. From visual inspection, these compounds cannot be discerned. Electrochemically, it was suggested that the Cu(III) compounds could be reduced at potentials below 1.6 V and can be identified by a peak at potentials slightly below 1.6 V.[76] With our experimental approach, it is, however, not possible to identify the Cu(III) compounds since our starting potential (0.31 V) in the chronoamperometry measurements in Figure 10 is already below 1.6 V. Nevertheless, it is very likely that both Cu(II) and Cu(III) compounds form during the electrolysis at high voltages. Additional experiments are, however, required to confirm this assumption and elucidate the nature of the surface oxides formed.

In contrast to Au, independent of the pre-treatment, *i.e.*, direct removal of the electrodes after the electrolysis (Cu fast) or keeping the electrode in the electrolysis solution (Cu slow), a reduction current is measured on all Cu electrodes. The corresponding charge density passed during the electrochemical reduction of the electrodes (Figure 6) is depicted in Figure 1b for all investigated electrodes, along with the results obtained for Pt and Au. Overall, the charge density decreases almost exponentially with increasing applied voltage. In comparison to Au, the oxide formation is also still significant during CGDE.

For almost all electrolysis voltages in Figure 1c, it is apparent that the charge densities passed for the electrodes removed immediately after the electrolysis (Cu fast – red) are larger than those kept in the electrolysis solution (Cu slow – orange). Hence the electrodes are partially reduced when they are kept in the solution after electrolysis. Similar to the case of Au discussed above, we suggest that species in the electrolysis solution formed during the electrolysis, *i.e.*, H_2O_2, cause the reduction. Considering that Cu(III) compounds are formed during electrolysis (see above) and that these compounds are reduced at more positive potentials than the oxides that are reduced in the potential window of our electrochemical reduction experiment in Figure 10, we suggest that Cu(III) compounds are reduced to Cu(II) compounds under these conditions. Since the difference in charge density is small for both experimental procedures, it further implies that the amount of Cu(III) compounds formed during electrolysis is comparatively low.

The structural changes induced by the electrolysis and subsequent electrochemical reduction of the electrodes were investigated by cyclic voltammetry. The CV of an as-prepared electrode is shown in Figure 11a and b (black), and these

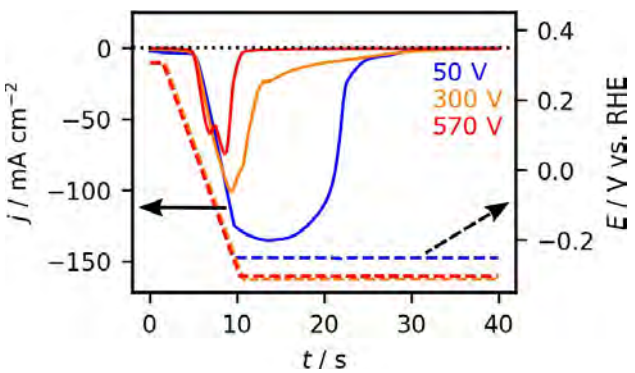

Figure 10. Characterization of the amount of oxide formed on Cu electrodes after the electrolysis at the given voltages, by sweeping the potential from 0.31 V to a potential beyond −0.2 V until the cathodic current almost vanished.

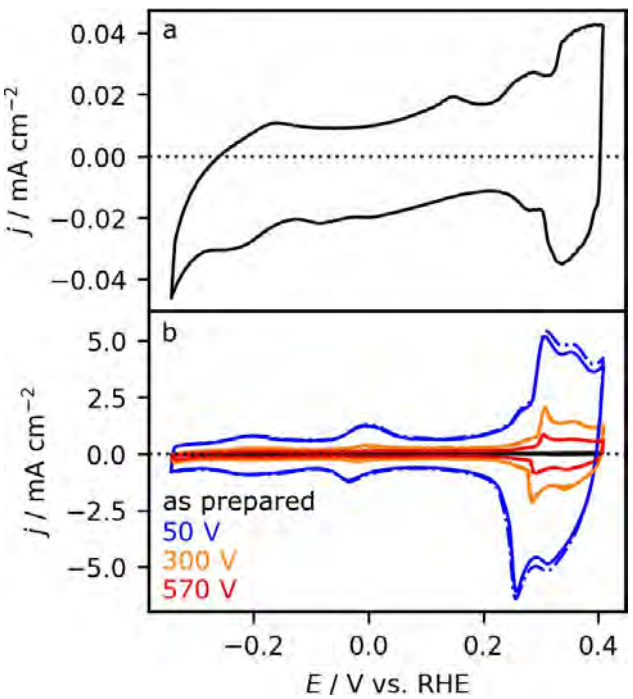

Figure 11. CVs of a) an as-prepared Cu wire in 0.1 M KOH (black) and b) the same electrode in comparison to the electrochemically reduced electrodes in Figure 10 (previously treated by electrolysis at the given voltages). The CVs were recorded at 50 mV s^{-1}. The CVs presented in b) with solid lines were measured after direct removal of the electrodes from the electrolysis solution and subsequent electrochemical reduction in Figure 10. In contrast, the CVs in dashed-dotted lines were recorded after keeping the electrodes in the electrolysis solution for 60 s and subsequent complete electrochemical reduction (reduction data not shown).

recorded after the electrolysis at 50, 300, and 570 V are shown in Figure 11b. In the latter, we also differentiate between electrodes, which were removed immediately from the electrolysis solution (solid lines), and those which were kept for additional 60 s in the electrolyte (dash-dotted lines). In general, for Cu electrodes the peaks at potentials larger than 0.2 V can be attributed to the formation and reduction of Cu_2O. The peaks at potentials smaller than 0.2 V can be attributed to surface OH adsorption and desorption on different low index surfaces.[78–81] From the comparison of the CVs of the as-prepared electrode with those recorded after electrolysis and subsequent reduction, it is apparent that the voltammetric features in the CV change, indicating that the crystallographic orientation of the electrode surface changed.[78] Interestingly, the characteristic features of the voltammograms recorded after electrolysis at different voltages are very similar for all electrodes, indicating that all electrodes have a similar surface crystallographic orientation. In addition, the RF of Cu increased in comparison to the as-prepared Cu electrodes shown in Figure 1c and is independent from the experimental procedure (immediate removal of the electrode after electrolysis or keeping the electrode in the electrolysis solution).

In turn, the RF decreases exponentially from 50 to 570 V, following the voltage-dependent evolution of the charge density. Note that for electrolysis in the CGDE region, the electrodes still have a six times larger surface area than the as-prepared Cu wire. The change in surface area is, to some extent, also apparent in the SEM images in Figure 9m–r (right column), where the surfaces became smoother with increasing voltage. Comparing the SEM images taken directly after the electrolysis (Figure 9g–l – middle column) with those taken after the electrochemical reduction (Figure 9m–r – right column) shows that the more rough surfaces obtained after electrolysis at low voltages stay rough after the electrochemical reduction (compare images in Figures 9a, g and m – first row). In a similar way the more flat surfaces obtained at high voltages also remain mostly flat after the electrochemical reduction (compare images in Figures 9f, l, and r – last row). Furthermore, SEM images taken at lower magnification in Figure S7 show, the formation of a porous structure after the electrochemical reduction. Overall, the structure formation of Cu is very similar to that observed for Au above, except that the oxide layer thickness and the porosity of the film shows a different voltage dependence.

3. Conclusions

In this work, we investigated the impact of electrolysis on the structural properties of Pt, Au, and Cu electrodes in a 0.01 M KOH solution in a voltage range from 50 to 580 V. We show that the *I–U* characteristics are mainly determined by the conductivity of the electrolyte or the gas film around the electrode at high voltages and that they are rather independent of the metal employed as well as the changes induced on the structural properties by the electrolysis. The difference in the structural properties has been explored by additional optical microscope, SEM, and electrochemical measurements. The following key observations were made, and questions remain:

1. Pt seems to be stable during electrolysis in agreement with previous studies in different electrolytes. Whether or not the electrodes are restructured at an atomic level or dissolve partially during electrolysis, cannot be deduced from our measurements and is the subject of further investigations.
2. During electrolysis, an oxide film is formed on the Au and Cu electrodes, where the rate of formation depends on the metal and the applied voltage. The red color of the Au wire suggests that Au_2O_3 is formed. In SEM images, the film appears rather flat and based on the charge density passed during the electrochemical reduction of the electrodes the oxide is thickest after electrolysis at the breakdown voltage of normal electrolysis (300 V). The black color of the Cu wire suggests that CuO is formed, which is rather textured (rough) and thickest for low voltages (50 V) and more flat and thinner in the CGDE region (540 V). Possible Cu(III) oxide formation, which was suggested to occur in the OER region under alkaline conditions, is very likely.[76] Further XPS measurements would be required to elucidate the oxidation state of the respective metals.
3. When the Au and Cu electrodes are kept for 60 s after the electrolysis in the electrolysis solution, their color changed from red to black for Au and from black to light black for Cu. Further electrochemical reduction measurements revealed that the Au oxide was completely and Cu oxide only partly reduced in the electrolysis solution. In the case of Cu, we suggest that the partial reduction is attributed to the reduction of Cu(III) compounds. The content of which is low and less stable than CuO or Cu_2O.[76] Our preliminary results to explain the reduction process on Au_2O_3 suggest that H_2O_2, present in the electrolysis solution after the electrolysis, is at the origin of the oxide reduction. While it is known that H_2O_2 is formed during CGDE,[11,17] the formation at lower voltages has so far not been considered.
4. Reducing the oxides formed during electrolysis, either by keeping the electrodes in the electrolysis solution (for Au) or reducing the oxide electrochemically (for Au and Cu), leads to the formation of a high surface area nanoporous film. The change in electrochemical surface area to the as-prepared electrodes follows the same trend as the charge density determined from the reduction experiments. In the case of Au, the final porous structure is also independent of the reduction procedure.

Overall, performing electrolysis at high voltages on Au and Cu can be used to form thick oxide layers on the electrodes. Based on our findings, the oxide structure and film thickness differ significantly for the different metals, and the oxide structure also depends on the applied voltage. Similarly, the surface area of the porous films depends on the applied voltage during electrolysis. Hence, if this approach was used to prepare oxide or porous films with specific film thickness on other metals, a systematic study of the whole voltage range is inevitable. Reasons for the voltage-dependent oxide growth rates still have to be elucidated. Note that it is also mandatory to remove the electrodes swiftly from the electrolysis solution

to assess properly the surface structures formed during electrolysis. Finally, such oxide-covered or highly-restructured materials with high surface area obtained from an initial electrolysis treatment could provide a new class of materials for possible applications as model electrodes in electrocatalysis, battery- and other energy-related research fields.

Experimental Section

Materials: All aqueous solutions were prepared by mixing Milli-Q water (18.2 MΩ cm, TOC $\leq$ 3 ppb) with KOH pellets (99.99%, Sigma-Aldrich), 30% HCl (Merck, Suprapur) or 85% phosphoric acid (Merck, Suprapur).

Wires of Pt, Au, and Cu with a diameter of 0.5 mm were purchased from MaTecK (purity at least 99.99%).

Sample preparation: In the case of Pt and Au, the same electrodes were used for all experiments, which were freshly prepared for each measurement. Both electrodes were flame annealed for three minutes in a propane flame (MTI). In some cases, when the Au wire was strongly restructured during the electrolysis experiment, it was electropolished in 1 M HCl solution (10 V vs. a graphite counter electrode) and subsequently annealed for further three minutes in the propane flame.

In the case of Cu, a new wire was freshly prepared for each measurement. The Cu wires were sonicated in 85% phosphoric acid for one minute at room temperature to remove the native surface oxide layer. Subsequently, the Cu wires were thoroughly rinsed with Milli-Q water and dried in air.

Electrolysis and electrochemical characterization: The electrolysis experiments (NE and CGDE) and the electrochemical characterization were performed with separate cells. This was necessary since usually during the electrolysis, the electrolyte properties change, *e.g.*, temperature and dissolved products such as H_2, O_2, and H_2O_2, which can affect the electrochemical characterization. All experiments were performed without stirring the electrolyte.

The electrolysis was performed in a glass cell containing 60 mL of 0.01 M KOH. A stainless steel plate of 15 mm × 20 mm × 3.5 mm was used as a counter electrode. The Pt and Au working electrode wires were immersed 10 mm into the electrolyte solution (4.5 or 10 mm for Cu) and were placed 2.5 cm apart from the counter electrode. The voltage for the electrolysis was applied for all electrodes for 30 s with a TDK-Lambda Power Supply (630 V/1.365 A) controlled *via* a LabVIEW software. Each electrolysis experiment was performed in a fresh electrolyte. The anode wire was either prepared again (Pt and Au), or a new electrode was used (Cu) to guarantee identical conditions for each experiment. For the presentation of the *I–U* plot in Figure 1, the data points were averaged for the 30 s electrolysis. The current density was determined from the geometric area of the wire electrode. During the 30 s electrolysis, the electrolyte temperature increases, leading to changes in the current density. Corresponding chronoamperometric curves are given in Figure S1 along with a more detailed description of the temperature effects. The measurements were repeated several times, and the values were averaged afterward. The error bars are derived from several experiments performed under similar conditions.

The electrochemical characterization of Pt and Au was performed in a glass beaker cell containing 150 mL of 0.01 M KOH. A homemade reversible hydrogen electrode (RHE) was used as a reference electrode and a Pt-sheet (10 × 7.5 mm) as a counter electrode. All potentials are given on the RHE scale unless otherwise mentioned. The potential was controlled with a FHI ELAB potentiostat. The electrochemical properties for Pt and Au electrodes were investigated before and after the electrolysis.

The initial scan direction in the CV was negative for Pt, starting from 0.95 V (close to the open circuit potential). Before the electrolysis, the potential window of the CV was fixed between 0.05 and 1.45 V. After electrolysis, first several cycles were recorded between 0.05 and 1.0 V to avoid significant surface restructuring. Subsequently, additional cycles with an upper potential limit of 1.45 V were recorded for comparison with the last CV recorded before the electrolysis.

The initial scan direction was negative for Au, starting from 1.1 V. The CVs were recorded in a potential window of 0.20 to 1.69 V. After the electrolysis, the surface was reduced electrochemically by holding the potential at 0.25 V in the first negative scan until the reduction currents became insignificant. The resulting charge densities are discussed in the manuscript.

For Cu, the electrochemical characterization was performed in a conventional three–electrode glass cell in 0.1 M KOH with a Hg/HgO reference electrode (RE-61AP, ALS) and a graphite rod as a counter electrode. The potential was controlled with a HEKA PG510 potentiostat. The starting potential to record the Cu CVs was 0.31 V, and the potential window was −0.34 V to 0.41 V. The characterization by cyclic voltammetry before the electrolysis was only performed on a few samples to ensure that the preparation procedure yielded reproducible CVs and hence similar surface structures. After the electrolysis, the surface oxide was reduced by holding the electrode at potentials lower than −0.2 V until the current densities related to oxide reduction became insignificant.

Surface area: All current densities are related to the original geometric surface area (Pt, Au: 0.16 cm^2, Cu: 0.07 or 0.16 cm^2) of the electrodes, determined from the length and diameter of the wires.

Charge density: The oxide formed on Au and Cu during electrolysis was reduced by scanning at 50 $mV\,s^{-1}$ from the starting potential of the CV (see above) to the lower potential limit and keeping the electrode at that potential until the cathodic currents disappeared. The charge density is obatained from integrating the current density, which in turn corresponds to the amount of oxide formed on the electrode. Note that a small fraction of the charge density might also be related to the reduction of residual molecular oxygen dissolved in the electrolyte. These currents are, however, small compared to the oxide reduction currents. The charge density is related to the geometric surface area deduced from the as-prepared electrodes, and it is a measure of the oxide thickness, which will be discussed in more detail elsewhere.

Roughness factor – RF: For all materials, we determined the increase in surface area from the current in the double–layer region of the CVs recorded at a scan rate of 50 $mV\,s^{-1}$ before and after electrolysis. This ratio is denoted as roughness factor (RF). The evaluation was performed on CVs where neither Faraday reactions nor adsorption processes occur before and after the electrolysis (or electrochemical reduction).[55] The respective potentials from which the RF was determined are 0.87 V for Au, 0.50 V for Pt, and −0.24 V for Cu. The last recorded CV before the electrolysis contained the information on the RF before the electrolysis. Direct information on the RF of Au and Cu after the electrolysis is not accessible since the oxide reduction currents strongly overlap with the double layer region in the CV. Therefore, we determined the RF after the electrolysis from the last CV recorded after the complete reduction of the surface. Note that strictly speaking, this approach reveals the increase in electrochemical active surface area. Also, since the RF describes a ratio between the initial and final roughness, information on the absolute surface roughness cannot be determined with this approach.

Structural characterization: The morphology and microscopic structural properties of the wires were investigated using a Quattro S scanning electron microscope (SEM) from Thermo Scientific operating at an acceleration voltage of 10 or 20 kV. The optical microscope images were taken with the Leica S9i.

Author Contributions

E. Artmann: Conceptualization, Formal Analysis, Funding Acquisition, Investigation, Validation, Visualization, Writing – Original Draft Preparation; P. V. Menezes: Investigation, Writing – Review & Editing; L. Forschner: Investigation, Writing – Review & Editing; M. M. Elnagar: Investigation, Writing – Review & Editing; L. A. Kibler: Writing – Review & Editing; T. Jacob: Funding Acquisition, Resources, Supervision, Writing – Review & Editing; A. K. Engstfeld: Conceptualization, Supervision, Writing – Review & Editing.

Acknowledgements

This work was supported by the Deutsche Forschungsgemeinschaft (DFG) through Grant No. SFB-CRC1316 (collaborative research center). EA would like to thank the "Stiftung Stipendien-Fonds des Verbandes der Chemischen Industrie (VCI)" for the financial support provided by a Kekulé scholarship. Open Access funding enabled and organized by Projekt DEAL.

Conflict of Interest

The authors declare no conflict of interest.

Keywords: alkaline electrolyte · contact glow discharge electrolysis · electrode stability · electrolysis · plasma chemistry

[1] A. Yerokhin, V. R. Mukaeva, E. V. Parfenov, N. Laugel, A. Matthews, *Electrochim. Acta* **2019**, *312*, 441–456.
[2] K. Uosaki, *Electrochemical Science for a Sustainable Society: A Tribute to John O'M Bockris*, Springer, **2017**.
[3] W. Schmickler, E. Santos, *Interfacial electrochemistry*, Springer Science & Business Media, **2010**.
[4] G. Yang, B. Wang, K. Tawfiq, H. Wei, S. Zhou, G. Chen, *Surf. Eng.* **2017**, *33*, 149–166.
[5] P. J. Bruggeman et al., *Plasma Sources Sci. Technol.* **2016**, *25*, 053002.
[6] P. N. Belkin, S. A. Kusmanov, E. V. Parfenov, *Appl. Surf. Sci.* **2020**, *1*, 100016.
[7] S. Horikoshi, N. Serpone, *RSC Adv.* **2017**, *7*, 47196–47218.
[8] A. I. Yanson, P. Rodriguez, N. Garcia-Araez, R. V. Mom, F. D. Tichelaar, M. T. M. Koper, *Angew. Chem. Int. Ed.* **2011**, *50*, 6346–6350; *Angew. Chem.* **2011**, *123*, 6470–6474.
[9] G. Saito, T. Akiyama, *J. Nanomater.* **2015**, *2015*, 1–21.
[10] H. H. Kellogg, *J. Electrochem. Soc.* **1950**, *97*, 133.
[11] A. Hickling, M. D. Ingram, *Trans. Faraday Soc.* **1964**, 783–793.
[12] S. K. Sen Gupta, R. Singh, *Plasma Sources Sci. Technol.* **2017**, *26*, 015005.
[13] X. Jin, X. Wang, J. Yue, Y. Cai, H. Zhang, *Electrochim. Acta* **2010**, *56*, 925–928.
[14] K. Azumi, T. Mizuno, T. Akimoto, T. Ohmori, *J. Electrochem. Soc.* **1999**, *146*, 3374–3377.
[15] A. L. Yerokhin, X. Nie, A. Leyland, A. Matthews, S. J. Dowey, *Surf. Coat. Technol.* **1999**, *122*, 73–93.
[16] S. K. Sengupta, O. P. Singh, *J. Electroanal. Chem. Interfacial Electrochem.* **1991**, *301*, 189–197.
[17] S. K. Sengupta, O. P. Singh, *J. Electroanal. Chem.* **1994**, *369*, 113–120.
[18] B. Zheng, K. Wang, M. Shrestha, T. Schuelke, Q. H. Fan, *Plasma Sources Sci. Technol.* **2019**, *28*, 085016.
[19] D. Landolt, *Electrochim. Acta* **1987**, *32*, 1–11.
[20] N. Arulmozhi, T. J. P. Hersbach, M. T. M. Koper, *Proc. Natl. Acad. Sci. USA* **2020**, *117*, 32267–32277.
[21] M. M. Elnagar, J. M. Hermann, T. Jacob, L. A. Kibler, *Electrochim. Acta* **2021**, *372*, 137867.
[22] M. M. Elnagar, J. M. Hermann, T. Jacob, L. A. Kibler, *Curr. Opin. Electrochem.* **2021**, *27*, 100696.
[23] S. K. Sen Gupta, *Plasma Chem. Plasma Process.* **2017**, *37*, 897–945.
[24] T. W. Clyne, S. C. Troughton, *Int. Mater. Rev.* **2019**, *64*, 127–162.
[25] X. Lu, M. Mohedano, C. Blawert, E. Matykina, R. Arrabal, K. U. Kainer, M. L. Zheludkevich, *Surf. Coat. Technol.* **2016**, *307*, 1165–1182.
[26] G. Barati Darband, M. Aliofkhazraei, P. Hamghalam, N. Valizade, *J. Magnes. Alloys* **2017**, *5*, 74–132.
[27] K. Nestler, F. Böttger-Hiller, W. Adamitzki, G. Glowa, H. Zeidler, A. Schubert, *Procedia Chem.* **2016**, *42*, 503–507.
[28] T. A. Kareem, A. A. Kaliani, *Ionics* **2012**, *18*, 315–327.
[29] A. Allagui, Z. Said, M. A. Abdelkareem, A. S. Elwakil, M. Yang, H. D. C. Alawadhi, *J. Electrochem. Soc.* **2017**, *164*, A2539–A2546.
[30] A. Allagui, E. A. Baranova, R. Wüthrich, *Electrochim. Acta* **2013**, *93*, 137–142.
[31] Y. Toriyabe, S. Watanabe, S. Yatsu, T. Shibayama, T. Mizuno, *Appl. Phys. Lett.* **2007**, *91*, 041501.
[32] G. Saito, Y. Nakasugi, T. Yamashita, T. Akiyama, *Nanotechnology* **2014**, *25*, 135603.
[33] F. Kurniawan, R. Rahmi, *Bull. Chem. React. Eng. Catal.* **2017**, *12*, 281.
[34] Q. Chen, J. Li, Y. Li, *J. Phys. D* **2015**, *48*, 424005.
[35] M. A. Malik, A. Ghaffar, S. A. Malik, *Plasma Sources Sci. Technol.* **2001**, *10*, 82–91.
[36] X. Wang, M. Zhou, X. Jin, *Electrochim. Acta* **2012**, *83*, 501–512.
[37] J. Gao, X. Wang, Z. Hu, H. Deng, J. Hou, X. Lu, J. Kang, *Water Res.* **2003**, *37*, 267–272.
[38] J. Pettersson, B. Ramsey, D. Harrison, *J. Power Sources* **2006**, *157*, 28–34.
[39] E. Antolini, *J. Appl. Electrochem.* **2004**, *34*, 563–576.
[40] J. K. Nørskov, T. Bligaard, A. Logadottir, J. R. Kitchin, J. G. Chen, S. Pandelov, U. Stimming, *J. Electrochem. Soc.* **2005**, *152*, J23–J26 .
[41] V. Climent, J. M. Feliu, *J. Solid State Electrochem.* **2011**, *15*, 1297–1315.
[42] S. Trasatti, *J. Electroanal. Chem. Interfacial Electrochem.* **1972**, *39*, 163–184.
[43] B. Hammer, J. K. Nørskov, *Nature* **1995**, *376*, 238–240.
[44] L. D. Burke, *Gold Bull.* **2004**, *37*, 125–135.
[45] G. Tremiliosi-Filho, L. H. Dall'Antonia, G. Jerkiewicz, *J. Electroanal. Chem.* **1997**, *422*, 149–159.
[46] Y. Hori, in *Modern Aspects of Electrochemistry*, Eds. C. G. Vayenas, R. E. White, M. E. Gamboa-Aldeco, Springer, New York, **2008**, vol. 42, pp. 89–189.
[47] D. Gao, I. Zegkinoglou, N. J. Divins, F. Scholten, I. Sinev, P. Grosse, B. Roldan Cuenya, *ACS Nano* **2017**, *11*, 4825–4831.
[48] S. Nitopi, E. Bertheussen, S. B. Scott, X. Liu, A. K. Engstfeld, S. Horch, B. Seger, I. E. L. Stephens, K. Chan, C. Hahn, J. K. Nørskov, T. F. Jaramillo, I. Chorkendorff, *Chem. Rev.* **2019**, *119*, 7610–7672.
[49] S. Yatsu, H. Takahashi, H. Sasaki, N. Sakaguchi, K. Ohkubo, T. Muramoto, S. Watanabe, *Arch. Metall. Mater.* **2013**.
[50] H. Tsai, E. Hu, K. Perng, M. Chen, J.-C. Wu, Y.-S. Chang, *Surf. Sci.* **2003**, *537*, L447–L450.
[51] S. Popović, M. Smiljanić, P. Jovanovič, J. Vavra, R. Buonsanti, N. Hodnik, *Angew. Chem. Int. Ed.* **2020**, *59*, 14736–14746; *Angew. Chem.* **2020**, *132*, 14844–14854.
[52] R. Akolkar, R. M. Sankaran, *J. Vac. Sci. Technol. A* **2013**, *31*, 050811.
[53] P. Mandin, R. Wüthrich, H. Roustan, *AIChE J.* **2010**, *33*, 2446–2454.
[54] L. A. Kibler, *Int. Soc. Electrochem.* **2003**, 1–55.
[55] M. Lukaszewski, *Int. J. Electrochem. Sci.* **2016**, 4442–4469.
[56] P. Daubinger, J. Kieninger, T. Unmüssig, G. A. Urban, *Phys. Chem. Chem. Phys.* **2014**, *16*, 8392–8399.
[57] K. Itaya, S. Sugawara, K. Sashikata, N. Furuya, *J. Vac. Sci. Technol. A* **1990**, *8*, 515–519.
[58] N. Arulmozhi, D. Esau, R. P. Lamsal, D. Beauchemin, G. Jerkiewicz, *ACS Catal.* **2018**, *8*, 6426–6439.

[59] L. Jacobse, Y.-F. Huang, M. T. M. Koper, M. J. Rost, *Nat. Mater.* **2018**, *17*, 277–282.
[60] T. Fuchs, J. Drnec, F. Calle-Vallejo, N. Stubb, D. J. S. Sandbeck, M. Ruge, S. Cherevko, D. A. Harrington, O. M. Magnussen, *Nat. Catal.* **2020**, *3*, 754–761.
[61] S. K. Sengupta, *J. Electrochem. Soc.* **1998**, *145*, 2209.
[62] X.-L. Jin, X.-Y. Wang, H.-M. Zhang, Q. Xia, D.-B. Wei, J.-J. Yue, *Plasma Chem. Plasma Process.* **2010**, *30*, 429–436.
[63] U. Gangal, M. Srivastava, S. K. Sen Gupta, *J. Electrochem. Soc.* **2009**, *156*, F131.
[64] Z. Li, P. Beck, D. A. Ohlberg, D. R. Stewart, R. S. Williams, *Surf. Sci.* **2003**, *529*, 410–418.
[65] M. Favaro, C. Valero-Vidal, J. Eichhorn, F. M. Toma, P. N. Ross, J. Yano, Z. Liu, E. J. Crumlin, *J. Mater. Chem. A* **2017**, *5*, 11634–11643.
[66] B. Kirchhoff, L. Braunwarth, C. Jung, H. Jónsson, D. Fantauzzi, T. Jacob, *Small* **2020**, *16*, e1905159.
[67] G. Jerkiewicz, G. Tremiliosi-Filho, B. E. Conway, *J. Electroanal. Chem.* **1992**, *334*, 359–370.
[68] F. Widdascheck, M. Kothe, A. A. Hauke, G. Witte, *Appl. Surf. Sci.* **2020**, *507*, 145039.
[69] A. Stadnichenko, S. Koshcheev, A. Boronin, *Moscow Univ. Chem. Bull.* **2007**, *62*, 343–349.
[70] A. Sukeri, M. Bertotti, *J. Braz. Chem. Soc.* **2018**, *29*, 226–231.
[71] A. Vitrey, R. Alvarez, A. Palmero, M. U. González, J. M. García-Martín, *Beilstein J. Nanotechnol.* **2017**, *8*, 434–439.
[72] H. Zheng, C. Picard, S. Ravaine, *Front. Chem. Sci. Eng.* **2018**, *12*, 247–251.
[73] H. Mistry, A. S. Varela, C. S. Bonifacio, I. Zegkinoglou, I. Sinev, Y.-W. Choi, K. Kisslinger, E. A. Stach, J. C. Yang, P. Strasser, B. Roldan Cuenya, *Nat. Commun.* **2016**, *7*, 1–9.
[74] A. Vvedenskii, S. Grushevskaya, S. Ganzha, D. Eliseev, *J. Solid State Electrochem.* **2014**, *18*, 2755–2770.
[75] A. Vvedenskii, S. Grushevskaya, S. Ganzha, D. Eliseev, L. I. Abakumova, *J. Solid State Electrochem.* **2014**, *18*, 3437–3451.
[76] Y. Deng, A. D. Handoko, Y. Du, S. Xi, B. S. Yeo, *ACS Catal.* **2016**, *6*, 2473–2481.
[77] P. V. Menezes, M. M. Elnagar, M. Al-Shakran, M. Eckl, P. W. Menezes, L. A. Kibler, T. Jacob, *Adv. Funct. Mater.* **2021**, accepted.
[78] A. K. Engstfeld, T. Maagaard, S. Horch, I. Chorkendorff, I. E. L. Stephens, *Chem. Eur. J.* **2018**, *24*, 17743–17755.
[79] K. J. P. Schouten, E. P. Gallent, M. T. M. Koper, *Journal of Electroanalytical Chemistry* **2013**, *699*, 6–9.
[80] A. Bagger, R. M. Arán-Ais, J. Halldin Stenlid, E. Campos Dos Santos, L. Arnarson, K. Degn Jensen, M. Escudero-Escribano, B. Roldan Cuenya, J. Rossmeisl, *ChemPhysChem* **2019**, *20*, 3096–3105.
[81] A. Tiwari, H. H. Heenen, A. S. Bjørnlund, T. Maagaard, E. Cho, I. Chorkendorff, H. H. Kristoffersen, K. Chan, S. Horch, *J. Phys. Chem. Lett.* **2020**, *11*, 1450–1455.

Manuscript received: June 6, 2021
Revised manuscript received: August 10, 2021
Accepted manuscript online: September 14, 2021
Version of record online: November 2, 2021

11.2 Appendix 2

Attached below is my first author publication with the title "Using auxiliary electrochemical working electrodes as probe during contact glow discharge electrolysis: A proof of concept study" as published in J. Vac. Sci. Technol. A.[199]

JVST A
Journal of Vacuum Science & Technology A

ARTICLE

avs.scitation.org/journal/jva

Using auxiliary electrochemical working electrodes as probe during contact glow discharge electrolysis: A proof of concept study

Cite as: J. Vac. Sci. Technol. A 40, 053005 (2022); doi: 10.1116/6.0001911
Submitted: 10 April 2022 · Accepted: 18 July 2022 ·
Published Online: 24 August 2022

Evelyn Artmann, Lukas Forschner, Timo Jacob,[a] and Albert K. Engstfeld[b]

AFFILIATIONS

Institute of Electrochemistry, Ulm University, D-89081 Ulm, Germany

Note: This paper is part of the Special Topic Collection on Atmospheric Plasma-Liquid Interfaces.
[a]**Electronic mail:** timo.jacob@uni-ulm.de
[b]**Electronic mail:** albert.engstfeld@uni-ulm.de

ABSTRACT

Plasma in-liquid by means of anodic contact glow discharge electrolysis (aCGDE) is a growing research field allowing the selective modification of the electrode and the electrolyte. The aim of this proof of concept study is to demonstrate that auxiliary electrochemical electrodes placed in the vicinity of the plasma electrode can be modified by aCGDE (ignited at the anode by applying a DC voltage between the driving electrodes). Furthermore, we illustrate in how far such auxiliary electrodes can be used as a probe to detect products (in particular, H_2, H_2O_2, and O_2) formed in the solution by aCGDE *via* electrochemical techniques. In this work, aCGDE is achieved by applying a voltage of 580 V to a small Pt wire (plasma electrode) versus a large stainless steel counter electrode. An auxiliary Pt electrochemical working electrode, operated in a three electrode configuration, is placed at different distances from the plasma working electrode. Depending on the distance, we find small changes in the working electrode structure. More importantly, we will show that, in principle, the local H_2O_2 concentration in the electrolyte can be monitored *operando*. After aCGDE, the concentration changes with time and depends on the distance from the plasma electrode.

I. INTRODUCTION

Studying plasma in-liquids has received increasing scientific interest over the last two decades for its possible application in, e.g., wastewater treatment,[1–5] nanoparticle formation,[2,4,6–13] catalyst material preparation,[14,15] plasma electrolytic oxidation,[16–18] or plasma electrolytic polishing.[19,20] These investigations provide information on the modification of the plasma electrode or changes induced within the electrolyte. Gas-phase plasma can be used in a similar way to modify the plasma electrode or the properties of a substrate placed close to the plasma source. Related to catalytic applications, the gas-phase plasma can also be used, e.g., to change the mechanism of a catalytic reaction on the target (gas-phase plasma catalysis)[21–23] or to tailor the structural properties of the target, for example, to form catalyst materials with distinct (electro)catalytic properties.[24–27] In contrast, much less is known about the effect of in-liquid plasma on target materials.

A better understanding of the impact of in-liquid plasma on an auxiliary target electrode placed in the same electrolyte in proximity to an in-liquid plasma electrode is of interest for the following applications. First, in-liquid plasma could be used to prepare an electrocatalyst *in situ*. This approach would have the advantage that the electrodes do not have to be transferred after the plasma treatment from a gas-phase atmosphere into an electrochemical cell, avoiding contamination or uncontrolled restructuring of the electrode. Furthermore, the electrode potential of the auxiliary electrode can be changed during the preparation process, allowing for more specific tailoring of its structural properties. Second, an auxiliary electrode could be used as an electrochemical probe to determine the species formed by the plasma in the electrolyte, to measure the solution pH, or the voltage drop in the electrolyte.

Such fundamental aspects have, to the best of our knowledge, so far not been considered in the ongoing research, but are vital in

the search for possible applications. The purpose of this work is to illustrate the influence of plasma in-liquid (ignited at the anode by applying a DC voltage between the driving electrodes) on the current–voltage behavior of an auxiliary electrode in solution placed in proximity of the plasma electrode and whether this auxiliary electrode can be used to determine products formed during the plasma. In general, plasma in-liquid can be generated by different approaches.[7,28] Here, we focus on anodic contact glow discharge electrolysis (aCGDE), which is achieved by applying a high voltage between a gas evolving electrode and a significantly larger counter electrode.[29–33] Pt is used as the plasma working electrode (PWE), since it was suggested to be stable under these conditions,[15,30,31,34–37] which means that neither the surface structure changes significantly nor nanoparticles are extruded from the electrodes as it is observed in other systems.[7–9] The auxiliary electrochemical working electrode (AE) is also made of Pt, which is an intensively studied electrochemical electrode material[38–43] and therefore an optimal benchmark system. Possible structural changes (if significant) can be inferred from changes in the *j*–*E* characteristics of the electrode.[38] The key products that form concomitantly during aCGDE are H_2, O_2, and H_2O_2.[30,34,44] The electrocatalytic reaction of these species with Pt electrodes in alkaline electrolyte are also described in detail in the literature.[45–50] It is also known that the electrode is well suited to detect products, when the electrode is controlled with a potentiostat. A key aspect is the detection of H_2O_2, which is usually determined after the electrolysis by means of titration.[30,51–53] This approach does, however, not provide any information on the spatial distribution or temporal evolution of H_2O_2 formed during aCGDE. Other methods are able to circumvent this issue to some extent.[22,23] In total, knowing about local concentrations is, for example, important to understand possible structural changes of the working electrode induced by H_2O_2 after aCGDE.[15] In electrocatalysis, Pt is used as collector electrode, which oxidizes H_2O_2 selectively, i.e., during the oxygen reduction reaction (ORR).[54–56] As a proof of concept, in this work, a Pt wire is placed as H_2O_2 probe at different distances from the PWE.

II. RESULTS AND DISCUSSION

The experiments were performed in a large cylindrical glass cell (diameter: 13.5 cm, height: 7.5 cm) containing 0.01 M KOH. The two electrodes for aCGDE (PWE and plasma counter electrode—PCE) and the three electrochemical electrodes (AE, reversible hydrogen electrode—RHE, and electrochemical counter electrode—ECE) are immersed in the cell as shown in the schematic illustration in Fig. 1. A glass tube (outer diameter: 2.6 cm; inner diameter: 2.2 cm; wall thickness: 2 mm) is placed around the plasma counter electrode to remove volatile products created at the PCE, an approach suggested by Hickling and Ingram.[30] Even though migration of species into the electrolyte cannot be completely ruled out, most of the products contained in bubbles formed at the counter electrode during the aCGDE are believed to be transported to the electrolyte surface within the perimeter of the glass tube. The plasma was ignited at the anode by applying a DC voltage between the driving electrodes and was apparent by a distinct purple glow, confined in a gas sheath surrounding the Pt wire

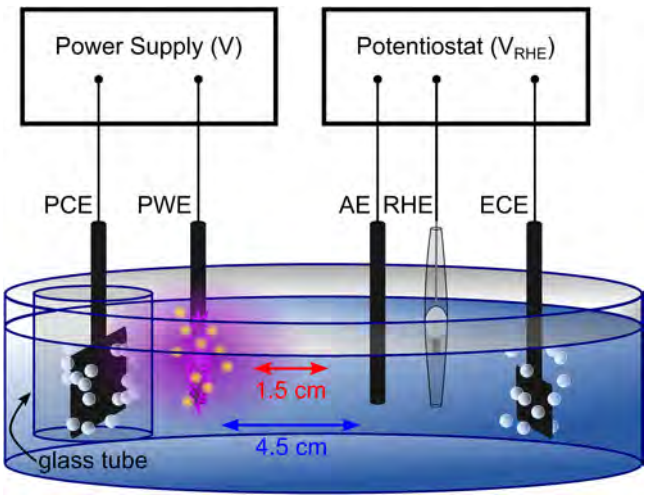

FIG. 1. Schematic illustration of the electrochemical cell including the plasma electrodes (PWE and PCE) and the electrochemical electrodes (AE, ECE, and RHE). See text for details.

plasma electrode, as well as a sharp hissing noise. In our studies, the distance between the plasma working and counter electrode was between 1.2 and 1.5 cm, and the AE was placed at a distance of either 1.5 or 4.5 cm from the PWE. The applied voltage between the PWE and the PCE is given in V, while the potential at the AE is given on the RHE scale (V_{RHE}). A detailed description of the experimental setup, materials used, and experimental procedures is provided in the Experiment section.

The effect of aCGDE on the AE was studied by comparing the variation of electrode potential (*E*) vs time (*t*) (Fig. 2, top row) with the current density (*j*) vs *t* (Fig. 2, middle and bottom rows). Each experiment consists of a combination of the following experimental steps:

Step A:
Cyclic voltammetry[57] (measuring the current response while applying a triangular wave potential) recorded at 50 mV s^{-1} between 0.0 and 1.05 V_{RHE} in the absence of aCGDE, followed by both or either one of the following steps B.

Step B1:
Keeping the AE at 1.0 V_{RHE} (unless otherwise mentioned) during 30 s of aCGDE (PWE anode at 580 V versus a stainless steel cathode, with a power of approximately 57 W).

Step B2:
Keeping the AE at 1.0 V_{RHE} for 15 min in the absence of aCGDE.

Step C:
Recording cyclic voltammograms (CVs) between 0.00 and 1.05 V_{RHE} in the absence of aCGDE.

Each column in Fig. 2 represents one of the experimental steps above. The time axis always counts from the beginning of each of these steps. The variation of the current density for an AE

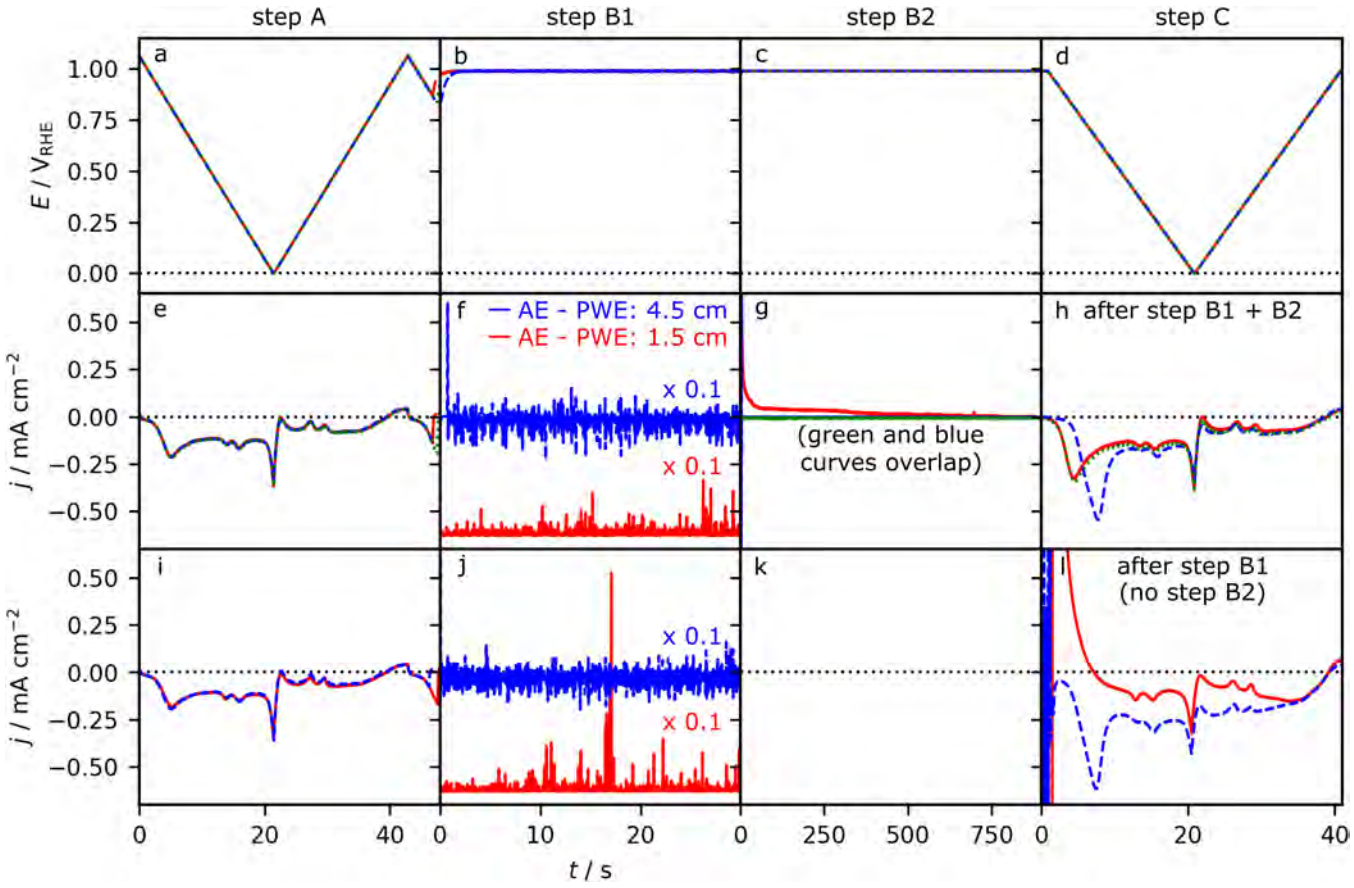

FIG. 2. Effect of aCGDE on the AE by (a)–(d) comparing the variation of the electrode potential (E) vs time (t) (top row) on (e)–(l) the current density (j) vs t (middle and bottom rows). The middle row (e)–(h) shows the sequence of experimental steps A, B1, B2, and C, whereas the bottom row (i)–(l) only comprises steps A, B1, and C. Each column represents the experimental steps described in the main text. Steps A, B2, and C are performed without aCGDE. In step B1, simultaneously aCGDE was performed at 580 V for 30 s. The red (solid lines) and blue curves (dashed lines) show the measurements for AEs placed at a distance of 1.5 or 4.5 cm from the PWE, respectively. For comparison, the green curve (dotted lines) shows the case where the AE was not exposed to aCGDE (no step B1).

located 1.5 cm from the PWE (close to the PWE) is shown as a red curve and that for a distance of 4.5 cm as a blue curve (far from the PWE). The green curve represents the case where the AE was not exposed to aCGDE (no step B1) and was kept for 15 min at 1.0 V_{RHE} (in step B2). The same color scheme is used throughout the article. At 1.0 V_{RHE}, H_2O_2 can be selectively oxidized at a Pt electrode. Note that in the literature, H_2O_2 is usually reported to be detected at 1.2 V_{RHE},[43] however, at that potential, Pt surface oxidation cannot be ruled out. After aCGDE, a waiting period of 15 min was applied to ensure that the species formed by the plasma have sufficient time to distribute evenly in the electrolyte. The waiting time was chosen based on continuous cyclic voltammetry measurements performed in the same voltage range as in step A. After 15 min, the cyclic voltammogram looked identical to that recorded in step A.

Figures 2(e) and 2(i) show the potential-dependent variation of the current density during cyclic voltammetry measurements. By applying a triangular wave potential in this voltage range, usually the current (density) shows electrode specific features. These are related to the capacitive charging of the surface and charge transfer reactions (adsorption/desorption of ions) occurring at the electrode surface. The interpretation of these features is provided in the discussion to Fig. 3. Here, it is important to note that for all experiments, the potential-dependent variation of current density versus time in step A is almost identical [Figs. 2(e) and 2(i)], indicating that the experimental conditions at the start of each experiment are the same. This is even more apparent by comparing the current density versus potential curves in the cyclic voltammograms described in Fig. S1.[58]

Performing aCGDE while applying a constant potential at an AE placed close to the PWE [step B1: Figs. 2(f) and 2(j), red curves], a large negative current density is recorded at the AE. The current density is several orders of magnitude larger compared to the redox currents obtained without aCGDE in step A. In contrast,

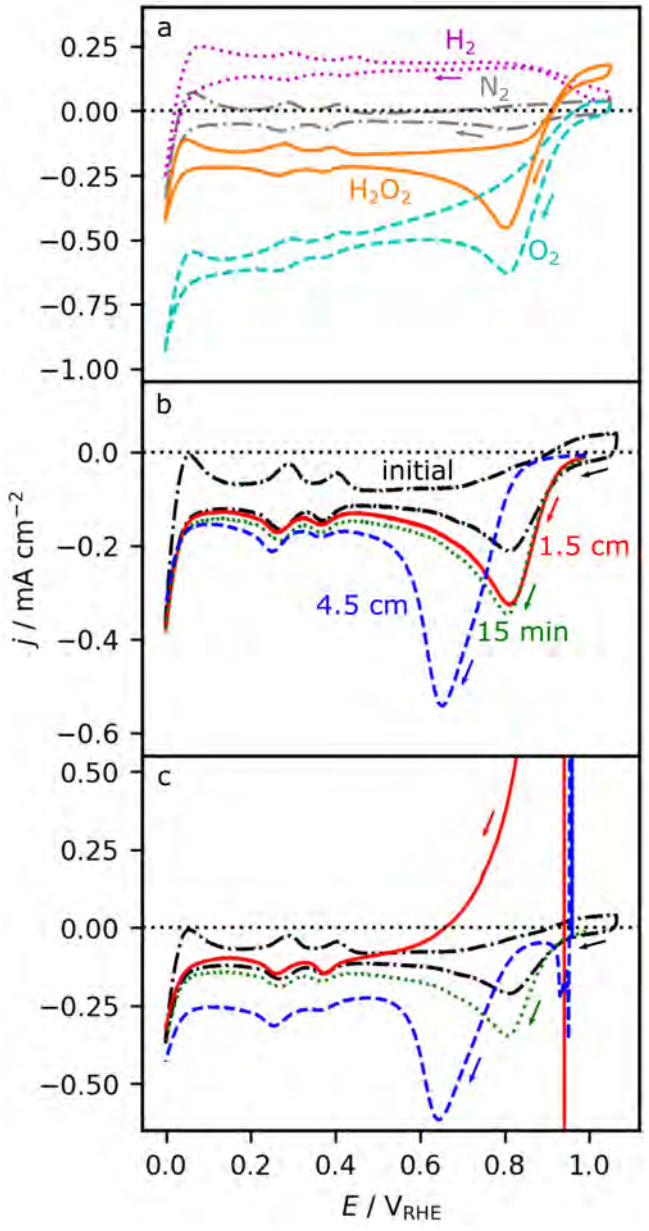

FIG. 3. (a) Cyclic voltammograms of a Pt wire recorded at 50 mV s^{-1} in 0.01 M KOH (a) either saturated with N_2 (gray dash-dotted), H_2 (pink dotted), O_2 (light blue dashed), or after addition of H_2O_2 (orange solid). (b) and (c) shows the data from Figs. 2(h) and 2(l) (step C) with the same color code for the individual measurements. CVs recorded in non-deaerated electrolyte before (black dash-dotted) and after aCGDE for 30 s at 580 V (red solid and blue dashed). The red solid curve shows the first half cycle after the plasma at a distance of 1.5 cm from the PWE and the one in blue dashed at a distance of 4.5 cm, respectively. Panel (b) shows the CVs obtained after performing the experimental steps B1 and B2 and (c) after step B1 (no step B2). The green dotted curve in (b) and (c) shows the current density voltage response after 15 min waiting at 1.00 V_{RHE}, without applying aCGDE before. The initial scan direction of all measurements was indicated with arrows.

much less negative current densities are recorded when the AE is placed far from the PWE (blue curves). Preliminary results indicate that the voltage drop between the PCE and PWE changes the electrolyte potential not only between the plasma electrodes but also further away from these electrodes in the electrochemical cell. Hence, depending on the position of the electrochemical electrodes, the potential at the AE cannot be controlled properly. Since we record a negative current at the AE during aCGDE it is likely that the AE potential shifts in the hydrogen evolution region. In addition, the currents recorded between the PWE and PCE are fluctuating strongly, which induces changes in the electric field and, in turn, induces a strong noise in the current densities recorded at the AE in step B1. Further measurements are required to clarify these assumptions. Note that the effect of electric fields on auxiliary electrodes is not unknown and is, for example, explored in ohmic microscopy[59–62] and bipolar electrochemistry.[63,64] Overall, to derive a more meaningful conclusion, the effect of voltage drop on auxiliary electrodes will be discussed elsewhere using an electrochemical cell with a more defined geometry, which also allows a more precise positioning of the electrodes.

In step B2, the plasma was turned off and the AE potential was kept for 15 min at 1.0 V_{RHE} [Fig. 2(g)]. When the AE is located far away from the PWE, the current density (blue curve) recorded at the AE is almost zero and remains constant for the rest of the waiting period. In the case where the AE is located close to the PWE, the current density (red curve) is high when the plasma is turned off. With time, the current density decreases and remains constant at slightly positive current densities during the entire waiting time. For comparison, keeping an AE at 1.0 V_{RHE} for 15 min without exposing it to aCGDE [no step B1—green curve in Fig. 2(g)], the current density is almost zero. This difference in current densities recorded at the AE placed at different distances from the PWE demonstrates that aCGDE certainly has an impact on the current-time profiles recorded at auxiliary electrodes.

After the chronoamperometry steps (measuring the current density at a constant AE potential as a function of time—B1 and B2 or only B2), cyclic voltammetry was performed at the AE in step C [Figs. 2(h) and 2(l)]. If the plasma, waiting time, or species formed by the plasma had no effect on the current density profiles, we would expect the same behavior as in step A. The results, however, clearly show that especially in the first few seconds of the first cycle in step C, the evolution of current densities strongly depends on the waiting time as well as on the position of the AE with respect to the PWE during aCGDE. Possible changes of the pH should not play a significant role in the magnitude of the current density or the features in the CV. According to the Nernst equation this only shifts the features along the potential scale. Changes induced by variations in conductivity within the electrolyte might change the features. In order to draw detailed conclusions, more detailed studies are required, elucidating, e.g., the actual local OH^- concentrations.

As described above, the key products that form concomitantly during aCGDE are H_2, O_2, and H_2O_2,[30,34,44] whose electrocatalytic properties with Pt electrodes are well described in the literature.[45–50] In order to assess whether or not the features observed in Figs. 2(h) and 2(l) are related to the presence of these species in the solution after aCGDE, we performed a separate set of

cyclic voltammetry measurements in electrolytes saturated with either one of the reactants possibly formed during aCGDE or N_2, shown in Fig. 3(a). Even though N_2 is not a product during aCGDE, it serves to remove residual O_2 from the electrolyte, which, in turn, allows studying surface specific redox processes. The gray curve shows the cyclic voltammogram (CV) of Pt recorded in N_2 saturated 0.01 M KOH, the light blue curve in O_2 saturated 0.01 M KOH, the pink curve in H_2 saturated 0.01 M KOH and the orange curve in 0.01 M KOH containing H_2O_2. Additional measurements with a larger upper potential limit are shown in Fig. S2.[58] All CVs were recorded at a scan rate of 50 mV s^{-1}.

The features observed in the CVs recorded in different types of electrolytes are extensively discussed in the literature and can be interpreted as follows. The CV recorded in 0.01 M KOH (gray curve) deaerated with N_2 shows a negative current at $E < 0.05\,V_{RHE}$, which is related to the hydrogen evolution reaction (HER), where water is split to form H_2 and OH^- ($2H_2O + 2e^- \rightarrow H_2 + 2OH^-$). The features between $0.05\,V_{RHE}$ and $0.5\,V_{RHE}$ are related to the adsorption of hydrogen in the negative going scan and the desorption of adsorbed hydrogen in the positive going scan ($H_2O + * \rightleftharpoons H^* + 1e^- + OH^-$ with * being a free surface site). These features are sensitive to changes in surface crystallographic orientation. The features for $E > 0.8\,V_{RHE}$ are related to the adsorption of hydroxyl ($OH^- + * \rightarrow OH^* + 1e^-$) or the formation of surface oxygen (O*) from adsorbed OH ($OH^* + OH^- \rightarrow O^* + H_2O + 1e^-$) in the positive going scan.[42,65] The slightly negative current densities for $E <$ ca. $0.95\,V_{RHE}$ in this gray curve are caused by the reduction of residual O_2 in the electrolyte in the so-called oxygen reduction reaction (ORR), where O_2 is reduced to water ($O_2 + 2H_2O + 4e^- \rightarrow 4OH^-$). Similar CVs to the gray curve are also obtained for all electrodes investigated before aCGDE in step A shown in Fig. S1.[58]

In H_2-containing 0.01 M KOH (pink curve), the positive current density between $0.05\,V_{RHE}$ and $1.0\,V_{RHE}$ is attributed to the hydrogen oxidation reaction (HOR) whereby H_2 is oxidized to form water ($H_2 + 2OH^- \rightarrow 2H_2O + 2e^-$). The oxidation process is inhibited in the region of surface Pt oxide formation at around $E > 0.95\,V_{RHE}$. In O_2-containing 0.01 M KOH (light blue curve), the negative current density at $E <$ ca. $0.95\,V_{RHE}$ is related to the ORR. In H_2O_2-containing 0.01 M KOH (orange curve) the negative current density at around $E < 0.95\,V_{RHE}$ is related to the hydrogen peroxide reduction reaction (HPRR), where H_2O_2 is reduced to form hydroxid ions ($HO_2^- + 2e^- + H_2O \rightarrow 3OH^-$) and the positive current density at around $E > 0.95\,V_{RHE}$ is related to the hydrogen peroxide oxidation reaction (HPOR) ($HO_2^- + OH^- \rightarrow O_2 + H_2O + 2e^-$). In all cases, the adsorption/desorption features observed in the CV recorded in 0.01 M KOH deaerated with N_2 (gray curve), overlap with the current density related to the electrocatalytic reactions (HOR, ORR, HPRR, and HPOR). In contrast to literature findings, the here reported current densities of the electrocatalytic reactions are low due to limited diffusion of the reactants to the electrode under stagnant electrolyte conditions.[45–50]

Figures 3(b) and 3(c) show the CVs from Figs. 2(h) and 2(l) (step C) recorded after aCGDE with and without waiting time, respectively. Similar results are also obtained when a lower voltage is applied between the PWE and the plasma counter electrode (550 V in Fig. S3[58]), as well as with and without shielding the plasma counter electrode by a glass tube (Fig. S4).[58] In addition, for comparison, a CV recorded in step A (before the aCGDE treatment) is included in black and a CV recorded after 15 min waiting time without applying aCGDE in green.

Comparing the black and the green curves (before and after holding the potential at $1.0\,V_{RHE}$ for 15 min) in Figs. 3(b) and 3(c), a larger reduction current is apparent in the green curve in the first negative going scan at around $0.8\,V_{RHE}$. This feature is related to the degree of electrode oxidation at high potentials. In general, the size of the reduction peak depends on the upper potential limit of the CV as well as on the time and potential at which the electrode is kept (see also Fig. S5).[66] Hence, the larger reduction peak in the green curve is caused by holding the potential at $1.05\,V_{RHE}$ for 15 min.

Cyclic voltammograms recorded on the AEs placed at different distances from the PWE, after aCGDE and subsequent waiting time at $1.0\,V_{RHE}$ (steps B1 and B2) are shown in Fig. 3(b). The CV recorded on an AE close to the PWE (red curve) is almost identical to the green curve (obtained without applying aCGDE). On the other hand, if the AE is placed further away from the PWE (blue curve), the size of the reduction peak in the first negative going scan is larger and shifted to more negative potentials ($0.65\,V_{RHE}$) compared to the red and green curves. This implies that the electrode is significantly more oxidized. As mentioned above, such an effect would be expected for longer waiting times or when the upper potential limit was higher (see Fig. S5[58] and more details below).

Skipping the waiting time after aCGDE and recording CVs directly thereafter (only step B1) for AEs placed at different distances from the PWE are shown in Fig. 3(c). For AEs close to the PWE (red curve), in the first negative going scan a large positive current density is observed at high potentials (0.8–$0.95\,V_{RHE}$). The current density decreases at more negative potentials until at ca. $0.5\,V_{RHE}$, the curve follows the CV recorded before aCGDE (black curve). Compared to the CVs presented in Fig. 3(a), this large positive current density can at least at high potentials ($> 0.95\,V_{RHE}$) be attributed to the oxidation of H_2O_2. Note that the HOR and the ORR are almost suppressed at these potentials, as shown in Figs. 3(a) and S2.[58] The H_2O_2 oxidation current is also measured at higher potentials ($> 0.95\,V_{RHE}$) in the following potential cycles, as shown in Fig. S6.[58] The temporal decrease of the positive current density is more clearly seen in the potentiostatic measurements in Fig. 2(g) (red curve). The CVs and the potentiostatic experiments indicate that H_2O_2 remains in the region around the AE for a certain time until it dissipates into the electrolyte or reacts with the Pt PWE to decompose into O_2 and H_2O.[67,68]

For AEs located farther from the PWE (blue curve), such a positive current density is not observed in the first negative going or subsequent scans, indicating that H_2O_2 is not measurably present in the electrolyte. Similar to the blue curve in Fig. 3(c), obtained directly after aCGDE, a large reduction peak is observed at around $0.65\,V_{RHE}$ in the first negative going scan in Fig. 3(b) (steps B1 and B2). This large peak, which is observed in both experiments, suggests that the electrode surface oxidizes significantly during aCGDE. Interestingly this suggests that the plasma or the species formed by the plasma only affect the structural properties of the Pt AE, when the AE is placed far away (4.5 cm) from the PWE. For the time being, it is not clear if the increase in Pt oxide

formation is induced (i) by the plasma (or plasma species) or whether it is related (ii) to changes in electrode potential induced by the electric fields during aCGDE, which could cause an uncontrolled oxidation of the electrode during aCGDE.

Overall, the CV measurements performed after aCGDE indicate that the plasma or the species formed by the plasma do not have a significant impact on the structural properties of the Pt AE. The additional current densities in the CVs, with respect to a CV recorded in N_2 saturated 0.01 M KOH (see black curves), are, therefore, attributed to the reaction of the Pt AE with the species formed by the plasma in the solution, where the reaction rates depend on the product distribution and its temporal evolution in the electrolyte. When the AE is located close (1.5 cm) to the PWE, significantly different current densities arise at the AE directly after aCGDE, which are tentatively attributed to the reaction of plasma created species (H_2, O_2, H_2O_2) with the Pt AE. In the CVs recorded right after aCGDE (step B1) and at potentials $< 0.65\,V_{RHE}$, a more significant negative current density is observed. Assigning these current densities to the reaction of different species with the Pt AEs is not straightforward, since the total current density is a sum of HOR current density (positive), ORR current density (negative), HPRR current density (negative), and surface redox processes. At high electrode potentials, especially $1.0\,V_{RHE}$, the situation is more clear. The observed positive current density can basically only be attributed to the oxidation of H_2O_2, with minor contributions from the oxidation of H_2. These positive current densities persist after multiple cycles (see Fig. S6).[58] Finally, the different behavior of the *j* versus *E* curve in the first negative going scan of the CV recorded after aCGDE for AEs placed at different distances from the PWE suggests that the product distribution in the solution changes with the distance from the PWE. The change in current density in Fig. 2(g) during the waiting time after aCGDE also implies that the product distribution changes with time.

III. CONCLUSION

In this work, we elucidated to what extent auxiliary electrochemical working electrodes can be used to determine by electrochemical methods the impact of aCGDE on (i) the structural properties of an auxiliary electrode and (ii) how far such electrodes can be used as a probe to detect products formed during and after aCGDE. In both cases, it was not yet possible to determine these properties during aCGDE. We suggested that changes in the electrode potential of the electrochemical electrodes might be responsible for this observation. This issue has to be addressed more specifically in a more detailed study where the electrode and electrochemical cell geometries are more defined.

After the aCGDE, we did not observe any significant changes in the Pt auxiliary electrodes. Hence Pt is a suitable probe to detect H_2O_2. Even though the absolute local H_2O_2 concentration in the electrolyte is not accessible yet, we were able to measure relative changes of the concentration in the electrolyte which depends on the distance from the plasma electrode as well as on the waiting time after electrolysis. This proof of concept study demonstrates that an electrochemical probe can indeed be used to detect H_2O_2 *operando* and also locally in the electrolyte, which is so far not accessible with other techniques. In order to gain more quantitative information, further studies elucidating local temperature changes or convection in the electrolyte are, however, required. Overall, such information is crucial for further studies aiming at a more detailed understanding of product formation during aCGDE, the composition of the plasma, the structure formation processes at the plasma electrode, or the reaction of these intermediates with species in the electrolyte.

IV. EXPERIMENT

All experiments were performed in a five electrode setup. This consisted of a classical three electrode setup usually used for electrochemical measurements with an auxiliary electrochemical working electrode (AE), a reference electrode (here a reversible hydrogen electrode—RHE), and an electrochemical counter electrode, as well as two electrodes to generate a plasma in-liquid, namely, a plasma working electrode (PWE), and a plasma counter electrode (PCE).

Materials: Pt wires with a diameter of 0.5 mm and a purity of 99.99 % from MaTecK were utilized as AE and PWE. As electrochemical counter electrode, a Pt-sheet (10×7.5 mm) and as plasma counter electrode, a stainless steel plate ($20 \times 20 \times 3.5\,mm^3$ size) were used.

The 0.01 M KOH solution was prepared from KOH pellets (99.99 %, Sigma-Aldrich) and Milli-Q water (18.2 MΩ cm, TOC $\leq$ 3 ppb).

Sample preparation: For the first measurement of each day, the Pt wires were annealed for 3 min in a propane (MTI) flame atmosphere. Since previous studies suggested that the Pt wire electrodes do not change measurably under our experimental conditions,[15] the wires were not freshly prepared for the subsequent measurements on the same day.

Electrochemical cell: In order to study the influence of the PWE on the AE, all electrodes were placed in the same electrochemical cell. The latter consists of a large glass beaker (diameter: 13.5 cm, height: 7.5 cm) containing 650 ml of 0.01 M KOH, where a glass tube was placed around the plasma counter electrode (illustrated in Fig. 1). In the case where no glass tube was employed (as in the measurements shown in Fig. S4[58]), the beaker was only filled with 500 ml electrolyte.

The Pt wire used as PWE was protected at both ends with polymer caps (fabricated from Eppendorf pipet tips). The cap around the wire apex is necessary to prevent the wire from melting during aCGDE.[69] The caps were adjusted such that 2 mm of the wire are exposed to the electrolyte (surface area of $0.031\,cm^2$). The PWE and plasma counter electrode were placed between 1.2 and 1.5 cm apart from one another.

The voltage between these electrodes was applied with a TDK-Lambda Power Supply (630 V/1.365 A). The power supply was controlled with a LABVIEW program. Unless otherwise mentioned, 580 V were applied for 30 s (plasma power approximately 57 W) between the PWE and plasma counter electrode. At this voltage, the plasma ignites immediately at the PWE, as compared to lower voltages.[15] This can be recognized by a fluctuating purple glow within the gas sheath surrounding the PWE, as well as a sharp hissing noise.

The Pt wire used as AE was immersed 10 mm in the electrolyte solution, where the distance was controlled by putting a protective polymer cap (see above) at the upper end of the wire (surface area of 0.159 cm^2). In this case, the apex of the wire does not need special protection, since the current densities are much lower compared to those recorded at the PWE. A homemade and freshly prepared reversible hydrogen electrode (RHE) was used as a reference electrode. The potential at the AE was controlled with a FHI ELAB potentiostat. All potentials are given on the RHE scale (V_{RHE}).

Experimental procedure. Since the aCGDE experiments lead to an accumulation of products in the solution, namely, H_2, O_2, and H_2O_2, the electrolyte was changed after each experiment to have the same initial conditions for all experiments. To reduce the possible impact of H_2 formed at the plasma counter electrode during aCGDE on the other electrodes (especially, the AE), a solid glass tube (outer diameter: 2.6 cm; inner diameter: 2.2 cm; wall thickness: 2 mm) was placed around the electrode, allowing the majority of the formed H_2, contained in bubbles, to leave the electrolyte within the perimeter of the glass tube.[30] The glass tube does not touch the bottom of the glass beaker but is immersed in the electrolyte slightly deeper than the plasma counter electrode.

All measurements were carried out at room temperature. The temperature of the electrolyte before and after the experiment was very similar in each case, with ca. 24 °C measured with a thermometer immersed in the solution. Note that after aCGDE, the temperature in the electrolyte is rather inhomogeneous, with higher electrolyte temperatures around the PWE. Since the formation of O_2 during aCGDE is inevitable, the electrolyte was not deaerated before the experiments. All experiments were performed without stirring the electrolyte.

For the electrochemical characterization, CVs were recorded before and after aCGDE. The initial potential for all measurements (unless otherwise mentioned) was set around the open circuit potential (ca. 1.00 V_{RHE}), the lower potential limit to 0.00 V_{RHE} and the upper potential limit to 1.05 V_{RHE}. For some measurements, the upper potential limit was increased to 1.25 V_{RHE}. When the upper potential limit was increased to 1.25 V_{RHE}, the initial potential was set to 1.20 V_{RHE}. The scan rate for all measurements was 50 mV s^{-1}, and the initial scan rate was always negative (negative potential scan). During the aCGDE in step B1 and in step B2, the potential of the AE was held at the initial potential (1.00 V_{RHE}).

ACKNOWLEDGMENTS

The authors gratefully acknowledge support by the DFG (German Science Foundation) through the collaborative research center SFB-1316 (Project ID: 327886311) as well as the state of Baden-Württemberg and the DFG through Grant No. INST 40/574-1 FUGG. E.A. would like to thank the "Stiftung Stipendien-Fonds des Verbandes der Chemischen Industrie (VCI)" for the financial support in form of a scholarship.

AUTHOR DECLARATIONS

Conflict of Interest

The authors have no conflicts to disclose.

Author Contributions

Evelyn Artmann: Conceptualization (equal); Formal analysis (equal); Funding acquisition (equal); Investigation (equal); Validation (equal); Visualization (equal); Writing – original draft (equal); Writing – review & editing (equal). **Lukas Forschner:** Writing – review & editing (equal). **Timo Jacob:** Funding acquisition (equal); Resources (equal); Supervision (equal); Writing – review & editing (equal). **Albert K. Engstfeld:** Conceptualization (equal); Funding acquisition (equal); Supervision (equal); Writing – review & editing (equal).

DATA AVAILABILITY

The data that support the findings of this study are openly available in Zenodo at http://doi.org/10.5281/zenodo.6424245, Ref. 70.

REFERENCES

[1]M. A. Malik, A. Ghaffar, and S. A. Malik, Plasma Sources Sci. Technol. **10**, 82 (2001).
[2]S. K. Sen Gupta, Plasma Chem. Plasma Process. **37**, 897 (2017).
[3]X. Wang, M. Zhou, and X. Jin, Electrochim. Acta **83**, 501 (2012).
[4]S. Horikoshi and N. Serpone, RSC Adv. **7**, 47196 (2017).
[5]J. Gao, X. Wang, Z. Hu, H. Deng, J. Hou, X. Lu, and J. Kang, Water Res. **37**, 267 (2003).
[6]T. A. Kareem and A. A. Kaliani, Ionics **18**, 315 (2012).
[7]G. Saito and T. Akiyama, J. Nanomater. **2015**, 1 (2015).
[8]A. Allagui, E. A. Baranova, and R. Wüthrich, Electrochim. Acta **93**, 137 (2013).
[9]A. Allagui, Z. Said, M. A. Abdelkareem, A. S. Elwakil, M. Yang, and H. Alawadhi, J. Electrochem. Soc. **164**, A2539 (2017).
[10]Y. Toriyabe, S. Watanabe, S. Yatsu, T. Shibayama, and T. Mizuno, Appl. Phys. Lett. **91**, 041501 (2007).
[11]G. Saito, Y. Nakasugi, T. Yamashita, and T. Akiyama, Nanotechnology **25**, 135603 (2014).
[12]F. Kurniawan and R. Rahmi, Bull. Chem. React. Eng. Catal. **12**, 281 (2017).
[13]Q. Chen, J. Li, and Y. Li, J. Phys. D: Appl. Phys. **48**, 424005 (2015).
[14]P. V. Menezes, M. M. Elnagar, M. Al-Shakran, M. J. Eckl, P. W. Menezes, L. A. Kibler, and T. Jacob, Adv. Funct. Mater. **32**, 2107058 (2022).
[15]E. Artmann, P. V. Menezes, L. Forschner, M. Elnagar, L. A. Kibler, T. Jacob, and A. Engstfeld, *Structural Evolution of Pt, Au, and Cu Anodes by Electrolysis up to Contact Glow Discharge Electrolysis in Alkaline Electrolytes* (ChemPhysChem, Wiley-VCH GmbH, Weinheim, 2021), Vol. 22, pp. 2429–2441.
[16]T. W. Clyne and S. C. Troughton, Int. Mater. Rev. **64**, 127 (2019).
[17]X. Lu, M. Mohedano, C. Blawert, E. Matykina, R. Arrabal, K. U. Kainer, and M. L. Zheludkevich, Surf. Coat. Technol. **307**, 1165 (2016).
[18]G. Barati Darband, M. Aliofkhazraei, P. Hamghalam, and N. Valizade, J. Magnesium Alloys **5**, 74 (2017).
[19]P. N. Belkin, S. A. Kusmanov, and E. V. Parfenov, Appl. Surf. Sci. Adv. **1**, 100016 (2020).
[20]K. Nestler, F. Böttger-Hiller, W. Adamitzki, G. Glowa, H. Zeidler, and A. Schubert, Procedia CIRP **42**, 503 (2016).
[21]A. Yayci, T. Dirks, F. Kogelheide, M. Alcalde, F. Hollmann, P. Awakowicz, and J. E. Bandow, ChemCatChem **12**, 5893 (2020).
[22]J. Winter *et al.*, J. Phys. D: Appl. Phys. **47**, 285401 (2014).
[23]T. R. Brubaker *et al.*, J. Appl. Phys. **122**, 213301 (2017).
[24]D. Gao, I. Zegkinoglou, N. J. Divins, F. Scholten, I. Sinev, P. Grosse, and B. Roldan Cuenya, ACS Nano **11**, 4825 (2017).
[25]H. Mistry *et al.*, Nat. Commun. **7**, 12123 (2016).
[26]H. Mistry *et al.*, Angew. Chem. Int. Ed. Engl. **56**, 11394 (2017).

[27]F. Yu, M. Liu, C. Ma, L. Di, B. Dai, and L. Zhang, Nanomaterials **9**, 1436 (2019).
[28]P. J. Bruggeman *et al.*, Plasma Sources Sci. Technol. **25**, 053002 (2016).
[29]A. L. Yerokhin, X. Nie, A. Leyland, A. Matthews, and S. J. Dowey, Surf. Coat. Technol. **122**, 73 (1999).
[30]A. Hickling and M. D. Ingram, Trans. Faraday Soc. **60**, 783 (1964).
[31]H. H. Kellogg, J. Electrochem. Soc. **97**, 133 (1950).
[32]A. Yerokhin, V. R. Mukaeva, E. V. Parfenov, N. Laugel, and A. Matthews, Electrochim. Acta **312**, 441 (2019).
[33]S. K. Sen Gupta, Plasma Sources Sci. Technol. **24**, 063001 (2015).
[34]S. K. Sengupta, J. Electrochem. Soc. **145**, 2209 (1998).
[35]X.-L. Jin, X.-Y. Wang, H.-M. Zhang, Q. Xia, D.-B. Wei, and J.-J. Yue, Plasma Chem. Plasma Process. **30**, 429 (2010).
[36]X. Jin, X. Wang, J. Yue, Y. Cai, and H. Zhang, Electrochim. Acta **56**, 925 (2010).
[37]U. Gangal, M. Srivastava, and S. K. Sen Gupta, J. Electrochem. Soc. **156**, F131 (2009).
[38]V. Climent and J. M. Feliu, J. Solid State Electrochem. **15**, 1297 (2011).
[39]S. Zhang, X.-Z. Yuan, J. N. C. Hin, H. Wang, K. A. Friedrich, and M. Schulze, J. Power Sources **194**, 588 (2009).
[40]H. A. Baroody, G. Jerkiewicz, and M. H. Eikerling, J. Chem. Phys. **146**, 144102 (2017).
[41]M. Farebrother, M. Goledzinowski, G. Thomas, and V. I. Birss, J. Electroanal. Chem. Interfacial Electrochem. **297**, 469 (1991).
[42]M. Favaro, C. Valero-Vidal, J. Eichhorn, F. M. Toma, P. N. Ross, J. Yano, Z. Liu, and E. J. Crumlin, J. Mater. Chem. A **5**, 11634 (2017).
[43]I. Katsounaros, W. B. Schneider, J. C. Meier, U. Benedikt, P. U. Biedermann, A. A. Auer, and K. J. J. Mayrhofer, Phys. Chem. Chem. Phys. **14**, 7384 (2012).
[44]S. K. Sengupta and O. P. Singh, J. Electroanal. Chem. **369**, 113 (1994).
[45]P. Rheinlander, S. Henning, J. Herranz, and H. A. Gasteiger, ECS Trans. **50**, 2163 (2013).
[46]S.-M. Park, S. Ho, S. Aruliah, M. F. Weber, C. A. Ward, R. D. Venter, and S. Srinivasan, J. Electrochem. Soc. **133**, 1641 (1986).
[47]I. Katsounaros and K. J. J. Mayrhofer, Chem. Commun. **48**, 6660 (2012).
[48]W. Sheng, Z. Zhuang, M. Gao, J. Zheng, J. G. Chen, and Y. Yan, Nat. Commun. **6**, 5848 (2015).
[49]V. Briega-Martos, E. Herrero, and J. M. Feliu, Curr. Opin. Electrochem. **17**, 97 (2019).
[50]V. Briega-Martos, E. Herrero, and J. M. Feliu, Electrochem. Commun. **85**, 32 (2017).
[51]G. Jinzhang, W. Aixiang, F. Yan, W. Jianlin, M. Dongping, G. Xiao, L. Yan, and Y. Wu, Plasma Sci. Technol. **10**, 30 (2008).
[52]J. Groele and J. Foster, Plasma **2**, 294 (2019).
[53]J. Julák, A. Hujacová, V. Scholtz, J. Khun, and K. Holada, Plasma Phys. Rep. **44**, 125 (2018).
[54]J. Schnaidt, S. Beckord, A. K. Engstfeld, J. Klein, S. Brimaud, and R. J. Behm, Phys. Chem. Chem. Phys. **19**, 4166 (2017).
[55]S. Beckord, S. Brimaud, and R. J. Behm, J. Electroanal. Chem. **819**, 401 (2018).
[56]S. Yang, A. Verdaguer-Casadevall, L. Arnarson, L. Silvioli, V. Čolić, R. Frydendal, J. Rossmeisl, I. Chorkendorff, and I. E. L. Stephens, ACS Catal. **8**, 4064 (2018).
[57]V. Climent and J. Feliu, "Cyclic voltammetry," in *Encyclopedia of Interfacial Chemistry*, edited by K. Wandelt (Elsevier, Oxford, 2018), pp. 48–74.
[58]See supplementary material at https://www.scitation.org/doi/suppl/10.1116/6.0001911 for additional information on reproducing the data (S1), the influence of upper potential limit on electrocatalytic properties (S2), the influence of the PWE voltage on the CV features recorded at the AE (550 V vs 580 V) (S3), the influence of tubes around the plasma counter electrode (S4), the influence of the upper potential limit on Pt surface oxidation (S5), and the temporal evolution of cyclic voltammograms after aCGDE (S6).
[59]C. A. Cartier, D. Kumsa, Z. Feng, H. Zhu, and D. A. Scherson, Anal. Chem. **84**, 7080 (2012).
[60]Y. Chen, A. Belianinov, and D. Scherson, J. Phys. Chem. C **112**, 8754 (2008).
[61]Z. Feng, N. S. Georgescu, and D. A. Scherson, Russ. J. Electrochem. **53**, 1003 (2017).
[62]Q. Han, N. S. Georgescu, J. Gibbons, and D. Scherson, Electrochim. Acta **325**, 134957 (2019).
[63]S. E. Fosdick, K. N. Knust, K. Scida, and R. M. Crooks, Angew. Chem. Int. Ed. **52**, 10438 (2013).
[64]G. Loget, D. Zigah, L. Bouffier, N. Sojic, and A. Kuhn, Acc. Chem. Res. **46**, 2513 (2013).
[65]P. Daubinger, J. Kieninger, T. Unmüssig, and G. A. Urban, Phys. Chem. Chem. Phys. **16**, 8392 (2014).
[66]G. Jerkiewicz, G. Tremiliosi-Filho, and B. E. Conway, J. Electroanal. Chem. **334**, 359 (1992).
[67]D. McKee, J. Catal. **14**, 355 (1969).
[68]R. Serra-Maia, J. D. Rimstidt, and F. M. Michel, Catal. Lett. **151**, 138 (2021).
[69]K. Azumi, T. Mizuno, T. Akimoto, and T. Ohmori, J. Electrochem. Soc. **146**, 3374 (1999).
[70]E. Artmann, L. Forschner, T. Jacob, A. K. Engstfeld (2022). DATASET: Using auxiliary electrochemical working electrodes as probe during contact glow discharge electrolysis: A proof of concept study (Version v1) [Data set]. Zenodo. https://doi.org/10.5281/zenodo.6424245

11.3 Appendix 3

The following attachment is my first author publication with the title "Nanoporous Au Formation on Au Substrates via High Voltage Electrolysis" as published in Chem. Phys. Chem.[169]

ChemPhysChem

Research Article
doi.org/10.1002/cphc.202200645

Chemistry Europe
European Chemical Societies Publishing

www.chemphyschem.org

Nanoporous Au Formation on Au Substrates via High Voltage Electrolysis**

Evelyn Artmann,[a] Lukas Forschner,[a] Konstantin M. Schüttler,[b] Mohammad Al-Shakran,[a] Timo Jacob,[a] and Albert K. Engstfeld*[a]

Nanoporous Au (NPG) films have promising properties, making them suitable for various applications in (electro)catalysis or (bio)sensing. Tuning the structural properties, such as the pore size or the surface-to-volume ratio, often requires complex starting materials such as alloys, multiple synthesis steps, lengthy preparation procedures or a combination of these factors. Here we present an approach that circumvents these difficulties, enabling for a rapid and controlled preparation of NPG films starting from a bare Au electrode. In a first approach a Au oxide film is prepared by high voltage (HV) electrolysis in a KOH solution, which is then reduced either electrochemically or in the presence of H_2O_2. The resulting NPG structures and their electrochemically active surface areas strongly depend on the reduction procedure, the concentration and temperature of the H_2O_2-containing KOH solution, as well as the applied voltage and temperature during HV electrolysis. Secondly, the NPG film can be prepared directly by applying voltages that result in anodic contact glow discharge electrolysis (aCGDE). By carefully adjusting the corresponding parameters, the surface area of the final NPG film can be specifically controlled. The structural properties of the electrodes are investigated by means of XPS, SEM and electrochemical methods.

Introduction

Nanoporous metals show distinct physico-chemical properties that often differ from those of the bulk materials.[1–4] These materials typically have pores in the range of 50 to 200 nm interconnected with ligaments of the bulk material. A rather intensively studied systems during the last years is nanoporous Au (NPG), for its possible application as, i.e., (bio)sensor,[1,5–9] in biomedicine,[9] as actuator,[10] heterogeneous catalyst material,[8,11–13] electrocatalyst,[1,2,14–18] or material in battery systems.[1,2]

A large number of approaches exist to prepare NPG, either free standing or on a support material.[1,2,7,8,19] The most common method discussed to synthesize nanoporous structures in general is dealloying, which is not limited to Au but is successfully employed for example to create nanoporous Ni (Raney-Ni).[2,20] Within this approach, an alloy is used as precursor, which can for example be fabricated by electrodeposition of one metal on another followed by alloying both elements. In a subsequent electrochemical dealloying step, the less noble metal is dissolved (electro)chemically and a nanoporous structure of the more noble metal remains.[11,21] This method is, however, mostly limited to noble metals.[2] To prepare NPG, the precursor alloy usually consists of a mixture of Ag and Au.[6,13,15,16,22,23]

Another frequently used method is the reduction of precursor molecules such as metal salts, e.g., $HAuCl_4$, in solution.[24] The reduction of the precursor molecules can, for example, be achieved by igniting a plasma above a liquid,[25–27] or by using another molecule that acts as a reducing agent.[28,29] By combining different preparation methods, not only NPG films but also nanoporous Au nanoparticles can be produced.[30]

NPG films can also be prepared by anodizing a Au substrate in aqueous solutions at potentials in the oxygen evolution region (for example 2.0 V *vs.* Ag/AgCl) and subsequent electrochemical reduction.[31,32] This approach bears the advantage that no additional chemicals or multimetallic precursors have to be used. Other groups also report on combining electrodeposition with subsequent anodization.[33] Overall, most of these common processes for producing nanoporous substrates are relatively complex, time-consuming, and require different, potentially harmful chemicals, which can also lead to the incorporation of impurities in the nanoporous film (in case of alloy precursors or salts). Impurities in particular can be problematic in further (electro)catalytic studies, where trace impurities can have a significant impact on the reaction rates such as for the CO

[a] *E. Artmann, L. Forschner, Dr. M. Al-Shakran, Prof. Dr. T. Jacob, Dr. A. K. Engstfeld*
Institute of Electrochemistry
Ulm University
D-89081 Ulm, Germany
+49 (0)731 25401
+49 (0)731 25409
E-mail: albert.engstfeld@uni-ulm.de
[b] *K. M. Schüttler*
Institute of Surface Chemistry and Catalysis
Ulm University
D-89081 Ulm, Germany

[**] *A previous version of this manuscript has been deposited on a preprint server (DOI: https://doi.org/10.26434/chemrxiv-2022-mx2qd).*

Supporting information for this article is available on the WWW under https://doi.org/10.1002/cphc.202200645

oxidation.[34,35] To scale up material production it is necessary that the production process is cheap, fast, reliable and preferentially does not pose any environmental hazards.

Recently, we demonstrated that NPG films can be prepared by anodization of a Au electrode in aqueous alkaline electrolyte at high voltages (between 100 and 540 V) leading to the formation of a Au oxide film, which upon subsequent electrochemical reduction turns into a NPG film.[36] NPG films with similar structures were also obtained by keeping the Au oxide after electrolysis in the electrolysis solution. We suggested that the Au oxide is reduced by H_2O_2 which forms during anodic contact glow discharge electrolysis (aCGDE).[37–40] Our results also indicate that H_2O_2 might also form at lower voltages (still in the range of a few 100 V) in the normal electrolysis region, as suggested previously.[41] This approach allows preparing samples within a few minutes. In addition, this method is also comparably environmental friendly since an alkaline KOH solution is the only chemical used in the preparation process.

In this work we systematically investigate the formation of NPG on bare Au wire and sheet electrodes. The experimental approach is based on our previous study, whereby a Au electrode is oxidized during electrolysis at high voltage (HV) in 0.01 M KOH and subsequently reduced either electrochemically or in a H_2O_2-containing 0.01 M KOH solution. The conclusions on the composition of the electrodes after this procedure by electrochemical measurements in the previous work are here confirmed by XPS measurements. Furthermore, with cross sectional SEM analyses we show that the Au oxide, obtained after HV electrolysis, as well as the NPG film, obtained after reducing the Au oxide, forms a several micrometer thick layer. In order to tune the NPG film, we systematically explore the possibility to reduce the Au oxide with H_2O_2 solutions with different concentration and temperature. The final NPG structures are compared to those obtained by electrochemical reduction. We also demonstrate that the thickness (or surface area) of the NPG film can be controlled by varying the electrolysis time, the electrolyte temperature, and the voltage applied during electrolysis. The structural properties are investigated primarily by SEM imaging and electrochemical measurements.

Results and Discussion

The results and discussion section is separated into four parts. Based on our previous study, first, we provide further complementary information on the structural properties of Au oxide structures obtained by HV electrolysis as well as the NPG films obtained by subsequent electrochemical reduction. Second, we discuss the impact of H_2O_2 concentration (in 0.01 M KOH) and temperature on the reduction of Au oxide films formed by HV electrolysis at 300 V. Third, we show the impact of the electrolysis voltage and the electrolyte temperature on the change in surface area of the NPG films after electrochemical reduction. Finally, we discuss the impact of the electrolysis time on the change in electrolyte temperature and, more importantly, on the structure formation.

Structural Properties

The structural properties of Au electrodes after HV electrolysis were investigated on wire and sheet Au anodes. The choice of the electrode type depends on the analytical approaches employed (see experimental section). In this section, we studied Au sheet electrodes modified by HV electrolysis at 300 V for 290 s, which were (i) directly removed from the electrolysis solution or (ii) subsequently reduced electrochemically, as reported previously.[36] At 300 V the structural changes are most significant, compared to lower voltages or voltages in the aCGDE region. Nevertheless, the following observations are also representative for other voltages in the range of 100 to 540 V.

Upon direct removal of the Au electrode from the electrolysis solution, the electrode's color is red, while the reduced electrode is black as illustrated in the optical microscope images in Figures 1a and b. Previously, we suggested that the red color is related to the formation of a Au_2O_3 film. This assumption is confirmed by XPS measurements of the Au 4*f* region shown in Figure 1c. The spectrum clearly shows features related to Au^0 (binding energies – BE: 84.0 eV and 87.7 eV[42–45]) and Au^{3+} (BE: 85.8 eV and 89.5 eV[42,43]), where the latter is significantly more pronounced. A contribution from Au^+, which should appear between the features of Au^0 and Au^{3+}, is not measurable. Au^+ would possibly be related to Au_2O, which is considered to be a metastable intermediate during the reduction of Au_2O_3.[46,47] The Au^0 feature in the Au 4*f* region can be attributed to areas that are not covered with Au oxide, resulting from the detachment of the Au oxide film from the Au substrate during the transfer (compare Figure 1a lower right edge). Plausibly, the Au oxide also decomposes during the XPS measurement due to beam damage.[48] In the O 1*s* region (see Figure S1), a typical oxidic oxygen state is observed as the main feature, which is most likely related to Au_2O_3.[49,50] The peak is, however, relatively broad compared to pure metal oxides, which, in general, is indicative for defects in the oxide. A second feature visible in the O 1*s* region can be ascribed to OH species.

The black color of the reduced electrodes was suggested to originate from a nanoporous Au (NPG) structure.[21,31–33,51] A corresponding XPS spectrum of the Au 4*f* region is shown in Figure 1d. The spectrum clearly shows that the electrode consists primarily of metallic Au^0. Minor contributions from oxidic Au^+- and Au^{3+}-species are also present. The corresponding O 1*s* peak has a much lower intensity than that of the oxidic sample. Nevertheless, the peak still consists of two features, which were ascribed to oxidic oxygen and OH (as discussed above and described along with Figure S1).

Corresponding SEM images of both electrodes are shown in Figures 1e and f. The image taken on the red electrode shows a relatively flat surface with some large cracks, while the images of the black electrode (after electrochemical

reduction) exhibit, in addition to the large cracks, a more patterned structure. Further SEM images of Au electrodes formed by HV electrolysis at 300 V are provided in Figure S2. Cross-sectional SEM images of both the red and black electrodes in Figures 1g and h, provide further information on the film thickness and structure. The schematic illustration shows the different regions of the cross-section, where the part above the dashed line shows the surface. The cross-section of the Au_2O_3 film (Figure 1g) shows a several 100 nm thick porous film. Note, however, that cutting the sample with an ion beam could also damage the structures and lead to the formation of porous structures observed in the Au oxide. The NPG film obtained by electrochemical reduction depicted in Figure 1h shows a more ordered porous structure with mostly vertically aligned pores. To be able to estimate the pore and ligament size of the NPG structures formed in this work more precisely, SEM images of the NPG structures with high resolution and magnification after 30 s at 300 V, as well as 540 V are shown in Section S3.

H_2O_2 Concentration and Temperature Dependence

As described above, the Au oxide formed during HV electrolysis is reduced when the electrode is kept in the electrolysis solution after HV electrolysis. It was suggested that the reduction process is caused by H_2O_2 in the electrolyte[36,40], which forms during HV electrolysis.[38,39,41] The general ability of H_2O_2 to reduce Au cations is already known in literature and can be explained by using the standard electrochemical potentials.[25–27,29] Therefore, we suggest the following reactions.

Reduction:

$$Au_2O_3 + 3H_2O + 6e^- \rightarrow 2Au + 6OH^- \quad (1)$$

Oxidation:

$$H_2O_2 + 2OH^- \rightarrow 2H_2O + 2e^- + O_2 \quad (2)$$

Overall reaction:

$$Au_2O_3 + 3H_2O_2 \rightarrow 2Au + 3O_2 + 3H_2O \quad (3)$$

To illustrate the role of H_2O_2 in the reduction of the Au oxide, we investigated changes in the surface structure induced by i) H_2O_2-containing KOH solutions of different concentration at constant temperature and ii) by varying the H_2O_2 solution temperature for a constant H_2O_2 concentration. In the following a "H_2O_2 solution" refers to a "H_2O_2-containing 0.01 M KOH solution". All H_2O_2 concentrations are referred to weigth%. Table S4 summarizes the following experimental conditions, observations, and evaluated RFs.

For these investigations, the Au oxide films were prepared on Au wire electrodes in 0.01 M KOH at 300 V for 30 s. The electrodes were directly removed from the electrolysis solution to minimize the reducing effect from the H_2O_2 in the electrolysis solution.

The concentration dependence was studied by immersing the Au oxide-covered electrodes at room temperature for 60 s in H_2O_2-containing KOH solutions with concentrations of 0.007%, 0.08%, and 0.8%. Upon removal from a 0.007% H_2O_2-containing 0.01 M KOH solution, the electrode still appears red, whereas, in a 0.08% and 0.8% H_2O_2-containing 0.01 M KOH solution, the electrodes turn black within 60 s.

Corresponding SEM images of the electrodes are shown in Figure 2 with large-scale images in the top row and regions with higher magnification of these surfaces in the bottom row.

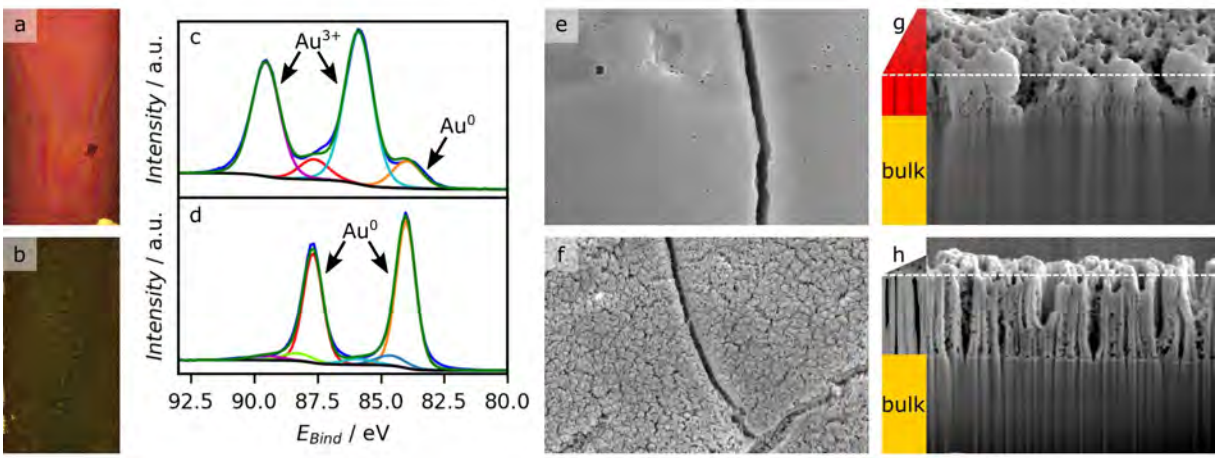

Figure 1. Top row: Structural properties of a Au sheet electrode after electrolysis at 300 V for 290 s in 0.01 M KOH. Bottom row: A Au sheet electrode which was reduced electrochemically after HV electrolysis. a) and b) show corresponding optical microscope images. c) and d) show XPS spectra of the Au 4*f* region, including the peaks fitted to Au^0 and Au^{3+}. e) and f) show top-view SEM images with image sizes of 6 μm × 4 μm. g) and h) show cross sectional SEM images of the surfaces in e) and f) with image sizes of 4 μm × 3 μm and 8 μm × 6 μm. The schematic illustration next to the cross sectional SEM images show the color of the sheets and the viewing angle during the image acquisition.

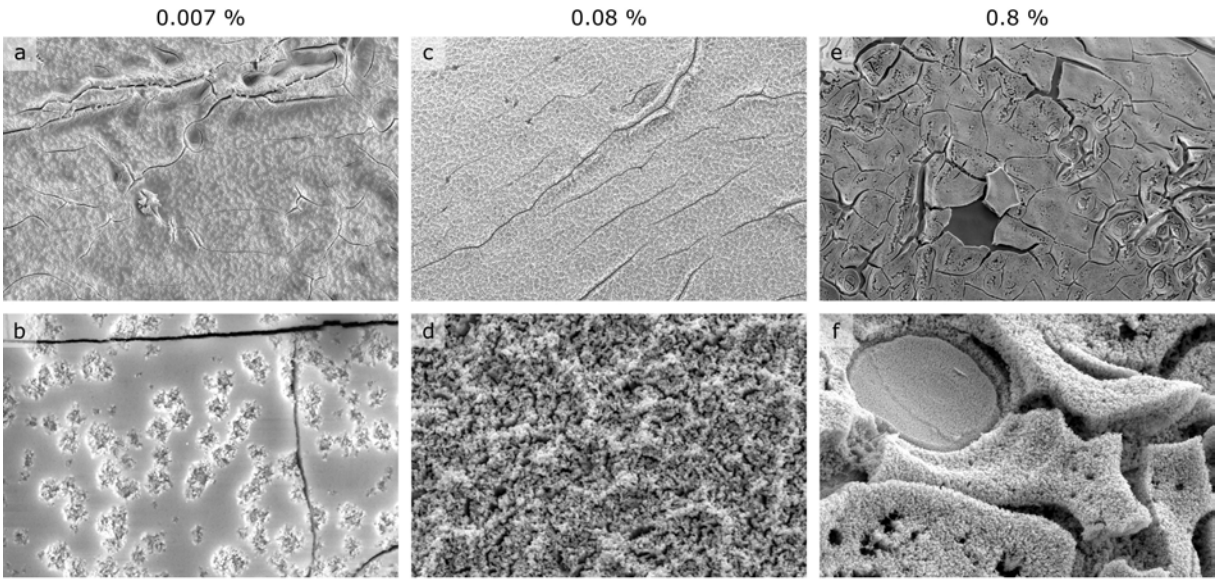

Figure 2. SEM images recorded on Au wire electrodes after electrolysis at 300 V for 30 s, direct removal from the electrolysis solution and subsequent reduction for 60 s in H_2O_2-containing 0.01 M KOH solutions (room temperature). The amount of H_2O_2 is given above the respective columns. The top row images show regions with sizes of 120 μm × 80 μm and the bottom row 12 μm × 8 μm.

It is apparent that the structure formation strongly depends on the H_2O_2 concentration. The electrode surface upon removal from the 0.007 % H_2O_2 solution (Figures 2a and b) still appears rather smooth and is only restructured in certain regions. Interestingly, it seems that the restructuring process starts in random regions on the surface, which are separated by about 0.5 μm. For electrodes immersed in a 0.08 % H_2O_2 solution (Figures 2c and d), the entire surface is nanostructured. Increasing the concentration further by one order of magnitude (0.8 % H_2O_2 – Figures 2e and f), large cracks appear on the surface. In some regions, the surface even peels off (Figure 2e), in others, large protrusions form on the surface (Figure 2f). The amount of oxide remaining on the electrode after removal from a H_2O_2 solution was determined by electrochemical reduction of the electrodes. The electrodes removed from low-concentrated H_2O_2 solutions still show a current density related to oxide reduction. This current density is significantly lower compared to that recorded on electrodes reduced electrochemically directly after the HV electrolysis. The electrode immersed in 0.8 % H_2O_2 solution is completely reduced after 60 s.

Even though H_2O_2 seems to play a critical role in the reduction of the Au oxide, the structures obtained after HV electrolysis and subsequent electrochemical reduction (compare with Figure 1f) do not resemble those observed upon immersion of the Au oxide in H_2O_2 solutions. Possible reasons for this discrepancy are that after HV electrolysis, the H_2O_2 concentration will be high in the region around the electrode and will decrease with increasing time, as shown elsewhere.[40] Furthermore, during HV electrolysis, the temperature of the electrolyte will increase,[39,41,52,53] which could also be a decisive factor for the structure formation.

To separate the effect of temperature and H_2O_2 concentration on the structure formation, Au oxide electrodes prepared by HV electrolysis at 300 V were immersed for 60 s in a freshly prepared 0.01 M KOH solution heated to 70 °C. Afterward, the electrode's color was still red, indicating that the Au oxide is stable at this temperature in pure 0.01 M KOH. This result is in line with the findings by Tsai et al. who studied the kinetics of dissociation of Au_2O_3 at different temperatures.[54] Hence, we can exclude that temperature alone has an effect on the transformation of Au oxide to pure Au or other structural changes of the electrode.

To study the influence of the combined effect of temperature and H_2O_2 on the NPG structure formation, Au oxide electrodes were immersed for 60 s in 0.007 % H_2O_2 solutions with electrolyte temperatures of 24, 40, and 70 °C. Au oxide electrodes immersed in a 0.007 % H_2O_2 solution at 24 °C or 40 °C remained red. At 70 °C, the color of the electrodes turned black with a touch of red. In all three cases, additional electrochemical reduction of the electrodes revealed that the electrodes still contained a significant amount of Au oxide. Hence, under these conditions, the electrodes do not reduce completely.

Corresponding SEM images of the resulting electrode surfaces are shown in Figure 3 with large-scale images in the top row and magnified regions of these surfaces in the bottom row. The conditions in Figures 3a and b are identical to those in Figures 2a and b and are only shown for comparison. The main observation is that the restructuring becomes more pronounced with higher temperature and that the number of cracks, observed already at room temperature, increases. Despite the significant restructuring, the surface structure is not identical to that obtained by HV electrolysis at 300 V and

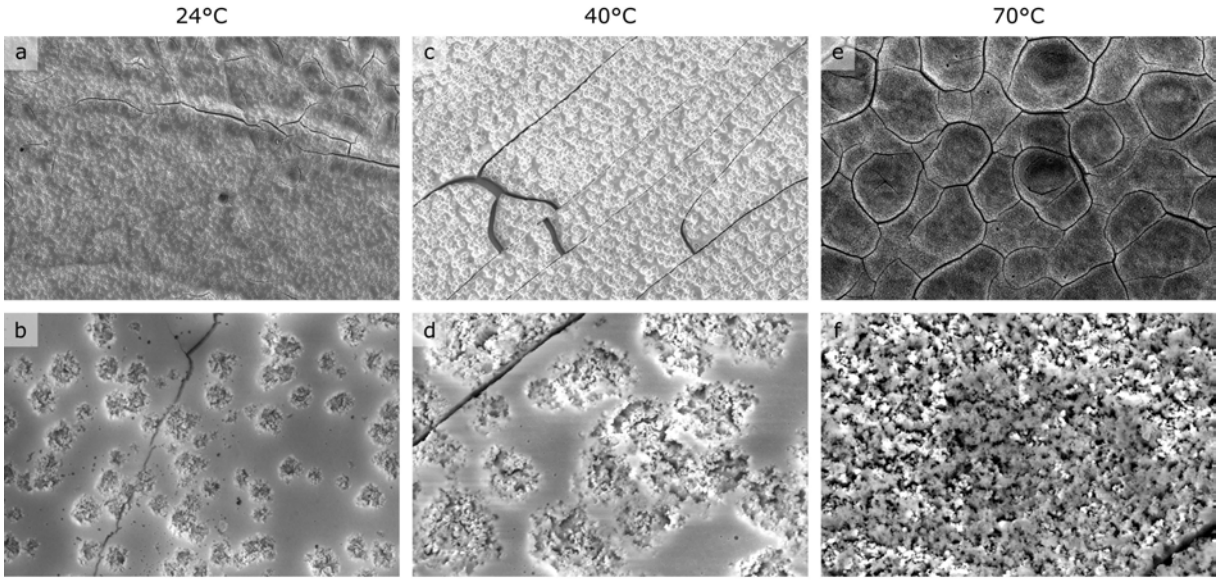

Figure 3. SEM images of Au wires after HV electrolysis at 300 V for 30 s and direct removal from the electrolysis solution with subsequent reduction through immersion in 0.01 M KOH solutions with a H_2O_2 concentration of 0.007% for 60 s and temperatures of a) and b) 24 °C (room temperature), c) and d) 40 °C and e) and f) 70 °C. The image size of a), c) and e) is 120 µm × 80 μm, from b), d) and f) 12 µm × 8 μm.

subsequent electrochemical reduction (see Figures 5a to d) or reduction in the electrolyte.

Overall, these results show that the H_2O_2 concentration and temperature play a major role in structure formation. This is an important aspect since these parameters change dynamically and in an uncontrolled way when the electrodes are kept in the electrolysis solution after HV electrolysis, i.e., the H_2O_2 concentration will probably decrease due to dissipation in the electrolyte,[40] and the local temperature will also decrease due to heat dissipation into the surrounding electrolyte.

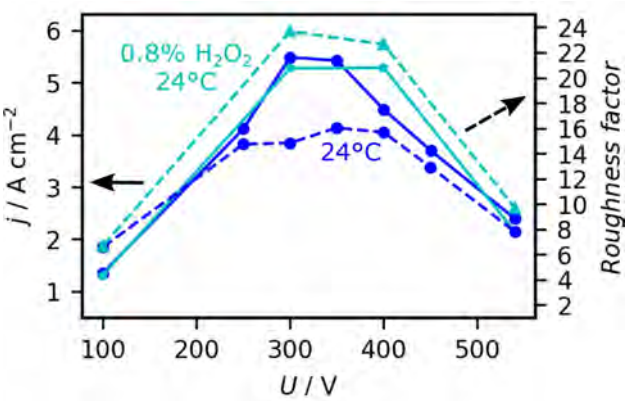

Figure 4. HV electrolysis of a Au wire electrode for 30 s at different voltages and an initial electrolyte temperature of 24 °C in 0.01 M KOH and subsequent electrochemical reduction (dark blue), as well as reduction by immersion of the electrode for 60 s in a 0.8% H_2O_2-containing 0.01 M KOH solution at 24 °C (cyan). The average current densities during HV electrolysis are shown by the points linked by solid lines, the roughness factors of the electrode after HV electrolysis and following reduction are shown by the points linked by dashed lines.

Effect of HV Electrolysis Parameters – Voltage and Temperature

In the following, we demonstrate and discuss how the surface area of the NPG film can be controlled by tuning the electrolysis voltage and electrolyte temperature. In our previous work, we demonstrated that independent of the applied voltage during HV electrolysis, the resulting Au oxide surface structures appear rather similar, as well as the fully-reduced Au oxide structures (also shown in an additional set of SEM images in Figure S5). The change in surface area, here discussed based on the roughness factor (RF – see Experimental Section), of the NPG film, however, depends on the electrolysis voltage and correlates with the average current density during HV electrolysis.[36] A corresponding *j*–*U* curve (dark blue solid line) is shown along with the RF (dark blue dashed line) in Figure 4. Note that each point in the plot represents an individual measurement on a freshly-prepared Au wire, where the voltage was applied for 30 s, and the electrode was subsequently reduced electrochemically. Overall, the *j*–*U* characteristic is described in the literature.[4,39,52,55–57] Thus, only the most important aspects are briefly introduced here.

For gas-evolving electrodes, the *j*–*U* curve can be divided into different regions. First, the current increases linearly with increasing voltage (Ohmic behavior) up to a certain breakdown voltage (V_B). Here, bubble formation becomes significant, and a gas sheath starts to form around the electrode, which increases the resistance at the electrode | electrolyte

interface and hence leads to a decrease in current density. With increasing voltage, the gas film becomes more stable, showing partial ionization of the gas in the sheath (partial aCGDE). At the midpoint voltage (V_D, here ca. 540 V), full aCGDE is observed.

First, to demonstrate possible differences between the electrochemical reduction and reduction by H_2O_2 on the RF, Au oxide samples were prepared at different voltages as described above and were reduced in an 0.8% H_2O_2 solution. At this H_2O_2 concentration, the reduction process was suggested to be complete. The corresponding *j–U* curve (cyan solid line) resulting from the electrolysis of the Au electrodes is shown in Figure 4, which shows a similar behavior to the curve in dark blue (illustrating the reproducibility of the approach). The RF of the Au oxide films reduced in the H_2O_2 solution is shown by the cyan dashed curve in Figure 4.

Comparing the RF of the Au oxide reduced electrochemically with that reduced in a H_2O_2 solution (dashed blue and cyan curves in Figure 4), the values are rather similar for Au electrodes treated by low and high electrolysis voltages. For intermediate electrolysis voltages around V_B, the Au oxides reduced in H_2O_2 have a larger RF than the electrochemically reduced Au oxides. This is also apparent from SEM images, where the NPG film formed by reducing Au oxide in a 0.8% H_2O_2 solution shown in Figures 5e–h is much more inhomogeneous than the electrochemically reduced film in Figures 5a–d.

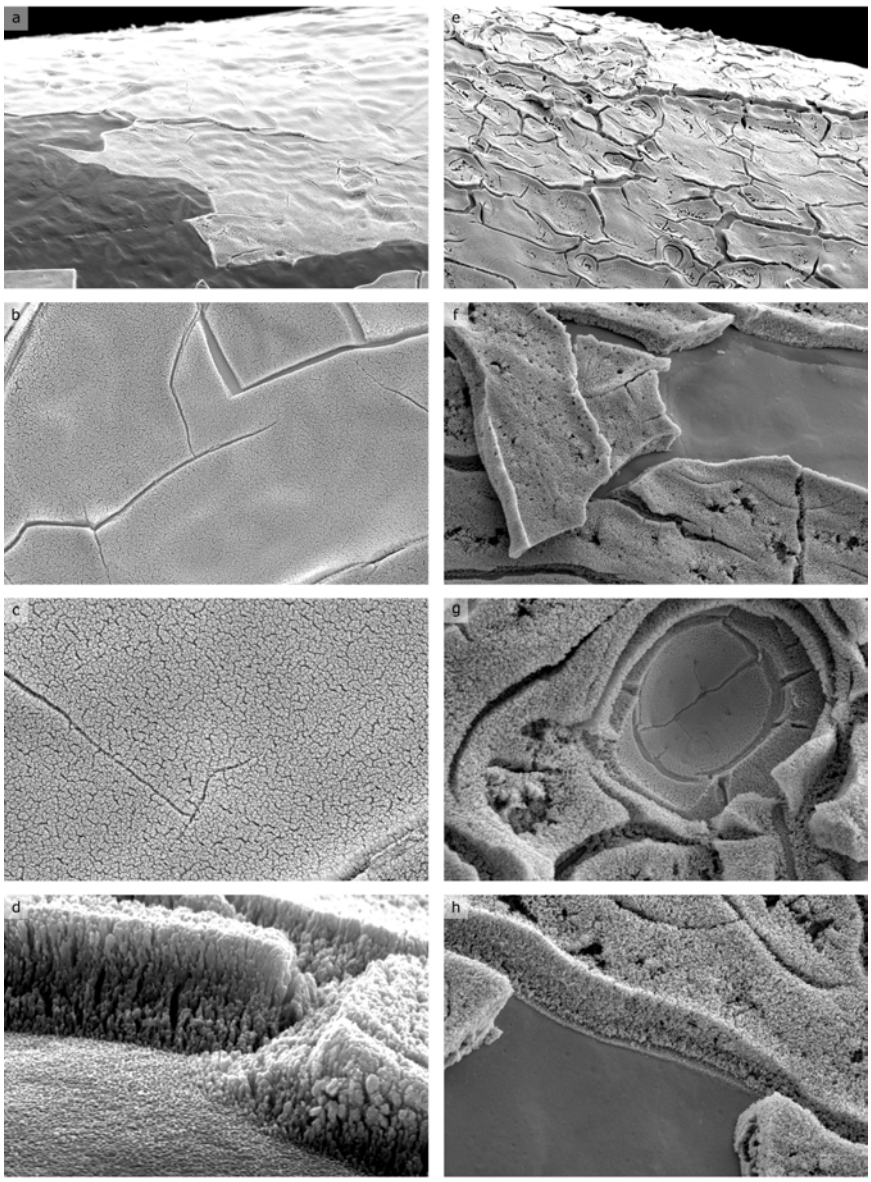

Figure 5. SEM images of Au wire electrodes after HV electrolysis at 300 V for 30 s and a) to d) subsequent electrochemical reduction, or e) to h) reduction in a 0.8% H_2O_2-containing 0.01 M KOH solution. The image size in a) and e) is 120 μm × 80 μm, b) and f) 30 μm × 20 μm, c) g) and h) 12 μm × 8 μm and d) 3 μm × 2 μm.

The effect of the electrolysis solution temperature on the RF of NPG films after the electrochemical reduction of Au oxide films is illustrated in Figure 6 by the dashed lines (24 °C – blue, 46 °C – orange and 70 °C – red). The corresponding *j–U* curves are shown by the solid lines. At higher initial electrolyte temperatures, the breakdown voltage (V_B) shifts to lower voltages. This shift can be explained by the fact that the boiling point of the electrolyte is reached on a shorter timescale at a higher initial electrolyte temperature.[39,53,58,59] In addition, the average current densities at low voltages increase due to an increase in ion conductivity in the electrolyte, whereas at high voltages, the current densities decrease with the temperature due to more facile gas sheath formation. More detailed information on the effect of the initial electrolyte temperature on the *j–U* curves can be found elsewhere.[39,53,58–60] Further information on the increase in electrolyte temperature at different initial electrolyte temperatures during HV electrolysis is explained along with Figure S6.

More importantly, after the electrochemical reduction, the evolution of the RF with applied voltage follows the evolution of the average current density for all temperatures and applied voltages. The largest increase in surface area is observed for low initial electrolyte temperatures and voltages in the range of V_B. For low and high voltages, the differences in RF at different initial electrolyte temperatures are less significant. In addition, for high voltages in the aCGDE region (≥450 V), the RF does not increase significantly compared to bare Au electrodes at higher initial electrolyte temperatures. Therefore, NPG films with high surface area are achieved for low initial electrolyte temperatures.

Time Dependence

To illustrate the impact of electrolysis time on the Au oxide formation and the RF of the final NPG film, we performed electrolysis experiments at 300 V and 540 V for different times ranging from 10 to 600 s. The 300 V experiments were also performed at 46 °C and 70 °C. Since the 300 V measurements could not be performed without complications (see below), we first discuss the results obtained for 540 V.

Figure 7a shows the evolution of the current density during 600 s HV electrolysis at 540 V (black line). The curves for shorter electrolysis times are not shown but they look very similar and follow the same trend. At the start of the measurement, the current density rises sharply, reaching a maximum within a second (see inset in Figure 7a). Immediately, strong bubble formation is observed, followed by the formation of a dynamic gas layer around the electrode. Furthermore, at this voltage a plasma develops in the resulting gas layer between the electrode surface and the electrolyte. With increasing time, the current drops until it becomes almost constant for longer electrolysis times (ca. 100 s).

The evolution of the structural properties was determined from several experiments with different electrolysis times on freshly prepared electrodes. For each sample, Figures 7b and c show (i) the amount of Au oxide formed during HV electrolysis

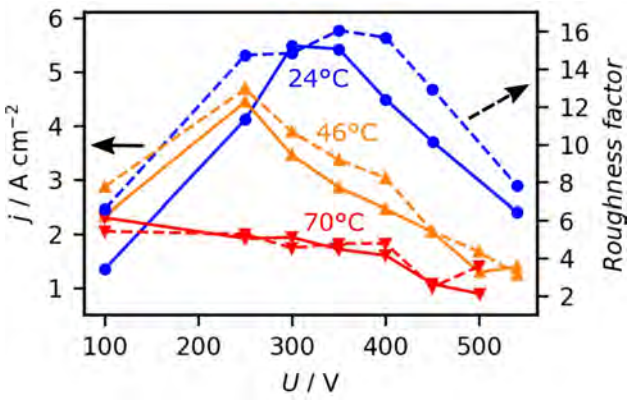

Figure 6. HV electrolysis of a Au wire electrode for 30 s at different voltages and initial electrolyte temperatures (24 °C – blue, 46 °C – orange and 70 °C – red) in 0.01 M KOH. The *j–U* traces are connected with solid lines, while the corresponding RF after electrochemical reduction are connected with dashed lines. Each data point marks an individual measurement. The current densities are averaged over 30 s (see experimental section). The lines only serve as a guide to the eye.

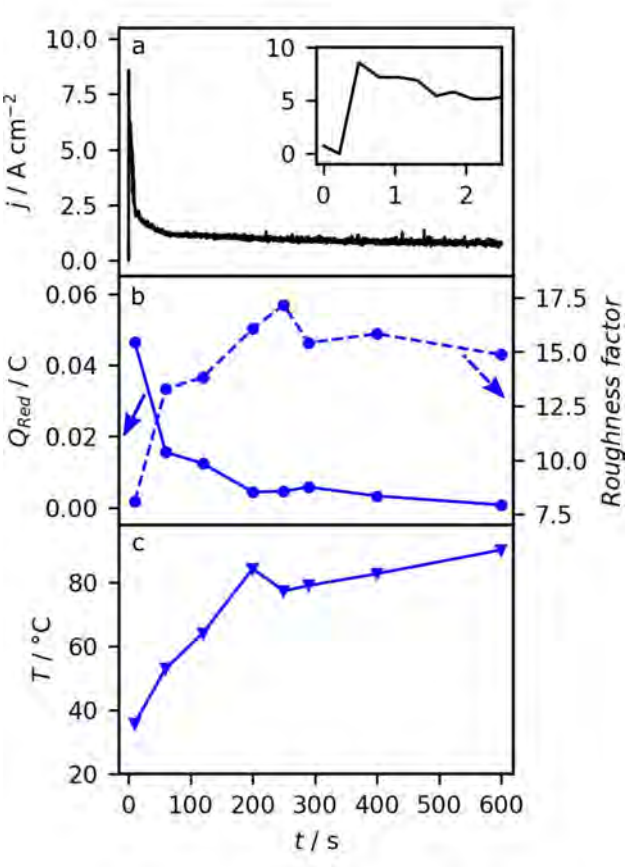

Figure 7. Time dependence of HV electrolysis on a Au wire electrode at 540 V in 0.01 M KOH. a) Current density during HV electrolysis. b) Amount of Au_2O_3 formed after different HV electrolysis times determined by electrochemical reduction (solid line) and RF (dashed line) of the NPG film. c) Electrolyte temperature after HV electrolysis (initial electrolyte temperature: 24 °C).

(Figure 7b – solid), (ii) the RF of the electrodes after electrochemical reduction (Figure 7b – dashed), and (iii) the electrolyte temperature after electrolysis (Figure 7c). The starting electrolyte temperature was, in each case, room temperature. For short electrolysis times (10 s) the amount of Au oxide is high (Figure 7b – solid), which decreases with longer electrolysis times exponentially. From approximately 200 s onward, the amount of Au oxide on the surface is very low and almost negligible at 600 s. In turn, the RF follows an opposite trend, whereby in the first 30 to 60 s, the RF of the NPG electrodes increases sharply. For longer electrolysis times, the increase in RF becomes smaller, reaching a plateau after approximately 200 s where the surface area is 15 times larger compared to that of the bare Au electrode. With increasing electrolysis time, the temperature rises up to ca. 80 °C within 200 s and increases only slightly within the next 400 s. By comparing all measurements in Figure 7, it is apparent that the amount of Au_2O_3 is not directly correlated with the increase in surface area obtained after the electrochemical reduction. Thus it seems that the Au oxide is reduced automatically, as discussed further below. More importantly, this set of measurements suggests, that the formation of NPG films via HV electrolysis does not necessarily require an additional step to reduce a Au oxide, but it can be formed directly via HV electrolysis when the electrolysis time is sufficiently long.

While a full explanation for the observed behavior is still missing, the following aspects can be excluded or considered to be at the origin. First, we often observed (also in previous measurements) that parts of the newly formed films (Au oxide or NPG) peeled off from the substrate surface during HV electrolysis. If this effect would be significant, especially at long electrolysis times, we would not only expect that the amount of Au oxide on the surfaces decreases but also the roughness factor will decrease (or both should be correlated with one another). Hence this aspect can be ruled out. Second, with increasing electrolysis time, the amount of H_2O_2 in the solution will increase, which in turn would increase the probability of reducing the Au oxide. However, performing electrolysis at 540 V leads to the formation of a gas sheath around the electrode, and hence the contact area between the electrode and electrolyte can be considered to be negligible. Whether or not H_2, which also forms under these conditions and might be present in the sheath,[41,58,61] plays a role is questionable. Based on separate experiments, where we immersed a Au oxide electrode in a H_2-containing 0.01 M KOH solution, we did not observe a reduction of the Au oxide. Third, during the electrolysis, not only does the electrolyte temperature increase, but most likely also that of the electrode. Under certain circumstances, the electrodes might even melt during aCGDE conditions.[39,53] Considering that the decomposition temperature of Au_2O_3 is only approximately 150 °C,[46,49,54] it is likely that the Au oxide decomposes to Au due to the high local electrode temperature. Overall, we suggest that this is presumably the most likely scenario.

We performed a similar set of experiments at an electrolysis voltage of 300 V and in electrolytes initially at room temperature. In contrast to electrolysis at 540 V, the averaged current densities during HV electrolysis are much higher, and the electrode is still, to some extent, in contact with the electrolyte, despite vivid bubble formation. The amount of H_2O_2 formed at this voltage may also differ from that formed at 540 V, since the literature only reports H_2O_2 formation above the midpoint voltage. However, we were recently able to show that H_2O_2 is most likely also formed at lower voltages and at 300 V.[36] The temporal evolution of the current density recorded at 300 V is shown in red in Figure 8 together with that recorded at 540 V in black. The inset shows the increase in current density at the beginning of the HV electrolysis.

A key issue in the experiments performed at 300 V was that for longer electrolysis times, the films formed on the surface significantly peeled off. Therefore, we limit ourselves to a more qualitative description. After 120 s of HV electrolysis, the electrode exhibits a red color, indicating that the electrode is covered with a Au oxide film. After the electrochemical reduction, the RF of the NPG electrode is larger compared to the bare Au electrode. From visual inspection, it is apparent that for longer electrolysis times (290 s up to 600 s), the Au oxide or NPG film significantly pealed off from the electrode and the electrode appears mostly golden. The RF determined after the electrochemical reduction is very low compared to the electrode which was treated by electrolysis for only 120 s. But since the resulting film seemed to peel off, this result is not very meaningful, except that it underlines that no Au oxide or NPG can be formed under these conditions, i.e. at long electrolysis times. To what extent the rise of the electrolyte temperature up to 80 °C or the vivid bubble formation plays a role in the removal of the films is unclear. Hence, at high current densities and during HV electrolysis with bubble formation, short time scales are required to form a stable Au oxide film, which can then be reduced in a second step to form a NPG film.

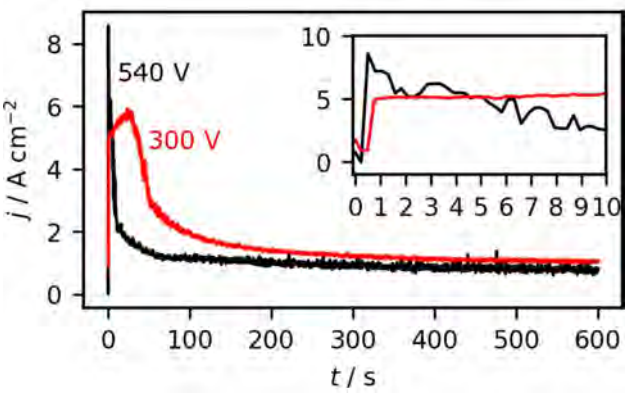

Figure 8. Evolution of the current density with time during HV electrolysis at 540 V (black) and 300 V (red) in 0.01 M KOH.

Conclusion

In this work, we demonstrated that NPG can be prepared by a simple and fast method, namely by (i) HV electrolysis alone or followed by (ii) electrochemical reduction or (iii) reduction in an H_2O_2-containing KOH solution. The thickness of the NPG film and surface structure can be controlled by several parameters:

1. The voltage applied during HV electrolysis.
2. The initial electrolyte temperature before HV electrolysis. The lower the initial electrolyte temperature, the greater is the surface area of the resulting NPG film, when the current densities during HV electrolysis are higher at low initial electrolyte temperatures.
3. The electrolysis time in the region of aCGDE. With short electrolysis times, the surface area increases sharply within a very short time period (30 to 60 s), while for longer electrolysis times the surface area remains almost constant.

Reduction of the Au_2O_3 films previously formed by HV electrolysis on the electrode surfaces in H_2O_2 solutions of different concentrations and temperatures additionally leads to different surface areas and surface structures. Depending on the application, these differences in surface structure and surface area should be considered during the preparation of NPG films in order to assess its impact for possible applications. HV electrolysis thus represents a suitable "green chemistry"-approach to produce well adaptable NPG films in a fast and efficient way.

Experimental

Materials

All Au wires used have a diameter of 0.5 mm (MaTeck, 99.99%). The Au sheets have a thickness of 0.127 mm (MaTecK, 99.99%).

The 0.01 M KOH solution used as an electrolyte was prepared from KOH pellets (Sigma-Aldrich, 99.99%) and Milli-Q water (18.2 MΩ cm, TOC $\leq$ 3 ppb). The 1 M HCl solution used for electropolishing was prepared from a 30% HCl (Suprapur, Merck). The H_2O_2 solutions were prepared from a 50 wt.% H_2O_2 solution (Acros Organics) stabilised in water. For all H_2O_2 containing solutions, the concentrations are referred to wt.%.

Sample Preparation

For each measurement, the Au wire/sheet was heated in a propane flame (MTI) for 3 min to remove impurities and flatten the surface. Wire electrodes with a highly restructured surface after the experiment were additionally electropolished in 1 M HCl at 10 V vs. a graphite electrode and subsequently annealed for 3 min. In the case of the Au sheets, a new piece was used for each measurement to ensure similar starting conditions.

Electrolysis Cell

The HV electrolysis experiments were performed in a glass cell filled with 60 mL of 0.01 M KOH. For XPS and cross-sectional SEM imaging Au sheets were used instead of Au wires in order to have larger surfaces and circumvent issues with the curvature of the electrodes posing problems for further analytics. The Au wire or sheet used as plasma working electrode (PWE) was placed 2.5 cm apart from the plasma counter electrode (PCE), made from a stainless steel plate (15 mm × 20 mm × 3.5 mm). Usually, 10 mm of the wire were immersed in the electrolyte (surface area: 0.16 cm^2). Depending on the measurement, a sheet (2 mm × 12.5 mm) was immersed either 4 mm (surface area: 0.1727 cm^2) or 10 mm in the electrolyte (surface area: 0.4280 cm^2). The voltage was applied with a TDK-Lambda Power Supply (630 V/1.365 A) which was controlled with a LabVIEW software. The temperature of the electrolyte was measured before and after the electrolysis. In addition, the electrolyte was exchanged after each measurement to avoid possible changes of the initial conditions (electrolyte temperature, dissolved products, etc.). Moreover, all HV electrolysis experiments were performed without stirring the electrolyte.

The current densities shown in Figures 4 and 6 are averages over the entire electrolysis time.

Electrochemical Cell

The electrochemical measurements were performed in a glass beaker[36] containing 150 mL of 0.01 M KOH. Before starting the measurements, the electrolyte was deaerated with N_2. All electrochemical measurements were performed without stirring the electrolyte. A homemade reversible hydrogen electrode (RHE) served as reference electrode, the Au wire and sheets used for the electrolysis experiments were used as working electrodes and a Pt-sheet (10 × 7.5 mm) as electrochemical counter electrode. The measurements were controlled with an FHI ELAB potentiostat.

Experimental Procedure

Two separate cells were used for the HV electrolysis and the electrochemical characterization since during HV electrolysis, the electrolyte properties change (O_2 accumulation, increase in H_2O_2 content, change in temperature), which does not allow recording reliable electrochemical results.

The current densities of the electrochemical measurements were obtained by relating the currents during the measurements to the original geometric surfaces of the samples. For each electrochemical measurement, the initial potential was set to 1.1 V. With a scan rate of 50 mV s^{-1}, the potential was subsequently decreased (negative scan direction). The potential was then cycled between 0.20 V and 1.69 V.

To reduce the Au oxide produced by HV electrolysis electrochemically, the potential was also decreased gradually with a scan rate of 50 mV s^{-1} starting from an initial potential of 1.1 V. At a potential of 0.25 V, it was then held in the first negative scan until the additional current present due to the reduction of the Au oxide had disappeared. Integrating this reductive current provides the charge related to the reduction of Au oxide. A detailed description of the experimental procedure can also be found in Ref. [36].

For the preparation of the samples for cross-sectional SEM imaging, the complete reduction was performed by holding the potential immediately at 0.25 V.

To determine the change of electrochemical surface area (ECSA) of the NPG films, we performed CV measurements before and after HV electrolysis. This will also reduce the remaining Au oxide from the surface. The change in surface area was determined in each case from the thickness of the double layer at 0.87 V. At this

potential, neither Faraday reactions nor adsorption processes take place. Exemplary CVs recorded before and after the electrolysis/reduction experiment are shown in Figure S7. The ratio between the values of the double layer before and after is denoted as roughness factor (RF), which in other words, describes the relative change in surface area compared to a bare Au electrode.

Structural Characterization

All SEM images were recorded with a Quattro S scanning electron microscope (SEM) from Thermo Scientific. An accelerating voltage of 10 kV or 20 kV was used to record the images. The cross-sectional SEM images were taken with a Scios2 from Thermo Scientific. A Ga source was used for surface milling to get the cross sections. The SEM images taken from the cross sections were recorded at an acceleration voltage of 10.00 kV. The microscope images of the Au electrodes were taken with a Leica S9i microscope, also from Thermo Scientific.

XPS

All XPS measurements were performed using monochromatic Al K_α (1486.6 eV) radiation. The signals were detected at an angle of 45°. To avoid possible charging effects, all XPS samples were measured with a neutralizer as a precaution, although all samples had metallic contact with the ground.

Credit

E. Artmann: Conceptualization, Formal Analysis, Funding Acquisition, Investigation, Validation, Visualization, Writing – Original Draft Preparation. L. Forschner: Investigation, Writing – Review & Editing. K. M. Schüttler: Investigation, Writing – Review & Editing. Dr. M. Al-Shakran: Investigation. Prof. Dr. T. Jacob: Funding Acquisition, Resources, Supervision, Writing – Review & Editing. Dr. A. K. Engstfeld: Funding Acquisition, Conceptualization, Supervision, Writing – Review & Editing

Acknowledgment

This work was funded by the SFB-CRC1316 of the DFG (German Research Foundation). Further, support by the state of Baden-Württemberg and the DFG through grant no INST 40/574-1 FUGG is gratefully acknowledged. E. A. would like to thank the "Stiftung Stipendien-Fonds des Verbandes der Chemischen Industrie (VCI)" for the financial support in the form of a scholarship. The authors also want to thank Joachim Bansmann for his support with the XPS measurements. Open Access funding enabled and organized by Projekt DEAL.

Conflict of Interest

The authors declare no conflict of interest.

Data Availability Statement

The data that support the findings of this study are openly available in Zenodo at http://doi.org/10.5281/zenodo.6973687.

Keywords: Contact Glow Discharge Electrolysis · Electrolysis · Gold · Gold oxide · Nanoporous Gold

[1] T. Juarez, J. Biener, J. Weissmüller, A. M. Hodge, *Adv. Eng. Mater.* **2017**, *19*, 1700389.
[2] J. Zhang, C. M. Li, *Chem. Soc. Rev.* **2012**, *41*, 7016.
[3] I. McCue, J. Stuckner, M. Murayama, M. J. Demkowicz, *Sci. Rep.* **2018**, *8*, 6761.
[4] R. Akolkar, R. M. Sankaran, *J. Vac. Sci. Technol. A* **2013**, *31*, 050811.
[5] K. Yan, P. Karthick Kannan, D. Doonyapisut, K. Wu, C.-H. Chung, J. Zhang, *Adv. Funct. Mater.* **2021**, *31*, 2008227.
[6] D. Jalas, L.-H. Shao, R. Canchi, T. Okuma, S. Lang, A. Petrov, J. Weissmüller, M. Eich, *Sci. Rep.* **2017**, *7*, 44139.
[7] J. K. Bhattarai, D. Neupane, B. Nepal, V. Mikhaylov, A. V. Demchenko, K. J. Stine, *Nanomaterials* **2018**, *8*.
[8] S. H. Kim, *Curr. Appl. Phys.* **2018**, *18*, 810.
[9] S. Xiao, S. Wang, X. Wang, P. Xu, *Nano Select* **2021**, *2*, 1437.
[10] J. Biener, A. Wittstock, L. A. Zepeda-Ruiz, M. M. Biener, V. Zielasek, D. Kramer, R. N. Viswanath, J. Weissmüller, M. Bäumer, A. V. Hamza, *Nat. Mater.* **2009**, *8*, 47.
[11] J. Biener, M. M. Biener, R. J. Madix, C. M. Friend, *ACS Catal.* **2015**, *5*, 6263.
[12] A. Wittstock, A. Wichmann, J. Biener, M. Bäumer, *Faraday Discuss.* **2011**, *152*, 87.
[13] X. Zhang, Y. Ding, *Catal. Sci. Technol.* **2013**, *3*, 2862.
[14] Z. Wang, S. Ning, P. Liu, Y. Ding, A. Hirata, T. Fujita, M. Chen, *Adv. Mater.* **2017**, *29*.
[15] P. Liu, P. Guan, A. Hirata, L. Zhang, L. Chen, Y. Wen, Y. Ding, T. Fujita, J. Erlebacher, M. Chen, *Adv. Mater.* **2016**, *28*, 1753.
[16] T. Fujita, P. Guan, K. McKenna, X. Lang, A. Hirata, L. Zhang, T. Tokunaga, S. Arai, Y. Yamamoto, N. Tanaka, Y. Ishikawa, N. Asao, Y. Yamamoto, J. Erlebacher, M. Chen, *Nat. Mater.* **2012**, *11*, 775.
[17] D. Li, Y. Zhu, H. Wang, Y. Ding, *Sci. Rep.* **2013**, *3*, 3015.
[18] A. Goyal, C. J. Bondue, M. Graf, M. T. M. Koper, *Chem. Sci.* **2022**, *13*, 3288.
[19] C. Zhu, Z. Qi, V. A. Beck, M. Luneau, J. Lattimer, W. Chen, M. A. Worsley, J. Ye, E. B. Duoss, C. M. Spadaccini, C. M. Friend, J. Biener, *Sci. Adv.* **2018**, *4*, eaas9459.
[20] Y. Ding, M. Chen, *MRS Bull.* **2009**, *34*, 569.
[21] R. Zhang, H. Olin, *Materials* **2014**, *7*, 3834.
[22] E. Seker, J. T. Gaskins, H. Bart-Smith, J. Zhu, M. L. Reed, G. Zangari, R. Kelly, M. R. Begley, *Acta Mater.* **2007**, *55*, 4593.
[23] E. Seker, M. Reed, M. Begley, *Mater.* **2009**, *2*, 2188.
[24] K. Nishio, H. Masuda, *Angew. Chem.* **2011**, *123*, 1641.
[25] J. Patel, L. Němcová, P. Maguire, W. G. Graham, D. Mariotti, *Nanotechnology* **2013**, *24*, 245604.
[26] Q. Chen, T. Kaneko, R. Hatakeyama, *Appl. Phys. Express* **2012**, *5*, 086201.
[27] P. Rumbach, D. B. Go, *Top. Catal.* **2017**, *60*, 799.
[28] S. Pedireddy, H. K. Lee, W. W. Tjiu, I. Y. Phang, H. R. Tan, S. Q. Chua, C. Troadec, X. Y. Ling, *Nat. Commun.* **2014**, *5*, 4947.
[29] B. R. Panda, A. Chattopadhyay, *J. Nanosci. Nanotechnol.* **2007**, *7*, 1911.
[30] D. Wang, P. Schaaf, *J. Mater. Chem.* **2012**, *22*, 5344.
[31] A. Sukeri, L. P. H. Saravia, M. Bertotti, *Phys. Chem. Chem. Phys.* **2015**, *17*, 28510.
[32] A. Sukeri, M. Bertotti, *J. Braz. Chem. Soc.* **2017**.
[33] H. Zheng, C. Picard, S. Ravaine, *Front. Chem. Sci. Eng.* **2018**, *12*, 247.
[34] Y. Gao, Y. Ding, *Chemistry* **2020**, *26*, 8845.
[35] J. A. Tapia Burgos, C. Mahr, A. R. S. Olaya, L. Robben, M. Schowalter, A. Rosenauer, G. Wittstock, A. Wittstock, M. Bäumer, *SSRN Electronic Journal* **2021**.
[36] E. Artmann, P. V. Menezes, L. Forschner, M. M. Elnagar, L. A. Kibler, T. Jacob, A. K. Engstfeld, *ChemPhysChem* **2021**, *22*, 2429.
[37] S. K. Sengupta, *J. Electrochem. Soc.* **1998**, *145*, 2209.
[38] S. K. Sengupta, O. P. Singh, *J. Electroanal. Chem.* **1994**, *369*, 113.
[39] A. Hickling, M. D. Ingram, *Trans. Faraday Soc.* **1964**, p. 783–793.
[40] E. Artmann, L. Forschner, T. Jacob, A. K. Engstfeld, *J. Vac. Sci. Technol. A* **2022**, *40*, 053005.

[41] A. Yerokhin, V. R. Mukaeva, E. V. Parfenov, N. Laugel, A. Matthews, *Electrochim. Acta* **2019**, *312*, 441.
[42] J. J. Pireaux, M. Liehr, P. A. Thiry, J. P. Delrue, R. Caudano, *Surf. Sci.* **1984**, *141*, 221.
[43] L. K. Ono, B. Roldan Cuenya, *J. Phys. Chem. C* **2008**, *112*, 4676.
[44] E. Irissou, M.-C. Denis, M. Chaker, D. Guay, *Thin Solid Films* **2005**, *472*, 49.
[45] M. P. Seah, G. C. Smith, M. T. Anthony, *Surf. Interface Anal.* **1990**, *15*, 293.
[46] J. Szlachetko, J. Sá, M. Nachtegaal, U. Hartfelder, J.-C. Dousse, J. Hoszowska, D. L. Abreu Fernandes, H. Shi, C. Stampfl, *J. Phys. Chem. Lett.* **2014**, *5*, 80.
[47] H. Shi, R. Asahi, C. Stampfl, *Phys. Rev. B* **2007**, *75*.
[48] T. Dickinson, A. F. Povey, P. M. A. Sherwood, *J. Chem. Soc. Faraday Trans. 1* **1975**, *71*, 298.
[49] A. Krozer, M. Rodahl, *J. Vac. Sci. Technol. A* **1997**, *15*, 1704.
[50] N. Saliba, D. Parker, B. Koel, *Surf. Sci.* **1998**, *410*, 270.
[51] A. Vitrey, R. Alvarez, A. Palmero, M. U. González, J. M. García-Martín, *Beilstein J. Nanotechnol.* **2017**, *8*, 434.
[52] K. Azumi, T. Mizuno, T. Akimoto, T. Ohmori, *J. Electrochem. Soc.* **1999**, *146*, 3374.
[53] H. H. Kellogg, *J. Electrochem. Soc.* **1950**, *97*, 133.
[54] H. Tsai, E. Hu, K. Perng, M. Chen, J.-C. Wu, Y.-S. Chang, *Surf. Sci.* **2003**, *537*, L447.
[55] A. L. Yerokhin, X. Nie, A. Leyland, A. Matthews, S. J. Dowey, *Surf. Coat. Technol.* **1999**, *122*, 73.
[56] X. Jin, X. Wang, J. Yue, Y. Cai, H. Zhang, *Electrochim. Acta* **2010**, *56*, 925.
[57] S. K. Sengupta, O. P. Singh, *J. Electroanal. Chem. Interfacial Electrochem.* **1991**, *301*, 189.
[58] S. K. Sen Gupta, R. Singh, *Plasma Sources Sci. Technol.* **2017**, *26*, 015005.
[59] G. Saito, Y. Nakasugi, T. Akiyama, *J. Appl. Phys.* **2015**, *118*, 023303.
[60] P. Mandin, R. Wüthrich, H. Roustan, *AIChE J.* **2010**, *33*, 2446.
[61] B. Zheng, K. Wang, M. Shrestha, T. Schuelke, Q. H. Fan, *Plasma Sources Sci. Technol.* **2019**, *28*, 085016.

Manuscript received: August 26, 2022
Revised manuscript received: October 27, 2022
Accepted manuscript online: November 3, 2022
Version of record online: ■■, ■■■

11.4 Appendix 4

Hereafter my first author publication with the title "Facet-Dependent Formation and Adhesion of Au Oxide and Nanoporous Au on Poly-Oriented Au Single Crystals" published on a preprint server is attached.[265]

Facet-Dependent Formation and Adhesion of Au Oxide and Nanoporous Au on Poly-Oriented Au Single Crystals

Evelyn Artmann, Tobias Schmider, Timo Jacob, and Albert K. Engstfeld*

Institute of Electrochemistry, Ulm University, D-89081 Ulm, Germany

E-mail: albert.engstfeld@uni-ulm.de
Phone: +49 (0)731 25401

Abstract

Nanoporous Au has different properties compared to bulk Au, making it an interesting material for numerous applications. Depending on the preparation procedure, the porosity, thickness, and homogeneity of the NPG films can be tuned. To modify the structure of NPG films in a targeted manner and thus adapt them to specific applications, a fundamental understanding of the structure formation is essential. In this work, we focus on NPG prepared from Au oxide formed during high voltage electrolysis in an alkaline electrolyte on a poly-oriented Au single crystal electrode. These poly-oriented single crystals consist of a single crystalline metal bead, with faces with different crystallographic orientations. Consequently, these POSCs allow screening of the influence of the crystallographic orientation on the structure formation of the Au oxide formed during high voltage electrolysis and the NPG film formed via electrochemical reduction of the Au oxide for different facets in a single experiment. The high voltage electrolysis is performed at current densities between 2.70 and 3.76 $A \cdot cm^{-2}$ (300 V) and between 0.24 and 6.39 $A \cdot cm^{-2}$ (540 V) with electrolysis times ranging from 100 ms to 30 s. The amount of Au oxide formed is determined by electrochemical measurements and the structural properties are investigated by scanning electron microscopy and optical microscopy. We show that the Au oxide formation is mostly independent of the crystallographic orientation except for thick Au oxide layers. In turn, the macroscopic structure of the NPG films depend on the experimental parameters, the thickness of the Au oxide precursor thickness, and the crystallographic orientation of the substrate. Possible reasons for the frequently observed exfoliation of the NPG films are discussed.

Introduction

Nanoporous Au (NPG) has a porous, sponge-like structure whose pores are connected by Au ligaments.[1,2] The sponge-like structure often shows different properties compared to the bulk material. Possible applications for NPG films are in the fields of (bio)sensing,[1,3–7] (electro)catalysis,[5,8–13] or in heterogeneous catalysis.[6,14–16]

Typically, NPG films are prepared by chemical dealloying, mostly of a Ag-Au alloy. In this process, the less noble metal is dissolved, *e.g.*, Ag, by using a HNO_3 solution.[6,9,10,17,18] Alternatively, the dealloying process can also be induced electrochemically.[4] A disadvantage of these dealloying processes is that Ag residues can remain in the resulting NPG film. Such trace impurities can play a significant role for example in catalytic processes.[6,19,20] Recently it has been shown that NPG films can also be prepared by anodization (Au oxide formation at a Au anode set to a potential of a few volts versus a fixed reference with current densities of approximately 0.035 $A{\cdot}cm^{-2}$) and subsequent electrochemical reduction.[21,22] Similarly, recently we have shown that NPG films can be produced by (electro)chemically reducing Au oxide films formed during high voltage (HV) electrolysis and anodic contact glow discharge electrolysis (aCGDE). The latter phenomenon refers to a plasma that forms in a gas sheath around the working electrode at high voltages.[23–25] In both cases, the voltages can reach several hundreds of volts and the current densities are in the range of 1 to 10 $A{\cdot}cm^{-2}$.[26–28] Advantages of this high voltage (current density) approach are that the preparation times are significantly shorter and only an (alkaline) electrolyte is required.[27] Furthermore, we demonstrated that the final structure of the NPG film depends on the method used to reduce the Au oxide, *i.e.*, electrochemically or in the presence of H_2O_2.[27] For long electrolysis times, it is even possible to form a NPG film *in-situ* in a single step.[27]

To further tune the formation of the NPG film, it is beneficial to understand both the growth and the interaction of the Au oxide films as well as the NPG films with the Au substrate. Within that context, Henkelmann *et al.* studied, for example, the densification/detachment of NPG films from Au substrates and found that the substrate's curvature and, thus, the surface morphology of the Au substrate plays an important role.[29] Khristosov *et al.* demonstrated that NPG single crystals can be grown on a SiO_2 substrate up to a size of several hundred micrometers.[30] For this purpose, a eutectic melt of Au and Ge is first prepared, which is then solidified. The Ge is subsequently removed by wet etching, NPG single crystals remain.[30]

In this work, we study the influence of the crystallographic orientation of the substrate on the formation of the Au oxide during HV electrolysis and the structure of the NPG film formed by electrochemical reduction. Such aspects can be investigated by using oriented single-crystal electrodes, an approach widely used in surface science and electrochemistry. For example, the facet-dependent oxide formation has been studied on noble metals such as Pt,[31] Au,[32] and on non-noble metals such as Al,[33,34] Ni,[35] Fe,[36] or Cu.[37,38] Conway and Jerkiewicz, for example, found that oxide formation occurs at different rates on the Pt(111) and the Pt(100) facets.[31] Vvedenskii *et al.* studied the influence of different Cu low-indexed crystallographic orientations regarding the Cu(I) and Cu(II) oxide formation.[37] Scholten *et al.* were able to show that O_2 plasma pre-treatment leads to the formation of CuO on the Cu(111) surface, while on Cu(100) primarily Cu_2O is formed after the same experimental procedure. Also, the surface morphology in both cases differed significantly.[38] The different structures obtained on the different facets during the pre-treatment can have a significant impact on the catalytic activity.[39] A caveat of using such oriented single crystals is that several differently oriented single crystals are required, to study the facet-dependent properties, which is a rather time-consuming task. In recent years, poly-oriented single crystals (POSCs) have been exploited to screen processes occurring at facets with different crystallographic orientations in a single experiment.[40–42] Such POSCs are created by melt-

ing the end of a metal wire, which leads to the formation of a liquid bead. This bead is then slowly cooled in a controlled atmosphere, resulting in a single crystal with facets exhibiting different crystallographic orientations.[43–49] Note that the distribution and size of these facets can vary depending on the metal used in the process and the size of the POSC.[49] These electrodes were used to determine the facet-dependent restructuring of Pt electrodes during oxidation and reduction cylces[41] or cathodic corrosion of Au and Pt.[40,42]

In this work, we study the growth of Au oxide on Au POSCs, prepared by HV electrolysis at a voltage close to the breakdown voltage (300 V / current density between 2.70 and 3.76 A·cm^{-2}) and in the region of aCGDE (540 V / current density between 0.24 and 6.39 A·cm^{-2}) for different electrolysis times (a few 100 ms up to 30 s) in 0.01 M KOH. The amount of Au oxide is inferred from the electrochemical reduction of the Au oxide film. In the second step, the Au oxide film is reduced electrochemically to form a NPG film on the Au POSC. The structural properties of the resulting Au oxides and the NPG films are investigated by optical microscopy and scanning electron microscopy (SEM). Aside from the overall structure of the entire POSC, we focus on the low-index regions, *i.e.*, Au(111) and Au(100), and the regions vicinal to those surfaces, which consist of extended Au(111) and Au(100) terraces.

Results and Discussion

Each measurement in this work was performed on a freshly-prepared Au POSC, shown in an SEM image in Fig. 1a. A detailed description of the preparation procedure, verification of the quality, and the size of the crystals can be found in the experimental section. From Laue X-ray diffraction (XRD) measurements, we determined the position of the low-index facets, *i.e.*, Au(111), Au(110), and Au(100). Typical Laue XRD patterns of all three low-index facets of a Au POSC can be found in the SI (Section S1). Once these regions were characterized, the Au(111) and the Au(100) facets can also be discerned by visual inspection of the POSC. Other facets, such as the Au(110), can then be inferred from their relative position to the other low-index facets. A magnification of the Au(111) and Au(100) facets is shown in the SEM images in Figs. 1b and d. The images in Figs. 1c and e show the region vicinal to the Au(111) and the Au(100) facets, which are referred to as Au(111*) and Au(100*) regions throughout this work. These regions have a significant amount of steps. We suggest that the crystallographic orientation in these regions is, however, predominately that of the adjacent low-index facet.

Au Oxide Film Formation

During HV electrolysis, a Au oxide film forms on the Au POSCs. This Au oxide film acts as a precursor for the formation of a NPG film via electrochemical reduction discussed below. We study the Au oxide growth at 300 V (before the breakdown of NE – average current density between 2.70 and 3.76 A·cm^{-2}) and at 540 V (in the aCGDE region – average current density between 0.24 and 6.39 A·cm^{-2}) for different electrolysis times.[26,27] Note, for the Au oxide formation, the current density is a more meaningful parameter since the applied voltage strongly depends on the electrodes' geometry, electrodes position, and the cell geometry.[28] Nevertheless, in this article we use the voltages to discern between the NE and aCGDE region. During the Au oxide growth at 300 V, vivid bubble formation is observed, and hence the electrode is only partially in contact with the electrolyte. The current is slightly increasing with increasing electrolysis time (see the red curve in Fig. S2). This is related to an increase in electrolyte temperature, which increases the electrolytes' conductivity. At 540 V the electrode is surrounded by a gas sheath in which a plasma can be ignited.[26,27] During HV electrolysis at 540 V the current is high and almost constant for short times until it breaks down to a lower constant value (see blue curve in Fig. S2). This marks the point when a plasma is formed within the gas sheath. Note that for short electrolysis times, the plasma is not al-

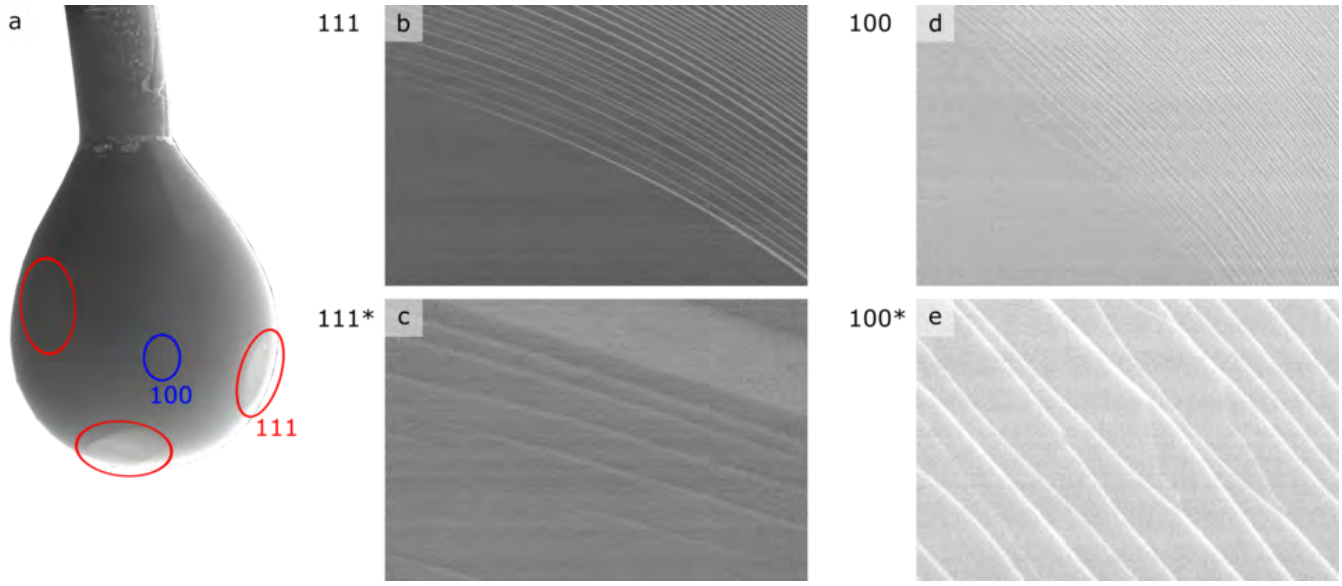

Figure 1: a) SEM image of an as-prepared Au POSC, and SEM images of b) the Au(111) facet, c) the surface vicinal to the Au(111) facet (Au(111*)), d) the Au(100) facet and e) the surface vicinal to the Au(100) facet (Au(100*)), respectively. The size of the POSC in a) can be estimated from the diameter of the wire, which is 1 mm. The image size in b) is 150 μm $\times$ 100 μm, in d) 30 μm $\times$ 20 μm and in c) and e) 3 μm $\times$ 2 μm.

ways perfectly discernable by the naked eye.

In general, the amount of Au oxide formed can be determined from the charge which passed during the electrochemical reduction of the Au oxide.[32] The experiment is performed in an electrochemical cell in 0.01 M KOH. The electrode potential is decreased starting from 1.1 V_{RHE} (vs. the reversible hydrogen electrode) with a scan rate of 50 mV s^{-1} and kept at 0.25 V_{RHE} until the measured current was negligible. A more detailed description can be found in the Experimental Section and elsewhere.[26,27] Figure 2 shows the evolution of the charge density during electrochemical reduction of the Au oxide formed on the Au POSCs for different HV electrolysis times at 300 V (red curve) and 540 V (blue curve). In both cases, the charge density increases in a linear way with increasing electrolysis time, indicating that the Au oxide film thickness increases with increasing electrolysis time up to 30 s. Note that POSCs modified with the same HV electrolysis treatment but with different bead sizes will show similar charge densities upon electrochemical reduction, although the size distribution of the facets on the crystal may change with the size of the bead. For short electrolysis times, the Au oxide film thickness is similar for electrodes prepared by HV electrolysis at 540 V and 300 V. For long electrolysis times, the Au oxide films are thicker at 300 V than at 540 V. This can be rationalized by the difference in current density for different times and applied voltages. The current density at 540 V is higher for short electrolysis times and lower for long electrolysis times. Moreover, the charge densities obtained after 30 s HV electrolysis are very similar to those reported previously for wire electrodes.[26]

Following we discuss the structural properties of the Au oxide films grown during HV electrolysis at both voltages and different electrolysis times, starting with electrodes prepared at 540 V.

Au Oxide Formation during aCGDE

Optical microscope and SEM images of Au POSCs taken after HV electrolysis at 250 ms, 2 s, and 30 s at 540 V are shown in Fig. 3. Additional optical microscope images for other electrolysis times can be found in the SI in Section S3. After 30 s the Au POSC is red, clearly indicating Au oxide formation.[21,22,26,27] For shorter electrolysis times, the red color is not as clearly apparent in the optical microscope images.From visual inspection, the red

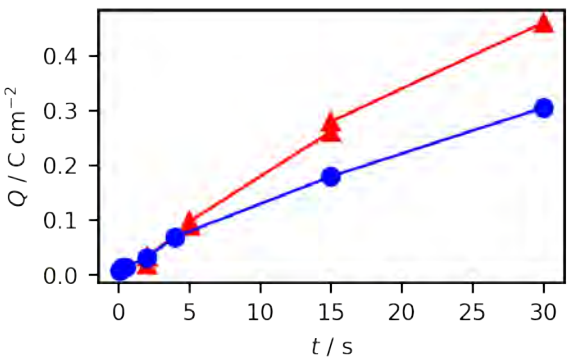

Figure 2: Charge densities inferred from electrochemical reduction of Au oxide formed after different HV electrolysis times on Au POSCs at 300 V between 2 s and 30 s (red) and 540 V between 100 ms and 30 s (blue) in 0.01 M KOH.

color is clearly apparent for electrolysis times longer than 2 s.The electrochemical characterization above (see Fig. 2) suggests that Au oxide also forms at shorter electrolysis times. Thus, the Au oxide films at electrolysis times shorter than two seconds are presumably too thin to be apparent by the red color by the naked eye. More detailed insights on the structural properties and the integrity of the Au oxide films are visualized by SEM images of the entire POSCs after all electrolysis times in Fig. S4. A magnification of the Au(111*) and Au(100*) regions can also be found in Fig. S4.

From the SEM images of the entire Au POSC no apparent structural changes were observed, indicating that the Au oxide film grows homogeneous on the entire surface independent from the crystallographic orientation or the electrolysis time (up to 30 s). From a closer look at both the Au(111*) and the Au(100*) (see Figs. S4h and o), no clear structural changes of the surface are observed after HV electrolysis for 100 ms at 540 V. After 250 ms, in some of the images of the Au(111*) region, minor changes in the form of elongated ripples at the step edges, are observed (marked by arrows in Fig. S4i). These features could be considered to be an artifact. Further below, we will indeed show that these features play a role in the NPG film formation. After 500 ms, a slight roughening of the Au(111*) surface is apparent (indicated by an arrow). The Au(100*) surface seems to change to a smaller extent compared to the Au(111*) surface (see Figs. S4j and q). On Au(100*), hardly any changes can be seen up to a HV electrolysis time of 500 ms. A distinct roughening of the surface can be seen after 2 s and longer electrolysis times (up to 30 s) on the Au(111*) and Au(100*) facets (see

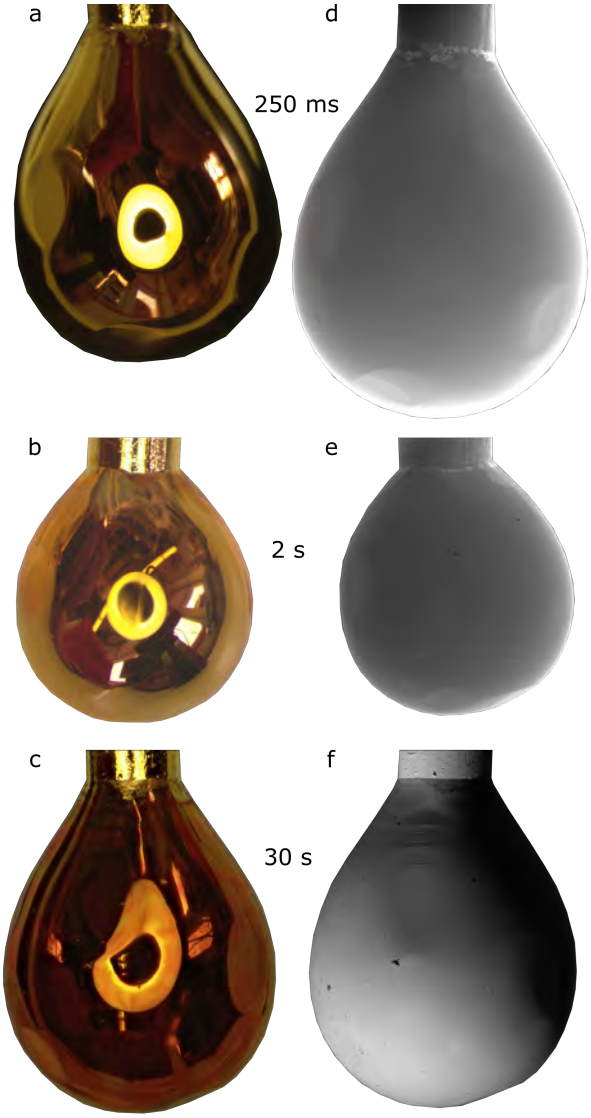

Figure 3: Optical microscope and SEM images of Au POSCs after HV electrolysis for 250 ms, 2 s and 30 s at 540 V in 0.01 M KOH. Optical microscope images after additional electrolysis times after HV electrolysis at 540 V can be found in Fig. S3 and SEM images of the whole POSCs, as well as magnifications of the Au(111*) and Au(100*) facets after the same conditions can be found in Fig. S4. The size of the beads can be estimated from the wire diameter, which is 1 mm.

Figs. S4k-n and Figs. S4r-u). The morphology of the Au oxide and the degree of roughening for the different facets observed in the SEM images are hereby similar for all electrolysis times considered.

Au Oxide Formation during NE

From visual inspection and optical microscope images of Au POSCs after HV electrolysis at 300 V, the distinct red color for the formation of a Au oxide is visible after 2 s and becomes more clear after 15 s (see Figs. 4a and b and Fig. S5). Here, also additional electrochemical measurements clearly indicate Au oxide formation for all electrolysis times (see Fig. 2 red curve). SEM images of the resulting electrodes are shown in Fig. 4c and d. Additional SEM images of the whole Au POSCs at all electrolysis times studied at 300 V, including a magnification of the Au(111*) region are shown in the SI in Fig. S6.

Up to 15 s the SEM images of the entire Au POSC in Fig. S6 do not suggest any kind of restructuring of the Au oxide. A closer inspection of, for example, the Au(111*) facet shows a slightly roughened surface in the range from 2 s to 15 s. The surface structures look similar to those observed at 540 V (compare Figs. S6e to g and Figs. S4k to m). After 30 s the formation of cracks within the Au oxide film is observed (see Fig. S6 or Figs. 5a and b).

Comparing the SEM images of the Au oxide taken on different regions of the POSC after 30 s HV electrolysis at 300 V in Figs. 5a to d, we observe distinctly different structural properties. First, it seems that the Au oxide film does not form a uniform film on smooth surfaces, namely the Au(111) and the Au(100) facets (Figs. 5a and c). In these regions, the Au oxide film contains many cracks and even seems to exfoliate from the surface. Interestingly, the Au oxide film also exfoliates on the Au(111*) facet (see Figs. 4b and d, Figs. 5a and b and Fig. S6). On the Au(100*) facet the Au oxide film is still rather smooth and does not show pronounced crack formation (Figs. 5c and d. The region marked with an arrow in Fig. 5c is magnified in Fig. 5d). For comparison with our previous experiments on polycrystalline (poly) Au wire electrodes, we included SEM images in

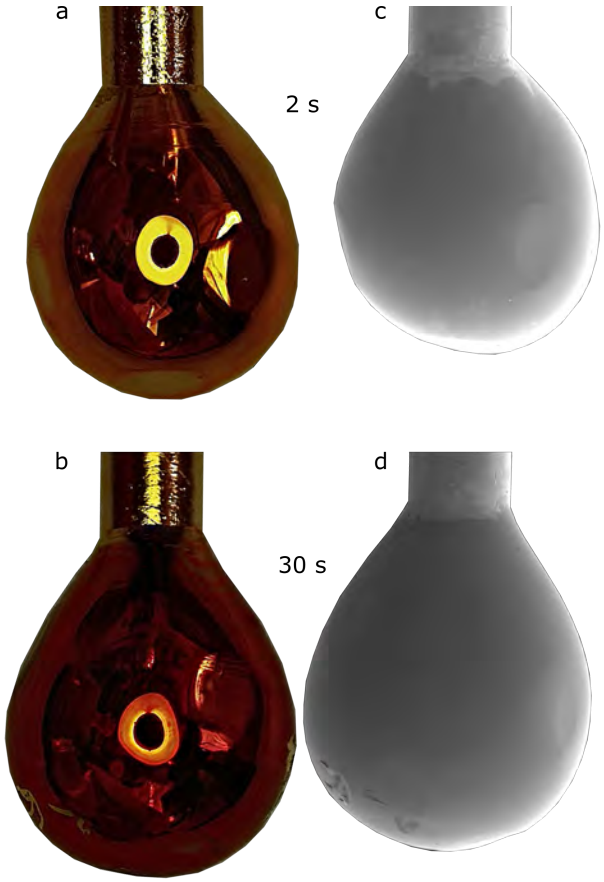

Figure 4: Optical microscope (left column) and SEM images (right column) of Au POSCs after HV electrolysis at 300 V for 2 s in a) and c) and 30 s in b) and d). More microscope and SEM images after other electrolysis times at 300 V can be found in Section S5 and S6, respectively. Additional SEM images of the Au(111*) facet can be found in Fig. S6. Based on the wire diameter of the POSCs (1 mm), the size of the Au POSCs can be estimated.

Figs. 5e and f. These electrodes show significant restructuring and crack formation on the entire surface. Intuitively, one could assume that the cracks might be related to grain boundaries present on the polycrystalline samples. In order to elucidate the impact of grain boundaries, we investigated the Au oxide growth on different POSCs containing one or more grain boundaries (see Fig. 6 and Fig. S7). Fig. 6 shows a region with a grain boundary after HV electrolysis at 300 V for 30 s. It is apparent that along the grain boundary merely some defects are observed. The cracks only appear on one side of the boundary. Hence the crack formation seems

to depend on the adhesion to the substrate and therefore mainly on the crystallographic orientation of the underlying substrate and not the grains itself.

In total, for both electrolysis voltages, a homogeneous Au oxide film is formed on the entire Au POSC. Only for 30 s HV electrolysis at 300 V, the Au oxide film is less homogeneous or exfoliates from the flat Au(111) and Au(100) regions as well as in the Au(111*) region. The origin of the crack formation can at this point not be explained. Possible reasons could be the difference in Au oxide thickness obtained for long electrolysis times or the differences in processes occurring at the electrodes at both voltages (electrolysis with bubble formation or plasma). It is also possible that the thick Au oxide film formed after 30 s HV electrolysis is disrupted upon emersion of the electrode from the electrolysis solution.

NPG Film Formation

NPG films were prepared by electrochemically reducing similar Au oxide electrodes to those presented in the previous section. Here, we also first focus on electrodes prepared by HV electrolysis at 540 V. Optical microscope and SEM images of electrochemically reduced Au POSCs after 250 ms, 15 s and 30 s are shown in Fig. 7. Additional optical microscope and SEM images for different electrolysis times are provided in Fig. S8. Although the Au POSCs in the optical microscope images tend to appear golden to some extent, they exhibit a black coloration, especially at electrolysis times longer than 500 ms. The black color is distinct for the formation of a NPG film.[21,22,26,27,50–52]
From the optical microscope and SEM images of the entire Au POSC in Fig. 7 and Fig. S8 it is apparent that after HV electrolysis at 540 V for 15 s (and more) and subsequent electrochemical reduction, the resulting NPG film randomly exfoliates from the surface. In some cases, exfoliation is also observed to some degree in the SEM images of the entire POSC in experiments with 2 s and 4 s electrolysis time.

For short electrolysis times (in the range of milliseconds), the optical microscope and the SEM images of the entire POSC do not show macroscopic exfoliation of the NPG film (Figs. 7a and d and Fig. S8). Small changes are, however, observed after different electrolysis times and in different regions of the Au POSC.This is illustrated with SEM images of the NPG films formed on the Au(111*) and the Au(100*) facets after 100 ms and 250 ms in Fig. S9. After 100ms, the NPG film is rather homogeneous on all facets, as the Au oxide film formed after 100 ms on the POSC (see Figs. S4a, h, o). After 250 ms small ripples were observed in the Au oxide film grown on the Au(111*) facet in Fig. S4i, which are also observed in the NPG film after electrochemical reduction in Fig. S9c. Thus, in the regions where a homogeneous Au oxide film was observed, also a homogeneous NPG film was formed (at least for short electrolysis times up to 250 ms).

The NPG film formed on the different facets after 500 ms is shown in Fig. 8, where Figs. 8a and b show the regions vicinal to the Au(111) and Au(100) facets and Figs. 8c to f the flat Au(111) and Au(100) regions (low index regions). According to Fig. 8a the NPG film starts to exfoliate from the Au(111*) facet, while on the Au(100*) facet in Fig. 8b the NPG film tends to be more stable/homogeneous with a small number of defects, such as the one in the center of the image. The NPG film on the Au(111) and Au(100) facets also exfoliates strongly, as shown in Figs. 8c to f. Overall, on the Au(100) facet, the exfoliation is more pronounced in certain regions than others. This aspect might be due to an inhomogeneity in the local atomic structure on the (100) facets. However, such detailed atomic insights can not be inferred from SEM imaging and require further studies on oriented single crystals.

For longer electrolysis times (2 to 30 s), the NPG film formed on the Au(111) facet always exfoliates significantly (Fig. S10), while it is rather stable on the Au(100) facet (Fig. S11). On the regions vicinal to the low index facets the situation is more complex. SEM images of these regions are provided in Fig. 9. The observations are briefly summarized and subsequently discussed.

After 2 s the NPG film strongly exfoliates

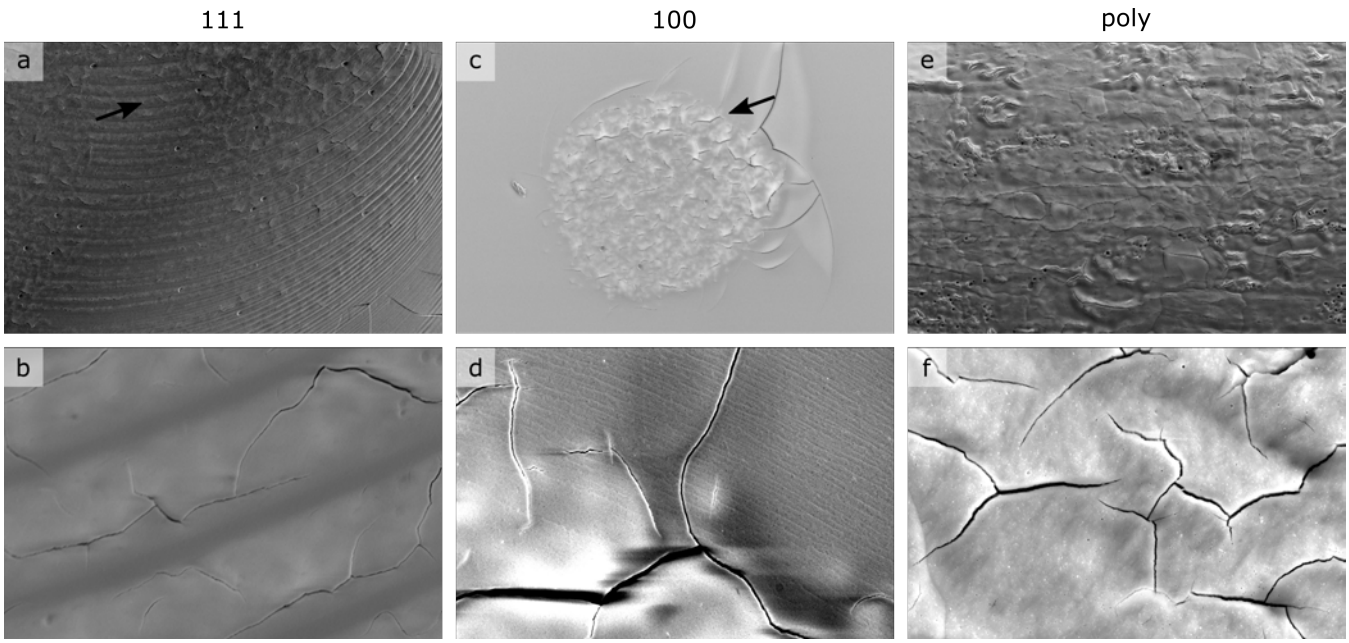

Figure 5: SEM images of a) and b) the Au(111), c) and d) the Au(100) facet, and e) and f) Au(poly) after HV electrolysis at 300 V for 30 s. The positions where the image magnifications in b) and d) were taken are marked with an arrow in a) and c). The size of the images in the top row are 300 μm $\times$ 200 μm and in the bottom row 30 μm $\times$ 20 μm. The contrast and brightness in a) and d) have been adjusted for better visibility.

Table 1: Exfoliation of the NPG film formed after electrochemical reduction (✓) or intact NPG film (-) after treatment of the Au POSCs at 540 V between 100 ms and 30 s. A bracket indicates the tendency of the film in terms of its stability, but its behavior is not as clear as in the cases without brackets.

	100 ms	250 ms	500 ms	2 s	4 s	15 s	30 s
111	-	-	✓	✓	(✓)	✓	✓
111*	-	-	✓	✓	(✓)	✓	✓
100	-	-	✓	-	-	(✓)	✓
100*	-	-	(✓)	-	-	(✓)	✓

in certain measurements and regions of the Au(111*) facet from the substrate, as shown in Fig. 9a, indicating that the adhesion of the film to the substrate is rather weak in these regions. Figures 9b' and b", show a magnification of the region where the film exfoliated and a region where the film appears mostly homogeneous. (regions are marked with arrows in Fig. 9a). In the region where the film exfoliated (Fig. 9b'), the surface seems significantly restructured. In Fig. 9b", where the film is still more or less intact, the porosity of the NPG film is very much different on the Au(111) terraces (bright region) than in the region which connects these terraces (dark region). In the Au(100*) region in Figs. 9c and d, exfoliation of the film is usually not observed. However, here we also observe a difference in the NPG film structure depending on the region on the Au(100*) facet. Unlike the Au(111*) facet, the NPG film structure is not different for the Au(100) terraces and the adjacent step edges, but the NPG film breaks up randomly between them. In the brighter areas, the NPG film is less dense or seems slightly torn apart. Figure 9d' shows a magnification of the homogeneous NPG region in Fig. 9c, *i.e.*, of the region where the NPG film is rather compact. Figure 9d" shows a region of the NPG film that is less compact. The two regions in Figs. 9d' and d" are marked in Fig. 9c. Overall, the NPG

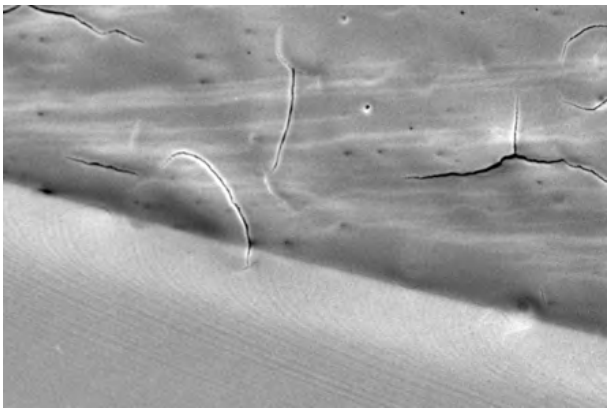

Figure 6: SEM image of a grain boundary adjacent to a Au(111) facet and its influence on the structure formation of Au oxide on the Au POSC after HV electrolysis for 30 s at 300 V. The image size is 30 μm $\times$ 20 μm.

film obtained on the Au(100*) facet is clearly more homogeneous than the one formed on the Au(111*) facet. As in the case of Au oxide formation, grain boundaries have no influence on the structural properties of the NPG films at 540 V as illustrated in Fig. S7b. The structure of the NPG film formed after 4 s on the Au(111*) facet in Figs. 9e and f, is very similar to that obtained after 2 s. Thus, a homogeneous NPG film forms on the Au(111) terraces, which is torn apart in the regions between these terraces apparent from Fig. 9f. On the Au(100*) facet in Figs. 9g and h, the NPG film is still homogeneous, showing similar structures on the terraces and the regions in between. Only in a few cases, we observed that the film was slightly torn apart at the regions vicinal to the Au(100) facet, as shown in Fig. S12. After 15 s and 30 s, from the microscopy and SEM images (see Fig. 7 and Fig. S8), the NPG film on the Au surface is rather irregular and inhomogeneous on the entire bead. After both electrolysis times, the NPG film significantly exfoliates from the Au(111) facet as shown in Figs. S10b and c. Interestingly, from a closer inspection of the individual facets shown in Figs. 9i to l, one observes that the NPG film on the Au(111*) facet is rather homogeneous in contrast to shorter electrolysis times, where the NPG films are much thinner (according to the electrochemical data presented in Fig. 2). On the Au(100*) facet, the

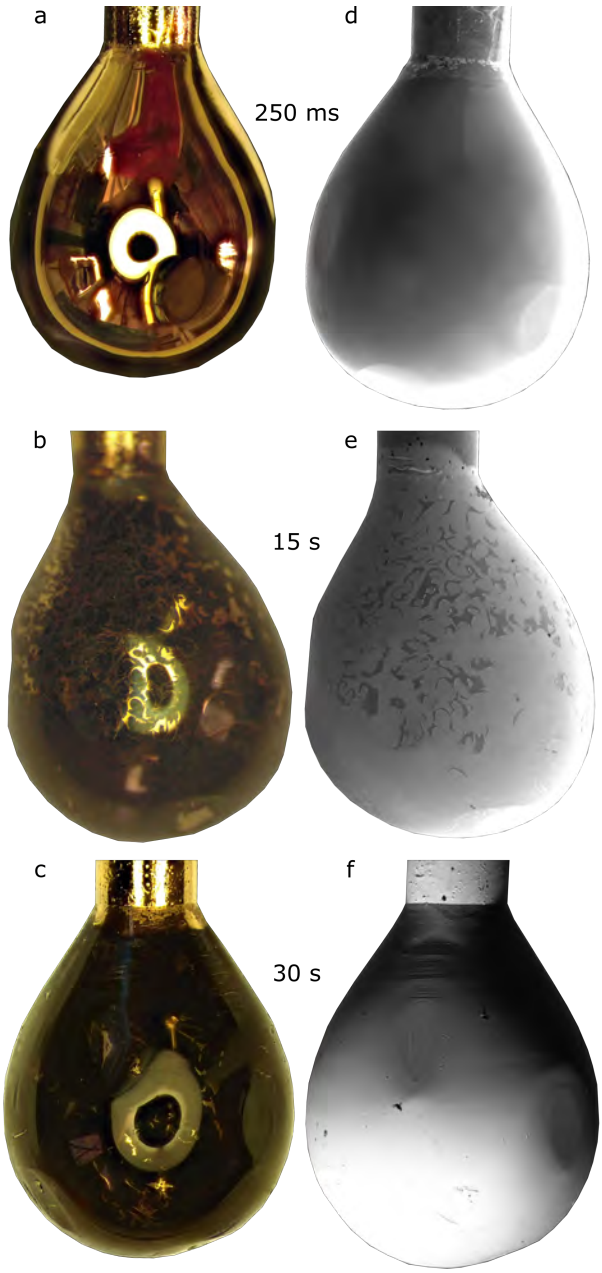

Figure 7: Optical microscope (a) to c)) and SEM images (d to f)) of Au POSCs after HV electrolysis at 540 V for a) and d) 250 ms, b) and e) 15 s, and c) and f) 30 s followed by electrochemical reduction of the POSCs. Optical microscope images, as well as SEM images after all studied electrolysis times at 540 V and subsequent electrochemical reduction can be found in Fig. S8. The size of the Au POSCs can be estimated based on the wire diameter of the POSCS which is 1 mm.

situation is different (see Figs. 9k and l). After 30 s, the NPG film is torn apart, though it does not exfoliate. This suggests strong interaction

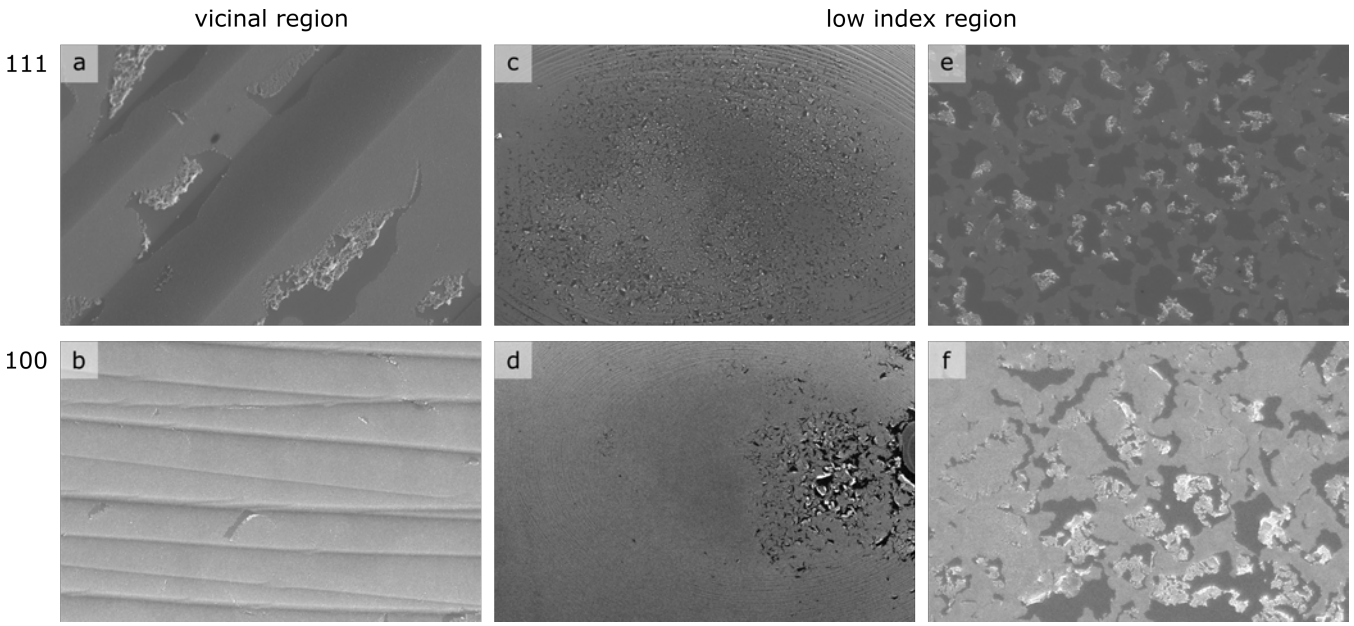

Figure 8: SEM image of the Au(111) and the Au(100) facet after HV electrolysis at 540 V for 500 ms and subsequent electrochemical reduction. a) and b) show the regions vicinal to the Au(111) and Au(100) facets. The image size in both cases is 9 μm $\times$ 6 μm. c) and d) show the entire facets with images sizes of 600 μm $\times$ 400 μm and 300 μm $\times$ 200 μm. The brightness and contrast were adjusted in both images. e) and f) show the same region with higher magnification (30 μm $\times$ 20 μm).

of the NPG film with the substrate. On the Au(100) facet, the NPG film is homogeneous, and almost no cracks were observed within the film (see Fig. S11).

We deduce the following from the findings for NPG film formation from electrochemically reducing Au oxides formed during HV electrolysis at 540 V and different times. First, even though the precursor Au oxide layer is homogeneous on the entire bead, it was observed that the resulting NPG film exfoliates for some of the samples from the surface. Since the Au oxide is homogeneous, we suggest that the exfoliation either occurs during the electrochemical reduction or the emersion of the electrodes from the electrolyte after the electrochemical reduction. From our experiment, we can not distinguish which experimental step is at the origin of the exfoliation process. Focusing on a region where the NPG film exfoliated in Fig. 9a, we observed that the underlying Au surface was rather inhomogeneous. We suggest that the inhomogeneity is due to residues or pinning points of the exfoliated NPG film. For short electrolysis times, after 500 ms, exfoliation primarily occurs in regions with Au(111) and Au(111*) orientation and to a certain extent also on the Au(100) facet, but not on the Au(100*) facet. More homogeneous NPG films are formed on the Au(111*) facet for longer electrolysis times, while it still exfoliates from the Au(111) facet. On the Au(100*) and the Au(100) facets, more homogeneous NPG films are formed. Between 2 and 30 s no exfoliation occurs on the Au(100) facet. Nonetheless, for electrolysis times longer than 15 s significant film exfoliation is observed on the entire POSC, making it difficult to assign a facet-dependent growth of the film to any region on the POSC. The reason for the exfoliation can be found in the thickness of the Au oxide film formed on the Au POSC, which increases with increasing electrolysis time (see Fig 2). Assuming that the film thickness is identical on all facets after the HV electrolysis, we suggest that the thin NPG films tend to exfoliate more easily than thick NPG films. The observed facet-dependent exfoliation for short electrolysis times might be related to the adhesion of the NPG film in some regions and/or the lateral interaction of the NPG film. For longer electrolysis times which produce thicker Au oxide films, exfoliation becomes less pro-

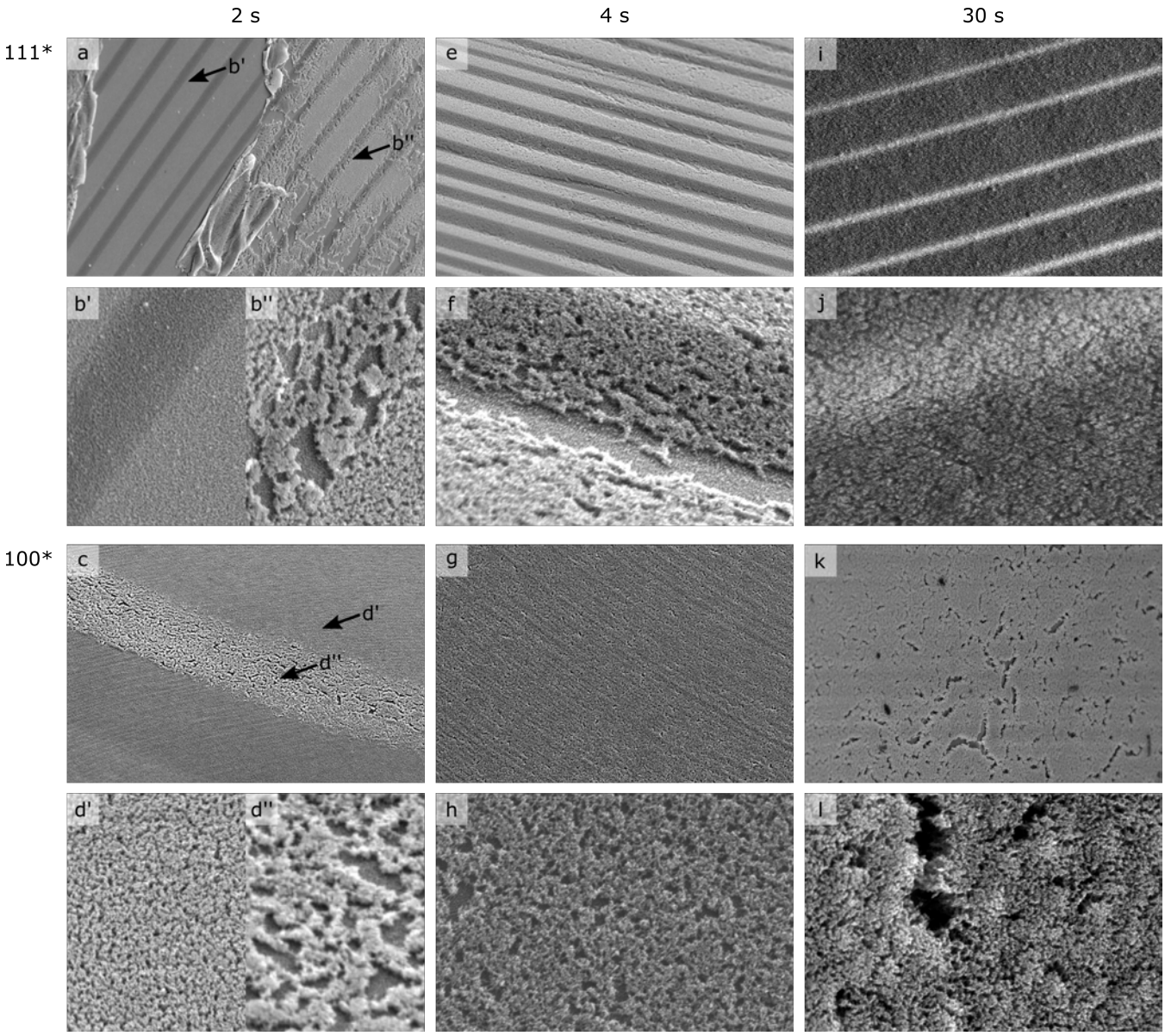

Figure 9: SEM images of the Au(111*) (first two rows) and the Au(100*) facet (third and fourth row) after 540 V for 2 s (a–d), 4 s (e–h) and 30 s (i–l) followed by electrochemical reduction. The images in the first and third rows have a size of 30 μm × 20 μm, and those in the second and fourth rows have a size of 3 μm × 2 μm. The contrast and brightness were adjusted in images c, g, and i.

nounced due to possible stronger lateral interactions within the formed NPG film. Further experimental and theoretical investigations on single crystals with preferential orientation are required to substantiate these assumptions.

300 V 2-30 s: Next, we focus on NPG films formed by the electrochemical reduction of Au oxide films, which were formed by HV electrolysis at 300 V at different times. Optical microscope images of the resulting POSCs are shown in the first row in Fig. 10. After 2 s the POSC still appears golden, and the distinctive black color for a NPG film is not observed. Electrochemical measurements (Fig. 2 red curve), however, clearly indicate that a Au oxide film covered the surface. Hence, the film is presumably too thin to change the optical properties of the POSC surface (at least from visual inspection). Electrodes prepared by electrolysis times longer than 5 s clearly show a distinct black color. These electrodes also show already by visual inspection clearly significant exfoliation of the NPG film from the surface. For comparison, the stability of NPG films at 300 V is

also shown in Table 2. Note that grain boundaries also do not influence the NPG formation, which is shown in Fig. S7d (2 s HV electrolysis at 300 V), as in the case of the Au oxide and also for the NPG film formed at 540 V. SEM images of the POSCs are also shown in Fig. 10. Homogeneous NPG films are observed for electrodes prepared by HV electrolysis at 300 V up to 15 s. After 30 s, the NPG film randomly exfoliates from different surface regions. A closer inspection of, for example, the Au(111*) region shows rather compact NPG structures up to electrolysis times of 15 s (Figs. 10c, f and i), while the NPG film after 30 s HV electrolysis is rather inhomogeneous (Fig. 10l). This aligns with the fact that the Au oxide film formed at 300 V and 30 s electrolysis time is not smooth (see Figs. 5a and b and Figs. S6d and h), but shows cracks and regions with exfoliated Au oxide.

Table 2: Intact NPG films (-) or NPG films with exfoliated areas (✓) after HV electrolysis at 300 V for 2 to 30 s followed by electrochemical reduction. In the case of a bracket, the behavior of the NPG film in terms of stability is not entirely clear, which is why the tendency is given in brackets.

	2 s	5 s	15 s	30 s
111	-	(✓)	-	✓
111*	-	(✓)	✓	✓
100	-	(✓)	(-)	✓
100*	-	(✓)	(-)	✓

From a closer inspection of the regions where the NPG film exfoliated in Fig. 11, we observe that the bare Au surface is no longer smooth. Compared to the NPG film formed from Au oxide prepared at 540 V and 30 s where the NPG structure was randomly torn apart, we find here instead randomly distributed holes within the underlying Au substrate. More specifically, from the SEM images with higher magnification in Fig. 11, it is apparent that the holes on the Au(111*) facet have a triangular shape, while those on the Au(100*) facet have a square/rectangular shape.[42] The shape of the holes is hereby directly related to the crystallographic orientation of the substrate, substantiating our assignment of the different regions to specific crystallographic orientations.

Overall, more homogeneous NPG films are formed from Au oxides prepared by HV electrolysis at 300 V compared to 540 V. Exfoliation of the Au oxide only occurs after 30 s electrolysis time at 300 V, where the Au oxide is thicker than that formed at 540 V, but is also less homogeneous. This suggests that thick Au oxide films might not adhere as well to the substrate as thin Au oxide films. Whether the Au oxide film exfoliates during the HV electrolysis or the emersion of the electrode from the electrolysis solution can not be deduced from our experiment. Why the structural properties of the Au substrate in the regions where the NPG film exfoliated are different for the preparation procedures at both voltages is currently unclear. Finally, the question remains, why NPG films formed from Au oxide films prepared by HV electrolysis at 300 V between times of 2 s to 15 s are more stable than those formed from Au oxides prepared by HV electrolysis at 540 V at the same times? Specifically, since for such short electrolysis times as at 2 s, no plasma was yet ignited around the POSC, but instead, normal electrolysis takes place according to the j–t curves in Fig. S2. Thus, the Au oxide film formed under these different conditions must have some distinctly different structural properties, such as adhesion to the substrate in general or lateral interactions within the NPG film.

Conclusion

In this work, we systematically investigated the formation of Au oxide on Au POSCs by HV electrolysis and the subsequent formation of a NPG film formed by electrochemical reduction of the Au oxide. The HV electrolysis was performed in the normal electrolysis region (at 300 V) and in the aCGDE region (at 540 V) for different times (100 ms to 30 s.) From electrochemical measurements, we infer that for both conditions the thickness of the Au oxide film increases with increasing electrolysis time, with a stronger increase for electrodes prepared at 300 V. Overall, the Au oxide films are mostly

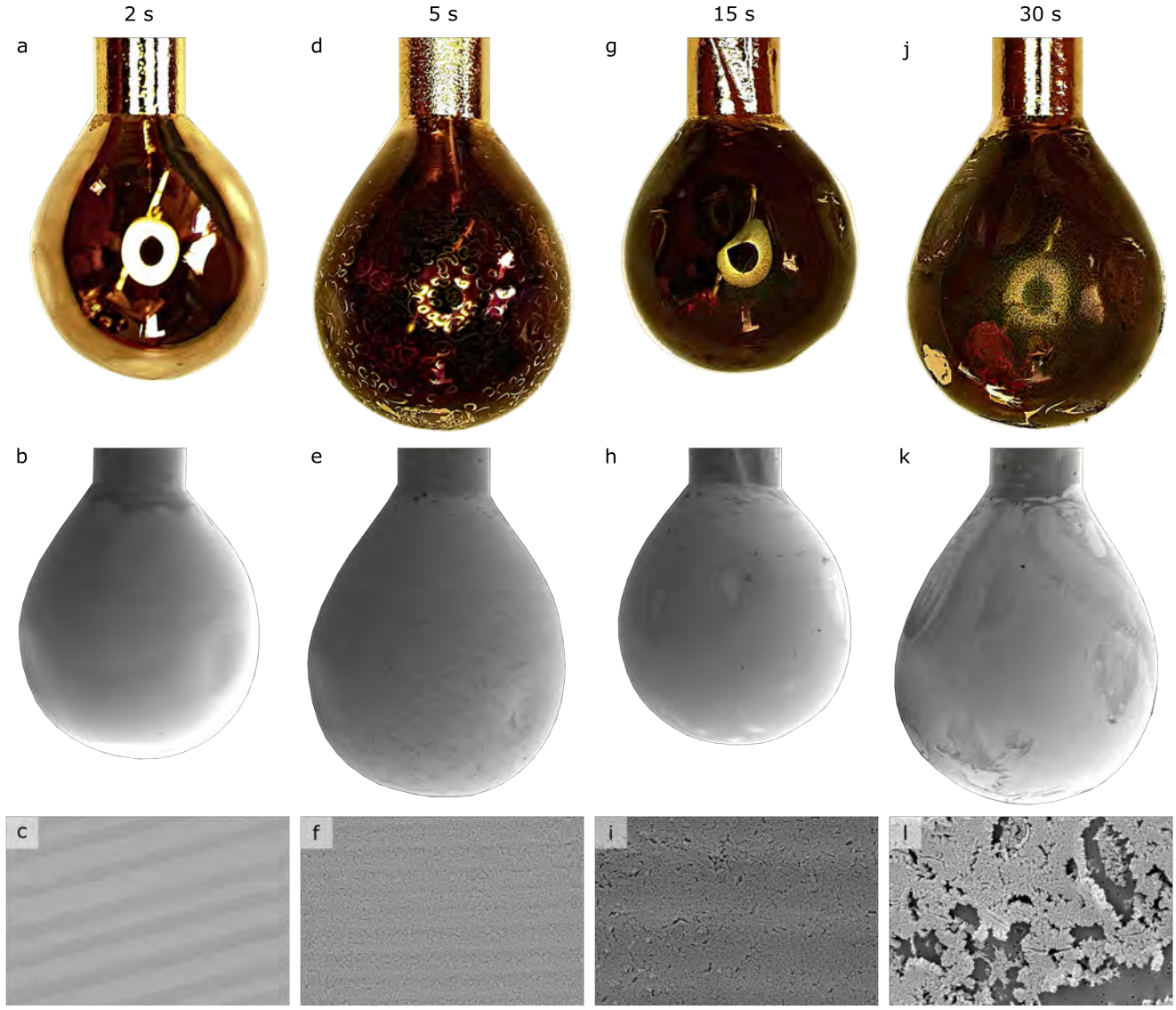

Figure 10: Optical microscope (first row) and SEM images (second row) of Au POSCs and the NPG film formed on Au(111*) (bottom row) after HV electrolysis at 300 V followed by electrochemical reduction. The electrolysis time was 2 s in images a to c, 5 s in images d to f, 15 s in images g to i, and 30 s in images j to l. The size of the POSCs can be estimated based on the diameter of the Au wire on which they are grown, which is 1 mm. The images in the bottom row have a size of 15 μm $\times$ 10 μm.

homogeneous on the POSCs for all conditions, except for HV electrolysis at 300 V for 30 s. In that case, the Au oxide shows different structures depending on the crystallographic orientation of the substrate and adhesion seems to be weakest on the low-index facets, *i.e.*, Au(111) and Au(100). Grain boundaries were found to play no role in the quality of the Au oxide or NPG films. In regions where the Au oxide film is inhomogeneous or exfoliated, also inhomogeneous or exfoliated NPG films are obtained. The NPG film formed from Au oxides prepared by HV electrolysis at 300 V is mostly homogenous on all facets up to 15 s electrolysis time. In turn, NPG films obtained from thin Au oxides prepared by HV electrolysis at 540 V tend to exfoliate even though the Au oxide film is homogeneous. This process seems to be facet-dependent and films are less stable on Au(111) or Au(111*) facets than on Au(100) or Au(100*) regions. The stability increases with increasing Au oxide thickness (longer electrolysis times). From our experiments, we cannot deduce whether the NPG film exfoliates during

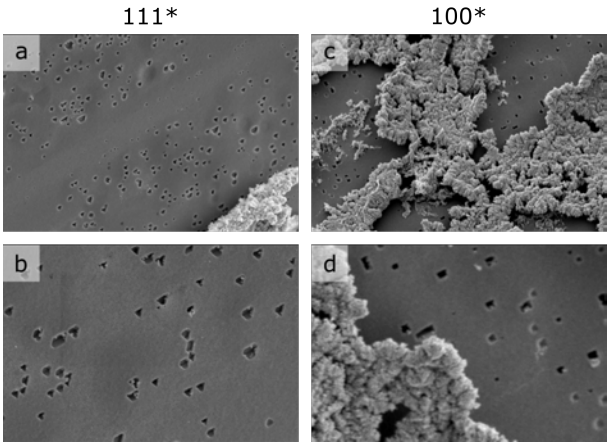

Figure 11: SEM images of the Au(111*) and the Au(100*) facet on a Au POSC after 30 s HV electrolysis at 300 V followed by electrochemical reduction of regions where the NPG film exfoliated. The size of the images in a) and c) is 15 μm $\times$ 10 μm and in b) and d) 6 μm $\times$ 4 μm.

the electrochemical reduction of the Au oxide or during the emersion of the electrode from the electrolyte. Gaining more fundamental insights into the exfoliation process could be beneficial to either find ways to systematically exfoliate NPG from a bare Au substrate or to form stable NPG films on a bare Au substrate.

Experimental

Materials:

The Au POSCs were prepared from a Au wire with a diameter of 1.0 mm (purity: 5N, MaTecK). The 0.01 M KOH electrolyte was prepared from KOH pellets (Sigma-Aldrich, 99.99 %) and Milli-Q water (18.2 MΩ cm, TOC $\leq$ 3 ppb). Aqua regia was used for cleaning and etching the POSCs, which was prepared from fuming HCl (37 %, Merck, for analysis) and HNO_3 (65 %, Merck, for analysis) with a ratio of 3:1.

POSC Preparation:

The Au POSCs were prepared by the controlled-atmosphere flame fusion (CAFF) approach.[48,49] A detailed description of the procedure, as well as the individual components of the single crystal growth setup, can be found in Refs. 49 and 48. The most important components and experimental steps for preparation are summarized in the following.

The Au POSCs were prepared from a Au wire, which was first melted in a H_2, O_2, Ar flame (0.7 H_2 (purity: 5.0, Westfalen AG), 0.1 O_2 (purity: 3.5 MTI IndustrieGase AG), 1.0 Ar (flame) (4.6, MTI IndustrieGase AG)) so that a Au bead was formed at the lower end of the Au wire. Once the bead had the desired size, the molten Au bead was slowly cooled at a defined rate, by pulling the bead out of the flame, resulting in the formation of a POSC.

Impurities from the wire, which accumulated at the top of the bead during cooling, were removed by etching in aqua regia for about 30 min after the bead had cooled completely. Subsequently, the bead was re-melted and cooled following the same procedure as starting from a Au wire. When the bead restructured during the experiments described in this manuscript, a fresh bead was prepared according to the same procedure described above.

Before each measurement, the prepared Au POSC was annealed in a propane flame (MTI) for 3 min to remove impurities.

Electrolysis:

The electrolysis experiments were performed in a glass cell with a diameter of 6 cm, which was filled with 60 mL 0.01 M KOH electrolyte. The measurements were performed at room temperature. Electrolysis was performed by applying a voltage of 540 V or 300 V, between the Au POSC and a stainless steel plate counter electrode (15 mm $\times$ 20 mm $\times$ 3.5 mm). The distance between the working and the counter electrode was 2.5 cm. The Au wire on which the POSC was grown was capped with an Eppendorf pipette tip to have a defined surface area during the experiment. All measurements were performed without stirring the electrolyte. After each measurement, the electrolyte was exchanged, since the measurement can result in changes of the electrolyte temperature or electrolyte composition. The voltage was applied with either a TDK-Lambda Power Supply (630 V / 1.365 A) or a PlasmaTec Power Supply (Plasmatec Bias 1k015k NDCR1727F01002). In the former case the data was acquired with a LabView program. In the latter case the

data was acquired using a Tektronix oscilloscope (Serial No. TBS1102B C013624, Voltage Range: 100-240 V (115 V); Frequency: 50-60 Hz (400 Hz), Power Max: 30 Watts). Both the Power Supply and a current probe (PICO TECHNOLOGY, TA189) were connected to the oscilloscope to read the applied voltages and the resulting currents. The data recorded with the current probe and the oscilloscope were subsequently smoothed.

Electrochemical Cell:

The Au oxide films prepared by HV electrolysis on the Au POSC were reduced electrochemically in a separate glass cell (diameter: 6 cm) to avoid the autocatalytic reduction of the Au oxide by H_2O_2 formed during electrolysis.[53] The electrochemical cell was filled with 150 mL 0.01 M electrolyte. The Au POSC was used as electrochemical working electrode, a Pt-sheet (10 × 7.5 mm) was used as electrochemical counter electrode, and a homemade reversible hydrogen electrode (RHE) served as the reference electrode. A FHI ELAB potentiostat was used to control the potential during the electrochemical reduction experiments. To reduce the Au oxide, the potential was lowered from an initial potential of 1.1 V_{RHE} to approximately 0.25 V_{RHE} with a scan rate of 50 mV s^{-1}. The potential was held until the current was almost zero. Subsequently the Au POSC was removed and the structural properties were characterized by optical microscopy and SEM.

For most measurements, the electrolyte was not deaerated, since the reductive current resulting from the reduction of Au oxide is much higher compared to the current resulting from the reduction of residual oxygen dissolved in the electrolyte. The electrolyte was not stirred.

Structural Characterization:

The structural properties of the POSCs were characterized using a Quattro S or Scios2 SEM from Thermo Scientific operated at accelerating voltages between 5 kV and 20 kV, and a Leica S9i optical microscope from Thermo Scientific. Laue images were acquired using a Laue X-ray back-scattering camera from Multiwire Laboratories Ltd.

Surface Area:

The geometric surface area of the Au POSCs were determined after the growth from SEM images of the entire POSC. Since the diameter of the wire is known, one can determine the diameter of the bead on a horizontal and vertical axis. Usually, the vertical diameter is larger than the horizontal diameter. Assuming that the POSC is a sphere, the surface area was calculated from the average diameter from the horizontal and vertical axis. Finally, the area of the Au wire in contact with the POSC was subtracted from the surface area of the bead (0.785 mm^2). The resulting surface areas for the POSCs ranged from 0.178 cm^2 to 0.322 cm^2. All current densities given refer to the geometric surfaces of the POSCs.

Acknowledgement

Acknowledgement This work was supported by the SFB-CRC1316 of the DFG. Further, support by the state of Baden-Württemberg and the DFG through grant no. INST 40/574-1 FUGG is gratefully acknowledged. E.A. would like to thank the "Stiftung Stipendien-Fonds des Verbandes der Chemischen Industrie (VCI)" for the support in the form of a scholarship.

CRediT

E. Artmann: Conceptualization, Formal Analysis, Funding Acquisition, Investigation, Validation, Visualization, Writing - Original Draft Preparation. **T. Schmider**: Investigation **T. Jacob**: Funding Acquisition, Resources, Supervision, Writing - Review & Editing. **A. K. Engstfeld**: Funding Acquisition, Conceptualization, Supervision, Writing - Review & Editing

TOC Figure and Text

The adhesion of Au oxide and NPG films on a Au substrate was investigated at high voltages with respect to the crystallographic orientation. While the Au oxide films formed are ho-

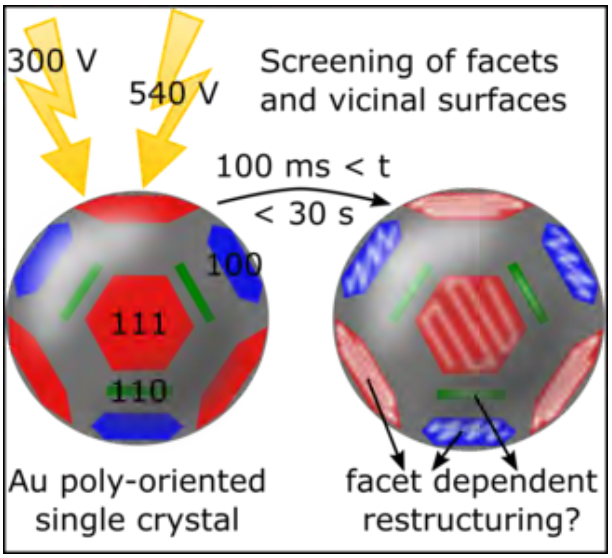

mogeneous in most cases, the NPG films show a strong dependence on the crystallographic orientation. Both very thin and thick NPG films tend to exfoliate.

References

(1) Bhattarai, J. K.; Neupane, D.; Nepal, B.; Mikhaylov, V.; Demchenko, A. V.; Stine, K. J. Preparation, Modification, Characterization, and Biosensing Application of Nanoporous Gold Using Electrochemical Techniques. *Nanomaterials* **2018**, *8*.

(2) McCue, I.; Stuckner, J.; Murayama, M.; Demkowicz, M. J. Gaining new insights into nanoporous gold by mining and analysis of published images. *Sci. Rep.* **2018**, *8*, 6761.

(3) Yan, K.; Karthick Kannan, P.; Doonyapisut, D.; Wu, K.; Chung, C.-H.; Zhang, J. Advanced Functional Electroactive and Photoactive Materials for Monitoring the Environmental Pollutants. *Adv. Funct. Mater.* **2021**, *31*, 2008227.

(4) Jalas, D.; Shao, L.-H.; Canchi, R.; Okuma, T.; Lang, S.; Petrov, A.; Weissmüller, J.; Eich, M. Electrochemical tuning of the optical properties of nanoporous gold. *Sci. Rep.* **2017**, *7*, 44139.

(5) Juarez, T.; Biener, J.; Weissmüller, J.; Hodge, A. M. Nanoporous Metals with Structural Hierarchy: A Review. *Adv. Eng. Mater.* **2017**, *19*, 1700389.

(6) Kim, S. H. Nanoporous gold: Preparation and applications to catalysis and sensors. *Curr. Appl. Phys.* **2018**, *18*, 810–818.

(7) Xiao, S.; Wang, S.; Wang, X.; Xu, P. Nanoporous gold: A review and potentials in biotechnological and biomedical applications. *Nano Select* **2021**, *2*, 1437–1458.

(8) Wang, Z.; Ning, S.; Liu, P.; Ding, Y.; Hirata, A.; Fujita, T.; Chen, M. Tuning Surface Structure of 3D Nanoporous Gold by Surfactant-Free Electrochemical Potential Cycling. *Adv. Mater.* **2017**, *29*.

(9) Liu, P.; Guan, P.; Hirata, A.; Zhang, L.; Chen, L.; Wen, Y.; Ding, Y.; Fujita, T.; Erlebacher, J.; Chen, M. Visualizing Under-Coordinated Surface Atoms on 3D Nanoporous Gold Catalysts. *Adv. Mater.* **2016**, *28*, 1753–1759.

(10) Fujita, T.; Guan, P.; McKenna, K.; Lang, X.; Hirata, A.; Zhang, L.; Tokunaga, T.; Arai, S.; Yamamoto, Y.; Tanaka, N.; Ishikawa, Y.; Asao, N.; Yamamoto, Y.; Erlebacher, J.; Chen, M. Atomic origins of the high catalytic activity of nanoporous gold. *Nature Mater.* **2012**, *11*, 775–780.

(11) Li, D.; Zhu, Y.; Wang, H.; Ding, Y. Nanoporous gold as an active low temperature catalyst toward CO oxidation in hydrogen-rich stream. *Sci. Rep.* **2013**, *3*, 3015.

(12) Zhang, J.; Li, C. M. Nanoporous metals: fabrication strategies and advanced electrochemical applications in catalysis, sensing and energy systems. *Chem. Soc. Rev.* **2012**, *41*, 7016–7031.

(13) Goyal, A.; Bondue, C. J.; Graf, M.; Koper, M. T. M. Effect of pore diameter

and length on electrochemical CO 2 reduction reaction at nanoporous gold catalysts. *Chem. Sci.* **2022**, *13*, 3288–3298.

(14) Biener, J.; Biener, M. M.; Madix, R. J.; Friend, C. M. Nanoporous Gold: Understanding the Origin of the Reactivity of a 21st Century Catalyst Made by Pre-Columbian Technology. *ACS Catal.* **2015**, *5*, 6263–6270.

(15) Wittstock, A.; Wichmann, A.; Biener, J.; Bäumer, M. Nanoporous gold: a new gold catalyst with tunable properties. *Faraday Discuss.* **2011**, *152*, 87–98; discussion 99–120.

(16) Zhang, X.; Ding, Y. Unsupported nanoporous gold for heterogeneous catalysis. *Catal. Sci. Technol.* **2013**, *3*, 2862.

(17) Seker, E.; Gaskins, J. T.; Bart-Smith, H.; Zhu, J.; Reed, M. L.; Zangari, G.; Kelly, R.; Begley, M. R. The effects of post-fabrication annealing on the mechanical properties of freestanding nanoporous gold structures. *Acta Mater.* **2007**, *55*, 4593–4602.

(18) Seker, E.; Reed, M.; Begley, M. Nanoporous Gold: Fabrication, Characterization, and Applications. *Mater.* **2009**, *2*, 2188–2215.

(19) Gao, Y.; Ding, Y. Nanoporous Metals for Heterogeneous Catalysis: Following the Success of Raney Nickel. *Chemistry* **2020**, *26*, 8845–8856.

(20) Tapia Burgos, J. A.; Mahr, C.; Olaya, A. R. S.; Robben, L.; Schowalter, M.; Rosenauer, A.; Wittstock, G.; Wittstock, A.; Bäumer, M. The Impact of the Manufacturing and Corrosion Steps of the AuCu Master Alloy on the Catalytic Activity of Nanoporous Gold for CO Oxidation. *SSRN Electronic Journal* **2021**,

(21) Sukeri, A.; Saravia, L. P. H.; Bertotti, M. A facile electrochemical approach to fabricate a nanoporous gold film electrode and its electrocatalytic activity towards dissolved oxygen reduction. *Phys. Chem. Chem. Phys.* **2015**, *17*, 28510–28514.

(22) Sukeri, A.; Bertotti, M. Nanoporous Gold Surface: An Efficient Platform for Hydrogen Evolution Reaction at Very Low Overpotential. *J. Braz. Chem. Soc.* **2017**,

(23) Kellogg, H. H. Anode Effect in Aqueous Electrolysis. *J. Electrochem. Soc.* **1950**, *97*, 133.

(24) Hickling, A and Ingram, MD, Contact glow-discharge electrolysis. *Transactions of the Faraday Society* **1964**, 783–793.

(25) Yerokhin, A.; Mukaeva, V. R.; Parfenov, E. V.; Laugel, N.; Matthews, A. Charge transfer mechanisms underlying Contact Glow Discharge Electrolysis. *Electrochim. Acta* **2019**, *312*, 441–456.

(26) Artmann, E.; Menezes, P. V.; Forschner, L.; Elnagar, M. M.; Kibler, L. A.; Jacob, T.; Engstfeld, A. K. Structural Evolution of Pt, Au and Cu Anodes by Electrolysis up to Contact Glow Discharge Electrolysis in Alkaline Electrolytes*. *Chem. Phys. Chem.* **2021**,

(27) Artmann, E.; Forschner, L.; Schüttler, K. M.; Al-Shakran, M.; Jacob, T.; Engstfeld, A. K. Nanoporous Au Formation on Au Substrates via High Voltage Electrolysis. *Chem. Phys. Chem.* **2022**, e202200645.

(28) Forschner, L.; Artmann, E.; Jacob, T.; Engstfeld, A. K. Electric Potential Distribution Inside the Electrolyte during High Voltage Electrolysis. *J. Phys. Chem. C* **2023**, *127*, 4387–4394.

(29) Henkelmann, G.; Waldow, D.; Liu, M.; Lührs, L.; Li, Y.; Weissmüller, J. Self-Detachment and Subsurface Densification of Dealloyed Nanoporous Thin Films. *Nano Lett.* **2022**, *22*, 6787–6793.

(30) Khristosov, M. K.; Bloch, L.; Burghammer, M.; Kauffmann, Y.; Katsman, A.;

Pokroy, B. Sponge-like nanoporous single crystals of gold. *Nat. Commun.* **2015**, *6*, 8841.

(31) Conway, B. E.; Jerkiewicz, G. Surface orientation dependence of oxide film growth at platinum single crystals. *J. Electroanal. Chem.* **1992**, *339*, 123–146.

(32) Dickertmann, D.; Schultze, J. W.; Vetter, K. J. Electrochemical formation and reduction of monomolecular oxide layers on (111) and (100) planes of gold single crystals. *J. Electroanal. Chem. Interfacial Electrochem.* **1974**, *55*, 429–443.

(33) Evertsson, J. et al. The thickness of native oxides on aluminum alloys and single crystals. *Appl. Surf. Sci.* **2015**, *349*, 826–832.

(34) Reichel, F.; Jeurgens, L.; Mittemeijer, E. J. The effect of substrate orientation on the kinetics of ultra-thin oxide-film growth on Al single crystals. *Acta Mater.* **2008**, *56*, 2897–2907.

(35) Graham, M. J.; Hussey, R. J.; Cohen, M. Influence of Oxide Structure on the Oxidation Rate of Nickel Single Crystals. *J. Electrochem. Soc.* **1973**, *120*, 1523.

(36) Jeon, B.; van Overmeere, Q.; van Duin, A. C. T.; Ramanathan, S. Nanoscale oxidation and complex oxide growth on single crystal iron surfaces and external electric field effects. *Phys. Chem. Chem. Phys.* **2013**, *15*, 1821–1830.

(37) Vvedenskii, A.; Grushevskaya, S.; Ganzha, S.; Eliseev, D.; Abakumova, L. I. Copper oxides: kinetics of formation and semiconducting properties. Part II. Copper single crystals. *J. Solid State Electrochem.* **2014**, *18*, 3437–3451.

(38) Scholten, F.; Nguyen, K.-L. C.; Bruce, J. P.; Heyde, M.; Roldan Cuenya, B. Identifying Structure-Selectivity Correlations in the Electrochemical Reduction of CO2 : A Comparison of Well-Ordered Atomically Clean and Chemically Etched Copper Single-Crystal Surfaces. *Angew. Chem. Int. Ed.* **2021**, *60*, 19169–19175.

(39) Gao, D.; Zegkinoglou, I.; Divins, N. J.; Scholten, F.; Sinev, I.; Grosse, P.; Roldan Cuenya, B. Plasma-Activated Copper Nanocube Catalysts for Efficient Carbon Dioxide Electroreduction to Hydrocarbons and Alcohols. *ACS Nano* **2017**, *11*, 4825–4831.

(40) Raaijman, S. J.; Arulmozhi, N.; Koper, M. T. M. Anisotropic Cathodic Corrosion of Gold Electrodes in the Absence and Presence of Carbon Monoxide. *J. Phys. Chem. C* **2020**, *124*, 28539–28554.

(41) Arulmozhi, N.; Esau, D.; Lamsal, R. P.; Beauchemin, D.; Jerkiewicz, G. Structural Transformation of Monocrystalline Platinum Electrodes upon Electro-oxidation and Electro-dissolution. *ACS Catal.* **2018**, *8*, 6426–6439.

(42) Arulmozhi, N.; Hersbach, T. J. P.; Koper, M. T. M. Nanoscale morphological evolution of monocrystalline Pt surfaces during cathodic corrosion. *Proc. Nat. Acad. Sci. U.S.A.* **2020**, *117*, 32267–32277.

(43) Clavilier, J.; Armand, D.; Sun, S. G.; Petit, M. Electrochemical adsorption behaviour of platinum stepped surfaces in sulphuric acid solutions. *J. Electroanal. Chem. Interfacial Electrochem.* **1986**, *205*, 267–277.

(44) Clavilier, J.; El Achi, K.; Rodes, A. In situ probing of step and terrace sites on Pt(S)-[n(111) × (111)] electrodes. *Chem. Phys.* **1990**, *141*, 1–14.

(45) Arulmozhi, N.; Jerkiewicz, G. Design and Development of Instrumentations for the Preparation of Platinum Single Crystals for Electrochemistry and Electrocatalysis Research. Part 1: Semi-Automated Crystal Growth. *Electrocatalysis* **2016**, *7*, 507–518.

(46) Arulmozhi, N.; Jerkiewicz, G. Design and Development of Instrumentations for the Preparation of Platinum Single Crystals for Electrochemistry and Electrocatalysis Research. Part 2: Orientation, Cutting, and Annealing. *Electrocatalysis* **2017**, *8*, 399–413.

(47) Arulmozhi, N.; Esau, D.; van Drunen, J.; Jerkiewicz, G. Design and Development of Instrumentations for the Preparation of Platinum Single Crystals for Electrochemistry and Electrocatalysis Research Part 3: Final Treatment, Electrochemical Measurements, and Recommended Laboratory Practices. *Electrocatalysis* **2018**, *9*, 113–123.

(48) Esau, D.; Schuett, F. M.; Varvaris, K. L.; Björk, J.; Jacob, T.; Jerkiewicz, G. Controlled-Atmosphere Flame Fusion Growth of Nickel Poly-oriented Spherical Single Crystals—Unraveling Decades of Impossibility. *Electrocatalysis* **2020**, *11*, 1–13.

(49) Schuett, F. M.; Esau, D.; Varvaris, K. L.; Gelman, S.; Björk, J.; Rosen, J.; Jerkiewicz, G.; Jacob, T. Controlled-Atmosphere Flame Fusion Single-Crystal Growth of Non-Noble fcc, hcp, and bcc Metals Using Copper, Cobalt, and Iron. *Angew. Chem. Int. Ed.* **2020**, *59*, 13246–13252.

(50) Vitrey, A.; Alvarez, R.; Palmero, A.; González, M. U.; García-Martín, J. M. Fabrication of black-gold coatings by glancing angle deposition with sputtering. *Beilstein J. Nanotechnol.* **2017**, *8*, 434–439.

(51) Zhang, R.; Olin, H. Porous Gold Films-A Short Review on Recent Progress. *Materials* **2014**, *7*, 3834–3854.

(52) Zheng, H.; Picard, C.; Ravaine, S. Nanostructured gold films exhibiting almost complete absorption of light at visible wavelengths. *Front. Chem. Sci. Eng.* **2018**, *12*, 247–251.

(53) Chen, H.; Wei, G.; Ispas, A.; Hickey, S. G.; Eychmüller, A. Synthesis of Palladium Nanoparticles and Their Applications for Surface-Enhanced Raman Scattering and Electrocatalysis. *J. Phys. Chem. C* **2010**, *114*, 21976–21981.

References

1. Shih, A. J. *et al.* Water electrolysis. *Nature Rev. Methods Primers* **2,** 84 (2022).
2. Zeng, K. & Zhang, D. Recent progress in alkaline water electrolysis for hydrogen production and applications. *Prog. Energy Combust. Sci.* **36,** 307–326 (2010).
3. Kibler, L. A. Hydrogen electrocatalysis. *Chem. Phys. Chem.* **7,** 985–991 (2006).
4. Elgrishi, N. *et al.* A Practical Beginner's Guide to Cyclic Voltammetry. *J. Chem. Educ.* **95,** 197–206 (2018).
5. Climent, V. & Feliu, J. in *Encyclopedia of Interfacial Chemistry* (ed Wandelt, K.) 48–74 (Elsevier, Oxford, 2018).
6. David, M., Ocampo-Martínez, C. & Sánchez-Peña, R. Advances in alkaline water electrolyzers: A review. *J. Energy Storage* **23,** 392–403 (2019).
7. Mohammadi, A. & Mehrpooya, M. A comprehensive review on coupling different types of electrolyzer to renewable energy sources. *Energy* **158,** 632–655 (2018).
8. van Pham, C., Escalera–López, D., Mayrhofer, K., Cherevko, S. & Thiele, S. Essentials of High Performance Water Electrolyzers – From Catalyst Layer Materials to Electrode Engineering. *Adv. Energy Mater.* **11,** 2101998 (2021).
9. Kirubakaran, A., Jain, S. & Nema, R. K. A review on fuel cell technologies and power electronic interface. *Renew. Sust. Energ. Rev.* **13,** 2430–2440 (2009).
10. Fan, L., Tu, Z. & Chan, S. H. Recent development of hydrogen and fuel cell technologies: A review. *Energy Rep.* **7,** 8421–8446 (2021).

11. Cigolotti, V., Genovese, M. & Fragiacomo, P. Comprehensive Review on Fuel Cell Technology for Stationary Applications as Sustainable and Efficient Poly-Generation Energy Systems. *Energies* **14,** 4963 (2021).
12. Bogaerts, A., Neyts, E., Gijbels, R. & van der Mullen, J. Gas discharge plasmas and their applications. *Spectrochim. Acta Part B: At. Spectrosc.* **57,** 609–658 (2002).
13. Chatterjee, R. Fundamental Concepts and Discussion of Plasma Physics. *TECHNO REVIEW J. Technol. Manag.* **2,** 01–14 (2022).
14. Horikoshi, S. & Serpone, N. In-liquid plasma: a novel tool in the fabrication of nanomaterials and in the treatment of wastewaters. *RSC Adv.* **7,** 47196–47218 (2017).
15. Oesterheld, G. and Brunner, E. über Anoden–und Wehnelt–Eekt. *Z. Elektrochem. angew. phys. Chem.,* 38–48 (1916).
16. Wüthrich, R. & Mandin, P. Electrochemical discharges—Discovery and early applications. *Electrochim. Acta* **54,** 4031–4035 (2009).
17. Kellogg, H. H. Anode Effect in Aqueous Electrolysis. *J. Electrochem. Soc.* **97,** 133 (1950).
18. Hickling, A and Ingram, MD. Contact glow-discharge electrolysis. *Trans. Faraday Soc.,* 783–793 (1964).
19. Saito, G. & Akiyama, T. Nanomaterial Synthesis Using Plasma Generation in Liquid. *J. Nanomater.* **2015,** 1–21 (2015).
20. Kareem, T. A. & Kaliani, A. A. Glow discharge plasma electrolysis for nanoparticles synthesis. *Ionics* **18,** 315–327 (2012).
21. Kaseem, M., Fatimah, S., Nashrah, N. & Ko, Y. G. Recent progress in surface modification of metals coated by plasma electrolytic oxidation: Principle, structure, and performance. *Prog. Mater. Sci.* **117,** 100735 (2021).
22. Menezes, P. V. *et al.* In–Liquid Plasma for Surface Engineering of Cu Electrodes with Incorporated SiO 2 Nanoparticles: From Micro to Nano. *Adv. Funct. Mater.,* 2107058 (2021).
23. Schneider, M. & Fürbeth, W. Anodizing—The pore makes the difference. *Mater. Corros.,* 1752–1765 (2022).

24. Paz Martínez-Viademonte, M., Abrahami, S. T., Hack, T., Burchardt, M. & Terryn, H. A Review on Anodizing of Aerospace Aluminum Alloys for Corrosion Protection. *Coatings* **10,** 1106 (2020).

25. Clyne, T. W. & Troughton, S. C. A review of recent work on discharge characteristics during plasma electrolytic oxidation of various metals. *Int. Mater. Rev.* **64,** 127–162 (2019).

26. Lu, X. *et al.* Plasma electrolytic oxidation coatings with particle additions – A review. *Surf. Coat. Technol.* **307,** 1165–1182 (2016).

27. Barati Darband, G., Aliofkhazraei, M., Hamghalam, P. & Valizade, N. Plasma electrolytic oxidation of magnesium and its alloys: Mechanism, properties and applications. *J. Magnes. Alloy.* **5,** 74–132 (2017).

28. Climent, V. & Feliu, J. M. Thirty years of platinum single crystal electrochemistry. *J. Solid State Electrochem.* **15,** 1297–1315 (2011).

29. Burke, L. D. Scope for new applications for gold arising from the electrocatalytic behaviour of its metastable surface states. *Gold Bull.* **37,** 125–135 (2004).

30. Nitopi, S. *et al.* Progress and Perspectives of Electrochemical CO2 Reduction on Copper in Aqueous Electrolyte. *Chem. Rev.* **119,** 7610–7672 (2019).

31. Carreon, M. L. Plasma catalysis: a brief tutorial. *Plasma Research Express* **1,** 043001 (2019).

32. Bogaerts, A. *et al.* The 2020 plasma catalysis roadmap. *J. Phys. D* **53,** 443001 (2020).

33. Whitehead, J. C. Plasma–catalysis: the known knowns, the known unknowns and the unknown unknowns. *J. Phys. D* **49,** 243001 (2016).

34. Malik, M. A., Ghaffar, A. & Malik, S. A. Water purification by electrical discharges. *Plasma Sources Sci. Technol.* **10,** 82–91 (2001).

35. Sen Gupta, S. K. Contact Glow Discharge Electrolysis: A Novel Tool for Manifold Applications. *Plasma Chem. Plasma Process.* **37,** 897–945 (2017).

36. Wang, X., Zhou, M. & Jin, X. Application of glow discharge plasma for wastewater treatment. *Electrochim. Acta* **83,** 501–512 (2012).

37. Gao, J. *et al.* Plasma degradation of dyes in water with contact glow discharge electrolysis. *Water Res.* **37,** 267–272 (2003).

38. Pettersson, J., Ramsey, B. & Harrison, D. A review of the latest developments in electrodes for unitised regenerative polymer electrolyte fuel cells. *J. Power Sources* **157,** 28–34 (2006).

39. Antolini, E. Review in Applied Electrochemistry. Number 54 Recent Developments in Polymer Electrolyte Fuel Cell Electrodes. *J. Appl. Electrochem.* **34,** 563–576 (2004).

40. Nørskov, J. K. *et al.* Trends in the Exchange Current for Hydrogen Evolution. *J. Electrochem. Soc.* **152,** J23 (2005).

41. Trasatti, S. Work function, electronegativity, and electrochemical behaviour of metals. *J. Electroanal. Chem. Interf. Electrochem.* **39,** 163–184 (1972).

42. Hammer, B. & Norskov, J. K. Why gold is the noblest of all the metals. *Nature* **376,** 238–240 (1995).

43. Tremiliosi-Filho, G., Dall'Antonia, L. H. & Jerkiewicz, G. Limit to extent of formation of the quasi-two-dimensional oxide state on Au electrodes. *J. Electroanal. Chem.* **422,** 149–159 (1997).

44. Biener, J., Biener, M. M., Madix, R. J. & Friend, C. M. Nanoporous Gold: Understanding the Origin of the Reactivity of a 21st Century Catalyst Made by Pre-Columbian Technology. *ACS Catal.* **5,** 6263–6270 (2015).

45. Juarez, T., Biener, J., Weissmüller, J. & Hodge, A. M. Nanoporous Metals with Structural Hierarchy: A Review. *Adv. Eng. Mater.* **19,** 1700389 (2017).

46. Zhang, J. & Li, C. M. Nanoporous metals: fabrication strategies and advanced electrochemical applications in catalysis, sensing and energy systems. *Chem. Soc. Rev.* **41,** 7016–7031 (2012).

47. McCue, I., Stuckner, J., Murayama, M. & Demkowicz, M. J. Gaining new insights into nanoporous gold by mining and analysis of published images. *Sci. Rep.* **8,** 6761 (2018).

48. Wang, D. & Schaaf, P. Nanoporous gold nanoparticles. *J. Mater. Chem.* **22,** 5344 (2012).

49. Bhattarai, J. K. *et al.* Preparation, Modification, Characterization, and Biosensing Application of Nanoporous Gold Using Electrochemical Techniques. *Nanomater.* **8** (2018).

50. Kim, S. H. Nanoporous gold: Preparation and applications to catalysis and sensors. *Curr. Appl. Phys.* **18,** 810–818 (2018).

51. Xiao, S., Wang, S., Wang, X. & Xu, P. Nanoporous gold: A review and potentials in biotechnological and biomedical applications. *Nano Select* **2,** 1437–1458 (2021).

52. Hori, Y. Electrochemical CO2 Reduction on Metal Electrodes. **42,** 89–189.

53. Gao, D. *et al.* Plasma-Activated Copper Nanocube Catalysts for Efficient Carbon Dioxide Electroreduction to Hydrocarbons and Alcohols. *ACS Nano* **11,** 4825–4831 (2017).

54. Sengupta, S. K. A Study on the Origin of Nonfaradaic Behavior of Anodic Contact Glow Discharge Electrolysis. *J. Electrochem. Soc.* **145,** 2209 (1998).

55. Jin, X.-L. *et al.* Influence of Solution Conductivity on Contact Glow Discharge Electrolysis. *Plasma Chem. Plasma Process.* **30,** 429–436 (2010).

56. Jin, X., Wang, X., Yue, J., Cai, Y. & Zhang, H. The effect of electrolyte constituents on contact glow discharge electrolysis. *Electrochim. Acta* **56,** 925–928 (2010).

57. Gangal, U., Srivastava, M. & Sen Gupta, S. K. Mechanism of the Breakdown of Normal Electrolysis and the Transition to Contact Glow Discharge Electrolysis. *J. Electrochem. Soc.* **156,** F131 (2009).

58. Climent, V. & Feliu, J. M. Thirty years of platinum single crystal electrochemistry. *J. Solid State Electrochem.* **15,** 1297–1315 (2011).

59. Zhang, S. *et al.* A review of platinum-based catalyst layer degradation in proton exchange membrane fuel cells. *J. Power Sources* **194,** 588–600 (2009).

60. Baroody, H. A., Jerkiewicz, G. & Eikerling, M. H. Modelling oxide formation and growth on platinum. *J. Chem. Phys.* **146,** 144102 (2017).

61. Farebrother, M., Goledzinowski, M., Thomas, G. & Birss, V. I. Early stages of growth of hydrous platinum oxide films. *J. Electroanal. Chem. Interf. Electrochem.* **297,** 469–488 (1991).

62. Favaro, M. *et al.* Elucidating the alkaline oxygen evolution reaction mechanism on platinum. *J. Mater. Chem. A* **5,** 11634–11643 (2017).

63. Katsounaros, I. *et al.* Hydrogen peroxide electrochemistry on platinum: towards understanding the oxygen reduction reaction mechanism. *Phys. Chem. Chem. Phys.* **14,** 7384–7391 (2012).

64. Saksono, N., Nugraha, I., Ibrahim & Febiyanti, I. A. Hydroxyl radical production on contact glow discharge electrolysis for degradation of linear alkylbenzene sulfonate. *Environ. Prog. Sustain. Energy* **35,** 962–968 (2016).

65. Zheng, B., Wang, K., Shrestha, M., Schuelke, T. & Fan, Q. H. Understanding the chemical reactions in cathodic plasma electrolysis. *Plasma Sources Sci. Technol.* **28,** 085016 (2019).

66. Artmann, E. *et al.* Structural Evolution of Pt, Au and Cu Anodes by Electrolysis up to Contact Glow Discharge Electrolysis in Alkaline Electrolytes. *Chem. Phys. Chem.* **22,** 2429–2441 (2021).

67. Sengupta, S. K. & Singh, O. P. Contact glow discharge electrolysis: a study of its chemical yields in aqueous inert-type electrolytes. *J. Electroanal. Chem.* **369,** 113–120 (1994).

68. Baranov, O. *et al.* From nanometre to millimetre: a range of capabilities for plasma-enabled surface functionalization and nanostructuring. *Mater. Horiz.* **5,** 765–798 (2018).

69. Bruggeman, P. J. *et al.* Plasma–liquid interactions: a review and roadmap. *Plasma Sources Sci. Technol.* **25,** 053002 (2016).

70. Saito, G., Nakasugi, Y. & Akiyama, T. Generation of solution plasma over a large electrode surface area. *J. Appl. Phys.* **118,** 023303 (2015).

71. Sen Gupta, S. K. Contact glow discharge electrolysis: its origin, plasma diagnostics and non-faradaic chemical effects. *Plasma Sources Sci. Technol.* **24,** 063001 (2015).

72. Poulain, C., Dugué, A., Durieux, A., Sadeghi, N. & Duplat, J. The plasma levitation of droplets. *Appl. Phys. Lett.* **107,** 064101 (2015).

73. Takai, O. Solution plasma processing (SPP). *Pure Appl. Chem.* **80,** 2003–2011 (2008).

74. Wohlgemuth, M., Weber, M. L., Heymann, L., Baeumer, C. & Gunkel, F. Activity-Stability Relationships in Oxide Electrocatalysts for Water Electrolysis. *Front. Chem.* **10,** 913419 (2022).

75. Liang, Q., Brocks, G. & Bieberle-Hütter, A. Oxygen evolution reaction (OER) mechanism under alkaline and acidic conditions. *J. Phys.: Energy* **3,** 026001 (2021).

76. Rossmeisl, J., Qu, Z.-W., Zhu, H., Kroes, G.-J. & Nørskov, J. K. Electrolysis of water on oxide surfaces. *J. Electroanal. Chem.* **607,** 83–89 (2007).

77. Suen, N.-T. *et al.* Electrocatalysis for the oxygen evolution reaction: recent development and future perspectives. *Chem. Soc. Rev.* **46,** 337–365 (2017).

78. Kibsgaard, J. & Chorkendorff, I. Considerations for the scaling-up of water splitting catalysts. *Nat. Energy* **4,** 430–433 (2019).

79. Han, Q., Georgescu, N. S., Gibbons, J. & Scherson, D. Electrode stimulation: Redox reactions induced by modulating the electrostatic potential in solution. *Electrochim. Acta* **325,** 134957 (2019).

80. Dickinson, E. J. & Wain, A. J. The Butler-Volmer equation in electrochemical theory: Origins, value, and practical application. *J. Electroanal. Chem.* **872,** 114145 (2020).

81. Forschner, L., Artmann, E., Jacob, T. & Engstfeld, A. K. Electric Potential Distribution Inside the Electrolyte during High Voltage Electrolysis. *J. Phys. Chem. C* **127,** 4387–4394 (2023).

82. Yerokhin, A. L., Nie, X., Leyland, A., Matthews, A. & Dowey, S. J. Plasma electrolysis for surface engineering. *Surf. Coat. Technol.* **122,** 73–93 (1999).

83. Vogt, H. & Thonstad, J. The Diversity and Causes of Current-Potential Behaviour at Gas-Evolving Electrodes. *Electrochim. Acta* **250,** 393–398 (2017).

84. Azumi, K., Mizuno, T., Akimoto, T. & Ohmori, T. Light Emission from Pt during High–Voltage Cathodic Polarization. *J. Electrochem. Soc.* **146,** 3374–3377 (1999).

85. Sen Gupta, S. K. & Singh, R. Cathodic contact glow discharge electrolysis: its origin and non-faradaic chemical effects. *Plasma Sources Sci. Technol.* **26,** 015005 (2017).

86. Sengupta, S. K. & Singh, O. P. Contact glow discharge electrolysis: a study of its onset and location. *J. Electroanal. Chem. Interf. Electrochem.* **301,** 189–197 (1991).

87. Yerokhin, A., Mukaeva, V. R., Parfenov, E. V., Laugel, N. & Matthews, A. Charge transfer mechanisms underlying Contact Glow Discharge Electrolysis. *Electrochim. Acta* **312,** 441–456 (2019).

88. Slovetskii, D. I. & Terent'ev, S. D. Parameters of an Electric Discharge in Electrolytes and Physicochemical Processes in an Electrolyte Plasma. *High Energy Chem.* **37,** 310–316 (2003).

89. Hickling, A. & Ingram, M. D. Glow-discharge electrolysis. *J. Electroanal Chem.* **8,** 65–81 (1964).

90. Kaneko, T., Baba, K., Harada, T. & Hatakeyama, R. Novel Gas-Liquid Interfacial Plasmas for Synthesis of Metal Nanoparticles. *Plasma Process. Polym.* **6,** 713–718 (2009).

91. Paulmier, T., Bell, J. M. & Fredericks, P. M. Development of a novel cathodic plasma/electrolytic deposition technique. *Surf. Coat. Technol.* **201,** 8771–8781 (2007).

92. Mandin, P., Wüthrich, R. & Roustan, H. Polarization curves for an alkaline water electrolysis at a small pin vertical electrode to produce hydrogen. *AIChE J.* **33,** 2446–2454 (2010).

93. Zeradjanin, A. R., Narangoda, P., Spanos, I., Masa, J. & Schlögl, R. How to minimise destabilising effect of gas bubbles on water splitting electrocatalysts? *Curr. Opin. Electrochem.* **30,** 100797 (2021).

94. Campbell, S. A., Cunnane, V. J. & Schiffrin, D. J. Cathodic contact glow discharge electrolysis under reduced pressure. *J. Electroanal. Chem.* **325,** 257–268 (1992).

95. Vogt, H. The actual current density of gas-evolving electrodes—Notes on the bubble coverage. *Electrochim. Acta* **78,** 183–187 (2012).

96. Dukovic, J. & Tobias, C. W. The Influence of Attached Bubbles on Potential Drop and Current Distribution at Gas–Evolving Electrodes. *J. Electrochem. Soc.* **134,** 331–343 (1987).

97. Angulo, A., van der Linde, P., Gardeniers, H., Modestino, M. & Fernández Rivas, D. Influence of Bubbles on the Energy Conversion Efficiency of Electrochemical Reactors. *Joule* **4,** 555–579 (2020).

98. Darband, G. B., Aliofkhazraei, M. & Shanmugam, S. Recent advances in methods and technologies for enhancing bubble detachment during electrochemical water splitting. *Renew. Sust. Energ. Rev.* **114,** 109300 (2019).

99. Sukeri, A., Saravia, L. P. H. & Bertotti, M. A facile electrochemical approach to fabricate a nanoporous gold film electrode and its electrocatalytic activity towards dissolved oxygen reduction. *Phys. Chem. Chem. Phys.* **17,** 28510–28514 (2015).

100. Lai, J., Petrov, V. & Foster, J. E. Understanding Plasma–Liquid Interface Instabilities Using Particle Image Velocimetry and Shadowgraphy Imaging Methods. *IEEE Trans. Plasma Sci.* **46,** 875–881 (2018).

101. Horn, A. Ultra-fast Diagnostics of Laser-induced Melting of Matter in ns to ms Time-scales. *J. Laser Micro/Nanoeng.* **1,** 264–268 (2006).

102. Zhao, X., Ren, H. & Luo, L. Gas Bubbles in Electrochemical Gas Evolution Reactions. *Langmuir* **35,** 5392–5408 (2019).

103. Hersbach, T. J. & Koper, M. T. Cathodic corrosion: 21st century insights into a 19th century phenomenon. *Curr. Opin. Electrochem.* **26,** 100653 (2021).

104. Hornbostel, K., Larsen, C. K. & Geiker, M. R. Relationship between concrete resistivity and corrosion rate – A literature review. *Cem. Concr. Compos.* **39,** 60–72 (2013).

105. Akpanyung, K. & Loto, R. Pitting corrosion evaluation: a review. *J. Phys. Conf. Ser.* **1378,** 022088 (2019).

106. Sample, C. & Golovin, A. A. Formation of porous metal oxides in the anodization process. *Phys. Rev. E Stat. Nonlin. Soft Matter Phys.* **74,** 041606 (2006).

107. Nishio, K. & Masuda, H. Anodization of Gold in Oxalate Solution To Form a Nanoporous Black Film. *Angew. Chem.* **123,** 1641–1645 (2011).

108. Skeldon, P., Thompson, G. E., Garcia-Vergara, S. J., Iglesias-Rubianes, L. & Blanco-Pinzon, C. E. A Tracer Study of Porous Anodic Alumina. *Electrochem. Solid-State Lett.* **9,** B47 (2006).

109. Sukeri, A. & Bertotti, M. Nanoporous Gold Surface: An Efficient Platform for Hydrogen Evolution Reaction at Very Low Overpotential. *J. Braz. Chem. Soc.* **29,** 226–231 (2018).

110. Jerkiewicz, G., Tremiliosi-Filho, G. & Conway, B. E. Significance of the apparent limit of anodic oxide film formation at Pt: saturation coverage by the quasi two-dimensional state. *J. Electroanal. Chem.* **334,** 359–370 (1992).

111. Conway, B. E. Electrochemical oxide film formation at noble metals as a surface-chemical process. *Prog. Surf. Sci.* **49,** 331–452 (1995).

112. Kunze, J., Maurice, V., Klein, L. H., Strehblow, H.-H. & Marcus, P. In Situ Scanning Tunneling Microscopy Study of the Anodic Oxidation of Cu(111) in 0.1 M NaOH. *J. Phys. Chem. B* **105,** 4263–4269 (2001).

113. Schmidt, T. J., Stamenkovic, V., Arenz, M., Markovic, N. M. & Ross, P. N. Oxygen electrocatalysis in alkaline electrolyte: Pt(hkl), Au(hkl) and the effect of Pd-modification. *Electrochim. Acta* **47,** 3765–3776 (2002).

114. Schmidt, T. J., Ross, P. N. & Markovic, N. M. Temperature-Dependent Surface Electrochemistry on Pt Single Crystals in Alkaline Electrolyte: Part 1: CO Oxidation. *J. Phys. Chem. B* **105,** 12082–12086 (2001).

115. Hamelin, A., Sottomayor, M. J., Silva, F., Chang, S.-C. & Weaver, M. J. Cyclic voltammetric characterization of oriented monocrystalline gold surfaces in aqueous alkaline solution. *J. Electroanal. Chem. Interf. Electrochem.* **295,** 291–300 (1990).

116. Higo, M. *et al.* Formation and decomposition of gold oxides prepared by an oxygen-dc glow discharge from gold films and studied by X-ray photoelectron spectroscopy. *Thin Solid Films* **699,** 137870 (2020).

117. Tsai, H. *et al.* Instability of gold oxide Au2O3. *Surf. Sci.* **537,** L447–L450 (2003).

118. Szlachetko, J. *et al.* Real Time Determination of the Electronic Structure of Unstable Reaction Intermediates during Au 2 O 3 Reduction. *J. Phys. Chem. Lett.* **5,** 80–84 (2014).

119. Shi, H., Asahi, R. & Stampfl, C. Properties of the gold oxides Au2O3 and Au2O : First-principles investigation. *Phys. Rev. B* **75,** 205125 (2007).

120. Kunze, J., Maurice, V., Klein, L. H., Strehblow, H.-H. & Marcus, P. In situ STM study of the duplex passive films formed on Cu(111) and Cu(001) in 0.1 M NaOH. *Corros. Sci.* **46,** 245–264 (2004).

121. Pourbaix, M. Electrochemical corrosion of metallic biomaterials. *Biomaterials* **5,** 122–134 (1984).

122. Beverskog, B. & Puigdomenech, I. Revised Pourbaix Diagrams for Copper at 25 to 300 ℃. *J. Electrochem. Soc.* **144,** 3476–3483 (1997).

123. Strehblow, H.-H., Maurice, V. & Marcus, P. Initial and later stages of anodic oxide formation on Cu, chemical aspects, structure and electronic properties. *Electrochim. Acta* **46,** 3755–3766 (2001).

124. Deng, Y., Handoko, A. D., Du, Y., Xi, S. & Yeo, B. S. In Situ Raman Spectroscopy of Copper and Copper Oxide Surfaces during Electrochemical Oxygen Evolution Reaction: Identification of Cu III Oxides as Catalytically Active Species. *ACS Catal.* **6,** 2473–2481 (2016).

125. Schmitt, E. h. H. Die Entwicklung des Eloxal-Verfahrens, Teil I. *Chemie Ing. Techn.* **37,** 622–624 (1965).

126. Elze, J. Die Entwicklung des Eloxal-Verfahrens, Teil II. *Chemie Ing. Techn.* **37,** 625–626 (1965).

127. Wang, L.-N. *et al.* Nanotubular surface modification of metallic implants via electrochemical anodization technique. *Int. J. Nanomed.* **9,** 4421–4435 (2014).

128. Lee, W. & Park, S.-J. Porous anodic aluminum oxide: anodization and templated synthesis of functional nanostructures. *Chem. Rev.* **114,** 7487–7556 (2014).

129. Keller, F., Hunter, M. S. & Robinson, D. L. Structural Features of Oxide Coatings on Aluminum. *J. Electrochem. Soc.* **100,** 411 (1953).

130. Simchen, F., Sieber, M., Kopp, A. & Lampke, T. Introduction to Plasma Electrolytic Oxidation—An Overview of the Process and Applications. *Coatings* **10,** 628 (2020).

131. Curran, J. A. & Clyne, T. W. Thermo-physical properties of plasma electrolytic oxide coatings on aluminium. *Surf. Coat. Technol.* **199,** 168–176 (2005).

132. Wielage, B., Alisch, G., Lampke, T. & Nickel, D. Anodizing – A Key for Surface Treatment of Aluminium. *Key Eng. Mater.* **384,** 263–281 (2008).

133. Elnagar, M. M., Hermann, J. M., Jacob, T. & Kibler, L. A. Tailoring the electrode surface structure by cathodic corrosion in alkali metal hydroxide solution: Nanostructuring and faceting of Au. *Curr. Opin. Electrochem.* **27,** 100696 (2021).

134. Yanson, A. I. *et al.* Cathodic corrosion: a quick, clean, and versatile method for the synthesis of metallic nanoparticles. *Angew. Chem. Int. Ed.* **50,** 6346–6350 (2011).

135. Duca, M., Rodriguez, P., Yanson, A. I. & Koper, M. T. M. Selective Electrocatalysis on Platinum Nanoparticles with Preferential (100) Orientation Prepared by Cathodic Corrosion. *Top. Catal.* **57,** 255–264 (2014).

136. Hersbach, T. J. P., Yanson, A. I. & Koper, M. T. M. Anisotropic etching of platinum electrodes at the onset of cathodic corrosion. *Nat. Commun.* **7,** 12653 (2016).

137. Yanson, A. I., Antonov, P. V., Yanson, Y. I. & Koper, M. Controlling the size of platinum nanoparticles prepared by cathodic corrosion. *Electrochim. Acta* **110,** 796–800 (2013).

138. Yanson, A. I. & Yanson, Y. I. Cathodic corrosion. II. Properties of nanoparticles synthesized by cathodic corrosion. *Low Temp. Phys.* **39,** 312–317 (2013).

139. Arulmozhi, N., Hersbach, T. J. P. & Koper, M. T. M. Nanoscale morphological evolution of monocrystalline Pt surfaces during cathodic corrosion. *Proc. Nat. Acad. Sci. U.S.A.* **117,** 32267–32277 (2020).

140. Elnagar, M. M., Hermann, J. M., Jacob, T. & Kibler, L. A. An affordable option to Au single crystals through cathodic corrosion of a wire: Fabrication, electrochemical behavior, and applications in electrocatalysis and spectroscopy. *Electrochim. Acta* **372,** 137867 (2021).

141. Hersbach, T. J. P., Mints, V. A., Calle-Vallejo, F., Yanson, A. I. & Koper, M. T. M. Anisotropic etching of rhodium and gold as the onset of nanoparticle formation by cathodic corrosion. *Faraday Discuss.* **193,** 207–222 (2016).

142. Elnagar, M. M., Jacob, T. & Kibler, L. A. Cathodic corrosion of Au in aqueous methanolic alkali metal hydroxide electrolytes: Notable role of water. *Electrochem. Sci. Adv.* (2021).

143. Hersbach, T. J. P. *et al.* Alkali Metal Cation Effects in Structuring Pt, Rh, and Au Surfaces through Cathodic Corrosion. *ACS Appl. Mater. Interfaces* **10,** 39363–39379 (2018).

144. Yang, S. & Luo, X. Mesoporous nano/micro noble metal particles: synthesis and applications. *Nanoscale* **6,** 4438–4457 (2014).

145. Sing, K. S. W. Reporting physisorption data for gas/solid systems with special reference to the determination of surface area and porosity (Recommendations 1984). *Pure Appl. Chem.* **57,** 603–619 (1985).

146. Solano-Umaña, V. & Vega-Baudrit, J. R. Micro, Meso and Macro Porous Materials on Medicine. *J. Biomater. Nanobiotechnol.* **06,** 247–256 (2015).

147. Föll, H., Carstensen, J. & Frey, S. Porous and Nanoporous Semiconductors and Emerging Applications. *J. Nanomater.* **2006,** 1–10 (2006).

148. Goyal, A., Bondue, C. J., Graf, M. & Koper, M. T. M. Effect of pore diameter and length on electrochemical CO 2 reduction reaction at nanoporous gold catalysts. *Chem. Sci.* **13,** 3288–3298 (2022).

149. Liu, P. *et al.* Visualizing Under-Coordinated Surface Atoms on 3D Nanoporous Gold Catalysts. *Adv. Mater.* **28,** 1753–1759 (2016).

150. Zhu, C. *et al.* Toward digitally controlled catalyst architectures: Hierarchical nanoporous gold via 3D printing. *Sci. Adv.* **4,** eaas9459 (2018).

151. Fujita, T. *et al.* Atomic origins of the high catalytic activity of nanoporous gold. *Nature Mater.* **11,** 775–780 (2012).

152. Jalas, D. *et al.* Electrochemical tuning of the optical properties of nanoporous gold. *Sci. Rep.* **7,** 44139 (2017).

153. Seker, E. *et al.* The effects of post-fabrication annealing on the mechanical properties of freestanding nanoporous gold structures. *Acta Mater.* **55,** 4593–4602 (2007).

154. Seker, E., Reed, M. & Begley, M. Nanoporous Gold: Fabrication, Characterization, and Applications. *Mater.* **2,** 2188–2215 (2009).

155. Zhang, X. & Ding, Y. Unsupported nanoporous gold for heterogeneous catalysis. *Catal. Sci. Technol.* **3,** 2862 (2013).

156. Zhang, R. & Olin, H. Porous Gold Films-A Short Review on Recent Progress. *Materials* **7,** 3834–3854 (2014).

157. Lu, Y., Wang, Q., Sun, J. & Shen, J. Selective dissolution of the silver component in colloidal Au and Ag multilayers: a facile way to prepare nanoporous gold film materials. *Langmuir* **21,** 5179–5184 (2005).

158. Vitrey, A., Alvarez, R., Palmero, A., González, M. U. & García-Martín, J. M. Fabrication of black-gold coatings by glancing angle deposition with sputtering. *Beilstein J. Nanotechnol.* **8,** 434–439 (2017).

159. Zheng, H., Picard, C. & Ravaine, S. Nanostructured gold films exhibiting almost complete absorption of light at visible wavelengths. *Front. Chem. Sci. Eng.* **12,** 247–251 (2018).

160. Erlebacher, J. An Atomistic Description of Dealloying. *J. Electrochem. Soc.* **151,** C614 (2004).

161. Erlebacher, J., Aziz, M. J., Karma, A., Dimitrov, N. & SIERADZKI, K. Evolution of nanoporosity in dealloying. *Nature* **410,** 450–453 (2001).

162. McCue, I., Benn, E., Gaskey, B. & Erlebacher, J. Dealloying and Dealloyed Materials. *Annu. Rev. Mater. Res.* **46,** 263–286 (2016).

163. Dotzler, C. J. *et al.* In Situ Observation of Strain Development and Porosity Evolution in Nanoporous Gold Foils. *Adv. Funct. Mater.* **21,** 3938–3946 (2011).

164. Detsi, E. *et al.* On the specific surface area of nanoporous materials. *Acta Mater.* **59,** 7488–7497 (2011).

165. Thommes, M. *et al.* Physisorption of gases, with special reference to the evaluation of surface area and pore size distribution (IUPAC Technical Report). *Pure Appl. Chem.* **87,** 1051–1069 (2015).

166. Henkelmann, G. *et al.* Self-Detachment and Subsurface Densification of Dealloyed Nanoporous Thin Films. *Nano Lett.* **22,** 6787–6793 (2022).

167. Gao, Y. & Ding, Y. Nanoporous Metals for Heterogeneous Catalysis: Following the Success of Raney Nickel. *Chemistry* **26,** 8845–8856 (2020).

168. Tapia Burgos, J. A. *et al.* The Impact of the Manufacturing and Corrosion Steps of the AuCu Master Alloy on the Catalytic Activity of Nanoporous Gold for CO Oxidation. *Preprint at SSRN Electronic Journal,* doi: 10.2139/ssrn.3955671 (2021).

169. Artmann, E. *et al.* Nanoporous Au Formation on Au Substrates via High Voltage Electrolysis. *Chem. Phys. Chem.* **24,** e202200645 (2022).

170. Sikdar, S., Menezes, P. V., Maccione, R., Jacob, T. & Menezes, P. L. Plasma Electrolytic Oxidation (PEO) Process-Processing, Properties, and Applications. *Nanomaterials* **11** (2021).

171. Allagui, A., Baranova, E. A. & Wüthrich, R. Synthesis of Ni and Pt nanomaterials by cathodic contact glow discharge electrolysis in acidic and alkaline media. *Electrochim. Acta* **93,** 137–142 (2013).

172. Allagui, A. *et al.* DC and AC Performance of Graphite Films Supercapacitors Prepared by Contact Glow Discharge Electrolysis. *J. Electrochem. Soc.* **164,** A2539–A2546 (2017).

173. Toriyabe, Y., Watanabe, S., Yatsu, S., Shibayama, T. & Mizuno, T. Controlled formation of metallic nanoballs during plasma electrolysis. *Appl. Phys. Lett.* **91,** 041501 (2007).

174. Saito, G., Nakasugi, Y., Yamashita, T. & Akiyama, T. Solution plasma synthesis of bimetallic nanoparticles. *Nanotechnol.* **25,** 135603 (2014).

175. Kurniawan, F. & Rahmi, R. Synthesis of SnO_2 Nanoparticles by High Potential Electrolysis. *Bull. Chem. React. Eng. Catal.* **12,** 281 (2017).

176. Yang, G. *et al.* Electropolishing of surfaces: theory and applications. *Surf. Eng.* **33,** 149–166 (2017).

177. Landolt, D. Fundamental aspects of electropolishing. *Electrochim. Acta* **32,** 1–11 (1987).

178. Wagner, C. Contribution to the Theory of Electropolishing. *J. Electrochem. Soc.* **101,** 225 (1954).

179. Rokicki, R. & Hryniewicz, T. Enhanced oxidation–dissolution theory of electropolishing. *Trans. Inst. Met. Finish.* **90,** 188–196 (2012).

180. Zeidler, H., Boettger-Hiller, F., Edelmann, J. & Schubert, A. Surface Finish Machining of Medical Parts Using Plasma Electrolytic Polishing. *Procedia CIRP* **49,** 83–87 (2016).

181. Nestler, K. *et al.* Plasma Electrolytic Polishing – An Overview of Applied Technologies and Current Challenges to Extend the Polishable Material Range. *Procedia CIRP* **42,** 503–507 (2016).

182. Belkin, P. N., Kusmanov, S. A. & Parfenov, E. V. Mechanism and technological opportunity of plasma electrolytic polishing of metals and alloys surfaces. *Appl. Surf. Sci. Adv.* **1,** 100016 (2020).

183. Danilov, I. *et al.* Process Understanding of Plasma Electrolytic Polishing through Multiphysics Simulation and Inline Metrology. *Micromachines* **10,** 214 (2019).

184. Cartier, C. A., Kumsa, D., Feng, Z., Zhu, H. & Scherson, D. A. Quantitative aspects of ohmic microscopy. *Anal. Chem.* **84,** 7080–7084 (2012).

185. Chen, Y., Belianinov, A. & Scherson, D. Spatially-Resolved Interfacial Electrochemistry: Ohmic Microscopy. *J. Phys. Chem. C* **112,** 8754–8758 (2008).

186. Feng, Z., Georgescu, N. S. & Scherson, D. A. New advances in ohmic microscopy. *Russ. J. Electrochem.* **53,** 1003–1010 (2017).

187. Hickling, A. & Newns, G. R. 1025. Glow-discharge electrolysis. Part V. The contact glow-discharge electrolysis of liquid ammonia. *J. Chem. Soc.,* 5186 (1961).

188. Locke, B. R. & Shih, K.-Y. Review of the methods to form hydrogen peroxide in electrical discharge plasma with liquid water. *Plasma Sources Sci. Technol.* **20,** 034006 (2011).

189. Jinzhang, G. *et al.* Analysis of Energetic Species Caused by Contact Glow Discharge Electrolysis in Aqueous Solution. *Plasma Sci. Technol.* **10,** 30–38 (2008).

190. Groele, J. & Foster, J. Hydrogen Peroxide Interference in Chemical Oxygen Demand Assessments of Plasma Treated Waters. *Plasma* **2,** 294–302 (2019).

191. Julák, J., Hujacová, A., Scholtz, V., Khun, J. & Holada, K. Contribution to the Chemistry of Plasma-Activated Water. *Plasma Phys. Rep.* **44,** 125–136 (2018).

192. Winter, J. *et al.* Tracking plasma generated H_2O_2 from gas into liquid phase and revealing its dominant impact on human skin cells. *J. Phys. D* **47,** 285401 (2014).

193. Brubaker, T. R. *et al.* Dynamic analysis of reactive oxygen nitrogen species in plasma-activated culture medium by UV absorption spectroscopy. *J. Appl. Phys.* **122,** 213301 (2017).

194. Burdo, T. G. & Seitz, W. R. Mechanism of cobalt catalysis of luminol chemiluminescence. *Anal. Chem.* **47,** 1639–1643 (1975).

195. Chen, Q., Li, J. & Li, Y. A review of plasma–liquid interactions for nanomaterial synthesis. *J. Phys. D* **48,** 424005 (2015).

196. Schuett, F. M. *et al.* Controlled-Atmosphere Flame Fusion Single-Crystal Growth of Non-Noble fcc, hcp, and bcc Metals Using Copper, Cobalt, and Iron. *Angew. Chem. Int. Ed.* **59,** 13246–13252 (2020).

197. Esau, D. *et al.* Controlled-Atmosphere Flame Fusion Growth of Nickel Polyoriented Spherical Single Crystals—Unraveling Decades of Impossibility. *Electrocatalysis* **11,** 1–13 (2020).

198. Cherevko, S., Zeradjanin, A. R., Keeley, G. P. & Mayrhofer, K. J. J. A Comparative Study on Gold and Platinum Dissolution in Acidic and Alkaline Media. *J. Electrochem. Soc.* **161,** H822–H830 (2014).

199. Artmann, E., Forschner, L., Jacob, T. & Engstfeld, A. K. Using auxiliary electrochemical working electrodes as probe during contact glow discharge electrolysis: A proof of concept study. *J. Vac. Sci. Technol. A* **40,** 053005 (2022).

200. Łukaszewski, M. Electrochemical Methods of Real Surface Area Determination of Noble Metal Electrodes – an Overview. *Int. J. Electrochem. Sci.,* 4442–4469 (2016).

201. Arulmozhi, N. & Jerkiewicz, G. Design and Development of Instrumentations for the Preparation of Platinum Single Crystals for Electrochemistry and Electrocatalysis Research. Part 2: Orientation, Cutting, and Annealing. *Electrocatalysis* **8,** 399–413 (2017).

202. Uosaki, K. *Electrochemical Science for a Sustainable Society: A Tribute to John O'M Bockris* (Springer, 2017).

203. Schmickler, W. & Santos, E. *Interfacial electrochemistry* (Springer Science & Business Media, 2010).

204. Yatsu, S. *et al.* Fabrication of Nanoparticles by Electric Discharge Plasma in Liquid. *Arch. Metall. Mater.* **58,** 425–429 (2013).

205. Popović, S. *et al.* Stability and Degradation Mechanisms of Copper-Based Catalysts for Electrochemical CO2 Reduction. *Angew. Chem. Int. Ed.* **59,** 14736–14746 (2020).

206. Akolkar, R. & Sankaran, R. M. Charge transfer processes at the interface between plasmas and liquids. *J. Vac. Sci. Technol. A* **31,** 050811 (2013).

207. Kibler, L. A. Preparation and characterization of noble metal single crystal electrode surfaces. *International Society of Electrochemistry,* 1–55 (2003).

208. Daubinger, P., Kieninger, J., Unmüssig, T. & Urban, G. A. Electrochemical characteristics of nanostructured platinum electrodes–a cyclic voltammetry study. *Phys. Chem. Chem. Phys.* **16,** 8392–8399 (2014).

209. Itaya, K., Sugawara, S., Sashikata, K. & Furuya, N. Insitu scanning tunneling microscopy of platinum (111) surface with the observation of monatomic steps. *J. Vac. Sci. Technol. A* **8,** 515–519 (1990).

210. Arulmozhi, N., Esau, D., Lamsal, R. P., Beauchemin, D. & Jerkiewicz, G. Structural Transformation of Monocrystalline Platinum Electrodes upon Electro-oxidation and Electro-dissolution. *ACS Catal.* **8,** 6426–6439 (2018).

211. Jacobse, L., Huang, Y.-F., Koper, M. T. M. & Rost, M. J. Correlation of surface site formation to nanoisland growth in the electrochemical roughening of Pt(111). *Nat. Mater.* **17,** 277–282 (2018).

212. Fuchs, T. *et al.* Structure dependency of the atomic-scale mechanisms of platinum electro-oxidation and dissolution. *Nat. Catal.* **3,** 754–761 (2020).

213. Li, Z., Beck, P., Ohlberg, D. A., Stewart, D. R. & Williams, R. S. Surface properties of platinum thin films as a function of plasma treatment conditions. *Surf. Sci.* **529,** 410–418 (2003).

214. Kirchhoff, B. *et al.* Simulations of the Oxidation and Degradation of Platinum Electrocatalysts. *Small* **16,** e1905159 (2020).

215. Widdascheck, F., Kothe, M., Hauke, A. A. & Witte, G. The effect of oxygen plasma treatment of gold electrodes on the molecular orientation of CuPc films. *Appl. Surf. Sci.* **507,** 145039 (2020).

216. Stadnichenko, A., Koshcheev, S. & Boronin, A. Oxidation of the polycrystalline gold foil surface and XPS study of oxygen states in oxide layers. *Moscow Univ. Chem. Bull.* **62,** 343–349 (2007).

217. Mistry, H. *et al.* Highly selective plasma-activated copper catalysts for carbon dioxide reduction to ethylene. *Nat. Commun.* **7,** 1–9 (2016).

218. Vvedenskii, A., Grushevskaya, S., Ganzha, S. & Eliseev, D. Copper oxides: kinetics of formation and semiconducting properties. Part I. Polycrystalline copper and copper-gold alloys. *J. Solid State Electrochem.* **18,** 2755–2770 (2014).

219. Vvedenskii, A., Grushevskaya, S., Ganzha, S., Eliseev, D. & Abakumova, L. I. Copper oxides: kinetics of formation and semiconducting properties. Part II. Copper single crystals. *J. Solid State Electrochem.* **18,** 3437–3451 (2014).

220. Engstfeld, A. K., Maagaard, T., Horch, S., Chorkendorff, I. & Stephens, I. E. L. Polycrystalline and Single-Crystal Cu Electrodes: Influence of Experimental Conditions on the Electrochemical Properties in Alkaline Media. *Chem. Eur. J.* **24,** 17743–17755 (2018).

221. P. Schouten, K. J., Gallent, E. P. & Koper, M. T. The electrochemical characterization of copper single-crystal electrodes in alkaline media. *J. Electroanal. Chem.* **699,** 6–9 (2013).

222. Bagger, A. *et al.* Ab Initio Cyclic Voltammetry on Cu(111), Cu(100) and Cu(110) in Acidic, Neutral and Alkaline Solutions. *Chem. Phys. Chem.* **20,** 3096–3105 (2019).

223. Tiwari, A. *et al.* Fingerprint Voltammograms of Copper Single Crystals under Alkaline Conditions: A Fundamental Mechanistic Analysis. *J. Phys. Chem. Lett.* **11,** 1450–1455 (2020).

224. Gilliam, R., Graydon, J., Kirk, D. & Thorpe, S. A review of specific conductivities of potassium hydroxide solutions for various concentrations and temperatures. *Int. J. Hydrog. Energy* **32,** 359–364 (2007).

225. Artmann, E., Forschner, L., Jacob, T. & Engstfeld, A. K. Using auxiliary electrochemical working electrodes as probe during contact glow discharge electrolysis: A proof of concept study. *Preprint at ChemRxiv,* doi: 10.26434/chemrxiv-2022–0v5sc (2022).

226. Malik, M. A., Ghaffar, A. & Malik, S. A. Water purification by electrical discharges. *Plasma Sources Sci. Technol.* **10,** 82–91 (2001).

227. Yayci, A. *et al.* Microscale Atmospheric Pressure Plasma Jet as a Source for Plasma–Driven Biocatalysis. *Chem. Cat. Chem.* **12,** 5893–5897 (2020).

228. Mistry, H. *et al.* Highly selective plasma-activated copper catalysts for carbon dioxide reduction to ethylene. *Nat. Commun.* **7,** 12123 (2016).

229. Mistry, H. *et al.* Enhanced Carbon Dioxide Electroreduction to Carbon Monoxide over Defect-Rich Plasma-Activated Silver Catalysts. *Angew. Chem. Int. Ed.* **56,** 11394–11398 (2017).

230. Yu, F. *et al.* A Review on the Promising Plasma-Assisted Preparation of Electrocatalysts. *Nanomaterials* **9,** 1436 (2019).

231. Rheinlander, P., Henning, S., Herranz, J. & Gasteiger, H. A. Comparing Hydrogen Oxidation and Evolution Reaction Kinetics on Polycrystalline Platinum in 0.1 M and 1 M KOH. *ECS Trans.* **50,** 2163–2174 (2013).

232. Park, S.-.-M. *et al.* Electrochemical Reduction of Oxygen at Platinum Electrodes in KOH Solutions – Temperature and Concentration Effects. *J. Electrochem. Soc.* **133,** 1641–1649 (1986).

233. Katsounaros, I. & Mayrhofer, K. J. J. The influence of non-covalent interactions on the hydrogen peroxide electrochemistry on platinum in alkaline electrolytes. *Chem. Commun.* **48,** 6660–6662 (2012).

234. Sheng, W. *et al.* Correlating hydrogen oxidation and evolution activity on platinum at different pH with measured hydrogen binding energy. *Nat. Commun.* **6,** 5848 (2015).

235. Briega-Martos, V., Herrero, E. & Feliu, J. M. Pt(hkl) surface charge and reactivity. *Curr. Opin. Electrochem.* **17,** 97–105 (2019).

236. Briega-Martos, V., Herrero, E. & Feliu, J. M. The inhibition of hydrogen peroxide reduction at low potentials on Pt(111): Hydrogen adsorption or interfacial charge? *Electrochem. Commun.* **85,** 32–35 (2017).

237. Schnaidt, J. *et al.* A combined UHV-STM-flow cell set-up for electrochemical/electrocatalytic studies of structurally well-defined UHV prepared model electrodes. *Phys. Chem. Chem. Phys.* **19,** 4166–4178 (2017).

238. Beckord, S., Brimaud, S. & Behm, R. J. The performance of structurally well-defined Ag_xPt_{1-x}/Pt(111) surface alloys in the oxygen reduction reaction – An atomic-scale picture. *J. Electroanal. Chem.* **819,** 401–409 (2018).

239. Yang, S. *et al.* Toward the Decentralized Electrochemical Production of H_2O_2: A Focus on the Catalysis. *ACS Catal.* **8,** 4064–4081 (2018).

240. Fosdick, S. E., Knust, K. N., Scida, K. & Crooks, R. M. Bipolar electrochemistry. *Angew. Chem. Int. Ed.* **52,** 10438–10456 (2013).

241. Loget, G., Zigah, D., Bouffier, L., Sojic, N. & Kuhn, A. Bipolar electrochemistry: from materials science to motion and beyond. *Acc. Chem. Res.* **46,** 2513–2523 (2013).

242. McKee, D. Catalytic decomposition of hydrogen peroxide by metals and alloys of the platinum group. *J. Catal.* **14,** 355–364 (1969).

243. Serra-Maia, R., Rimstidt, J. D. & Michel, F. M. Kinetic Effect of Surface Chemisorbed Oxygen on Platinum-Catalyzed Hydrogen Peroxide Decomposition. *Catal. Lett.* **151,** 138–146 (2021).

244. Akolkar, R. & Sankaran, R. M. Charge transfer processes at the interface between plasmas and liquids. *J. Vac. Sci. Technol. A* **31,** 050811 (2013).

245. Yan, K. *et al.* Advanced Functional Electroactive and Photoactive Materials for Monitoring the Environmental Pollutants. *Adv. Funct. Mater.* **31,** 2008227 (2021).

246. Biener, J. *et al.* Surface-chemistry-driven actuation in nanoporous gold. *Nature Mater.* **8,** 47–51 (2009).

247. Wittstock, A., Wichmann, A., Biener, J. & Bäumer, M. Nanoporous gold: a new gold catalyst with tunable properties. *Faraday Discuss.* **152,** 87–98, discussion 99–120 (2011).

248. Wang, Z. *et al.* Tuning Surface Structure of 3D Nanoporous Gold by Surfactant-Free Electrochemical Potential Cycling. *Adv. Mater.* **29,** 1703601 (2017).

249. Li, D., Zhu, Y., Wang, H. & Ding, Y. Nanoporous gold as an active low temperature catalyst toward CO oxidation in hydrogen-rich stream. *Sci. Rep.* **3,** 3015 (2013).

250. Ding, Y. & Chen, M. Nanoporous Metals for Catalytic and Optical Applications. *MRS Bull.* **34,** 569–576 (2009).

251. Patel, J., Němcová, L., Maguire, P., Graham, W. G. & Mariotti, D. Synthesis of surfactant-free electrostatically stabilized gold nanoparticles by plasma-induced liquid chemistry. *Nanotechnol.* **24,** 245604 (2013).

252. Chen, Q., Kaneko, T. & Hatakeyama, R. Reductants in Gold Nanoparticle Synthesis Using Gas–Liquid Interfacial Discharge Plasmas. *Appl. Phys. Express* **5,** 086201 (2012).

253. Rumbach, P. & Go, D. B. Perspectives on Plasmas in Contact with Liquids for Chemical Processing and Materials Synthesis. *Top. Catal.* **60,** 799–811 (2017).

254. Pedireddy, S. *et al.* One-step synthesis of zero-dimensional hollow nanoporous gold nanoparticles with enhanced methanol electrooxidation performance. *Nature Comm.* **5,** 4947 (2014).

255. Panda, B. R. & Chattopadhyay, A. Synthesis of au nanoparticles at " all " pH by H_2O_2 reduction of $HAuCl_4$. *J. Nanosci. Nanotechnol.* **7,** 1911–1915 (2007).

256. Pireaux, J. J., Liehr, M., Thiry, P. A., Delrue, J. P. & Caudano, R. Electron spectroscopic characterization of oxygen adsorption on gold surfaces. *Surf. Sci.* **141,** 221–232 (1984).

257. Ono, L. K. & Roldan Cuenya, B. Formation and Thermal Stability of Au 2 O 3 on Gold Nanoparticles: Size and Support Effects. *J. Phys. Chem. C* **112,** 4676–4686 (2008).

258. Irissou, E., Denis, M.-C., Chaker, M. & Guay, D. Gold oxide thin film grown by pulsed laser deposition in an O2 atmosphere. *Thin Solid Films* **472,** 49–57 (2005).

259. Seah, M. P., Smith, G. C. & Anthony, M. T. AES: Energy calibration of electron spectrometers. I?an absolute, traceable energy calibration and the provision of atomic reference line energies. *Surf. Interface Anal.* **15,** 293–308 (1990).

260. Dickinson, T., Povey, A. F. & Sherwood, P. M. A. X-ray photoelectron spectroscopic studies of oxide films on platinum and gold electrodes. *J. Chem. Soc., Faraday Trans. 1* **71,** 298 (1975).

261. Krozer, A. & Rodahl, M. X-ray photoemission spectroscopy study of UV/ozone oxidation of Au under ultrahigh vacuum conditions. *J. Vac. Sci. Technol. A* **15,** 1704–1709 (1997).

262. Saliba, N., Parker, D. & Koel, B. Adsorption of oxygen on Au(111) by exposure to ozone. *Surf. Sci.* **410,** 270–282 (1998).

263. Zheng, B., Wang, K., Shrestha, M., Schuelke, T. & Fan, Q. H. Understanding the chemical reactions in cathodic plasma electrolysis. *Plasma Sources Sci. Technol.* **28,** 085016 (2019).

264. Chang, Y. *et al.* Effects of crystal quality, grain-size and oxygen vacancy of nanocrystalline CeO2 films under 1.5 MeV Au ion irradiation. *J. Nucl. Mater.* **518,** 41–47 (2019).

265. Artmann, E., Schmider, T., Jacob, T. & Engstfeld, A. K. Facet-Dependent Formation and Adhesion of Au Oxide and Nanoporous Au on Poly-Oriented Au Single Crystals. *Preprint at ChemRxiv,* doi: 10.26434/chemrxiv-2023–nf7v3 (2023).

266. Khristosov, M. K. *et al.* Sponge-like nanoporous single crystals of gold. *Nature Comm.* **6,** 8841 (2015).

267. Conway, B. E. & Jerkiewicz, G. Surface orientation dependence of oxide film growth at platinum single crystals. *J. Electroanal. Chem.* **339,** 123–146 (1992).

268. Dickertmann, D., Schultze, J. W. & Vetter, K. J. Electrochemical formation and reduction of monomolecular oxide layers on (111) and (100) planes of gold single crystals. *J. Electroanal. Chem. Interfacial Electrochem.* **55,** 429–443 (1974).

269. Evertsson, J. *et al.* The thickness of native oxides on aluminum alloys and single crystals. *Appl. Surf. Sci.* **349,** 826–832 (2015).

270. Reichel, F., Jeurgens, L. & Mittemeijer, E. J. The effect of substrate orientation on the kinetics of ultra-thin oxide-film growth on Al single crystals. *Acta Mater.* **56,** 2897–2907 (2008).

271. Graham, M. J., Hussey, R. J. & Cohen, M. Influence of Oxide Structure on the Oxidation Rate of Nickel Single Crystals. *J. Electrochem. Soc.* **120,** 1523 (1973).

272. Jeon, B., van Overmeere, Q., van Duin, A. C. T. & Ramanathan, S. Nanoscale oxidation and complex oxide growth on single crystal iron surfaces and external electric field effects. *Phys. Chem. Chem. Phys.* **15,** 1821–1830 (2013).

273. Scholten, F., Nguyen, K.-L. C., Bruce, J. P., Heyde, M. & Roldan Cuenya, B. Identifying Structure-Selectivity Correlations in the Electrochemical Reduction of CO2 : A Comparison of Well-Ordered Atomically Clean and Chemically Etched Copper Single-Crystal Surfaces. *Angew. Chem. Int. Ed.* **60,** 19169–19175 (2021).

274. Raaijman, S. J., Arulmozhi, N. & Koper, M. T. M. Anisotropic Cathodic Corrosion of Gold Electrodes in the Absence and Presence of Carbon Monoxide. *J. Phys. Chem. C* **124,** 28539–28554 (2020).

275. Arulmozhi, N., Esau, D., Lamsal, R. P., Beauchemin, D. & Jerkiewicz, G. Structural Transformation of Monocrystalline Platinum Electrodes upon Electro-oxidation and Electro-dissolution. *ACS Catal.* **8,** 6426–6439 (2018).

276. Clavilier, J., Armand, D., Sun, S. G. & Petit, M. Electrochemical adsorption behaviour of platinum stepped surfaces in sulphuric acid solutions. *J. Electroanal. Chem. Interfacial Electrochem.* **205,** 267–277 (1986).

277. Clavilier, J., El Achi, K. & Rodes, A. In situ probing of step and terrace sites on Pt(S)-[n(111) $\times$ (111)] electrodes. *Chem. Phys.* **141,** 1–14 (1990).

278. Arulmozhi, N. & Jerkiewicz, G. Design and Development of Instrumentations for the Preparation of Platinum Single Crystals for Electrochemistry and Electrocatalysis Research. Part 1: Semi-Automated Crystal Growth. *Electrocatalysis* **7,** 507–518 (2016).

279. Arulmozhi, N., Esau, D., van Drunen, J. & Jerkiewicz, G. Design and Development of Instrumentations for the Preparation of Platinum Single Crystals for Electrochemistry and Electrocatalysis Research Part 3: Final Treatment, Electrochemical Measurements, and Recommended Laboratory Practices. *Electrocatalysis* **9,** 113–123 (2018).

Erklärung

Ich versichere hiermit, dass ich die Arbeit selbständig angefertigt habe und keine anderen als die angegebenen Quellen und Hilfsmittel benutzt, sowie die wörtlich oder inhaltlich übernommenen Stellen als solche kenntlich gemacht habe und die Satzung der Universität Ulm zur Sicherung guter wissenschaftlicher Praxis in der jeweils gültigen Fassung beachtet habe. Ich bin damit einverstanden, dass die Dissertation auch zum Zweck der Überprüfung der Einhaltung allgemein geltender wissenschaftlicher Standards benutzt wird, insbesondere auch unter Verwendung elektronischer Datenverarbeitungsprogramme.

Ulm, den .....

Evelyn Artmann